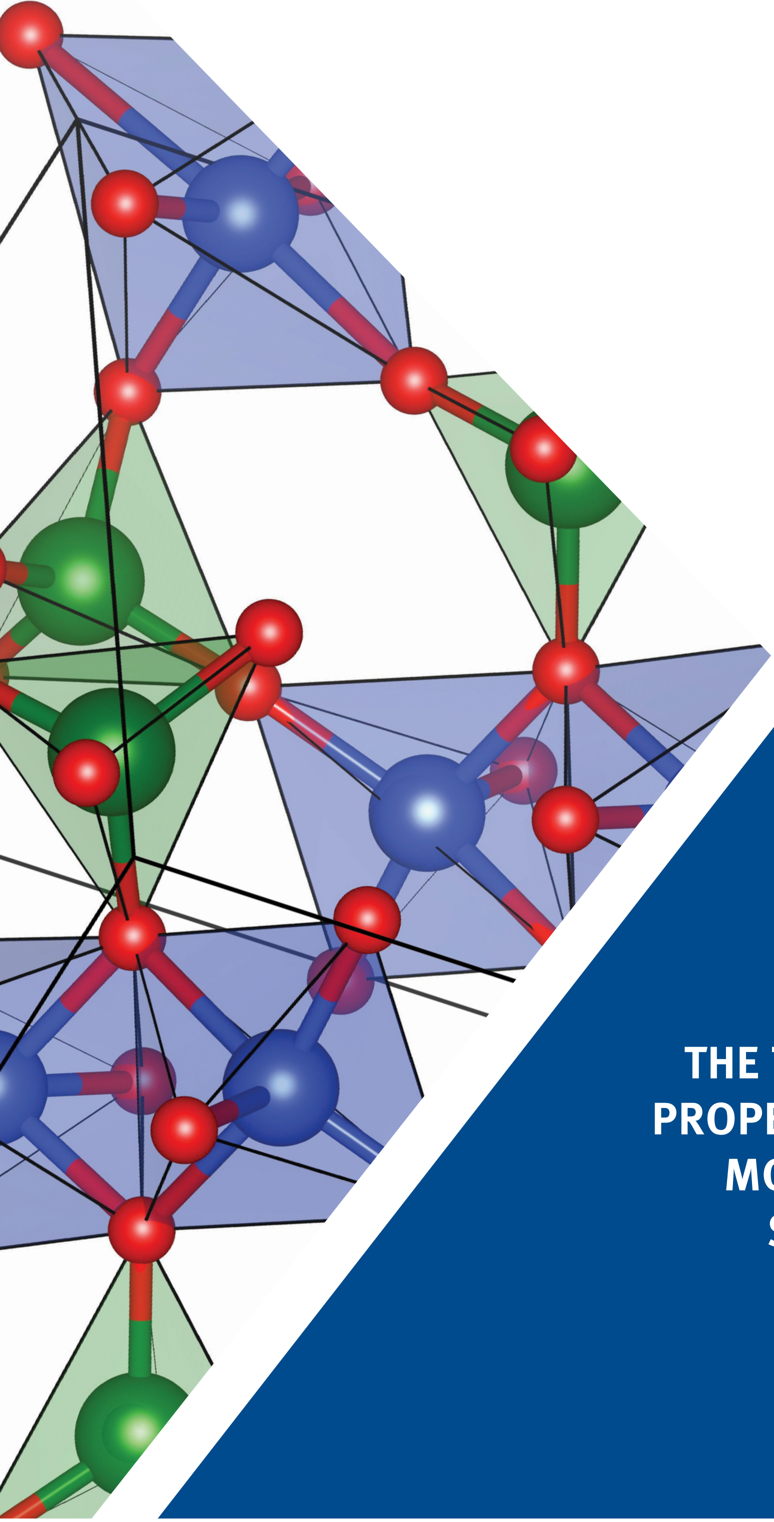

UNIVERSITY
OF LATVIA

Doctoral Thesis

Riga 2022

Inga Pudža

IMPACT OF THE LOCAL STRUCTURE ON THE THERMOCHROMIC PROPERTIES OF COPPER MOLYBDATE AND ITS SOLID SOLUTIONS

Promocijas darbs LOKĀLĀS STRUKTŪRAS IETEKME UZ VARA MOLIBDĀTA UN TĀ CIETO ŠĶĪDUMU TERMOHROMAJĀM ĪPAŠĪBĀM

UNIVERSITY
OF LATVIA

FACULTY OF PHYSICS, MATHEMATICS AND OPTOMETRY

Inga Pudža

IMPACT OF THE LOCAL STRUCTURE ON THE THERMOCHROMIC PROPERTIES OF COPPER MOLYBDATE AND ITS SOLID SOLUTIONS

DOCTORAL THESIS

Submitted for the Doctoral degree in Physics and Astronomy

Subfield of Solid State Physics

Riga 2022

The doctoral thesis was carried out at the Institute of Solid State Physics, University of Latvia from 2017 to 2021.

The thesis contains the introduction, 9 chapters, conclusions and thesis, reference list.

Form of thesis: dissertation in Physics and Astronomy, subfield of solid state physics.

Scientific supervisor:
Dr. phys. **Aleksejs Kuzmins**, senior researcher and the head of the EXAFS Spectroscopy Laboratory at Institute of Solid State Physics, University of Latvia.

Reviewers:

1) *Dr. phys.* **Anatolijs Šarakovskis**, University of Latvia;
2) *Dr. rer. nat.* **Wolfgang A. Caliebe**, Photon Science – Deutsches Elektronen-Synchrotron (DESY) (Germany);
3) Prof. *Ph.D.* **Anatoly I. Frenkel**, Stony Brook University (USA).

The thesis will be defended at the public session of Doctoral Committee of Physics, Astronomy and Mechanics, University of Latvia at 15:00 on May 11, 2022 in the conference hall of the Institute of Solid State Physics of University of Latvia.

The doctoral thesis and its summary are available at the Library of the University of Latvia (Kalpaka blvd 4., Riga) and Latvian Academic Library (10 Rupniecibas Str, Riga).

Chairman of the Doctoral Committee *Dr. phys.* **Anatolijs Šarakovskis**

Secretary of the Doctoral Committee **Agnese Ozoliņa**

Dedicated to the memory of my mum...

Abstract

Copper molybdate ($CuMoO_4$) and related solid solutions are multifunctional materials exhibiting chromic properties, including thermochromism and piezochromism. Their colour change is caused by the lattice expansion/contraction, which affects the band gap, or a modification of the material structure upon a phase transition. Therefore, the knowledge of the structure and its temperature and composition dependence is crucial for understanding and controlling the functionality of these materials that determines their practical applications.

In this thesis, the structure-property relationships in $CuMoO_4$ and two series of solid solutions ($CuMo_{1-x}W_xO_4$ and $Cu_{1-x}Zn_xMoO_4$) were studied by X-ray absorption and resonant X-ray emission spectroscopies (XAS and RXES). The experimental results were supported by the reverse Monte Carlo (RMC) simulations coupled with *ab initio* multiple-scattering calculations. The RXES method was used to determine changes in the local coordination of tungsten ions from the crystal field induced splitting of the 5d(W) states across the phase transitions in $CuMo_{1-x}W_xO_4$ solid solutions.

The obtained results enhance our understanding of the connection between structural and thermochromic properties of $CuMoO_4$ and related compounds. The ability to tune the thermochromic properties of the material to more desired temperature range by the addition of tungsten or zinc ions makes it more promising for applications, for instance, as a cost-effective indicator for monitoring storage/processing conditions of temperature-sensitive products (drugs, vaccines, chemicals, biological materials etc.).

Anotācija

Vara molibdāts ($CuMoO_4$) un tā cietie šķīdumi ir daudzfunkcionāli materiāli, kuriem piemīt vairākas ar krāsu saistītas īpašības, tai skaitā termohromisms un pjezohromisms. To krāsas maiņu izraisa režģa izplešanās/saraušanās, kas ietekmē aizliegto zonu, vai materiāla struktūras izmaiņas, notiekot fāžu pārejai. Zināšanas par struktūru un tās atkarību no temperatūras un sastāva ir svarīgas, lai izprastu un kontrolētu šo materiālu funkcionalitāti, kas galu galā nosaka to praktiskos pielietojumus.

Šajā darbā tiek pētīta korelācija starp struktūru un īpašībām $CuMoO_4$ un divām cieto šķīdumu sērijām ($CuMo_{1-x}W_xO_4$ un $Cu_{1-x}Zn_xMoO_4$), izmantojot rentgenstaru absorbcijas un rezonanses rentgenstaru emisijas spektroskopijas (XAS un RXES). Eksperimentālie dati tiek interpretēti, balstoties uz apgrieztās Monte-Karlo metodes simulācijām kopā ar *ab initio* daudzkārtējās izkliedes aprēķiniem. RXES metode tiek izmantota, lai pēc kristāliskā lauka izraisītās 5d(W) stāvokļu sašķelšanās noteiktu volframa jonu lokālās koordinācijas izmaiņas $CuMo_{1-x}W_xO_4$ cietajos šķīdumos, notiekot fāžu pārejām.

Iegūtie rezultāti uzlabo mūsu izpratni par saikni starp $CuMoO_4$ un saistīto savienojumu strukturālajām un termohromajām īpašībām. Iespēja pielāgot materiāla termohromās īpašības vēlamākiem temperatūras diapazoniem, pievienojot volframa vai cinka jonus, padara to daudzsološāku pielietojumiem, piemēram, kā lētu indikatoru temperatūras jutīgu produktu (zāļu, vakcīnu, ķimikāliju, bioloģisko materiālu utt.) uzglabāšanas/apstrādes apstākļu kontrolēšanai.

Contents

List of Figures

List of Tables

List of abbreviations

ANN	Artificial neural networks
BADF	Bond angle distribution function
BFT	Back-Fourier transform
CMD	Classical molecular dynamics
EA	Evolutionary algorithm
EM	Electromagnetic
EXAFS	Extended X-ray absorption fine structure
FF	Fitness function
FDM	Finite difference method
FMS	Full-multiple-scattering
FT	Fourier transformation
FWHF	Full-width at half-maximum
HERFD	High energy resolution fluorescence detected
LCA	Linear combination analysis
MAD	Median absolute deviation
MC	Monte Carlo
MD	Molecular dynamics
MFP	Mean-free path
ML	Machine learning
MS	Multiple-scattering
MT	Muffin-tin
MSD	Mean-square displacement
MSRD	Mean square relative displacement
NEXAFS	Near-edge X-ray absorption fine structure
NXES	Normal X-ray emission spectroscopy
PBC	Periodic boundary conditions
RDF	Radial distribution function
RMC	Reverse Monte Carlo

RT	Room temperature
RXES	Resonant X-ray emission spectroscopy
SR	Synchrotron radiation
SS	Single-scattering
TEY	Total electron yield
UV	Ultraviolet
WT	Wavelet transform
XAFS	X-ray absorption fine structure
XANES	X-ray absorption near edge structure
XAS	X-ray absorption spectroscopy
XEOL	X-ray excited optical luminescence
XES	X-ray emission spectroscopy
XRD	X-ray diffraction
XRF	X-ray fluorescence

Chapter 1

Introduction

1.1 General introduction and motivation

Smart materials have properties that can be altered in a controllable manner by external stimuli. For instance, they can respond to light, changes in temperature, pressure, pH, electric and magnetic fields. They play an ever-increasing role in our developing society and are widely used in different technological applications.

One such advanced multifunctional material is copper molybdate ($CuMoO_4$) with several perspective chromic properties such as thermochromism, piezochromism, tribochromism, halochromism [1–5]. Copper molybdate also has photoelectrochemical, catalytic and antibacterial features [6–9]. Physical properties of $CuMoO_4$ depend on temperature and/or pressure and can also be affected by modifying its chemical composition [1, 2, 10, 11]. Therefore, the structure-property relationship must be understood to learn how to control the functionality of the material. In this thesis, $CuMoO_4$-based thermochromic compounds are investigated to elucidate the structural origin of their optical properties.

Thermochromic materials change their colour in response to temperature changes. In the solid inorganic materials, a gradual colour change may occur due to the lattice expansion/contraction, which affects the band gap, or a distinct colour change may occur when the structure is modified upon a phase transition [12, p.42].

Pure $CuMoO_4$ has thermochromic properties both at low (100–300 K) and high (400–700 K) temperatures; however, the origin of the observed chromic effects is different. Above room temperature, the material exists in the α-phase, however at low temperatures, $CuMoO_4$ exhibits a reversible structural phase transition between α and γ phases with a hysteretic behaviour, which is accompanied by a drastic colour change between greenish and brownish [1]. Note that the thermochromic phase transition is strongly affected by chemical composition. For instance, the substitution of Mo^{6+} ions in $CuMoO_4$ by W^{6+} results in the formation of $CuMo_{1-x}W_xO_4$ solid solutions with different temperature response. Similarly, the substitution of Cu^{2+} ions by other divalent ions as Zn^{2+} is possible.

In the low-temperature range, the considerable optical contrast between the two polymorphic phases makes $CuMoO_4$ appealing for thermochromic applications, for instance, in the fields where one needs to monitor storage/transportation conditions of temperature-sensitive products (food, drugs, vaccines, chemicals, biological materials, etc.). At the same time, such inorganic materials with a thermochromism at high temperatures (above 400 K) attract much attention because of their potential applications for temperature sensing in the ranges where the majority of organic compounds and liquid crystals are unstable [13]. Possible chromic applications extend from user-friendly temperature and pressure indicators [2, 3, 10, 14] to cost-effective "smart" inorganic pigments and sensors [15].

Thermochromic properties of $CuMoO_4$ and related materials are closely connected with the local atomic structure of constituting metal ions. The knowledge of the structure is crucial for understanding and optimizing the properties of materials which ultimately determine their practical applications.

A breakthrough in the study of the atomic structure of materials is associated with the discovery of X-rays in 1895 by German physicist Wilhelm Röntgen. Nowadays, large scale research infrastructures such as synchrotron radiation (SR) facilities play a decisive role in science for studying the structure and dynamics of materials since they provide high intensity, tunable electromagnetic (EM) radiation in a wide spectral range, including X-rays. Theoretical calculations and modelling are equally important in structural studies.

The main experimental techniques for structural studies are X-ray diffraction (XRD) and X-ray absorption spectroscopy (XAS). XRD provides information on the long-range order in the material, while XAS probes the local atomic structure around a specific chemical element. Both methods complement each other.

Today SR sources are available worldwide, and XAS has become an extremely valuable technique for characterising materials. The structural information in XAS is encoded in tiny fluctuations of the X-ray absorption coefficient. It is common to divide the X-ray absorption spectrum into two parts: X-ray absorption near edge structure (XANES), located near the absorption edge, and extended X-ray absorption fine structure (EXAFS), which extends far beyond the edge. Though the two parts have the same physical origin, their distinction is convenient for the interpretation.

The first observations of EXAFS were published more than 100 years ago [16]. Since then, significant progress in the field of XAS has been made. Both instrumentation and theory have developed. However, the experimental XAS data interpretation still might be challenging, especially for low-symmetry materials as tungstates and molybdates.

During the past years, significant efforts have been made to develop advanced data analysis approaches based on atomistic simulations to improve the reliability, accuracy and amount of structural information that can be extracted from experimental EXAFS spectra. EXAFS "sees" the structure of a material as averaged over a huge number of "frozen" atomic configurations, in each of which all atoms are slightly displaced from their equilibrium position due to thermal vibrations. Advanced theoretical technique such as reverse Monte Carlo (RMC) provides a natural way to incorporate static and thermal disorder into the structural model and allows one to extract information encoded in X-ray absorption spectra, thus opening new possibilities for the investigation of the structure-property relationships. However, the RMC method is a computationally complex and time-consuming approach.

A complementary technique to XAS is resonant X-ray emission spectroscopy (RXES). It probes a second-order process that includes both X-ray absorption and subsequent emission. By selectively extracting the emitted photon intensity in the narrow energy range that corresponds to the transitions between energy levels with long lifetimes, one can obtain high energy resolution fluorescence detected XAS spectrum (HERFD-XAS spectrum) with a drastically enhanced sensitivity to the local coordination of the absorbing atoms.

Thus, a combination of XAS, RXES and theoretical studies might shed light on the correlation between structural and functional properties of such materials as $CuMoO_4$ and its solid solutions.

1.2 Aim and objectives of the work

The **aim** of this study is to explore and explain the relationship between the structure and thermochromic properties of copper molybdate ($CuMoO_4$) and its solid solutions with tungsten ($CuMo_{1-x}W_xO_4$) and zinc ($Cu_{1-x}Zn_xMoO_4$) using X-ray absorption and resonant X-ray emission spectroscopies.

The **objectives** of the study are:

- to synthesise and characterize a set of pure $CuMoO_4$, $CuWO_4$, $ZnMoO_4$ compounds and two series of $CuMo_{1-x}W_xO_4$ and $Cu_{1-x}Zn_xMoO_4$ solid solutions;
- to perform temperature and composition-dependent X-ray absorption and resonant X-ray emission spectroscopies studies of $CuMo_{1-x}W_xO_4$ and $Cu_{1-x}Zn_xMoO_4$ solid solutions at synchrotron radiation facilities;

- to analyse experimental X-ray absorption and RXES spectra using modern theoretical approaches based on *ab initio* (full-) multiple-scattering theory and reverse Monte Carlo simulations to obtain structural information on the local environment of absorbing atoms;
- to understand the structure-thermochromic properties relationship in the studied materials.

1.3 Scientific novelty of the work

The research presented in the thesis consists of both experimental (XAS and RXES measurements at synchrotron radiation facilities supplemented with lab-based techniques) and theoretical (computer simulations) parts. The results of the research are of scientific novelty and have been published in several international journals.

The impact of the W^{6+} ions on the local environment in thermochromic solid solutions $CuMo_{1-x}W_xO_4$ has been studied for the first time by XAS and RXES. It was found that an increase of tungsten content promotes the coordination change of molybdenum atoms from tetrahedral to octahedral that is accompanied by the material colour change from greenish to brownish.

XAS data analysis was performed using modern theoretical approaches, including the RMC method. It was shown that the structural model obtained in RMC calculations can be employed to incorporate thermal disorder effects in XANES simulations and to interpret temperature-dependent experimental XANES data.

In $CuMoO_4$, a specific dynamic effect has been discovered at the Cu K-edge. It is associated to different rigidity of metal-oxygen coordination polyhedra and influences the thermochromic properties of $CuMoO_4$ above room temperature.

For the first time $Cu_{1-x}Zn_xMoO_4$ were studied by XAS and it was found that, among sampled solid solutions, only $Cu_{0.90}Zn_{0.10}MoO_4$ exhibits the thermochromic phase transition with a hysteretic behaviour. It is explained by the instability of molybdenum coordination which changes from tetrahedral to octahedral under lattice contraction at low temperatures.

1.4 Author’s contribution

The presented research consists of both experimental and theoretical parts. Main experiments were conducted at international synchrotron radiation facilities. During the period 2015-2021, the Author has taken part in 17 experiments using synchrotron radiation that have been carried out at PETRA

III (Hamburg, Germany), ELETTRA (Trieste, Italy) and SOLEIL (Paris, France) synchrotrons. In particular, three XAS and one RXES experiments are directly relevant to the present work.

Sample synthesis, XRD measurements and experimental XAS and RXES data processing using different programs was performed by the Author at the Institute of Solid State Physics, University of Latvia (ISSP, UL). All RMC simulations with EvAX code [17] as well as theoretical XANES calculations with FDMNES code [18,19] have been carried out by the Author at the Latvian SuperCluster facility [20]. Interpretation of the obtained results was performed in collaboration with the supervisor.

The Author has participated in 9 international summer schools during 2014-2021. The results of the research have been presented at 20 international conferences and workshops. The main results have been published in 21 SCI papers, and the Author is the first contributor for 11 of them. 8 scientific publications are directly related to this thesis. The h-index of the Author is 7.

1.5 Contents of the thesis

This thesis is organized into 12 chapters. The first chapter includes general introduction and motivation where the scope of the thesis is defined, as well as the objectives, scientific novelty and contribution of the Author are stated.

Chapter 2 is devoted to the overview of an X-ray absorption spectroscopy (XAS) method. The fundamental physical principles and experimental aspects concerning XAS are given.

Chapter 3 includes the description of XAS (both XANES and EXAFS) data analysis. A brief overview of recently developed simulation-based techniques such as molecular dynamics, machine learning and reverse Monte Carlo for EXAFS data interpretation is given. Reverse Monte Carlo method with evolutionary algorithm approach widely used in this thesis is described more in details.

Chapter 4 is devoted to the overview of a resonant X-ray emission spectroscopy (RXES) method. Advantages of RXES over XAS are listed and information encoded in the experimental RXES plane is discussed.

State of the art related to $CuMoO_4$ and its solid solutions is reviewed in Chapter 5.

The following Chapter 6, contains details about the synthesised samples and their characterization. Important technical aspects of XAS and RXES experiments are also included.

In Chapters from 7 to 10, the main results regarding structural investigations of $CuMoO_4$, $CuMo_{1-x}W_xO_4$ and $Cu_{1-x}Zn_xMoO_4$ are reported. First, the low-temperature XAS study of a thermochromic phase transition between α and γ phases in pure $CuMoO_4$ is described. It is shown that the hysteresis loop of the phase transition is well evident from the Mo K-edge XANES spectra. Two approaches of EXAFS data interpretation using regularization-based technique and reverse Monte Carlo method with evolutionary algorithm approach (RMC/EA) are presented. Next, high-temperature XAS data are analysed and XANES sensitivity to thermal disorder is discussed. The origin of strong temperature-dependent variation of the Cu K-edge XANES spectra is correlated with the thermochromic properties of the material.

In Chapters 8 and 9, we discuss the role of W^{6+} ions on the structure and thermochromic properties of $CuMo_{1-x}W_xO_4$ solid solutions based on XAS and RXES data analysis. The influence of Zn^{2+} ions on the properties of $Cu_{1-x}Zn_xMoO_4$ solid solutions is discussed in Chapter 10.

Chapter 11 contains the summary and the most important conclusions. Finally, the main theses of this study are given in Chapter 12.

In the Appendix, the lists of publications and conferences where the research results were presented are given. The international schools and experiments at international synchrotron radiation facilities where the Author has participated are also listed.

Chapter 2

X-ray absorption spectroscopy (XAS)

2.1 Basic theory of XAS

2.1.1 Phenomenological description of XAS

X-rays are EM radiation, discovered by Wilhelm Röntgen in 1895, with a wavelength λ in the range of 0.01–10 nm corresponding to the energies in the range of $\sim$100 eV to 100 keV. The relationship between wavelength and energy is given by the equation $\lambda(nm) = hc/E(eV) = 1239.84/E(eV)$, where h is the Plank's constant and c is the speed of light. Depending on the energy, X-rays are usually divided into three regions: soft X-rays (below 2 keV), tender X-rays (between 2 keV and $\sim$8 keV) and hard X-rays (above $\sim$8 keV).

In a photoelectric X-ray absorption process, an X-ray photon is absorbed by an electron in a tightly bound quantum core level (K, L or M shell) of an atom, as shown in Fig. 2.1.1 [21]. The absorption phenomenon of EM radiation is described by the Beer-Lambert law:

$$I(E) = I_0(E)e^{-\mu(E)x}, \tag{2.1}$$

where $I_0(E)$ is the incident X-ray intensity, x is the sample thickness, $I(E)$ is the intensity of radiation transmitted through the sample, and $\mu(E)$ is the linear absorption coefficient describing the fraction of an X-ray beam that is absorbed per unit thickness of the absorber. Since the linear absorption coefficient $\mu(E)$ depends on the density ρ of the material, mass absorption coefficient ($\mu_a(E)$=$\mu(E)/\rho$) is often used:

$$I(E) = I_0(E)e^{-\mu_a(E)\rho x}. \tag{2.2}$$

For a material composed of n elements with concentrations c_1, c_2, ..., c_n (%), the total mass absorption coefficient μ_a is calculated as:

$$\mu_a = \frac{1}{100}\sum_{i=1}^{n} c_i \mu_{a,i}. \tag{2.3}$$

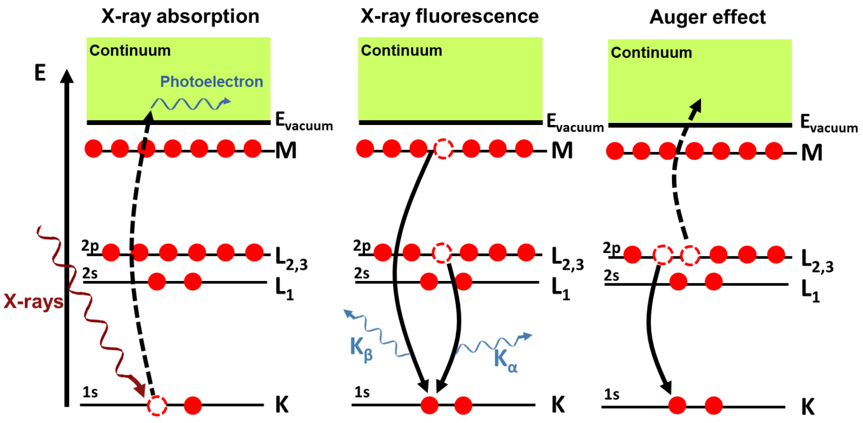

Figure 2.1.1: **A scheme of the photoelectric effect:** the atom absorbs an X-ray photon and the 1s core electron is promoted out of the atom to the continuum, creating a photoelectron and a core hole (left panel); Decay of the excited state – X-ray fluorescence (middle panel) and Auger effect (right panel).

The flux of photons propagating through the material is reduced exponentially due to the interactions of the incident radiation with atoms in the probed sample. Thus, in the transmission XAS experiment, the incident intensity I_0, and the transmitted intensity I are measured to obtain μx as a function of the X-ray energy E. The absorption coefficient characterizes the material and depends on the density of the sample ρ, the atomic number Z, relative atomic mass A, and the X-ray energy E and can be described by the empirical relation [21]:

$$\mu(E) \approx \frac{\rho Z^4}{AE^3}. \tag{2.4}$$

Due to the proportionality $\mu(E) \sim Z^4$, the absorption coefficient for light and heavy elements is very different, and good contrast between different materials can be obtained.

However, the smooth energy dependence of the absorption coefficient predicted by Eq. 2.4, is interrupted at specific energies by a sharp rise in the absorption, so-called absorption edges or absorption jumps. They occur when the incident X-ray energy is equal to that of the binding energy of a core-level electron, which is excited in the photoabsorption process [21]. Therefore, energy positions of absorption edges are characteristics of a given element. Depending on the electronic level being involved ($1s$, $2s$, $2p_{1/2}$, $2p_{3/2}$, etc.), the absorption edges of elements are denoted as K, L_1, L_2, L_3, etc. edges.

Thus, one can selectively choose the element to probe by tuning the X-ray energy to the desired absorption edge region. Energies of absorption edges are tabulated for all elements of the periodic table and those corresponding to the core levels of heavy elements are well separated in the energy space. The edge

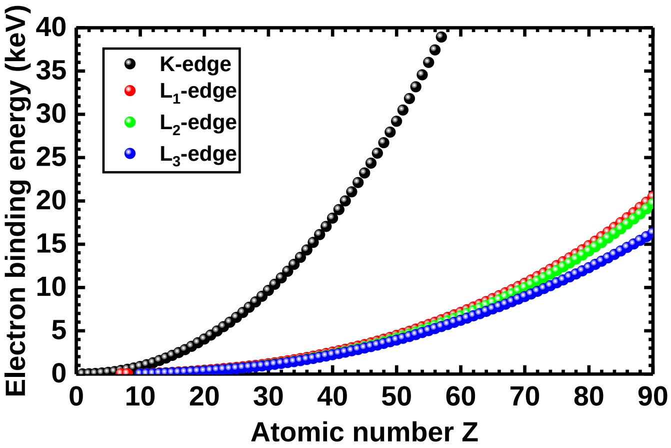

Figure 2.1.2: **Electron binding energies as a function of atomic number Z.**

energies E_0 vary with the atomic number approximately as Z^2 (Fig. 2.1.2) [22]. Corresponding energies of the atomic core levels for the atoms studied by XAS in this thesis are summarized in Table 2.1.1.

Table 2.1.1: **Energies of the absorption edges for selected elements.**

Z	Atomic symbol	Absorption Edge	Energy (eV)
29	Cu	K	8979
30	Zn	K	9659
42	Mo	K	20000
74	W	L_3	10207

After the X-ray absorption event, the atom is left in the excited state with a positively charged core hole (empty place at the electronic level) whose characteristic lifetime[1] is $\sim 10^{-15}$s. The lifetime of the excited state is much smaller than the characteristic time of thermal motion ($\sim 10^{-13} - 10^{-14}$s), thus the position of all surrounding atoms does not change during the photoabsorption process [23]. However, the presence of the core hole induces relaxation of all other electrons in the atom, so that its excited state differs from the ground one. Finally, the atom returns into the ground state via one of the relaxation processes, which is accompanied either by the emission of an X-ray photon (X-ray fluorescence) or by the ejection of an Auger electron (Fig. 2.1.1).

In the case of X-ray fluorescence (XRF), an electron from a higher energy level fills the deeper core hole while emitting a photon with a well-defined energy corresponding to the difference between these two levels. The energy

---

[1] The characteristic lifetime τ can be evaluated from the Heisenberg's uncertainty principle $\Delta E \Delta \tau \sim \hbar/2$, where ΔE is ar natural width of an electronic level.

of the emitted XRF photon is also in the X-ray range[2] and is a characteristic of the atom. For instance, the electronic transition between L and K or M and K electron levels results in K_α or K_β emission lines, respectively (Fig. 2.1.1).

The second decay process, the Auger effect, involves electron transition from the higher electronic level to the empty core level and simultaneous excitation to the continuum or ejection of the second electron. The probability of whether relaxation occurs by XRF or Auger emission depends on atomic number Z and energy level. Light elements with small Z relax mainly non-radiatively via the production of Auger electrons, whereas relaxation of heavy elements is mostly radiatively with the emission of XRF photons. In the hard X-ray regime (E>10 keV), XRF has a larger probability to occur than the Auger emission. The probability of emission is directly proportional to the absorption probability, so either of the two processes can be used to measure the absorption coefficient μ indirectly [21].

An example of the W L_3-edge X-ray absorption spectrum of tungsten foil measured in the transmission mode is shown in Fig. 2.1.3. The absorption edge at E_0=10207 eV corresponds to the excitation of the $2p_{3/2}$ electron to the empty 5d-states. The amplitude of the absorption edge depends on the sample thickness x and the absorbing chemical element concentration. The shape of the absorption edge and the region around it are governed by the electronic (density of unoccupied states) and atomic (number and type of neighbouring atoms) structure of the material.

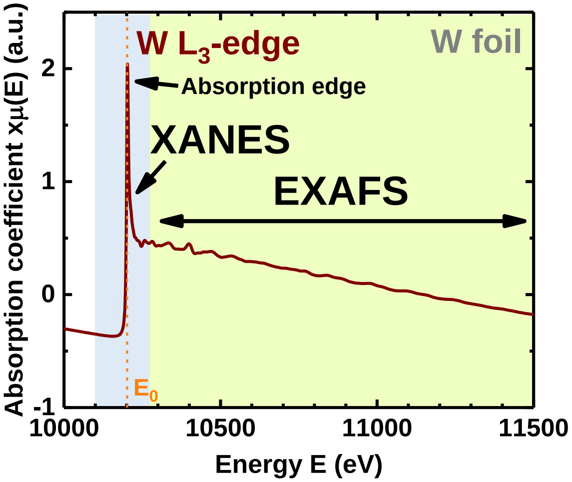

Figure 2.1.3: **X-ray absorption spectrum $x\mu(E)$ of tungsten foil at the W L_3 absorption edge**, showing the near-edge (XANES) region and extended fine structure part (EXAFS).

---

[2] Electrons from shallow levels will release ultraviolet (UV) or visible light. It is exploited in the X-ray excited optical luminescence (XEOL) method [24, p.12].)

As it is shown in Fig. 2.1.3, the X-ray absorption spectrum can be divided into two parts: X-ray absorption near edge structure (XANES), also known as near-edge XAFS (NEXAFS), located around the absorption edge (up to ∼30-50 eV after the edge), and extended X-ray absorption fine structure (EXAFS), which extends far (thousands of electronvolts) beyond the absorption edge. The border between the two regions is not strictly defined. Though the physical origin of both regions is the same, some important approximations allow one to interpret the extended part of the spectrum in a more quantitative way than it is possible for the XANES part.

The EXAFS region contains information on the local atomic structure around the absorbing element (spatial arrangements of nearest neighbours around the absorbing atoms), including pair and many-atom distribution functions. From the EXAFS analysis, one can get information on the coordination numbers, interatomic distances, and their variations due to the static and thermal disorder.

The XANES part is sensitive to the density of unoccupied electronic states near the Fermi level and gives information on the local electronic structure, local symmetry of the probed element, oxidation state and multi-electron effects. Therefore, the analysis of EXAFS and XANES regions gives complementary information.

2.1.2 Origin of X-ray absorption fine structure (XAFS)

During the photoabsorption process, the X-ray energy is transferred to the core electron which is excited and often called a **photoelectron**. The maximum kinetic energy E_k that the photoelectron can reach is:

$$E_k = \frac{m_e v^2}{2} = E - E_0, \tag{2.5}$$

where m_e is the mass of the electron, E is the incident photon energy and E_0 is electron binding energy, i.e. the minimum energy required to eject the photoelectron (it is also called a threshold energy [21]). On the other hand, E_k can be expressed as:

$$E_k = \frac{p^2}{2m_e} = \frac{\hbar^2 k^2}{2m_e}, \tag{2.6}$$

where $p = h/\lambda_e$ – the momentum of an electron, $k = 2\pi/\lambda_e$ – the wavenumber of the electron, and $\hbar = h/2\pi$ (the reduced Planck constant). λ_e is the de Broglie wavelength of an electron. Thus, one can obtain the relationship between the wavevector k, X-ray photon energy E, and the biding energy E_0[3]:

$$k = \sqrt{\frac{2m_e}{\hbar^2}(E - E_0)}. \tag{2.7}$$

So, the ejected photoelectron can be viewed as a spherical wave that propagates away from the absorbing atom and is scattered at the neighbouring atoms (Fig. 2.1.4).

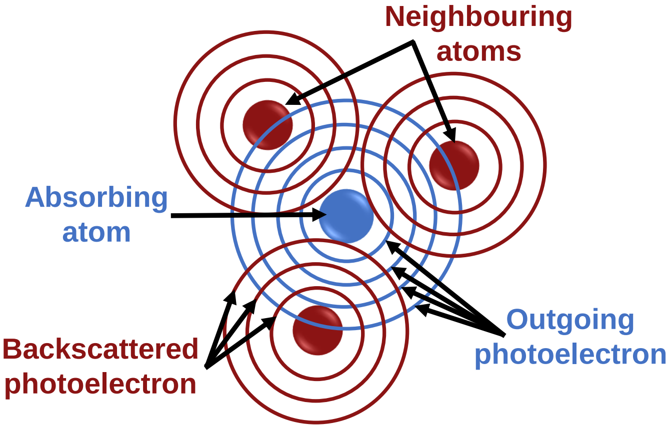

Figure 2.1.4: **Photoelectron scattering by neighbouring atoms.**

The origin of the oscillating structure – X-ray absorption fine structure (XAFS) in the X-ray absorption spectrum is the interference between the excited photoelectron (outgoing spherical photoelectron wave) and photoelectron waves scattered by potentials of all atoms surrounding the absorbing atom. Therefore, the photoelectron scattering process is affected by the local atomic environment of the material. The interference at the absorbing atom modulates the absorption probability (absorption coefficient μ), giving rise to an increase when the interference is constructive or a decrease when it is destructive (Fig. 2.1.5).

In the case of EXAFS, we are interested in the oscillations above the absorption edge. Therefore, the X-ray absorption coefficient μ(E) can be expressed as:

$$\mu(E) = \mu_0(E)[1 + \chi(E)], \tag{2.8}$$

where $\mu_0(E)$ corresponds to the absorption of an isolated atom and $\chi(E)$ describes the oscillatory part of the spectrum.

---

[3] One can rewrite the equation above with numerical values and if energies E and E_0 are given in eV, the wavenumber k(Å^{-1})=0.51232$\sqrt{E - E_0}$.

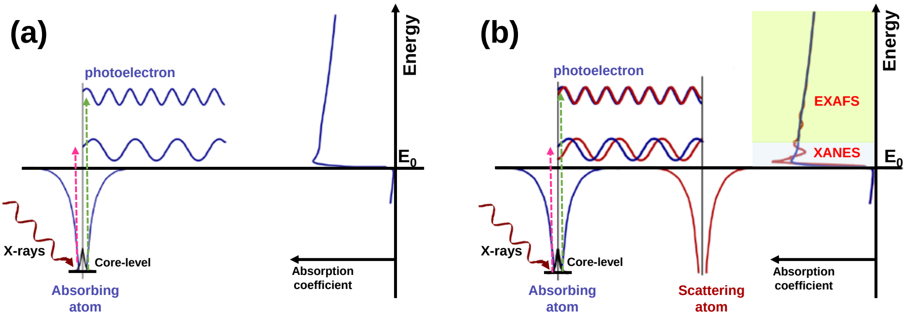

Figure 2.1.5: **Illustration of an X-ray absorption process:** When incident X-ray energy coincides with the core electrons binding energy E_0, the absorption coefficient has a sharp rise. The core electron is excited to the continuum, and the photoelectron is created, which travels as a wave with the wavenumber $\lambda \sim (E - E_0)^{-1/2}$ (a); The photoelectron interaction with the neighbouring atom (scattering) that results in a modulation of the photoelectron wave function at the absorbing atom and oscillations in the XAS – XAFS (b).

2.1.3 Fermi's Golden rule

The X-ray absorption process can be described by Fermi's Golden rule [21,25]. In general, it gives the probability of the transition between two quantum states of an atom (an initial (ground) state $|i\rangle$ and a final (excited) state $|f\rangle$) due to some interaction described with an operator $\hat{\mathcal{H}}$. In the case of X-ray absorption (Fig. 2.1.6), the initial state $|i\rangle$ includes an atom with all core levels filled and an X-ray photon, while a final state $|f\rangle$ has one electron (the photoelectron) excited to a higher energy level (localized or delocalized) and other electrons relaxed due to the presence of the core hole with a positive charge.

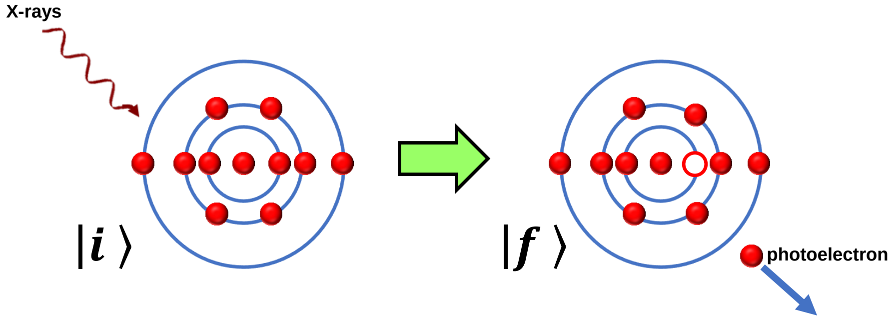

Figure 2.1.6: **Initial and final states of an atom during the X-ray absorption process.**

The transition between two states takes place due to the absorption of an X-ray photon, and its probability can be described with the squared scalar product $|\langle f| \hat{\mathcal{H}} |i\rangle|^2$. The operator $\hat{\mathcal{H}}$ describes the interaction of the electron with the photon and can be treated in a dipole or quadrupole approximation.

The absorption coefficient μ is proportional to the probability of transition to a new state [21]:

$$\mu(E) \propto \left| \langle f | \hat{\mathcal{H}} | i \rangle \right|^2 \rho(E_f), \tag{2.9}$$

where $\rho(E_f)$ is the density of empty electronic states.

In the X-ray absorption spectra, the electric-dipole-induced ($\hat{\mathcal{H}} = \hat{\epsilon} \cdot \vec{r}$) transitions dominate, so that the electric dipole selection rules have to be applied[4]: $\Delta l = \pm 1$, $\Delta j = 0, \pm 1$, $\Delta s = 0$, and the projection of the orbital angular momentum on the quantization axis $\Delta m_l = 0, \pm 1$. For example, the K-edge X-ray absorption spectrum corresponds to transitions from $1s_{1/2}$ level to empty np states, L$_2$-edge from $2p_{1/2}$ level to empty $nd_{3/2}$ states and, L$_3$-edge from $2p_{3/2}$ level to empty $nd_{3/2}$ and $nd_{5/2}$ states. Transitions from $2p$ to ns states are also allowed but have a very low intensity and are usually neglected.

The initial state $|i\rangle$ is not very affected by the surrounding atoms because the core-level electron is strongly bound to the absorbing atom. At the same time, the final state $|f\rangle$ is strongly affected by the neighbouring atoms, since the excited photoelectron interacts with their potentials.

One can split $|f\rangle$ into two contributions: one that is the isolated atom's part $|f_0\rangle$ and the second part that corresponds to the change in photoelectron's final state due to the scattering from the neighbouring atoms Δf as:

$$|f\rangle = |f_0\rangle + |\Delta f\rangle \,. \tag{2.10}$$

Then, the X-ray absorption coefficient $\mu(E)$ can be expressed as:

$$\mu(E) \propto \left| \langle f | \hat{\mathcal{H}} | i \rangle \right|^2 \rho(E_f) = \mu_0(E)[1 + \chi(E)], \tag{2.11}$$

where $\mu_0(E) = \left| \langle f_0 | \hat{\mathcal{H}} | i \rangle \right|^2$ and the oscillatory part of the absorption coefficient is:

$$\chi(E) \propto \langle \Delta f | \hat{\mathcal{H}} | i \rangle \,. \tag{2.12}$$

Equation above indicates that the EXAFS originates from the interaction of the initial absorbing atom and the scattered portion of the photoelectron.

---

[4] The electronic state of an electron in an atom is defined by quantum numbers with a general form "nl_j", where n is the principal quantum number, l is the orbital angular momentum and $j = l + s$ – the total angular momentum, where s is the spin quantum number ($s = \pm 1/2$ for an electron).

2.2 XAS experiment

2.2.1 Synchrotron radiation

A tunable monochromatic X-ray source with high stability and intensity is required for XAS. Thought during the last decades there has been remarkable progress with lab-based equipment [26], the primary X-ray source used for XAS measurements is a synchrotron which is 10^{11} times brighter[5] than a conventional X-ray tube. A synchrotron radiation (SR) source provides a highly collimated X-ray beam in a broad range of energies – from infrared to hard X-rays. The first SR sources were available to scientists at around the 1970s. Four generations of synchrotron radiation facilities have been developed till now. ESRF-EBS synchrotron in France after its upgrade in the year 2020 belongs to the fourth generation. During these years, the quality of XAS data has increased significantly.

Synchrotron radiation is the EM radiation emitted in the tangential direction to the trajectory by charged particles (usually electrons) which are travelling with a speed close to the speed of light (relativistic velocities) along trajectories curved by a strong magnetic field. A scheme of a typical synchrotron is shown in Fig. 2.2.1. Electrons are first produced in the electron gun, where they can be ejected from a heated metal filament by thermionic emission. Next, electrons are accelerated by the evacuated linear accelerator using electric fields, and then they enter a booster ring where they are accelerated further until the corresponding energy of the main storage ring is reached (typically few GeV). In the storage ring the kinetic energy of the electrons is kept constant (for instance, $\sim$2 GeV at Elettra and $\sim$6 GeV at PETRA-III in 2020).

Electrons are injected into the storage ring where they remain circulating and are used for electromagnetic radiation generation. In both the booster and the storage ring, the electrons are required to remain in a closed orbit. Every time the magnets deflect the path of electrons circulating in the storage ring, they emit synchrotron radiation forwards in a narrow cone, at a tangent to the electron's path. Strong magnetic fields are applied perpendicular to the electron trajectory by bending (dipole) magnets or the so-called insertion devices (undulators and/or wigglers), made from arrays of magnets with alternating polarity. During radiation emission, electrons lose their energy, and therefore in some parts of the storage ring, a radio-frequency electromagnetic field is applied to additionally accelerate the slowest particles and regain desired energy. By employing different optical elements (mirror

---

[5] A figure-of-merit called "spectral brightness" equals the intensity expressed in photons per second, divided by the product of the horizontal and vertical beam divergences, the source size, and the relative spectral bandwidth [27].

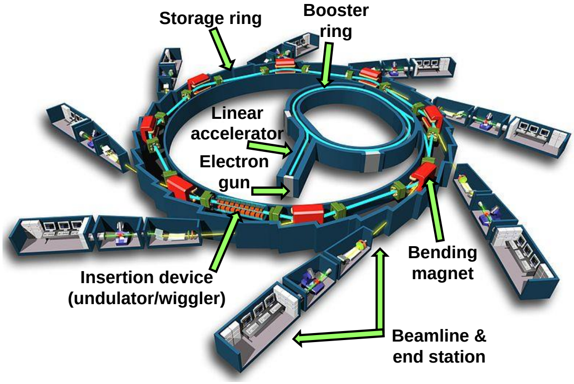

Figure 2.2.1: **A schematic diagram of a typical synchrotron radiation source (adapted, Copyright ©EPSIM 3D/JF Santarelli, Synchrotron Soleil):** Charged particles (typically electrons) produced via an electron gun are accelerated in a linear accelerator and then additionally in the booster ring. Once the particles reach high enough speeds, they are injected into the storage ring where they are traveling continuously in their orbits. The trajectories of charged particles in the storage ring are perturbed either by a bending magnet or by insertion devices (undulators or wigglers). As a result of such perturbation, synchrotron radiation is emitted. The beam of EM radiation is exploited in beamlines dedicated to different experiments.

systems, crystal monochromators, X-ray lenses, filters etc.), the emitted synchrotron radiation is directed towards beamlines.

2.2.2 X-ray absorption experiment

During the XAS experiment, the X-ray absorption coefficient $\mu(E)$ is measured as a function of the incident X-ray energy. The typical experimental setup for XAS measurements at the synchrotron is shown in Fig. 2.2.2. The monochromator consists of two parallel and nearly perfect crystals that are typically made from silicon and cut along a specific crystallographic plane direction (e.g., Si(111), Si(311)). X-rays with a particular wavelength λ are selected by rotating monochromator crystals so that they satisfy Bragg's law:

$$n\lambda = 2dsin\theta, \tag{2.13}$$

where d is the crystal lattice spacing, θ is the incidence angle for the X-rays and n is an integer (Bragg order). X-ray mirrors with different coatings (e.g., Si, Rh, Pt) located before the monochromator are used to remove higher harmonics (X-rays when $n > 1$) contributions.

A monochromatic X-ray beam is irradiating the sample and the intensities of incident I_0 and transmitted I_1 X-rays are measured with ionization chambers filled with an appropriate amount of inert gas (such as N_2, Ar, Kr). The X-rays ionize the gas atoms and released electrons and charged ions follow the electric

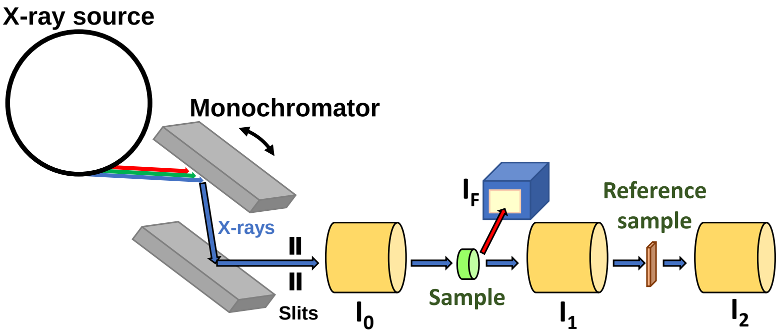

Figure 2.2.2: **A schematic representation of an experimental setup for XAS measurements:** X-ray source, monochromator, tree ionization chambers for X-ray intensity detection: I$_0$ - before the sample, I$_1$- after the sample, I$_2$- after the reference sample and a fluorescence detector for X-ray fluorescence I$_F$ registration.

field applied across the ionization chamber and generate a small current ($\sim$ several pA). This current is proportional to the X-rays intensity. The current signal is amplified and converted into the voltage signal. A series of slits are employed to define the X-ray profile at the sample.

Usually, together with the sample, a reference sample (e.g., metal foil) containing the same absorbing element as in the investigated sample is also measured to control the stability of the energy scale during measurements. The same reference sample is initially used for the energy scale calibration. In the transmission regime absorption coefficient $\mu(E)$ for the sample can be calculated by the equation:

$$\mu(E) = \frac{1}{x} ln \frac{I_0(E)}{I_1(E)}, \tag{2.14}$$

where x is the sample thickness. Analogously, for the reference (ref) sample $\mu_{ref}(E) = \frac{1}{x_{ref}} ln \frac{I_1(E)}{I_2(E)}$, where I_2 corresponds to the intensity after the reference sample (Fig. 2.2.2). Note that it is not necessary to know the exact sample thickness since the contribution of this term is cancelled out during the normalization procedures made during standard XAS data processing.

Additionally, an XRF detector can be employed for indirect XAS measurements:

$$\mu \propto I_F/I_0, \tag{2.15}$$

where I_f is the fluorescence intensity associated with the absorption process. The solid-state XRF detector (typically with Ge or Si as the X-ray absorber) is located perpendicular with respect to the X-ray beam to reduce the background signal originated from the elastic scattering. To better face the detector, the sample is rotated by 45° with respect to the incoming X-ray beam. Measurements in XRF mode are usually performed for samples on thick substrates or diluted samples (down to the ppm level). For thick and concentrated samples the spectral features suffer from distortions (amplitude reduction) due to the fact that in the concentrated sample X-ray beam that hits an atom has already interacted with previous atoms, which changes the spectrum of X-ray radiation – the self-absorption effects [28, 29].

Similarly, an X-ray absorption coefficient $\mu(E)$ can be measured using Auger electron yield and total electron yield (TEY) modes and X-ray excited optical luminescence (XEOL) mode. X-ray absorption experiments can be realized using different sample environments, for instance, it is possible to install a cryostat, furnace and equipment for high-pressure or different *in situ* and *in operando* experiments. Thus, it is possible to study the evolution of the local structure of the sample as a function of different parameters.

2.2.3 Powder sample preparation

For XAS measurements in transmission mode, the sample should be sufficiently homogeneous, with a size larger than the X-ray beam (on the scale of μm^2), and have an optimal thickness x to ensure an appropriate signal-to-noise ratio. Also, the concentration of absorbing atoms in the sampled area should be high enough to ensure significant X-ray absorption. At the same time, the sample should not absorb too much, since X-ray intensity I_2 has to be measured after passing the sample. A good practice is to carefully adjust the amount of the sample to have an absorption jump $\Delta\mu x$ equal to about 1.0 and total absorption - μx less than $\sim$3 [30, p. 87].

One of the powder sample preparation techniques that usually allows one to obtain highly homogeneous samples is the deposition on nitrocellulose Millipore filter (Fig. 2.2.3(a)). The powder is ground in an agate mortar and suspended in distilled water or other appropriate liquid using an ultrasonic bath. Then the obtained suspension is filtered through the Millipore membrane using the filtration set with a vacuum or water pump. Finally, the sample is dried in air and fixed to the membrane using Kapton or Scotch tape. However, an organic filter membrane is not heat-resistant; thus, this sample preparation techniques cannot be applied for high temperature measurements.

An alternative is to make a pellet by employing a diluent material that is transparent to X-rays and is heat resistant, for instance, boron nitride (BN). In this case, the BN powder is ground and mixed with the sample powder in an agate mortar. Usually, about 100–200 mg of boron nitride is enough for a 13 mm diameter pellet. Then the mixed powder is inserted into the pressing die between two punches and pressed together using a hydraulic pellet press (Fig. 2.2.3(b)). For X-ray measurements at room and low temperatures, cellulose powder can be used to make a pellet.

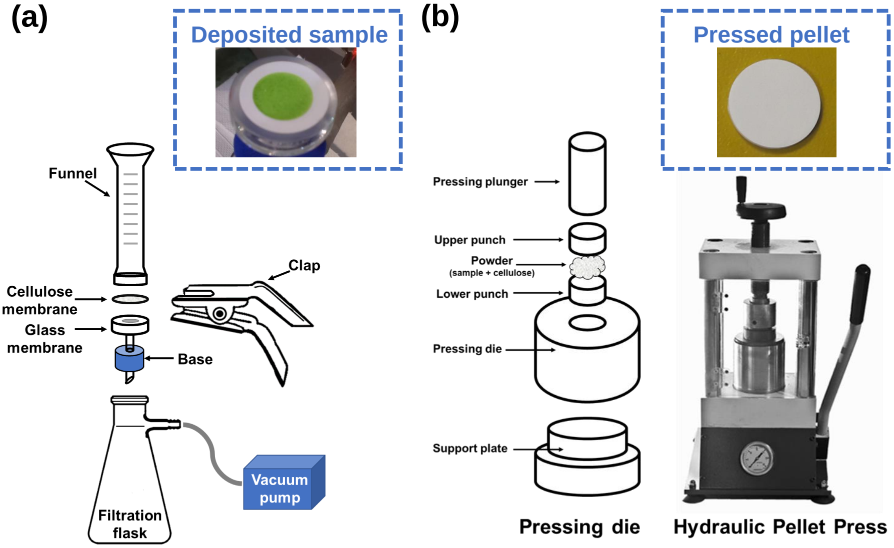

Figure 2.2.3: **Powder sample preparation methods for XAS measurements:** (a) deposition on a cellulose membrane filter and (b) pressing of a pellet with cellulose.

If there is a small amount of the sample or the concentration of absorbing atoms is too low to achieve a reasonable signal-to-noise ratio, measurements in the fluorescence mode can be done.

2.3 Extended X-ray absorption fine structure (EXAFS)

2.3.1 EXAFS data reduction

The experimental X-ray absorption spectrum $\mu(E)$ can be decomposed into three contributions (Fig. 2.3.1): background absorption $\mu_b(E)$ originated from the excitations of electrons with smaller binding energies, the atomic absorption $\mu_0(E)$ which is a smooth background function corresponding to the absorption of an isolated atom, and the EXAFS $\chi(E)$ oscillations due to the excited photoelectron scattering by the potentials of surrounding atoms. EXAFS $\chi(E)$ can be extracted from the experimental spectrum $\mu(E)$ as:

$$\chi(E) = \frac{\mu(E) - \mu_0(E) - \mu_b(E)}{\mu_0(E)}. \tag{2.16}$$

Several program packages such as EDA [31], Athena [29], XAESA [32], Larch [33] are available for XAS data processing. The background ($\mu_b(E)$) and atomic ($\mu_0(E)$) contributions are determined empirically by fitting a

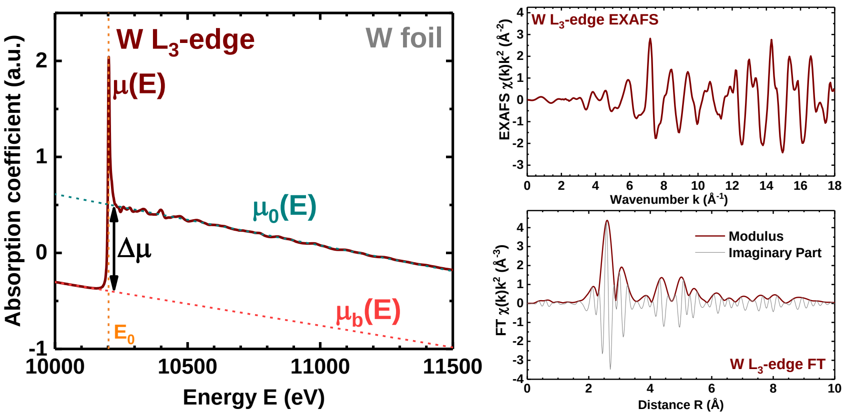

Figure 2.3.1: **EXAFS data reduction (left panel), extracted EXAFS spectrum $\chi(k)k^2$ and its Fourier transform (right panels).**

polynomial or spline functions to the experimental data $\mu(E)$ in the pre-edge and post-edge regions. The difference between $\mu_0(E)$ and $\mu_b(E)$ functions at the threshold energy E_0 is known as the absorption jump $\Delta\mu$. The energy scale of the EXAFS $\chi(E)$ is defined relative to the value of E_0 corresponding to the zero kinetic energy of the photoelectron, i.e. the wavenumber $k = 0$. It is more common to rewrite EXAFS as a function of wavenumber $\chi(k)$ using relation $k = \sqrt{\frac{2m_e}{\hbar^2}(E - E_0)}$. An example of the W L$_3$-edge EXAFS for tungsten foil is shown in Fig. 2.3.1.

Since the EXAFS oscillations $\chi(k)$ decay quickly with k, they are usually multiplied by k^n, where n most often is 2 or 3. Such k-weighting allows one both emphasize features at large k values and suppress oscillations in the XANES region that can be poorly described by the EXAFS theory and are more sensitive to the inaccuracies in the background subtraction and estimation of the energy reference E_0 [34, p.19].

2.3.2 EXAFS equation

The increasing quality of the experimental data obtained at synchrotron radiation sources coupled with advances in computer technologies was a driving force for developing accurate theories to analyse experimental results. The experimental EXAFS spectrum $\chi(k)$ contains information on the local atomic structure around the absorbing atom, including pair and many-atom correlation functions. Pair correlation functions, also known as radial distribution functions (RDFs), contribute into EXAFS through the single-scattering (SS) processes. Many-atom correlation functions give origin to the multiple-scattering (MS) events when the photoelectron scatters from more than one atom before returning back to the absorbing atom. Therefore, the real-space MS theory [25] is used for a quantitative description of EXAFS.

As mentioned before, EXAFS originates due to the interference between outgoing and backscattered from neighbouring atoms photoelectron waves. The EXAFS spectrum can be described within the MS approximation as a sum of contributions of different scattering paths [25]:

$$\chi(k) = \sum_{n=2}^{\infty} \chi_n(k), \tag{2.17}$$

$$\chi_n(k) = \sum_i A_n(k, R_i) \sin(2kR_i + \phi_n(k, R_i)), \tag{2.18}$$

where $\chi_n(k)$ includes contributions from the (n-1)–order scattering processes of the excited photoelectron by the potentials of neighbouring atoms before it returns to the absorbing atom. $A_n(k, R_i)$ is the total EXAFS amplitude, and $\phi_n(k, R_i)$ corresponds to the total phase shift. Since the scattering process of the photoelectron by an atom depends on its energy and the scattering angle, the scattering functions $A_n(k, R_i)$ and $\phi_n(k, R_i)$ dependent on both the photoelectron wavenumber k and path geometry R_i.

While the series is infinite, in reality, only the first few terms produce a significant contribution to the total EXAFS $\chi(k)$, because of the finite lifetime of the excited state, the disorder and cancellation effects. This simplifies the theoretical description of the spectrum. Single-scattering (n=2), double-scattering (n=3) and triple-scattering (n=4) effects are usually the most important ones (Fig. 2.3.2), however, in some cases higher-order MS processes should be also considered.

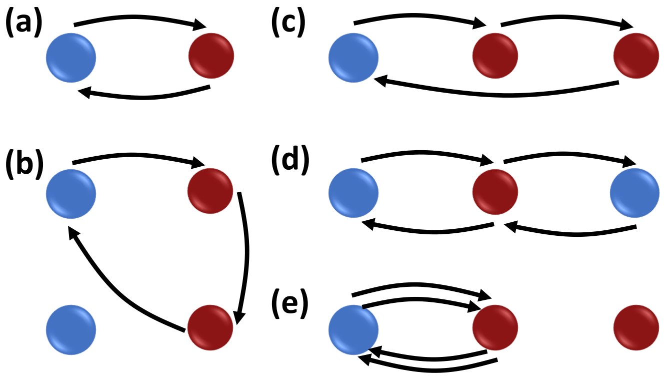

Figure 2.3.2: **Different photoelectron scattering paths:** single-scattering (a), double-scattering (b), linear double scattering (c), triple-scattering (d,e).

For an in instantaneous atomic configuration, Eq. 2.18 can be rewritten in a more conventional way [25,35,36] as:

$$\chi_n(k) = S_0^2 \sum_i \frac{N_i |f_i(k,R_i)|}{kR_i^2} \sin(2kR_i + 2\delta(k) + \phi_i(k,R_i)) e^{\frac{-2R_i}{\lambda(k)}}. \quad (2.19)$$

In the SS approximation, R_i is half-length of the scattering path (i.e., the radius of the i-th coordination shell), and N_i is the number of atoms in the i-th coordination shell (the coordination number). The backscattering amplitude $f(k)$ and phase shift $\phi(k)$ of the photoelectron depend on the type of the neighbouring atom (its atomic number Z). Thus, EXAFS has chemical sensitivity. Distinct atoms contribute differently to the EXAFS spectrum. However, the scattering functions for elements which are neighbours in the Periodic Table are quite close and cannot be reliably discriminated. One can distinguish between two elements if their Z differs by 5 or so [21]. The phase shift of the absorbing atom $\delta(k)$ is taken into account twice since the photoelectron is leaving and returning to the absorbing atom. An example of scattering functions is shown in Fig. 2.3.3(a-c).

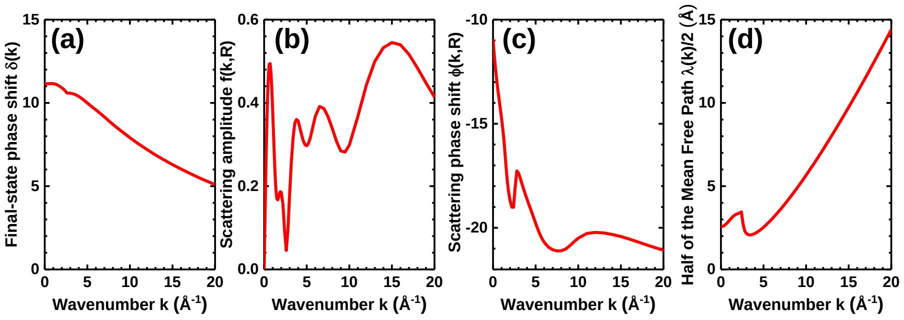

Figure 2.3.3: **Scattering functions of tungsten in bcc W calculated by the FEFF code [25,37]:** the absorbing atom phase shift $\delta(k)$ (a), the backscattering amplitude $f(k,R)$ (b), the backscattering phase shift $\Phi(k,R)$ (c) and the half of the effective mean free path of the photoelectron $\lambda(k)/2$ (d).

Half of the effective mean-free path (MFP) $\lambda(k)/2$ (Fig. 2.3.3(d)) gives an estimate of how far the excited photoelectron can propagate from the absorbing atom to be able to return before the core hole is filled. $\lambda(k)$ depends strongly on the photoelectron wavenumber k. Terms $e^{-2R/\lambda(k)}$ and $\frac{1}{kR^2}$ are responsible for the reduction of the contribution of distant coordination shells and make the EXAFS a local probe with a possibility to extract structural information up to about 10 Å [23,38].

The parameter S_0^2 accounts for the reduction of the EXAFS amplitude due to the multi-electron effects [25]. It strongly correlates with the coordination number N. Typically the S_0^2 has values between 0.7 and 1. It can be calculated theoretically [25] or obtained from the analysis of the reference compound with known structure.

Since the time-scale of the photo-absorption process (10^{-16}-10^{-17} s) is much shorter than the characteristic time of thermal vibrations (10^{-13}-10^{-14} s), the atoms are considered to be "frozen" at their instantaneous positions. Thus, the measured EXAFS is an average over all atomic configurations during the time of the experiment. The effect of thermal disorder within the harmonic approximation is introduced in Eq. 2.18 through the additional exponential term $e^{-2\sigma_i^2 k^2}$:

$$\chi_n(k) = S_0^2 \sum_i \frac{N_i |f_i(k,R_i)|}{kR_i^2} \sin(2kR_i + 2\delta(k) + \phi_i(k,R_i)) e^{\frac{-2R_i}{\lambda(k)}} e^{-2\sigma_i^2 k^2}. \tag{2.20}$$

This equation is known as a conventional EXAFS formula [25]. Here, σ^2 is called the Debye-Waller factor or the mean-square relative displacement (MSRD) factor, i.e., the relative variation of interatomic distance. It is responsible for damping of EXAFS amplitude with increasing wavenumber k and determines its temperature dependence. Indeed, σ^2 describes both thermal disorder σ_{th}^2 and static disorder σ_{st}^2, so that:

$$\sigma^2 = \sigma_{th}^2 + \sigma_{st}^2. \tag{2.21}$$

The MSRD factor extracted from EXAFS data contains information on relative rather than absolute atomic displacements and is affected by the correlation between atomic displacements. For example, if displacements from equilibrium positions of atoms A and B are $\vec{u}_A^2$ and $\vec{u}_B^2$, respectively, then the MSRD factor σ_{AB}^2:

$$\sigma_{AB}^2 = \langle \vec{u}_A^2 \rangle + \langle \vec{u}_B^2 \rangle - 2\langle \vec{u}_A \vec{u}_B \rangle, \tag{2.22}$$

where $\langle \vec{u}_A^2 \rangle$ and $\langle \vec{u}_B^2 \rangle$ are the mean-square displacement (MSD) factors probed by diffraction experiment and $\langle \vec{u}_A \vec{u}_B \rangle$ term describes the correlation of atomic motion.

If the interatomic distances have a more complex distribution that do not correspond to the simple Gaussian distribution (as in harmonic approximation), Eq.2.18 can be rewritten in a form:

$$\chi_n(k) = S_0^2 \int_0^{+\infty} g_i(R) \frac{|f_i(k,R_i)|}{kR_i^2} e^{\frac{-2R_i}{\lambda(k)}} \sin(2kR_i + 2\delta(k) + \phi_i(k,R_i)) dR, \tag{2.23}$$

where $g_i(R)$ corresponds to the radial distribution function (RDF). The number N of atoms with distances between R$_{min}$ to R$_{max}$ then can be calculated by simple integral:

$$N = \int_{R_{min}}^{R_{max}} g(R) dR. \tag{2.24}$$

2.3.3 EXAFS spectrum processing

One can decompose the total EXAFS signal into separate contributions corresponding to different coordination shells by employing Fourier filtering procedure. The contribution from the nearest atoms containing only SS effects can be analysed separately because high-order (n>2) scattering effects have longer path lengths.

The different oscillation frequencies present in $\chi(k)$ correspond to contributions from atoms located at different distances (coordination shells) or from higher-order scattering paths. The direct Fourier transform (FT) allows one to transfer EXAFS spectrum into the R-space and, thus, to visualize contributions from different scattering paths:

$$FT(R) = \sqrt{\frac{2}{\pi}} \int_{k_{min}}^{k_{max}} \chi(k) k^n W(k) e^{-2ikR} dk, \tag{2.25}$$

where $W(k)$ is the so-called window function, and k^n is the weighting factor. Note that FT(R) is a complex function. The modulus of the Fourier transform is equal to:

$$|FT(R)| = \sqrt{\Re(FT(R))^2 + \Im(FT(R))^2}, \tag{2.26}$$

where $\Re(FT(R))$ and $\Im(FT(R))$ are, respectively, real and imaginary parts of the FT(R) function. The window function $W(k)$ softens the abrupt behaviour of the $\chi(k)$ spectrum at k_{min} and k_{max}. For instance, 10%-Gaussian, Kaiser-Bessel and Hanning window functions are widely used [29].

As one can see in the right bottom panel in Fig. 2.3.1, FT(R) of the W L_3-edge EXAFS contains several relatively well-defined peaks as a function of the distance R. Note that positions of these peaks do not correspond to crystallographic distances from the absorbing atom due to the phase shift of the backscattered photoelectron. The crystallographic distances are slightly larger by about 0.3-0.5 Å and can be determined from the analysis of the EXAFS spectrum. Furthermore, not all of these peaks correspond to a particular bond (but are rather overlap of several contributions, including MS).

The contribution $\chi_{1st-shell}(k)$ of the first coordination shell into the total EXAFS spectrum can be obtained using the back-Fourier transform (BFT):

$$\chi_{1st-shell}(k) = BFT(k) = \frac{1}{k^n W(k)} \sqrt{\frac{2}{\pi}} \int_{R_{min}}^{R_{max}} FT(R) e^{2ikR} dR, \tag{2.27}$$

where R_{min} and R_{max} define the range of the isolated coordination shell in R-space. It can be further fitted in the SS approximation using the theoretical model described by the Eq. 2.20. As a result of the best fit, the coordination number N, interatomic distance R and the MSRD factor σ^2 corresponding to the first coordination shell can be obtained. The analysis of outer shells requires more advanced approaches due to the contribution of MS effects.

2.3.4 *Ab initio* EXAFS calculations

The total EXAFS spectrum corresponds to the average of the EXAFS signals for all absorbing atoms of the same type in the atomic configuration. These signals can be calculated by *ab initio* EXAFS codes such as FEFF [25, 37] or GNXAS [39].

The theoretical EXAFS spectra in this thesis are computed using *ab initio* self-consistent real space multiple-scattering approximation, also called the real-space Green's function approximation, implemented in the FEFF8.5L code [25, 37].

The calculations are performed for a cluster of atoms centered on the absorbing one. The cluster potential is described in the so-called muffin-tin (MT) approximation, in which potentials V_i of individual atoms located at sites $\vec{R}_i$ are spatially localized and are spherically symmetric, while the interstitial potential V_{mt} between the MT spheres is constant (Fig. 2.3.4). The total potential can be written in the form:

$$V_{tot}(\vec{r}) = V_{mt} + \sum_i V_i(\vec{r} - \vec{R}_i). \tag{2.28}$$

The radius of the muffin-tin sphere is selected based on the Norman criterion [37]. If spheres overlap, charge transfer can also occur. Such simple MT potential approximation works rather well in the EXAFS range, however, non-muffin-tin corrections to the potential are often required in the XANES range [18].

In this thesis, the complex energy-dependent exchange-correlation Hedin-Lundqvist potential was employed to account for inelastic effects, which determine the mean-free path of the photoelectron [25]. The core-hole natural broadening was included in tabulated form as reported in [40].

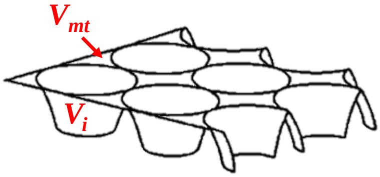

Figure 2.3.4: **Model of the muffin-tin potential.** Potentials of individual atoms V_i and interstitial potential V_{mt} are indicated.

Chapter 3

XAS data analysis

3.1 Analysis of X-ray absorption near-edge structure (XANES) spectra

3.1.1 XANES features

Spectral features in the XANES originate from the transition of the excited photoelectron to unoccupied localized and delocalized states. These features contain information on the atomic and electronic structure of the material. The XANES region is sensitive to changes in oxidation state, coordination chemistry, local structure and ligand symmetry around the absorbing atom. The resolution of XANES features is determined by the excited state lifetime. It can be improved by exploiting the high energy resolution fluorescence detected XANES (HERFD-XANES) spectroscopy described in Chapter 4.

In the XANES region, the photoelectron has a large mean-free path, therefore it participates in a huge number of scattering events, which take place on a large number of atoms. So, fitting and modelling of XANES features can be challenging, and most often this region is used as a fingerprint to identify chemical species in mixtures and complex materials. In this case, the XANES spectrum of the investigated sample is compared with the references having known atomic and electronic structure.

During the XANES analysis, one should pay attention to (i) the position of the absorption edge, (ii) the intensity of XANES features, (iii) the presence and intensity of the XANES pre-edge features and (iv) the post-edge region [41].

The position of the absorption edge is directly related to the oxidation state of the absorbing atom. An increase of its effective atomic number Z_{eff} with oxidation state increases the binding energy of the core electron, leading to a small shift of the absorption edge to the higher energies. Such shift is called the chemical shift. Since a definition of the absorption edge is not certain, it is common to set its value to the maximum of the first derivative of the normalized XAS spectrum [21]. Note that the edge position is affected not only by the Z_{eff} but also by the coordination geometry and configuration of the valence electrons [42, p.18].

3.1.2 Linear combination analysis of XANES

Linear combination analysis (LCA) is a semi-quantitative method that allows one to quantify the relative amount of chemical species in mixtures and multiphase compounds contributing to the averaged XAS spectrum [43, p.218]. It is well suited for situations when the absorber may be found in different local environments, phases or chemical states.

During the LCA, the normalized experimental spectrum $\mu(E)$[1] is fitted to a theoretical curve $\mu_{th}(E)$ which is calculated as a linear combination of normalized reference spectra:

$$\mu(E) = \sum_j \alpha_j \mu_{th}(E), \tag{3.1}$$

where α_j is a fraction of photo-absorbers in the corresponding local environment or chemical state.

LCA requires good quality of reference spectra. Both the investigated samples and references should be measured during the same experimental run to avoid ambiguities due to different set-up configurations. For instance, the energy resolution strongly affects the smoothness of the XANES features.

3.1.3 Theoretical XANES calculations

Quantitative description and interpretation of XANES requires theoretical calculations of the absorption coefficient $\mu(E)$ based on the Eq.2.9. Significant development has been made in the *ab initio* XANES modelling. Nowadays, it is possible to calculate XANES spectra within *ab initio* full multiple scattering (FMS) formalisms for a given structure model by employing codes like FEFF [25, 44] and FDMNES [18, 19]. FDMNES calculations can be also performed based on the finite difference method (FDM). This approach allows free potential shape, thus avoids the muffin-tin approximation. However, it is more time consuming and computing power demanding.

Direct fitting of the structural parameters to experimental XANES features can be done by codes like MXAN [45] and FitIt [46]. Recently supervised machine learning (ML) and artificial neural networks (ANN) have been demonstrated as a great tool for extracting structural parameters from XANES spectra [47]. Note that such interpretation of experimental data strongly depends on the precision of the *ab initio* XANES calculations.

---

[1] LCA can be done on XANES data in energy and derivative space, EXAFS in energy ($\chi(E)$) or k-space ($\chi(k)$), or on the BFT of EXAFS [34, p.222].

3.2 EXAFS curve fitting

While XANES contains information on the chemical state and symmetry around the absorbing atom, EXAFS analysis gives more detailed information on the local atomic environment.

A set of structural parameters (NS_0^2, R, σ^2) can be obtained by nonlinear least-square fitting of the experimental data with a theoretical model based on Eq. 2.20. It is known as a conventional EXAFS analysis [25]. Additionally, E_0 and S_0^2 parameters have to be determined. Since there is a strong correlation between the E_0 and interatomic distances R, it is essential to align the experimental spectra and the theory on the same wavenumber scale. For that one needs to adjust the E_0 position for the experimental data till there is an agreement in the frequency (especially in the low-k range) with the theoretically calculated EXAFS. An alternative is to shift the theoretically calculated spectrum. S_0^2 parameter correlates with the coordination number N; thus, it should be determined in advance for a reference compound with a known structure.

The $f_i(k), \phi_i(k)$ that are non-structural functions, and $\lambda(k)$ should be calculated theoretically for each scattering path with codes like FEFF [29, 37, 44] and GNXAS [39] or extracted from experimental data measured for a reference compound. Practically, the MS contributions up to the 8^{th} order can be calculated using *ab initio* real space MS FEFF code [25,37].

Computer codes like EDA [31], FEFFIT [48], Arthemis [29], Larch [33], XAESA [32] can be used for EXAFS curve fitting. However, due to the MS contributions at larger distances, most often the analysis of only the first coordination shell of the absorbing atom can be analysed without further significant approximations. The contribution from the first shell is isolated by performing direct-FT (Eq. 2.25) and BFT (Eq. 2.27) of the experimental EXAFS signal.

The conventional EXAFS data analysis may underestimate some of the structural parameters if large disorder (static or thermal) is present and the bond-lengths cannot be approximated with a Gaussian distribution. One can try to solve this problem by the mathematical model employing $g(R)$ functions with a more complex shape or by the expansion of $g(R)$ in the cumulant series [41]. Cumulant decomposition may be advantageous for the analysis of anharmonic effects, thermal expansion, nanoparticles and materials with medium disorder [23]. For strongly distorted materials cumulant series might not converge.

An alternative is the regularization-like approach [31] described in the next section or simulation-based EXAFS analysis (see Section 3.5).

3.3 Regularization-based technique

The first coordination shell analysis can be done with a regularization-based technique, realised, for example, in EDARDF [31] program. It has an advantage over the conventional multi-component fitting in cases of strongly distorted or disordered local environment as one finds, for instance, in amorphous compounds and low-symmetry crystals like tungstates and molybdates where the Janh-Teller effect is one of the reasons for strongly distorted structural units.

The fitting is done by employing general EXAFS expression Eq. 2.23. This approach is model-independent and, thus, does not require any preliminary assumptions on the coordination of absorbing atoms. Regularization-based approach solves the common least-square-fitting problem [49]. Two regularizing criteria have to be satisfied after each iteration to limit the shape of the RDF $g(R)$ to physically significant solutions. Firstly, $g(R)$ must be a non-negative function, so if there are negative values, they are changed to zeros. Secondly, $g(R)$ is expected to be a smooth function; therefore a smoothing algorithm is applied to eliminate possible non-physical behaviour such as steps, breaks and sharp peaks [49]. The initial approximation for $g(R)$ is chosen arbitrarily (for example, Gaussian). The theoretical backscattering amplitude and phase shift functions, used in Eq. (2.23), can be calculated using the FEFF code [25,37].

As a result of the regularization process, the RDF $g(R)$ and corresponding EXAFS $\chi(k)$ can be obtained for each experimental first-shell signal.

3.4 Thermal and static disorder

The MSRD factor σ^2 in Eq.2.20 is responsible for the exponential reduction of the EXAFS signal at higher k values limiting available information that can be extracted from EXAFS data measured at high temperatures or for disordered materials.

For a perfect crystal the RDF for one coordination shell would be $g(R) = N_i\delta(R-R_i)$, where $\delta(R-R_i)$ is Dirac delta function and N_i is the coordination number – number of atoms at distances R_i. However, distributions of atomic positions are smeared out due to the static and thermal disorder, and so is the RDF. In Gaussian approximation, the RDF is expressed as:

$$g_i(R) = \frac{N_i}{\sqrt{2\pi\sigma_i^2}} e^{-\frac{(R-R_i)^2}{2\sigma_i^2}}, \tag{3.2}$$

where R_i is an average interatomic distance and σ_i^2 corresponds to the MSRD factor. Note that the distance R_i probed by EXAFS is the averaged distance between the two atoms while diffraction allows one to estimate the equilibrium distance R_{eq} (distance between average atomic positions) (Fig. 3.4.1). Thus, $R_i > R_{eq}$ [34, p.266].

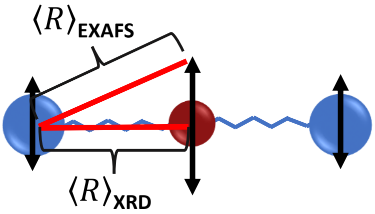

Figure 3.4.1: **An average interatomic distance probed by EXAFS and XRD.**

The contribution of thermal disorder σ^2_{th} is related to the density of vibrational states and interatomic bond strengths [41, 50]:

$$\sigma^2_{th}(T) = \frac{\hbar}{2\mu} \int_0^{\omega_{max}} \frac{d\omega}{\omega} \rho(\omega) \coth\left(\frac{\hbar\omega}{2k_B T}\right), \tag{3.3}$$

where k_B is Boltzmann's constant, μ is reduced mass of involved atoms, $\rho(\omega)$ is local projected phonon density of states and ω – vibrational frequency. Within Debye model, $\rho(\omega)$ is expressed as:

$$\rho(\omega) = \frac{3\omega^2}{\omega_D^3} \left(1 - \frac{sin(\omega R/c)}{\omega R/c}\right), \tag{3.4}$$

where $c = \omega_D/k_D$, $k_D = \left(\frac{6\pi^2 n}{V}\right)^{\frac{1}{3}}$, and V/n term corresponds to crystal volume per atom. The Debye model reproduces relatively well MSRD factors for mono-atomic systems (e.g., metals) with one atom per unit cell, where only acoustic phonons are present [51].

An alternative is to use a correlated Einstein model [50] where the density of phonon states is approximated with a Dirac-delta function so that $\rho(\omega) = \delta(\omega - \omega_E)$ and:

$$\sigma^2_{th}(T) = \frac{\hbar}{2\mu\omega_E} \coth\left(\frac{\hbar\omega_E}{2k_B T}\right), \tag{3.5}$$

where ω_E is a characteristic vibrational frequency or simply an Einstein frequency. It is connected to the effective bond-stretching force constant κ [50] and the characteristic Einstein temperature Θ_E as:

$$\kappa = \mu\omega_E^2, \tag{3.6}$$

$$\Theta_E = \frac{\hbar\omega_E}{k_B}. \tag{3.7}$$

The Einstein model is more suitable for systems where optical phonons with a narrow dispersion dominate in the vibrational spectrum.

When one is interested in the approximation of the temperature dependence of the MSRD factor, both the Einstein and Debye models can be used to describe σ^2_{th} since the difference between the two approximations is typically less than the uncertainty of the MSRD factor values estimated from the experimental data [51].

3.5 Simulation-based EXAFS analysis

3.5.1 Introduction

In crystalline and nanocrystalline materials, EXAFS contains valuable information on distant coordination shells determined by MFP of the photoelectron. Several coordination shells included in the conventional EXAFS fitting procedure make interpretation of the experimental data challenging because of many fitting parameters and correlation between them. According to the Nyquist criterion maximum number of fitting parameters that can be included in the EXAFS model is

$$N_{par} = \frac{2\Delta k \Delta R}{\pi}, \tag{3.8}$$

where Δk and ΔR are intervals of the EXAFS spectrum in the k- and R-spaces, respectively.

The analysis of outer coordination shells requires more advanced approaches due to the contribution from many-atom distribution functions – MS effects. Furthermore, there is additional EXAFS signal damping due to the thermal disorder for higher temperature measurements.

In the meantime, it is simple to calculate the EXAFS spectrum for corresponding structure, taking into account MS effects by employing Eqs. 2.17-2.18 and compare it with an experimental one. However, EXAFS probes a “frozen” atomic configuration with all atoms slightly displaced from their equilibrium positions due to the thermal vibrations. One needs to include that into the theoretical structure model. Several simulation-based techniques may be used to solve this issue and have a static and thermal disorder in the structural model (Fig. 3.5.1).

For instance, molecular dynamics (MD) methods [52, 53] allow one to follow the evolution of atomic coordinates in time. However, interatomic forces have to be provided in advance. During *ab initio* MD simulations Newton equations of motion are solved based on Schrödinger equation. Note that such *ab initio* calculations demand an intensive use of high-performance

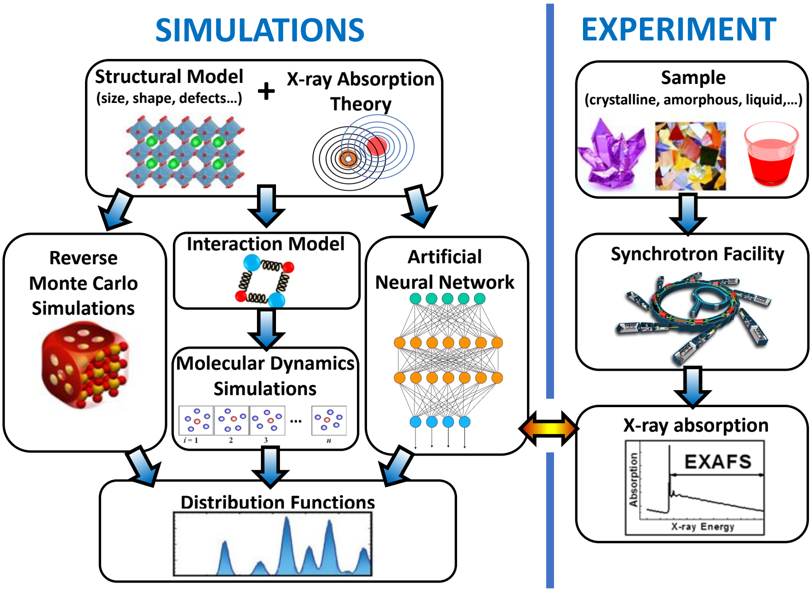

Figure 3.5.1: **A simplified scheme of X-ray absorption spectra analysis using reverse Monte Carlo, molecular dynamics and artificial neural network methods.**

computing sources. Classical MD exploits empirical potentials and significantly reduces the requirements for computing sources.

An alternative method to MD is the Monte Carlo (MC) method [54], which does not require to use Newton equations. Basically, in MC method atoms are randomly shifted away from their equilibrium positions in the structure model to minimize the total energy of the system so that it follows a particular energy distribution. Also, in this case, it is necessary to define a force field to describe interatomic interactions. The MC method is time-consuming and computationally demanding.

Nevertheless, the agreement between experimental and theoretically calculated data strongly depends on the interatomic potential accuracy. Small deviations in the structure model may lead to significant mismatch with experimental data. Thus, an inverse problem – building a structure model from the experimental spectrum might give much better agreement between the spectrum from the optimized structure and experimental one.

Reverse Monte Carlo (RMC) method is an atomistic simulation approach based on the iterative random changes within atomic structure model of the material aimed to minimize the difference between structure-sensitive calculated and experimentally determined functions [55]. This method does not require any knowledge of interatomic potentials as it is in conventional MC or MD simulations.

Recently, machine learning (ML) algorithms based on artificial neural networks (ANN) have been demonstrated as a valuable tool for *in situ* and *in operando* X-ray absorption spectra analysis for distant coordination shells [56].

A more detailed description of mentioned simulation-based techniques having potential for EXAFS data interpretation is provided below.

3.5.2 Molecular dynamics (MD) method

Molecular dynamics (MD) is a method to simulate the motion of atoms in the structural model of the material under defined environmental conditions (for example, temperature, pressure) [57, 58]. As a result, a time-dependent 3D structure model of the material is obtained. The first MD simulations combined with EXAFS data analysis were performed in the middle 1990s to study the hydration of ions in aqueous solutions [23]. The idea of the method is shown in the Fig. 3.5.1.

During the classical MD (CMD) simulations, the Newton equations of motion describe the evolution of the system in time. For each atom in the system, one can apply an equation:

$$\vec{F} = m\frac{d\vec{v}}{dt}. \tag{3.9}$$

If the force $\vec{F}$ acting on the atom is known, it is possible to determine the instantaneous acceleration $d\vec{v}/dt$ of the atom and obtain its trajectory. The force can be determined from the potential used in the calculations, which describes the potential energy between the particular atom under consideration and the surrounding atoms. Relationship between potential energy U and force $\vec{F}$ is evaluated as:

$$\vec{F} = -\frac{\partial U}{\partial \vec{r}}. \tag{3.10}$$

Thus, the motion of atoms depends on the force of atomic interaction which are determined by the choice of potential parameters. When performing modelling, it is necessary to obtain optimal values for all variable parameters in the used potential function. Material properties, such as elastic constants, atomic coordinates, elementary cell dimensions, obtained by other methods, are used to optimize potential parameters. The potential is considered to be good if the sum D of the weighted squared difference between the known values of the material properties f_i^{obs} and the calculated values f_i^{calc} is minimal:

$$D = \sum_{i=1}^{N} \omega_i (f_i^{calc} - f_i^{obs})^2, \tag{3.11}$$

where w_i is the weighting factor and N is the number of parameters to be considered. By changing the potential parameters, the values of f_i^{calc} are changed. By performing D minimization, the optimal values of the potential parameters are obtained.

MD calculations can be performed in NVT (canonical ensemble), NPT (isothermal-isobaric ensemble) or NVE (micro-canonical ensemble) approximations. Each letter in the ensemble name refers to a value that will be kept constant during modelling (N – total number of particles used in the simulation, V – volume, T – temperature, P – pressure, E – total system energy). Remaining values not mentioned in the ensemble name may change arbitrarily during the simulation. To maintain a constant temperature or pressure, the model uses a thermostat or barostat, respectively (special algorithms that provide the required temperature/pressure).

As a result of MD simulations, atomic coordinates, trajectories and velocities are obtained as functions of time.

The MD-EXAFS method, integrated, for instance, in the EDACA code [59, 60], combines MD calculations with X-ray absorption experimental data and allows to evaluate the quality of the atomic interaction potential (force-field) used in the theoretical calculations. The theoretical EXAFS spectrum can be calculated for each atomic configuration obtained in MD modelling. By comparing the experimental EXAFS signal of the material with the time-averaged spectrum in the calculations over all atomic configurations, it is possible to validate the force-field model used in MD. If the agreement between experiment and calculated EXAFS spectrum is good, the corresponding structure model can be used for the experimental data interpretation.

An example of the MD-EXAFS method applied to bcc tungsten L_3-edge is shown in Fig. 3.5.2. The CMD simulations were performed in the NVT ensemble with periodic boundary conditions by the GULP4.3 code [52]. The simulation box with bcc tungsten crystal structure was a $7\times7\times7$ supercell containing 686 atoms. The MD simulations were performed by employing two force-field models: the Finnis-Sinclair embedded atom model (EAM) potential [61] and the second nearest-neighbour modified embedded atom method (2NN MEAM) potential [62]. For more technical details, see [38]. Both force-field models were able to reproduce well the experimental W L_3-edge EXAFS spectrum of tungsten; however, the simulation using the 2NN MEAM potential resulted in about twice smaller residual.

The main advantage of the MD-EXAFS method is that no fitting of experimental data is performed and structure obtained in MD calculations is used “as it is” for the calculation of configuration-averaged EXAFS. From MD calculations, it is possible to get information about the structure of the material and the lattice dynamics (thermal fluctuations of atoms). Besides,

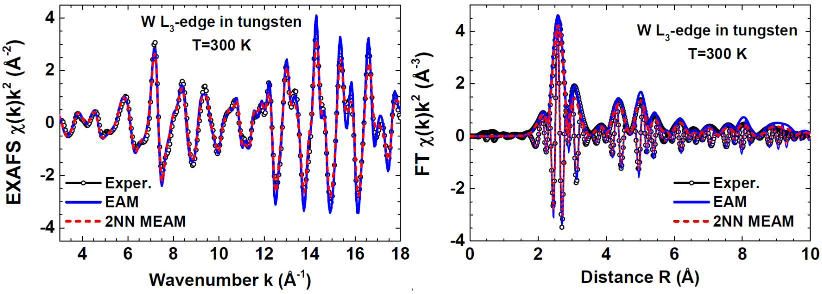

Figure 3.5.2: **The comparison of the experimental and calculated W L_3-edge MD-EXAFS spectra and their Fourier transforms:** Results of simulations with two force-field models (EAM and 2NN MEAM) are compared [38].

specific information (such as contributions from individual coordination spheres) can be obtained from theoretical calculations which is difficult to get from the experimental data. The main disadvantage of the method is that the accuracy of the obtained results depends on the force-field model used. It should be noted that this type of calculation requires large computational resources, especially if the system under study consists of hundreds or thousands of atoms.

3.5.3 Machine Learning (ML) method

Supervised Machine learning (ML) methods being capable to recognise patterns and correlations in large data sets have opened new opportunities for experimental data analysis. It has been shown that ML can also be successfully applied to both XANES [63, 64] and EXAFS [56] data treatment.

The idea under supervised machine learning is to numerically find a mathematical model that estimates the relationship between some input and output data. When the relation is established based on some set of training data points, the algorithm is employed to predict the unknown output data for the input, which is different from the training data. When the artificial neural network (ANN) method is used, the mentioned mathematical model can be represented as a network of nodes (Fig. 3.5.1). Typically, nodes are aggregated into layers. Each node receives input data x_i, applies mathematical operation $f(x_i, \theta_i)$, where θ_i are weights, and computes an output that can be similarly further processed by following layers. The weights are adjusted as training proceeds via a back-propagation algorithm [65]. The complexity of the mathematical model can be easily increased by enlarging the number of nodes and layers.

In the case of EXAFS, the first layer (input data) can be initialised using EXAFS spectra. The nodes in the last layer (output layer) should correspond to the structural features of interest. Since the structure of a material can be described with partial radial distribution functions (histograms of interatomic bond-lengths), the nodes in the output layer can be assigned to a height of the corresponding histogram bin [47, 56].

Many thousands of training data (spectra), for which the corresponding structure is known are necessary to approach the underlying relationship between data points. Furthermore, since the EXAFS spectra are sensitive to temperature induced atomic vibrations, the thermal disorder has to be included in the theoretical models used for training the ANN. CMD calculations appeared as a good tool for generating thousands of slightly different structural models, taking into account thermal vibrations [47]. Such calculations are relatively computationally cheap and provide one with realistic structures consistent with the used force-field model.

Recently, ANN trained based on the results of the CMD simulations was utilised to follow structural changes during the transition from a body-centred to a face-centred cubic iron phase [56]. The ANN results can be validated by comparing the extracted RDF with the RDF obtained, for instance, by RMC-EXAFS method.

Once the ANN is trained, experimental spectra can be processed within seconds, making this method attractive for *in situ*, *operando* and high-throughput studies. So, the ML method is advantageous for rapid analysis of raw experimental EXAFS spectra. However, the results should be critically evaluated.

3.5.4 Reverse Monte Carlo (RMC) method

Reverse Monte Carlo (RMC) method, developed by McGreevy and Pusztai in the late 1980s, is an atomistic simulation approach, in which atomic coordinates are optimized in an iterative random process. The method allows one solving an inverse problem – building a structure model from the experimental spectrum. In the beginning, the RMC method was developed for building atomic models of disordered materials such as glasses and liquids by employing diffraction data [55]. However, later the technique has been successfully applied also for crystalline [66–68] and nanocrystalline [69, 70] compounds. It has been demonstrated that it is a valuable tool for EXAFS data analysis.

RMC method provides one with physically meaningful information on the lattice structure and dynamics obtained from the EXAFS spectrum without using any force-field models. However, its applications are still limited because the RMC method requires extremely high computational resources. Simulations take thousands of iterations till the system reaches a (global) minimum.

RMC method was realised in a number of computer codes as RMCprofile [68], SpecSwap-RMC [71], RMC++ [72] and EvAX [17]. The last one – EvAX (Evolutionary Algorithms for XAS analysis) program for the analysis of EXAFS spectra using reverse Monte Carlo (RMC) [73, 74] and evolutionary algorithm (EA) [17] methods – is described below.

3.6 RMC method with the evolutionary algorithm (EA) approach

3.6.1 Introduction

The reverse Monte Carlo method with the evolutionary algorithm approach (RMC/EA) was developed by J. Timoshenko at the EXAFS spectroscopy laboratory (ISSP, UL) [17, 74, 75]. EA algorithm allows one to explore the possible configuration space and accelerates convergence in high-dimensional space more efficiently. Unlike the traditional RMC method, in this case several atomic configurations are used at the same time and information between these configurations is exchanged.

EA makes these calculations computationally more efficient. Thus, it is possible to include in the analysis a larger number of photoelectron scattering paths and perform analysis of distant coordination shells considering all significant MS contributions. Furthermore, EvAX code allows one to construct a single structure model, consistent with the experimental EXAFS data, obtained at several absorption edges. The experimental and calculated spectra are compared in k- and R-spaces simultaneously using continuous Morlet wavelet transform (WT), which gives better control over the agreement between the spectra.

The RMC algorithm implemented in the EvAX code allows only small atomic displacements from their initial positions. Hence, it can be applied for the analysis of well-defined structures such as crystalline or nanocrystalline materials. The method does not allow one to refine the coordination numbers (they are defined by the initial structure model), but one can obtain complex bond-length distributions (i.e. RDFs), bond angle distribution functions (BADFs) and analyse changes in interatomic distances, disorder and thermal effects. Since RMC simulations are based on random processes, they result in a structural model with the highest disorder (entropy). However, most often, if the initial structure model guess is close to the real one, the resulting structure fits the experimental data well. Note that the information encoded in the experimental data is also limited.

During the last years, the method was successfully used by our group in the analysis of several materials. Among them are cubic Y_2O_3 [76, 77], tungstates

[78–81], perovskites [17,82,83], W [38], MoO_3 [84,85], YH_3 [86] just to name a few. In this thesis, RMC/EA method is successfully applied to the analysis of $CuMoO_4$ and its solid solutions ($CuMo_{1-x}W_xO_4$, $Cu_{1-x}Zn_xMoO_4$) [87–89]. In the following subsections, the main features (Fig. 3.6.1) implemented in the EvAX code [17] will be described. For more details see [17, 74, 75].

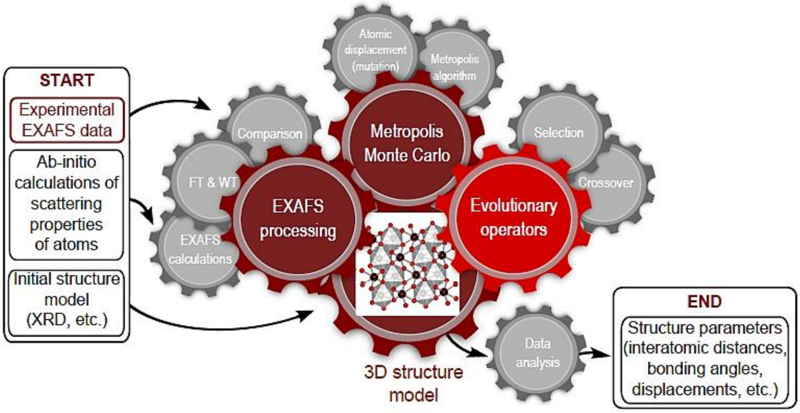

Figure 3.6.1: **A schematic representation of the EvAX algorithm [75]:** During the RMC/EA simulation *ab initio* calculations of a theoretical EXAFS spectrum are performed for a defined structure. Next, the experimental and theoretically calculated EXAFS spectra and corresponding WTs are compared. Then, the structural model is optimized based on EA and Metropolis algorithms. Finally, the obtained set of atomic coordinates is analysed to extract required information.

3.6.2 An initial structure model

The RMC calculation starts with an arbitrary chosen initial atomic configuration. A good starting point for crystalline materials usually is a supercell (a cell composed of several unit cells) constructed from an average structure known from diffraction studies. Note that diffraction techniques allow one to obtain the lattice parameters of the crystalline materials with much higher accuracy ($\sim 10^{-3}$ Å) than modern EXAFS analysis ($\sim 10^{-2}$ Å) [23, 38]. Thus, information on lattice parameters, symmetry, and Wyckoff positions can be effectively utilized when constructing a structural model of the material. Small random initial displacements for all or some atoms can be applied at the beginning of the RMC procedure to mimic thermal disorder. Periodic boundary conditions (PBC) are also applied to avoid surface-related effects.

EXAFS method is sensitive to the local atomic structure around the absorbing atom (up to $\sim$10 Å) [38]. The maximum distance is limited due to the finite lifetime of the excited state and thermal disorder. The supercell size should be at least two times larger than the largest radial distance in the FT of the corresponding EXAFS spectrum. The number of atoms in the cell should correspond to the experimental value of the atomic number density. The supercell size must be large enough to contain enough absorbers to provide good statistics.

A new atomic configuration is generated by randomly displacing some or all atoms in the supercell and the corresponding EXAFS spectrum $\chi^{new}(k)$ is calculated. In the EvAX code [17], random displacements of all atoms are realized using a set of pseudo-random numbers generated by the Mersenne-Twister algorithm [90]. Since in real crystals atomic displacements from their equilibrium positions due to thermal vibrations are usually less than a few tenths of angstroms, one can use some constraints, setting maximal or minimal allowed shift from equilibrium positions.

3.6.3 Calculation of the EXAFS signal

At each iteration, the RMC simulation requires to calculate the total EXAFS signal $\chi(k)$ corresponding to the present atomic configuration and to compare it with experimental one $\chi_{exp}(k)$. The total EXAFS spectrum corresponds to the average of the EXAFS signals for all absorbing atoms of the same type in the atomic configuration. These signals can be calculated by *ab initio* EXAFS codes such as FEFF [25, 37] or GNXAS [39]. In all cases presented in this thesis, we use the *ab initio* self-consistent real space multiple-scattering approach as is implemented in the FEFF8.5L code [25, 37], where theoretical EXAFS spectrum is calculated using Eq. 2.20.

The effective scattering amplitude ($f_{eff}(k, R)$) and phase shift ($\phi(k, R)$) functions in the Eq. 2.20 describe the interaction of the photoelectron with atoms along the scattering process. Calculation of these functions requires a knowledge of the cluster potential. The potential can be estimated either for the average atomic configuration neglecting potential deviations due to the thermal disorder effects or recalculated at each RMC iteration. To reduce the total computation time, in all our cases presented in this thesis, we calculate the self-consistent cluster potential within the muffin-tin approximation using complex exchange-correlation Hedin-Lundqvist potential for an average crystal structure known from diffraction measurements just once before the RMC run. Calculation of the EXAFS signal is the most time-consuming part of simulations. *Clustering algorithms* are employed to agglomerate similar paths and reduce the number of required FEFF calculations.

3.6.4 Comparison of experimental and theoretical spectra

Then, the two calculated EXAFS signals $\chi^{old}(k)$ and $\chi^{new}(k)$ are compared with the experimental one $\chi_{exp}(k)$, and depending on the agreement, the new atomic configuration is either accepted or discarded. Iterations are repeated till the sum of weighted squared differences ξ (or simply a residual) between theoretically calculated $\chi(k)$ and experimental $\chi_{exp}(k)$ EXAFS signals is minimized. In the k-space, it is calculated using the equation:

$$\xi_k = \frac{\|\chi(k)k^n - \chi_{exp}(k)k^n\|_2}{\|\chi_{exp}(k)k^n\|_2}, \tag{3.12}$$

where $\|...\|_2$ is the Euclidean norm and k^n (n=1, 2 or 3) is the weighting factor for EXAFS signal. As an experimental data $\chi_{exp}(k)$ one can use the full EXAFS spectrum or just a part of it obtained by the Fourier filtering. Similarly, the comparison can be done also in R-space by comparing the Fourier transforms of experimental and theoretically calculated EXAFS spectra:

$$\xi_R = \frac{\|FT(R) - FT_{exp}(R)\|_2}{\|FT_{exp}(R)\|_2}. \tag{3.13}$$

One more way is to minimize the difference between spectra in both k and R- spaces simultaneously by employing, a so-called Morlet wavelet transform (WT) [91]:

$$\xi_{k,R} = \frac{\|WT(k,R) - WT_{exp}(k,R)\|_2}{\|WT_{exp}(k,R)\|_2}, \tag{3.14}$$

where $WT(k,R)$ and $WT_{exp}(k,R)$ are the WTs of theoretical and experimental EXAFS spectra, respectively.

The three criteria mentioned above have different sensitivity. For instance, in k-space, there is good discrimination between heavy and light chemical elements producing stronger contributions into the EXAFS signal at the large and small k-values, respectively. However, in R-space it is possible to discriminate contributions by frequencies (radial distances). Note that the FT spectrum depends on the available EXAFS signal range in k-space and the window function choice.

It is believed that the two-dimensional representation of the EXAFS signal in k and R-spaces simultaneously (in w-space) by WT will give the best results during the minimisation procedure [91]. WT decomposes the analysed spectrum in k and R-spaces, revealing, which frequencies (R-values) are present in the spectrum, and, at the same time, at which wavenumber (k) values the components corresponding to each R-value contribute. A good agreement between two signals in the wavelet space means a good agreement between them in k and R-spaces. WT can also be

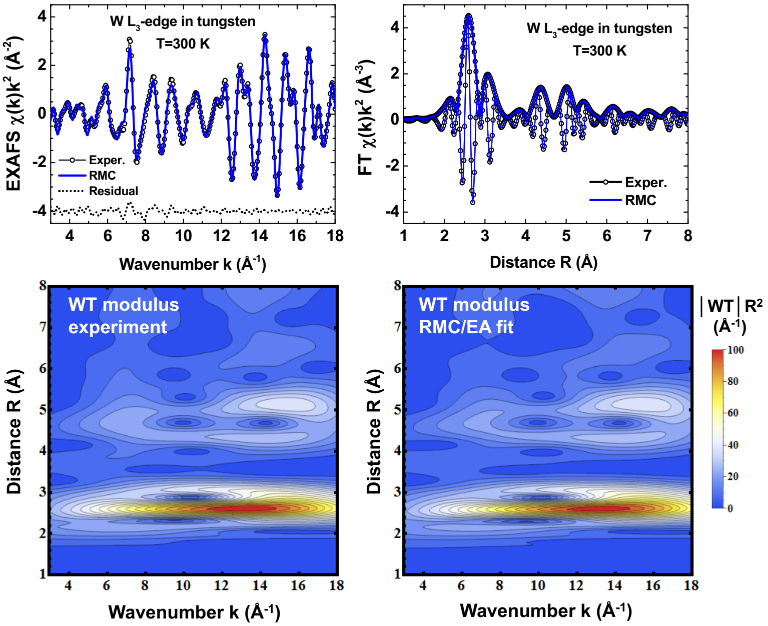

Figure 3.6.2: **Comparison of the experimental and RMC/EA calculated W L3-edge EXAFS spectra for bcc tungsten at T=300 K [38]:** $\chi(k)k^2$ and their FTs (upper panels) as well as the moduli of their Morlet wavelet transforms (WTs) (lower panels). The difference between the experimental and calculated EXAFS spectra is shown by dotted line. Both modulus and imaginary parts are shown for FTs.

useful for qualitative EXAFS data analysis. An example of the RMC/EA fit for W L3-edge EXAFS spectrum in bcc tungsten at $T = 300$ K in k, R and w-spaces is shown in Fig. 3.6.2. Calculation details can be found in [38].

3.6.5 Metropolis algorithm

The (global) minimum of the minimization problem is reached via the Metropolis algorithm [54]. Its basic idea is that if the move reduces the disagreement between the calculated and experimental data (ξ becomes smaller), then the move is accepted; if it increases, then the move is accepted with a reduced probability:

if $\xi^{new} < \xi^{old}$, the move is accepted,
if $\xi^{new} > \xi^{old}$, the move is accepted, if

$$\exp(\frac{-(\xi^{new} - \xi^{old})}{\Theta}) > \zeta \tag{3.15}$$

and discarded otherwise,

where ξ^{old} and ξ^{new} denotes the difference between the calculated and experimental signal for the previous and new atomic configuration, respectively, ζ is a random number in the range between 0 and 1 and Θ is a scaling (also called "temperature" [74]) parameter. If the Θ parameter is too large, ξ will reach the global minimum value but will fluctuate around it with a large amplitude. However, if Θ is too small, the calculation may be stuck at one of the of local minimums. The conventional approach is to set the Θ parameter value to be proportional to the noise level of the experimental spectrum. An alternative way is to use a so-called *simulated annealing* approach [92] where the Θ parameter is not fixed but slowly decreases. The simulation starts with a large Θ value to stimulate a fast approach to the global minimum and then Θ is reduced to lower fluctuations of the system until it is equal to 0. If the annealing is done slowly enough, the system reaches a global minimum.

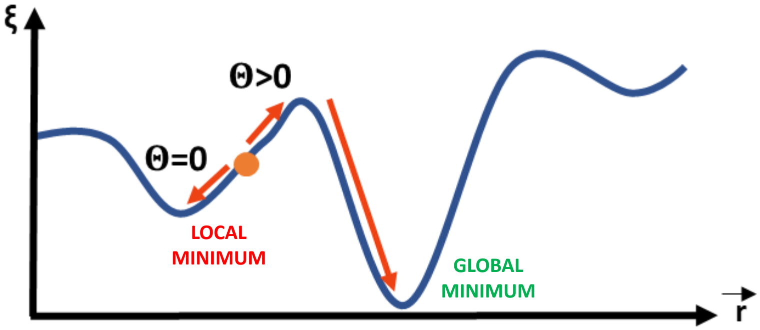

Figure 3.6.3: **A schematic representation of the Θ parameter role in the Metropolis algorithm.**

3.6.6 Evolutionary Algorithm

The evolutionary algorithm (EA) describes population based techniques for parameter optimization that tends to mimic biological evolution processes in nature. In the EvAX code, EA is proposed as an optimization algorithm for obtaining a 3D structure model from EXAFS spectra [17].

Generally, in the EA, a set of all parameters that should be optimized is called an "individual". The function of these parameters, which has to be maximized, is called a *fitness function* (FF). Many sets of parameters (many individuals) having different values form a "population". At each iteration of the simulation, some manipulations with the population are carried out to obtain the new one. In this case, the aim is to maximize the FF.

When EA is applied to the analysis of EXAFS spectra from crystalline materials, similarly to conventional RMC, the variable parameters are the x, y, z coordinates of the atoms in the supercell. Thus, the “individual” is an atomic configuration. The FF corresponds to the difference between theoretically calculated EXAFS signal for an atomic configuration and experimental spectrum. Its maximum value is when this difference is the smallest. So, in analogy with conventional RMC, the FF can be defined as $-\xi$.

There are three EA operations usually applied to a given population: selection, crossover, and mutation, which are also implemented in the EvAX code (Fig. 3.6.4).

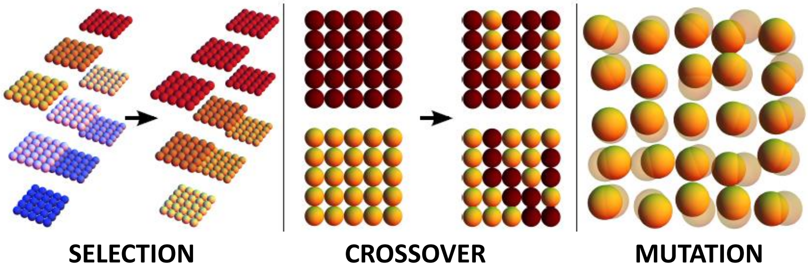

Figure 3.6.4: **Basic operations of the evolutionary algorithm [75].**

During the selection operation, one creates a new population (a new set of atomic configurations) from the individuals of the old population by preferring those with larger FF. So, the probability to be selected for the new generation is proportional to the value of an individual’s FF. To keep the total number of individuals in the population constant, the new population will have several copies of the atomic configurations with high values of the FF and only a few with lower FF.

In the crossover process, one replaces some atoms of one randomly selected atomic configuration with atoms of the other configuration. The mutation operator applies some random small changes to all individuals of the population. In our case, all atoms in all configurations are slightly displaced from their positions in random directions. It is possible to take into account the information from XRD and constrain the maximally allowed shift.

Although EA is very similar to the RMC approach, it permits a much more efficient exploration of the possible configuration space, thus requires fewer computation resources and makes feasible advanced analysis of complex compounds with low symmetry. It is possible to take into account a much larger number of photoelectron scattering paths and analyse more distant coordination shells, including MS contributions.

3.6.7 Extraction of structural information

The main result of the RMC/EA simulation is the final atomic configuration that gives a 3D structure model of the material consistent with the experimental EXAFS data. One should note that such a result is not unique. Calculations performed with other pseudo-random numbers will give slightly different atomic coordinates. However, the obtained distributions of interatomic distances and angles should be statistically close.

The bond lengths histograms, so-called radial distribution functions (RDFs), represent the obtained structural model from the perspective of absorbing atoms. They can be used to extract the structural parameters as mean interatomic distances and variance of them.

Another way to estimate the variance of interatomic distances directly from coordinates is the median absolute deviation (MAD) method [93]. In our case, a standard deviation σ of distribution is estimated as:

$$\sigma = c \times \sigma_{MAD} = c \times median(|R_i - median(R)|), \tag{3.16}$$

where R_i are interatomic distances in the structural model and $median(R)$ is the average distance. The σ_{MAD} parameter is converted in a consistent estimator of σ by multiplying MAD value by a scaling constant c corresponding to particular distribution function. For Gaussian distribution $c = 1.4826$ [93]. For other distributions, the c values can be obtained analytically or in numerical simulations. So, the MAD method is advantageous when the shape of the distribution function is more complex.

Several calculations with different sequences of pseudo-random numbers or different initial conditions should be performed to evaluate statistical uncertainty. Note that RMC simulations tend to converge to the most disordered structural model consistent with experimental data [68].

When RMC/EA simulations are used to fit experimental EXAFS spectra, one can validate the obtained sets of atomic coordinates also against diffraction data. To do this, one should project coordinates of all atoms in the supercell into a single unit cell. Cartesian coordinates are converted to the fractional coordinate system by employing the following matrix operations:

$$\begin{bmatrix} u \\ v \\ w \end{bmatrix} = \begin{bmatrix} \frac{1}{a} & -\frac{\cos\gamma}{a\sin\gamma} & bc\frac{\cos\alpha\cos\gamma-\cos\beta}{\Omega\sin\gamma} \\ 0 & \frac{1}{b\sin\gamma} & ac\frac{\cos\beta\cos\gamma-\cos\alpha}{\Omega\sin\gamma} \\ 0 & 0 & \frac{ab\sin\gamma}{\Omega} \end{bmatrix} \begin{bmatrix} x \\ y \\ z \end{bmatrix} \tag{3.17}$$

$$\Omega = abc\sqrt{1 - \cos^2\alpha - \cos^2\beta - \cos^2\gamma + 2\cos\alpha\cos\beta\cos\gamma},$$

where the unit cell (a parallelepiped) is defined by lattice parameters a, b, c and α, β, γ. (u, v, w) are components of fractional coordinate vector and

(x, y, z) are components of the vector describing atomic positions in Cartesian coordinates. Ω is volume of the parallelepiped cell.

The average positions for each non-equivalent atom correspond to the Wyckoff positions and they are used to calculate the diffraction pattern. Thus, theoretically calculated diffraction pattern can be compared with experimental one known from the diffraction experiment.

3.6.8 EXAFS-RMC results for XANES interpretation

Structural disorder effects are weak close to the absorption edge, thus the temperature dependence of XANES is usually minor [43, p.214]. However, it has been shown in literature that in particular cases XANES is sensitive to thermal disorder [94–98]. Examples include Ti K-edge XANES in $LiTi_2O_4$ [94] and $SrTiO_3$ [95], Al K-edge of corundum and beryl [96, 98], Mg K-edge of MgO [97, 98]. In this thesis, we demonstrate Cu K-edge XANES of $CuMoO_4$ sensitivity to thermal disorder at high temperatures [87].

We show that the results of RMC/EA calculations (sets of atomic coordinates) can be employed to interpret XANES changes upon temperature increase (Fig. 3.6.5). An advantage of such approach is that atomic configurations used in the XANES calculations are already validated against EXAFS spectra and they contain information about correlation effects.

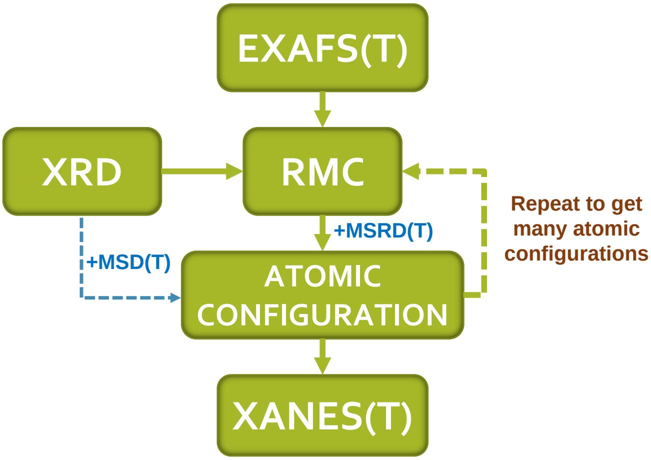

Figure 3.6.5: **A scheme for including thermal disorder in the structure for XANES theoretical calculations:** One option is to take diffraction data, apply some random shifts for atoms within MSD factor radius and check these atomic configurations by performing theoretical XANES calculations. An alternative is to use diffraction (XRD) data as an initial configuration for RMC calculations were temperature-dependent EXAFS data are fitted. The last configuration then can be used to calculate XANES spectra.

Chapter 4

Resonant X-ray emission spectroscopy (RXES)

4.1 X-ray emission spectroscopy (XES)

While XAS is the first-order optical process that includes only one photon, X-ray emission spectroscopy (XES) is a second-order optical process in which a core electron is first excited by the incident X-ray beam, and the core hole is next filled by an electron from higher-energy level with the emission of an X-ray photon. A scheme of main emission lines denoted in Siegbahn's notation is shown in Fig. 4.1.1. High energy resolution fluorescence detected XANES (HERFD-XANES) (and in general fluorescence detected XAS) take advantage of a secondary process (the radiative decay of the excited states) which is, in the hard X-ray range, to a very good approximation proportional to the absorption coefficient.

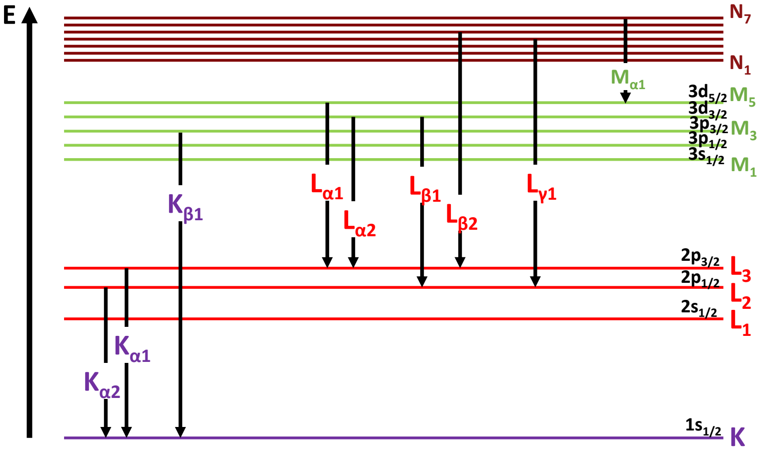

Figure 4.1.1: **A scheme of the principal emission lines**: Siegbahn's notation is used. In this study, the $L\alpha_1$ and $L\alpha_2$ emission lines of tungsten were measured.

It is common to divide the XES into two categories. The first one is normal XES (NXES), when the core electron is excited to the high-energy continuum. It is also called a non-resonant XES. The second category is a resonant XES (RXES) when the incident X-ray energy "resonates" with the excitation threshold of the core electron [24, p.335]. The energy difference between incoming and emitted photon corresponds to the inelastically transferred energy. The emitted photon can result from the relaxation of a valence electron into the empty core hole or by an allowed core-to-core transition (Fig. 4.1.2). The difference between the energies of the incoming E_{in} and emitted E_{out} X-ray photons is called energy transfer. Both resonant and non-resonant XES are described theoretically by the Kramers-Heisenberg formalism [99–101].

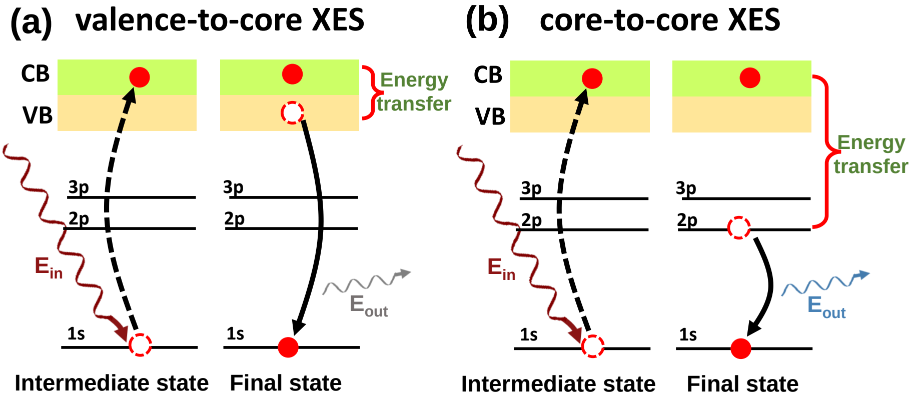

Figure 4.1.2: **A single electron model of the valence-to-core XES (a) and core-to-core XES (b):** CD is conduction band, VB is valence band.

The width of the experimentally measured spectral line is governed by the lifetime of intermediate and final states (Fig. 4.1.2) involved in the RXES process and the energy resolution of the employed detector. The lifetime of the core hole τ is related to the uncertainty in its energy (broadening Γ) following to the Heisenberg uncertainty principle $\Gamma\tau \geq \hbar/2 \sim 10^{-16}\ eV \cdot s$. Note that the intermediate state of RXES is the same as the final state of the first-order optical process in XAS [101–103]. Detecting the emitted X-ray radiation with an instrumental resolution on the order of the core hole lifetime broadening enables to resolve fine structure in the X-ray emission spectra. The observed fine structure contains information on the electronic configuration and chemical environment of the emitting atom that is complementary to what can be obtained in XAS measurements [104].

4.2 RXES experiment

Resonant X-ray emission spectroscopy (RXES) can be considered a particular case of X-ray fluorescence (emission) spectroscopy. Although it is not a new technique[1], its resent development is due to the available undulator radiation from the third-generation synchrotron radiation sources and highly-efficient detectors.

RXES is a photon-in photon-out technique used to probe the local coordination and electronic structure of the material. It is complementary to XAS and can be advantageous in cases when it is necessary to differentiate contributions from different elements, or the sample is not suitable for XAS measurements (not homogeneous, diluted, etc.). RXES gives bulk-sensitive, element-specific, and site-selective information about the sample. Its sensitivity to the electronic structure depends on the final state electronic configuration that is detected. Note that penetrating properties of hard X-rays allow probing composition and electronic states of the material under *operando* conditions (also in non-vacuum environment) [107].

Since the efficiency of the X-ray emission is low, the signal-to-background ratio plays a significant role. The experimental setup requires high-intensity and tunable X-ray photon source such as a synchrotron and an X-ray spectrometer based on perfect-crystal Bragg optics [104]. Such spectrometers have an energy bandwidth similar to the lifetime induced broadening of the corresponding core level and allows one to obtain superior resolution compared to conventional XANES.

An example of the experimental setup for hard RXES spectroscopy is shown in Fig. 4.2.1. The X-ray beam is monochromatized by a double-crystal monochromator and focused in a vertical and horizontal planes by two mirrors with different coatings positioned downstream of the monochromator. The ionization chamber is usually used for incident X-ray intensity monitoring.

The two most popular emission spectrometer schemes for RXES measurements are von Hamos-type [108] and Johann-type spectrometers [109]. The spectrometer acts as a secondary monochromator for the emitted X-rays with an instrumental energy resolution higher to that of the primary crystal monochromator that is used for the incident energy selection. A Bragg crystal spectrally analyses the fluorescence from the sample and directs it onto the position-sensitive pixelated 2D photon detector. The solid angle can be enlarged when several analyser crystals are used in parallel.

---

[1] The first laboratory XES experiments were conducted by utilizing the electron beam in 1924 by Lindh and Lundquist [105]. A few years later, Coster and Druyvesteyn performed the first XES experiments with photon excitation [106].

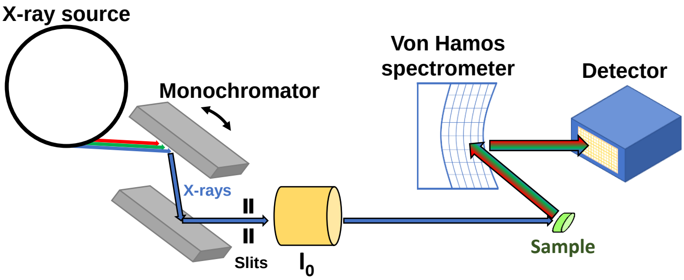

Figure 4.2.1: **A schematic representation of the experimental setup for RXES measurements:** X-ray source (synchrotron), monochromator, an ionization chamber for X-ray intensity detection I_0 before the sample, spectrometer to disperse XES signal and a position-sensitive pixelated 2D detector. Two focusing mirrors located after the monochromator are not shown for clarity.

In the experiment, the intensity of both incident and emitted X-rays (inelastically scattered X-rays and fluorescence signals) is recorded and after the signal processing (pixels are transformed into the energy scale) a so-called RXES plane is obtained [101]. The double-crystal monochromator is usually calibrated using a reference foil, and the energy scale of the spectrometer can be set according to the position of the elastic line on the detector.

By selectively extracting the emitted photon intensity in the narrow energy range, one can obtain high energy resolution fluorescence detected XAS spectrum (HERFD-XAS spectrum) with a drastically enhanced sensitivity to the local coordination of the absorbing atoms. HERFD-XAS provides a possibility to study the structural and electronic properties of the material in more details by detecting XANES with an experimental resolution on the order of the core hole lifetimes of the intermediate and final electronic states of the absorbing element [101].

Non-resonant XES spectrum is obtained by scanning the emitted fluorescence with a crystal analyser spectrometer at a fixed incident X-ray energy well above an absorption edge of the investigated element [24, p.337]. In this case, the X-ray emission spectrum is independent of the incident energy [101]. The X-ray emission spectra obtained by scanning the emitted radiation slightly below [110] or above the absorption edge are called off-resonant X-ray emission spectra [111].

4.3 RXES plane

In the RXES experiment, the intensities and energies of the incoming and emitted X-ray radiation is monitored. One way of presenting the RXES intensity plane is to plot the energy of emitted photons against the incident photon energy (Fig. 4.3.1(a,e)) and the second way is to plot the energy transfer against the incident energy (Fig. 4.3.1(b,f)). Comparison between different spectra and quantitative analysis are usually made for line plots extracted from the 2D RXES planes. Different plane cuts can reveal valuable information on the structural and electronic properties of the material.

RXES plane obtained by collecting the $L\alpha$ emission lines is denoted as 2p3d RXES indicating electronic levels involved in intermediate and final states (an electron from 2p level is excited and the system relaxes by filling the created core hole with an electron from 3d state).

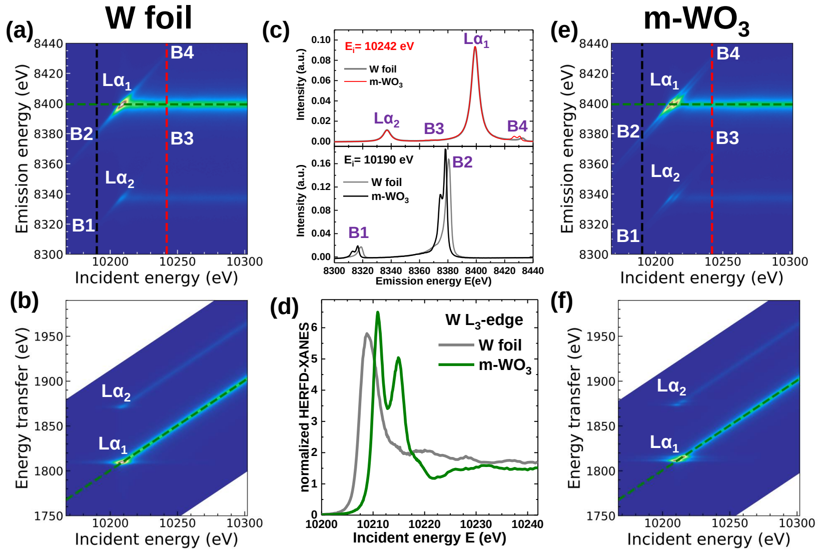

Figure 4.3.1: **W 2p3d RXES plane and plane cuts for tungsten foil and monoclinic tungsten trioxide:** RXES intensity map as a function of incident and emitted energies for W foil (a) and m–WO$_3$ (e); RXES intensity map as a function of incident energy and energy transfer for W foil (b) and m–WO$_3$ (f); Vertical cuts of the RXES planes at the incident energies E_i=10190 eV and 10242 eV, shown in (a,e) by black and red dashed lines. Principal observed bands ($L\alpha_1$, $L\alpha_2$, B1-B4) are labelled; (c) The W L$_3$-edge HERFD-XANES spectra measured at emission energy 8399.4±0.25 eV, indicated by the green dashed line in (a,b) and (e,f) are shown in panel (d).

Examples of the 2p3d RXES planes and their cuts in body centred cubic tungsten (W) and monoclinic tungsten trioxide (m-WO$_3$) are shown in Fig. 4.3.1. Two W emission lines $L\alpha_1$ ($3d_{5/2} \rightarrow 2p_{3/2}$ transition) and $L\alpha_2$ ($3d_{3/2} \rightarrow 2p_{3/2}$ transition) can be distinguished in the RXES planes at emission energies 8398 eV and 8335 eV, respectively. However, there are significant differences in the shape of the spectral features. While the dominant feature in the W foil RXES plane is a strong $2p_{3/2} \rightarrow 3d_{5/2}$ resonance (at incident energy ~10209 eV), two resonances (at incident energies of ~10211 eV and ~10215 eV) are observed in the case of m-WO$_3$.

The two resonances in m-WO_3 originate from the crystal field induced splitting of the W 5d states into the W t_{2g} and e_g subbands, since tungsten atoms have distorted octahedral coordination [107].

The width of a measured X-ray line results from the lifetime broadening of the corresponding transition (also called intrinsic broadening) and the energy resolution of the employed detector. For instance, theoretical core-hole induced line-widths for tungsten different edges are: $\Gamma_{2p_{3/2}}$=4.57 eV (L_3-edge), $\Gamma_{3d_{3/2}}$=4.51 eV (M_4-edge), $\Gamma_{3d_{5/2}}$=2.01 eV (M_5-edge) [29]. This width is called the natural width, and the shape of the spectral line can be described with a Lorentzian function. Since the lifetime of the deep core hole is shorter than that of the shallower ones, $\Gamma_n > \Gamma_f$, HERFD-XANES allows one to obtain spectral features with smaller line width than in conventional XANES measured in transmission mode. However, high resolution detectors are required. The instrumental response of a detector most often can be reproduced by a Gaussian function. The idea of the HERFD-XANES is to detect the fluorescence line with an energy bandwidth on the order or below the core-hole lifetime broadening. This is achieved through the use of a crystal analyser.

The W L_3-edge HERFD-XANES spectra shown in Fig. 4.3.1(d) can be obtained from Fig. 4.3.1(a) by integrating the emission intensity in the narrow emission energy region (8399.4±0.25 eV) close to the $L\alpha_1$ line (green dashed cut). At the same time, the conventional X-ray fluorescence spectrum is obtained when the emission intensity is integrated in a wide emission energy range. The HERFD-XANES spectrum corresponds to the case with constant emitted energy and appears as a diagonal cut in the energy transfer vs incident energy plane Fig. 4.3.1(b,f). Such a plane cut allows one to partially subtract the intermediate state broadening that is well seen as horizontal tails from the main emission lines at constant energy transfer. Since W in the oxide has a higher oxidation state (6+) than in metal, its absorption edge, estimated from the maximum of the XANES first derivative, is shifted by about 2.7 eV to higher binding (incident) energies in Fig. 4.3.1(d).

Besides the HERFD-XANES spectra, several vertical cuts of the RXES plane with constant incident energy can be made. They can be used to additionally obtain high energy resolution off-resonant X-ray emission spectra by extracting them slightly below (bands B1 and B2 in Fig. 4.3.1(c)) and above (bands B3 and B4) the resonance (W L_3 absorption edge), respectively. Also, these emission spectra contain information on the crystal field splitting (Fig. 4.3.1(c)), while with a smaller signal-to-noise ratio compared to HERFD-XANES.

More detailed analysis of the tungsten 2p3d RXES plane of $CuMo_{1-x}W_xO_4$ solid solutions and crystal field induced splitting of 5d(W)-states is presented in the Chapter 9.

Chapter 5

Structure and thermochromic properties of molybdates

5.1 Introduction

Molybdates of divalent metal ions with the general formula $AMoO_4$, where A=Mn, Fe Co, Ni, Cu, Zn, etc., form a wide class of functional materials, considered as promising for different technological applications [112]. Among them, copper molybdate ($CuMoO_4$) and its solid solutions with tungsten ($CuMo_{1-x}W_xO_4$) are one of the most fascinating multifunctional materials that exhibit thermochromic [1, 2, 4, 5, 10, 11, 15], piezochromic [2, 4, 113, 114], tribochromic [2], halochromic [3], thermosalient [4], photoelectrochemical [6, 8], photoluminescence [115], also promising catalytic [9, 116, 117], and antibacterial properties [7]. Some of functional properties are illustrated in Fig. 5.1.1.

In the literature, much attention has been paid to the material's ability to change its colour due to the influence of temperature and pressure in the context of sensing applications [5,10,15]. Pure $CuMoO_4$ has thermochromic properties both, at low (~100–300 K) and high temperature (~400–700 K) ranges.

The chromic properties of $CuMoO_4$ at low temperatures (below 300 K) originate due to a reversible structural phase transition accompanied by a drastic colour change between greenish and brown [113]. It is also possible to modify the structure of the material by doping to have its thermochromic properties in the more accessible temperature ranges [10]. Recently, the possibility to stabilize the low temperature phase at room temperature by cryogenic quenching was demonstrated in [5]. Such sample consists of low and high temperature polymorph mixture and changes its colour irreversibly in the temperature range ~300–473 K [5]. Thus, it is possible to obtain a $CuMoO_4$ material as a permanent temperature-time indicator with potential applications, for instance, in the fields where one needs to monitor storage/transportation conditions of temperature-sensitive products (food, drugs, chemicals, biological materials, etc.) [5].

At the same time, such inorganic materials with a thermochromism (colour change from greenish to brownish upon heating) at high temperatures (above ~400 K) attracts much attention because of their potential applications

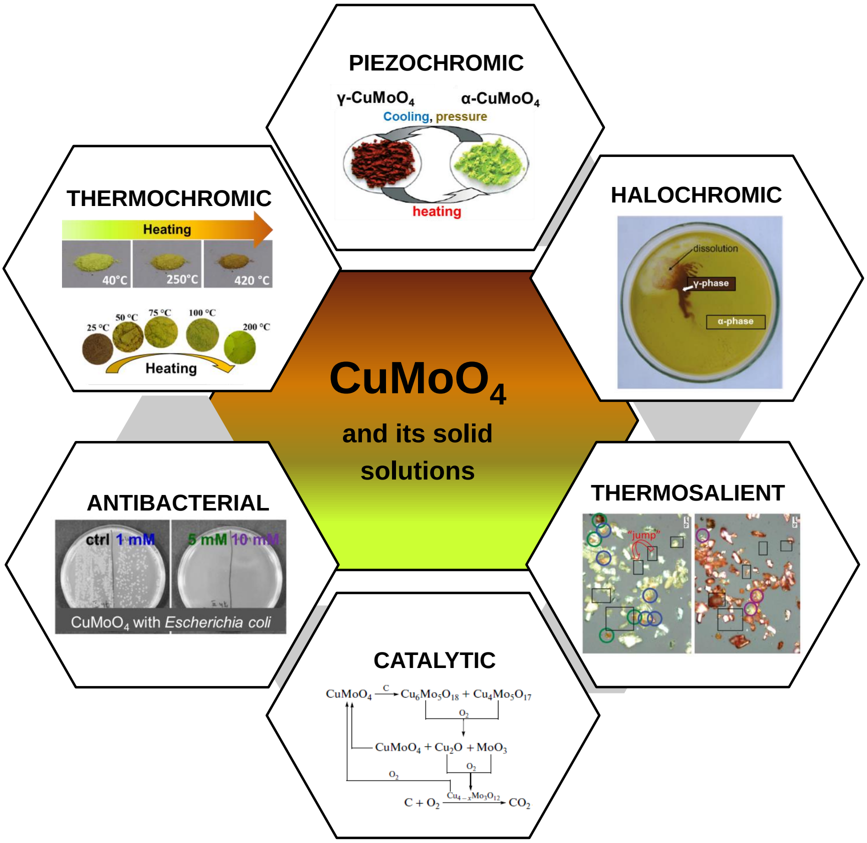

Figure 5.1.1: **A schematic representation of $CuMoO_4$ and/or $CuMo_{1-x}W_xO_4$ functional properties reported in the literature:** thermochromic (adapted from [5]), piezochromic (adapted form [2]), halochromic (adapted from [3]), thermosalient (adapted from [4]), catalytic [117], antibacterial (adapted from [7]).

for temperature sensing in the ranges where the majority of organic compounds and liquid crystals are unstable [13]. Possible chromic-related applications extend from the user-friendly temperature and pressure indicators [2, 3, 10, 14] to "smart" inorganic pigments [15].

5.2 Crystal structure and chromatic properties

Currently, at least seven different structural phases of pure $CuMoO_4$ are known in the literature: α-$CuMoO_4$, γ-$CuMoO_4$, β-$CuMoO_4$, $CuMoO_4$-II, $CuMoO_4$-III, ϵ-$CuMoO_4$, and η-$CuMoO_4$ [1, 118, 119]. The phase depends on the temperature, pressure, and other conditions used for the synthesis. In this thesis, the author focuses on two allotropic forms of copper molybdate –

greenish α-$CuMoO_4$ and brownish γ-$CuMoO_4$ phases that are stable at high and low temperatures, respectively.

Structure, optical, electrical, and magnetic properties of $CuMoO_4$ were studied previously in [1, 10, 13, 120–122]. The pressure–temperature diagram (Fig. 5.2.1) for $CuMoO_4$ was determined based on a single crystal diffraction data by Wiesmann *et al.* in [1]. The first order α-to-γ phase transition occurs upon cooling the material below ∼200 K (or by applying pressure above ∼0.2 GPa). In addition to the colour change, the α-to-γ phase transition is accompanied by a volume decrease of 12–13% that makes the two phases easily distinguishable [1]. The phase transition was also studied previously using optical spectroscopy, differential scanning calorimetry, magnetic susceptibility, and dielectric measurements [10, 13, 14, 123]. It was found that the transition has hysteretic behaviour so that higher temperature is required to promote the γ-to-α transition than α-to-γ. As expected for a first-order phase transition, both phases are separated by a region where they coexist.

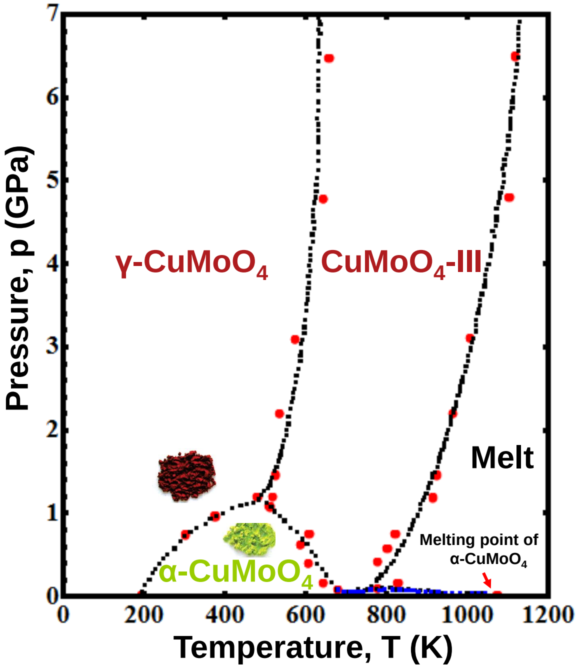

Figure 5.2.1: **Pressure-temperature phase diagram for $CuMoO_4$** (adapted from [1]).

At ambient pressure, $CuMoO_4$ remains in the triclinic $P\bar{1}$ symmetry up to the melting point temperature (∼1070 K) [1]. Note that the existence of the β-$CuMoO_4$ phase with hexagonal symmetry was proposed for temperatures above 840 K in Ref. [124], but its existence was not confirmed in the further studies [1]. However, in some studies [9, 125], the β-phase is still mentioned.

Similarly, there was no evidence for the existence of high-pressure $CuMoO_4$-II phase reported previously [1].

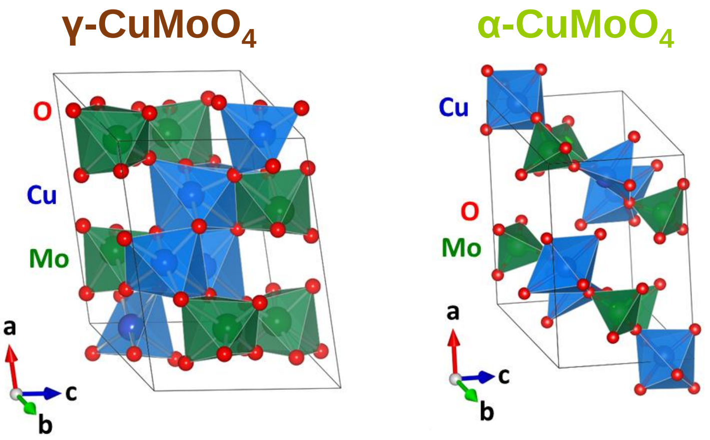

Figure 5.2.2: **The unit cell of γ-$CuMoO_4$ (left panel) and α-$CuMoO_4$ (right panel).**

There are significant differences in the crystallographic structure of α and γ phases (Fig. 5.2.2). The lattice parameters reported in the literature are compared in Table 5.2.1. The γ-phase of $CuMoO_4$ is built up of distorted CuO_6 and distorted MoO_6 octahedra [1, 121], while α-$CuMoO_4$ is composed of distorted CuO_6 octahedra, CuO_5 square-pyramids, and distorted MoO_4 tetrahedra [1, 126]. The first-order ($Cu^{2+}[3d^9]$) and second-order ($Mo^{6+}[4d^0]$) Jahn-Teller effects are responsible for the distortion of CuO_6 and MoO_6 octahedra. The unit cell of $CuMoO_4$ structure in both phases contains six formula units (Z=6) with three non-equivalent copper (Cu1, Cu2, Cu3) and three non-equivalent molybdenum (Mo1, Mo2, Mo3) atoms, which have different local environments, shown in Table 5.2.2 [1]. Thus, the unit cell of $CuMoO_4$ consist of 36 atoms, and the structural analysis is challenging.

Table 5.2.1: **Lattice parameters for α-$CuMoO_4$, γ-$CuMoO_4$, α-$ZnMoO_4$, $CuMoO_4$-III and $CuWO_4$ reported in the literature.** All have triclinic symmetry with space group $P\bar{1}$.

Material	**Cond.**	**a**	**b**	**c**	α	β	γ	**Ref.**
α-$CuMoO_4$	RT	9.901	6.786	8.369	101.13	96.88	107.01	[126]
γ-$CuMoO_4$	180 K	9.699	6.299	7.966	94.62	103.36	103.17	[121]
γ-$CuMoO_4$	0.2 GPa	9.708	6.302	7.977	94.76	103.35	103.26	[1]
α-$ZnMoO_4$	RT	9.625	6.965	8.373	103.28	96.30	106.72	[127]
α-$ZnMoO_4$	RT	6.966	8.371	9.685	96.74	106.87	101.73	[128]
α-$CuMoO_4$	RT	6.788	8.372	9.904	96.89	107.01	101.13	[128]
$CuMoO_4$-III	RT	4.714	5.848	4.879	91.51	92.48	82.35	[1]
$CuWO_4$	RT	4.694	5.830	4.877	91.64	92.41	82.91	[129]

Table 5.2.2: **Metal-oxygen interatomic distances in α-CuMoO$_4$ and γ-CuMoO$_4$ phases** [1].

Interatomic distances in α-CuMoO$_4$ (R, Å)					
Cu1-O	**Cu2-O**	**Cu3-O**	**Mo1-O**	**Mo2-O**	**Mo3-O**
1.930	1.937	1.909	1.745	1.714	1.702
1.956	1.953	1.910	1.756	1.765	1.705
1.967	1.966	1.931	1.758	1.771	1.839
1.987	1.970	1.987	1.818	1.793	1.851
2.287	2.219	2.339	2.832	2.819	2.808
2.330	2.628	3.555	3.488	2.943	2.922
Interatomic distances in γ-CuMoO$_4$ (R, Å)					
Cu1-O	**Cu2-O**	**Cu3-O**	**Mo1-O**	**Mo2-O**	**Mo3-O**
1.928	1.910	1.922	1.690	1.683	1.701
1.933	1.945	1.949	1.776	1.781	1.764
1.937	1.961	1.976	1.875	1.881	1.841
1.972	1.966	1.977	1.930	1.926	2.017
2.295	2.268	2.306	2.132	2.105	2.065
2.428	2.527	2.488	2.478	2.471	2.494

Recently, a mixture of α- and γ-CuMoO$_4$ polymorphs acquired by a cryogenic quenching approach was presented in Ref. [5] as promising permanent temperature recorder due to the thermochromic irreversible phase transition from the polymorph mixture into the α-phase.

It is worth mentioning that a colour change from green to brown but of different origin occurs in pure α-phase of CuMoO$_4$ upon heating up to ~673 K [13]. This colour change is reversible, and the crystal structure is not broken during the temperature cycle.

The green colour of CuMoO$_4$ at ambient conditions is caused by the transmission window in the energy range of ~1.9–2.5 eV 500–650 nm (500–650 nm) (Fig. 5.2.3(a)) [13]. The chromatic properties of CuMoO$_4$ are associated with the interplay between two optical absorption bands. The first band, located in the red spectral range above ~650 nm, is related to the copper $3d^9 \rightarrow 4p$ [13] or d-d transitions [10, 120, 130]. The second band, located in the blue spectral range below ~500 nm, is still not fully understood. It is attributed to the oxygen-to-metal ($O^{2-} \rightarrow Mo^{6+}$ or $O^{2-} \rightarrow Cu^{2+}$) [10, 13, 120, 130] or $Cu^{2+} \rightarrow Mo^{6+}$ [131] charge transfer processes. Nevertheless, when the temperature increases from 296 K to 673 K, the transmission window shrinks due to the blue band shift towards longer wavelengths (Fig. 5.2.3(a)), and the crystal changes both transmittance and colour [13]. This effect is explained with the electronic properties of the crystal instead of structural change or chemical decomposition [13].

The control over the structural phase transition temperature of the material is critical for technological applications at desired temperature ranges. It has been reported that the properties of CuMoO$_4$ can be tailored by reducing the particle size or by chemical doping and producing solid solutions [4, 10, 11, 132–134].

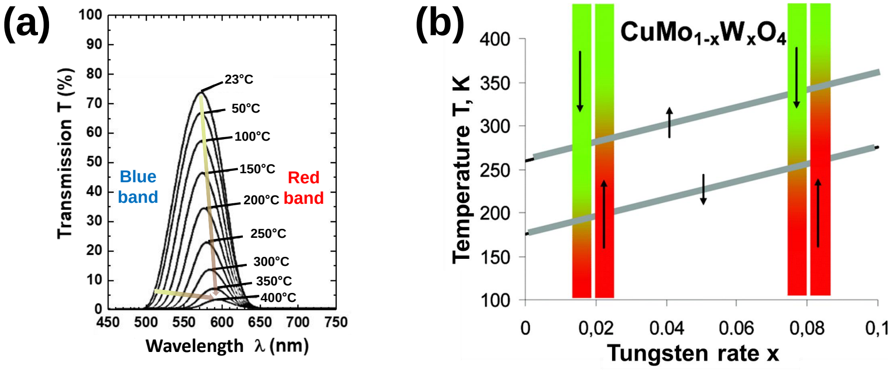

Figure 5.2.3: **Temperature–dependent transmission spectra of $CuMoO_4$ (adapted from [13])(a); Correlation between the phase transition temperatures (gray lines) and tungsten rate x in $CuMo_{1-x}W_xO_4$ solid solutions (adapted from [10]) (b).**

5.3 Effect of doping

According to the pressure-temperature diagram [1], the phase transition from the γ-to-α phase can be adjusted to more desired temperatures by applying pressure or by means of chemical doping [1]. One possibility is to substitute Cu^{2+} ions by divalent ions as Zn^{2+}, Co^{2+} or Mg^{2+} and the other is to substitute Mo^{6+} by W^{6+}. In both cases, the ion radius size difference induces so-called “chemical” or “inner” pressure that together with a specific nature of the ions leads to a particular change of the metal-oxygen polyhedron deformation that, in turn, modifies the molybdate electronic structure and affects the temperature of the thermochromic phase transition in the material significantly [2].

Several studies have revealed that the thermochromic properties can be strongly affected by tungsten addition to $CuMoO_4$, resulting in a formation of $CuMo_{1-x}W_xO_4$ solid solutions [2, 3, 10, 11, 15]. Three different crystal structures with triclinic $P\bar{1}$ symmetry are known at ambient conditions for the $CuMo_{1-x}W_xO_4$ solid solutions [1]. Depending on the tungsten concentration, phases isostructural to high pressure phases of $CuMoO_4$ (α-$CuMoO_4$, γ-$CuMoO_4$, and $CuMoO_4$-III) with different Cu, Mo, and W coordination can be obtained [1, 15, 133]. The solubility limit of tungsten in $CuMo_{1-x}W_xO_4$ solid solutions to retain both α and γ structure types under ambient conditions is between $\sim$10 and 15% [10]. Furthermore, the $\alpha \leftrightarrow \gamma$ phase transition temperature depends strongly on tungsten concentration and becomes higher when the tungsten content increases (Fig. 5.2.3(b)) [2, 10, 11, 133]. Such behaviour was attributed to the stronger preference of tungsten ions to the octahedral environment, as compared to molybdenum [2, 10].

Tungsten concentration above ~15% in $CuMo_{1-x}W_xO_4$ solid solutions leads to wolframite-type ($CuMoO_4$-III) phase with the octahedral coordination of metal ions and do not exhibit pronounced thermochromic behaviour. However, these materials have properties that are promising for possible use as photoanodes in water splitting photoelectrochemical cells [1, 6, 8, 10].

Among all $CuMo_{1-x}W_xO_4$ solid solutions, $CuMo_{0.90}W_{0.10}O_4$ seems to be the most prospective material for technological applications. The most attractive feature is that both allotropic forms are stable in the temperature range between 0 and 100°C. It is possible to synthesize stable γ-$CuMo_{0.90}W_{0.10}O_4$ at room temperature and induce the γ-to-α phase transition by heating up to 100°C [2, 4, 10, 133]. Besides, Gaudon et al. demonstrated that a pressure induced by a "finger push" is enough to promote the α-to-γ phase transition in $CuMo_{0.90}W_{0.10}O_4$ at room temperature. In Ref. [113] a shock detector based on a mixture of two piezochromic compounds ($CoMoO_4$ and $CuMo_{0.90}W_{0.10}O_4$), capable to work at different temperatures, has been demonstrated.

$CuMo_{0.90}W_{0.10}O_4$ also exhibits halochromic properties, i.e. its colour depends on the solution's pH (Fig.5.1.1) [3]. This phenomenon has been explained in terms of surface protonation, which leads to the α-to-γ phase transition [3].

Furthermore, Gaudon with his co-workers observed thermosalient effect (also called "jumping crystal effect") while investigating the temperature induced structural evolution of $CuMo_{0.90}W_{0.10}O_4$ (Fig.5.1.1) [4]. During the α-to-γ phase transition, some crystallites are able to propel themselves upwards, thereby changing their physical positions which can be detected as red lights (γ crystallites) in an optical microscope. This effect is related to the transfer from thermal to mechanical kinetic energy. Such energy conversion in crystals could be of interest to a various range of applications.

Note that the last two properties are not typical for inorganic oxides and have never been reported in the literature before. These observations support the conclusion that the α-to-γ phase transition in $CuMoO_4$ and $CuMo_{0.90}W_{0.10}O_4$ can be described with "domino-cascade" model [4]. However, further studies are necessary to fully understand the structural background of phase transitions and optical properties of $CuMoO_4$, $CuMo_{0.90}W_{0.10}O_4$, and other solid solutions from $CuMo_{1-x}W_xO_4$ series.

In contrast, there have been only a few papers reporting the effect of substituting Cu^{2+} ions in $CuMoO_4$. The closest ionic radius to Cu^{2+} (0.73 Å) is for Zn^{2+} (0.74 Å) ion. Indeed, copper and zinc molybdates also form a complete solid solution series $Cu_{1-x}Zn_xMoO_4$ ($0 \leq x \leq 1$) [128, 135]. Note that α-$ZnMoO_4$ phase is isostructural to α-$CuMoO_4$ (triclinic $P\bar{1}$ symmetry

(Table 5.2.1) (Fig. 5.3.1) [136] and is stable in the whole temperature range till it decomposes at 1280 K [127, 135]. α-$ZnMoO_4$ is composed of distorted ZnO_6 octahedra, ZnO_5 square-pyramids and MoO_4 tetrahedra [128]. The interatomic distances for all non-equivalent zinc (Zn1, Zn2, Zn3) and molybdenum (Mo1, Mo2, Mo3) atoms with the nearest oxygen atoms are shown in Table 5.3.1. The β-$ZnMoO_4$ phase being stable at high pressure has monoclinic structure where both Zn and Mo atoms are bonded to six oxygen atoms [136].

Table 5.3.1: **Metal-oxygen interatomic distances in α-$ZnMoO_4$** [128].

Interatomic distances in α-$ZnMoO_4$ (R, Å)

Zn1-O	**Zn2-O**	**Zn3-O**	**Mo1-O**	**Mo2-O**	**Mo3-O**
2.043	1.988	1.946	1.742	1.728	1.719
2.065	2.048	2.031	1.745	1.751	1.730
2.072	2.054	2.033	1.761	1.792	1.794
2.080	2.060	2.035	1.809	1.806	1.817
2.103	2.144	2.111	3.496	2.811	3.027
2.144	2.260	3.117	3.654	3.579	3.288

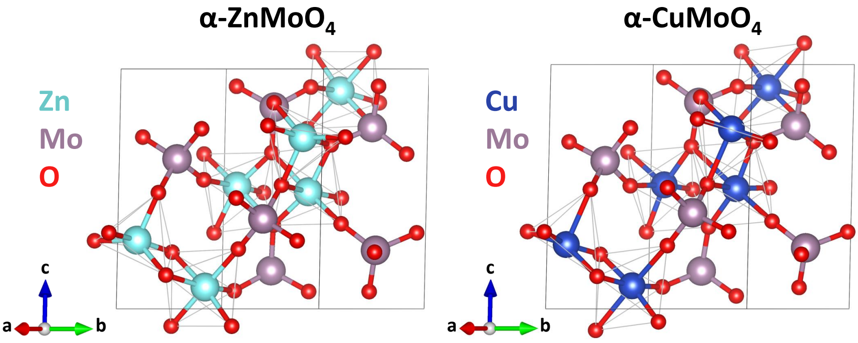

Figure 5.3.1: **The unit cell of α-$ZnMoO_4$ (left panel) and α-$CuMoO_4$ (right panel) [128].** Both phases are isostructural. However, strong distortions of the first coordination shell of copper ions is caused by the first-order Jahn-Teller effect due to the $Cu^{2+}[3d^9]$ electronic configuration which is absent for Zn^{2+} ions with $3d^{10}$ electronic configuration.

Magnetic susceptibility measurements of $Cu_{1-x}Zn_xMoO_4$ ($0 \leq x \leq 0.1$) samples reported in [137] indicate on the shift of the phase transition point to the lower temperatures with increasing Zn content (Fig. 5.3.2). Yanase *et al.* [134] studied the thermochromic phase transition in the $CuMo_{0.94}W_{0.06}O_4$ material doped with small amount of Zn ($0 \leq x \leq 0.05$). The results showed that the substitution of Cu^{2+} by Zn^{2+} reduces the phase transition temperature of $CuMo_{0.94}W_{0.06}O_4$ and stabilizes the α-phase, which is natural for α-$ZnMoO_4$ [128]. The transition occurs in the temperature range of

303–343 K. Recently, structural, morphological and optical properties of solid solutions with large Zn content ($0.92 \leq x \leq 1.00$) were studied [138]. In [139], luminescence and pigment properties of $Cu_{0.10}Zn_{0.90}MoO_4$ were also reported.

Since α-$ZnMoO_4$ is a non-toxic compound with excellent chemical and thermal stability, it can be used as a good host matrix for different rare-earth dopants. For instance, $ZnMoO_4:Eu^{3+}$ and $ZnMoO_4:Tb^{3+}$ are considered as perspective phosphors for white light-emitting diodes [140,141]. Furthermore, $ZnMoO_4$ is also a prospective material for applications in humidity sensors [142], scintillators [143,144], battery materials [145] and anti-corrosive paints [146].

A deep understanding of the structure-thermochromic property relationship in molybdates requires detailed information on the temperature dependence of their local atomic structure, which can be obtained using X-ray absorption spectroscopy. This question is one of the goals of the thesis and is addressed in the further chapters.

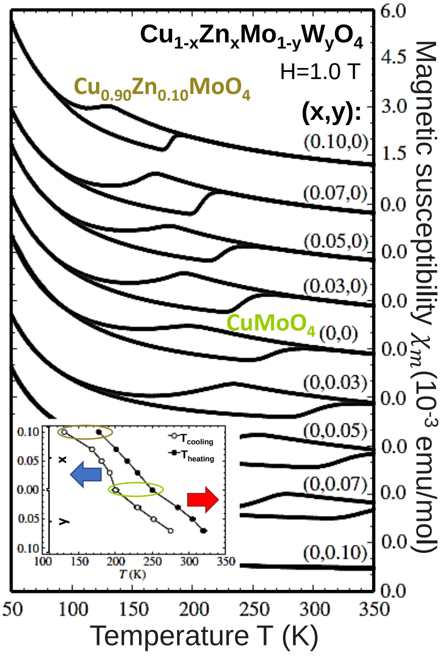

Figure 5.3.2: **Illustration of ability to affect the temperature-dependent properties of $CuMoO_4$ by doping with Zn and W: temperature dependence of the magnetic susceptibility in $Cu_{1-x}Zn_xMo_{1-y}W_yO_4$ solid solutions** (adapted from [137]). The temperatures associated with the structural phase transitions in the solid solutions with different Zn (x) and W (y) content during cooling and heating are shown in the inset.

Chapter 6

Samples and their characterization

6.1 Synthesis

Polycrystalline $CuMo_{1-x}W_xO_4$ powders (x=0, 0.04, 0.06, 0.10, 0.12, 0.15, 0.20, 0.50, 0.75, 1.00) were synthesized using a simple solid-state route by heating an appropriate mixture of CuO and MoO_3 powders with added stoichiometric amount of WO_3 at 650°C in the air for 8h followed by cooling down naturally to the room temperature. One set of as-prepared samples with $x \leq 0.15$ had greenish colour, and the second set with $x \geq 0.20$ was brownish (Fig. 6.1.1(a)). The phase of as-prepared powders was confirmed by X-ray powder diffraction and micro-Raman spectroscopy.

An example of the γ-$CuMo_{0.96}W_{0.04}O_4$ sample stabilized at room temperature by treatment α-$CuMo_{0.96}W_{0.04}O_4$ powder sample at 77 K in liquid nitrogen (cryogenic quenching) is shown in Fig. 6.1.1(b).

Polycrystalline $Cu_{1-x}Zn_xMoO_4$ powders (x=0.10, 0.25, 0.50, 0.75, 0.90, 1.00) were also synthesized using a solid-state reaction method. Namely, a mixture of ZnO, MoO_3, and CuO powders in a stoichiometric amount was heated at 650 °C in the air for 8 hours and left to cool down naturally to room temperature. Photos of selected samples are shown in Fig. 6.1.1(c).

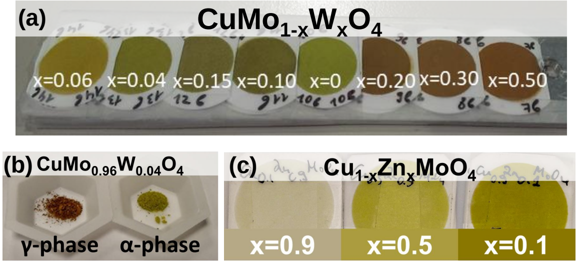

Figure 6.1.1: **Photos of selected samples:** Selected polycrystalline $CuMo_{1-x}W_xO_4$ powder samples prepared on Millipore filters for XAS measurements (a), $CuMo_{0.96}W_{0.04}O_4$ sample after treatment at 77 K in liquid nitrogen (γ-phase) and at room temperature (α-phase) (b), and selected polycrystalline $Cu_{1-x}Zn_xMoO_4$ powder samples prepared on Millipore filters for XAS measurements (c).

6.2 X-ray diffraction measurements

X-ray diffraction patterns of $\mathrm{CuMo}_{1-x}\mathrm{W}_x\mathrm{O}_4$ powder samples (Fig. 6.2.1 (a)) was measured at room temperature using Brucker AXS D2 PHASER Bragg-Brentano θ-θ powder diffractometer equipped with the LynxEye detector and copper anode (Cu Kα) tube. The samples were rotated during the measurements, and their patterns were collected in the angular range 2θ from 10° to 90° with the step of $\Delta(2\theta)$=0.04°.

In samples with low tungsten rate (below $x\sim0.15$), α-CuMoO_4 phase dominates. However, with increasing W concentration, some additional peaks appear indicating the presence of γ-phase (where molybdenum and tungsten atoms are in the octahedral environment). It is known from the literature that samples with $0.075<x<0.1$ can exist in both α and γ allotropic forms at ambient temperature-pressure conditions [147]. The transition from α-CuMoO_4 phase to wolframite-type phase occurs above $x\sim0.15$ together with a colour change from greenish to brownish (Fig. 6.1.1(a)).

The X-ray diffraction patterns of as-prepared $\mathrm{Cu}_{1-x}\mathrm{Zn}_x\mathrm{MoO}_4$ powders (Fig. 6.2.1 (b)) were obtained by Rigaku MiniFlex 600 diffractometer with Bragg-Brentano θ-2θ geometry equipped with the 600 W Cu anode (Cu Kα radiation, λ = 1.5406 Å) X-ray tube operated at 40 kV and 15 mA. $\mathrm{Cu}_{1-x}\mathrm{Zn}_x\mathrm{MoO}_4$ samples with $x \leq 0.10$ corresponds to the α-CuMoO_4 phase. In samples with $x > 0.10$, the α-ZnMoO_4 phase is dominating in agreement with literature data [128].

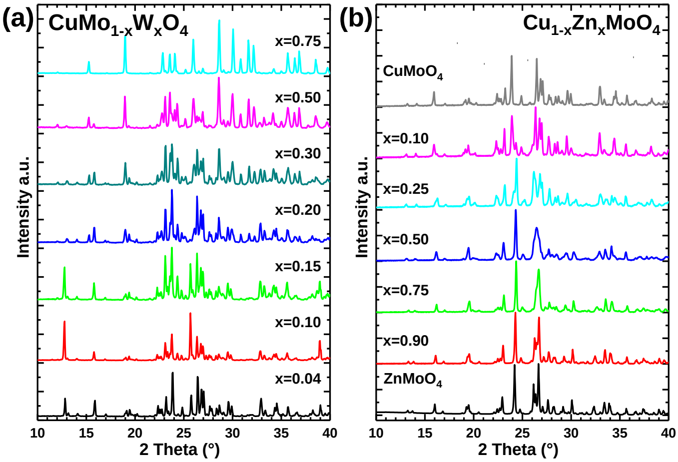

Figure 6.2.1: **Selected X-ray diffraction patterns of polycrystalline $\mathrm{CuMo}_{1-x}\mathrm{W}_x\mathrm{O}_4$ (a) and $\mathrm{Cu}_{1-x}\mathrm{Zn}_x\mathrm{MoO}_4$ (b) solid solutions.**

6.3 Micro-Raman measurements

Micro-Raman scattering spectra of $CuMo_{1-x}W_xO_4$ powder samples were measured using a confocal microscope with spectrometer Nanofinder-S (SOLAR TII) [148]. A diode-pumped solid-state Nd:YAG laser (λ=532 nm and maximum continuous wave power P_{ex}=150 mW) was used as an excitation source. The laser power was reduced by the variable neutral filter down to $\sim$1 mW at the focussing point. The inelastically scattered light separated from the elastic component by the Semrock 532 nm RazorEdge® ultrasteep long-pass edge filter (LP03-532RE) was focused at the entrance of the monochromator with a 520 mm focal length and dispersed by a 600 lines/mm grating onto a Peltier-cooled back-thinned CCD camera (ProScan HS-101H). All measurements were performed in the back-scattering geometry at room temperature through a Nikon CFI Plan Apochromat 20× (NA=0.75) optical objective.

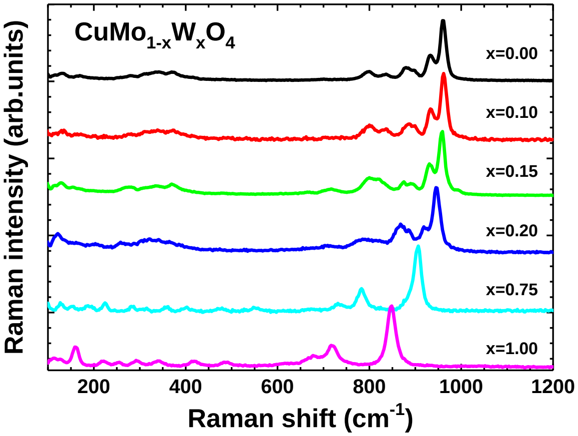

Figure 6.3.1: **Selected micro-Raman scattering spectra of polycrystalline $CuMoO_4$ (x=0), $CuMo_{1-x}W_xO_4$ solid solutions and $CuWO_4$ (x=1).**

The Raman scattering spectra of polycrystalline $CuMo_{1-x}W_xO_4$ ($0 < x < 1$) solid solutions are reported in Fig. 6.3.1. The spectra are dominated by the internal vibrations within the metal-oxygen polyhedra (MoO_x and WO_x) appearing at high frequencies. In pure compounds, these are MoO_4 in $CuMoO_4$ and WO_6 in $CuWO_4$. The highest frequency metal–oxygen stretching mode has the largest amplitude and is located at $\sim$850 cm^{-1} in copper tungstate and at $\sim$970 cm^{-1} in copper molybdate. In $CuWO_4$, the position of the stretching mode is shifted to smaller frequency compare to the data in literature [149, 150] due to the laser induced heating of the sample having dark colour. More detailed interpretation of the observed Raman bands in $CuWO_4$ and $CuMoO_4$ were published previously in Refs. [149–151]. When increasing the amount of tungsten atoms in the $CuMo_{1-x}W_xO_4$ solid solutions above ~0.15, the shape of the Raman spectra starts to deviated significantly from that in pure $CuMoO_4$ indicating on structural changes.

6.4 XAS experimental details

X-ray absorption experiments were performed within four beamtime projects at PETRA III (Germany) and ELETTRA (Italy) synchrotron radiation facilities. Low-temperature (from 10 K to 300 K) XAS experiments for $CuMo_{1-x}W_xO_4$ and $Cu_{1-x}Zn_xMoO_4$ samples (projects I-20160149 EC and I-20190277 EC) were conducted at the HASYLAB PETRA III P65 undulator beamline [152]. High-temperature measurements were performed at the ELETTRA XAFS bending-magnet beamline [153] in the temperature range from 296 K to 973 K (project 20150303). The fourth synchrotron radiation experiment (RXES measurements) was performed at the HASYLAB PETRA III P64 undulator beamline [154] (project I-20180615 EC).

During the low-temperature XAS measurements for $CuMo_{1-x}W_xO_4$ samples, the PETRA-III storage ring operated at E=6.08 GeV and current I=95 mA in top-up 40 bunch mode. The harmonic rejection was achieved by uncoated (Cu K and W L_3 edge) and Rh-coated (Mo K-edge) silicon plane mirrors. The X-ray absorption spectra were collected in transmission mode at the Cu (8979 eV) and Mo (20000 eV) K-edges and W (10207 eV) L_3-edge. Fixed exit Si(311) double-crystal monochromator was used in an experimental set-up. Two ionization chambers were employed for the X-ray intensity measurements before and after the sample. The Oxford Instruments liquid helium flow cryostat was used to maintain the sample temperature. Each XAS measurement was conducted after the sample temperature was stabilized for $\sim$ 20 min.

Analogous XAS experiments were conducted for $Cu_{1-x}Zn_xMoO_4$ samples. The PETRA III storage ring operated at E=6.08 GeV and current I=120 mA in top-up 480 bunch mode. The harmonic rejection was achieved by uncoated (Cu/Zn K-edges) and Rh-coated (Mo K-edge) silicon plane mirrors. Fixed exit Si(111) and Si(311) monochromators were used. The X-ray absorption spectra at the Cu (8979 eV), Zn (9659 eV) and Mo (20000 eV) K-edges were collected in transmission mode. The Oxford Instruments liquid helium flow cryostat was used for temperature-dependent measurements.

The powder samples for low-temperature XAS stuides were gently milled in an agate mortar and deposited on Millipore membrane (Fig. 6.1.1(c)). The thickness of the samples was optimized as much as possible for each absorption edge in order to obtain the value of the absorption edge jump $\Delta\mu x$ close to 1.

XAS spectra for $CuMoO_4$ sample at the Cu and Mo K-edges in the high-temperature range (296–973 K) were recorded in transmission mode at the XAFS bending-magnet beamline [153]. Composition dependent measurements for $CuMo_{1-x}W_xO_4$ samples (Fig. 6.1.1(a)) at Cu and Mo K-edges, and W L_3-edge were performed at room temperature. The storage ring was operating in the top-up multibunch mode at the energy E=2.4 GeV and current I=160 mA. The synchrotron radiation was monochromatized using a Si(111) (for the Cu K and W L_3 edges) and Si(311) (for the Mo K-edge) double-crystal monochromators. The sample for high-temperature XAS measurements was prepared by mixing $CuMoO_4$ powder with boron nitride and then pressing into a pellet. The thickness of the sample was optimized to obtain the absorption edge jump as close as possible to one. The sample was heated in the vacuum using the l'Aquila-Camerino glass furnace [153]. Each measurement was conducted after the sample temperature was stabilized for 15-20 min.

6.5 RXES experimental details

The temperature and composition-dependent RXES experiments for $CuMo_{1-x}W_xO_4$ solid solutions presented in this thesis (Chapter 9) were conducted at P64 Advanced X-Ray Absorption Spectroscopy beamline of the PETRA III (HASYLAB/DESY, Hamburg) storage ring using recently constructed RXES endstation [154, 155]. The X-ray beam from an undulator was monochromatized by a liquid-nitrogen-cooled Si(311) double-crystal monochromator, and focused in vertical and horizontal planes (100 μm $\times$ 240 μm) by two mirrors with rhodium coating. The high stability and high intensity ($5{\cdot}10^{11}$ photons/s) of the P64 beamline provided a possibility to accumulate high quality and resolution RXES data. The incident X-ray intensity was monitored using an ionization chamber. The XES signal was dispersed by von Hamos-type spectrometer equipped with cylindrical bent Si(444) analyser crystals [155] and collected by Dectris 2D Pilatus 300K detector. The energy of monochromator was calibrated at the W L_3-edge using tungsten foil and the energy scale of the spectrometer was set according to the position of the elastic line on the detector. The inelastically scattered X-ray signal and W $L\alpha_1$ and $L\alpha_2$ fluorescence were acquired in the RXES plane. The high-resolution W L_3-edge XANES (HERFD-XANES) was extracted from the RXES plane at fixed emission energy equal to 8398.5±0.2 eV. During the temperature-dependent measurements, the temperature of the sample was controlled using liquid nitrogen cryostat Linkam THMS600 in the temperature range of 90–450 K.

Chapter 7

XAS study of $CuMoO_4$

7.1 $CuMoO_4$ at low temperatures[1]

In this section, the *in situ* temperature-dependent (10–300 K) Cu and Mo K-edge XAS study of a thermochromic phase transition between brownish γ-$CuMoO_4$ and greenish α-$CuMoO_4$ performed at the DESY/HASYLAB PETRA III P65 undulator beamline [152] is reported. Experimental details can be found in Section 6.4. The Cu and Mo K-edge XANES and EXAFS parts of the X-ray absorption spectra were isolated and analysed separately. The influence of structural changes on the XANES spectra was also investigated by theoretical full-multiple-scattering (FMS) XANES calculations using *ab initio* real-space FDMNES code [18, 19].

7.1.1 XANES analysis

The experimental Mo and Cu K-edge XANES spectra corresponding to γ-$CuMoO_4$ at 10 K and α-$CuMoO_4$ at 300 K are shown in Fig. 7.1.1(a,b). The Cu K-edge XANES spectrum is weakly affected by the phase transition because the local environment around copper atoms does not change significantly (only 1/3 of all Cu atoms change their coordination from CuO_5 square-pyramids to CuO_6 octahedra [1]). At the same time, the Mo K-edge XANES is significantly affected by temperature variation. The differences can be related to the change in the coordination of molybdenum atoms from tetrahedral MoO_4 to octahedral MoO_6 upon cooling.

The pre-edge peak at the Mo K-edge is visible at $\sim$20 000 eV. It corresponds to the $1s(Mo)\rightarrow 4d(Mo)+2p(O)$ transition. The transition is forbidden in the dipole approximation for a regular MoO_6 octahedron, having an inversion center, but becomes allowed when inversion symmetry is broken as in distorted octahedron [156, 157] or tetrahedron [158]. The amplitude of the pre-edge peak depends on the distortion degree of the MoO_6 octahedra

---

[1] The material, presented in this section, has been published as: I. Jonane, A. Cintins, A. Kalinko, R. Chernikov, A. Kuzmin, **X-ray absorption near edge spectroscopy of thermochromic phase transition in $CuMoO_4$**, Low Temp. Phys. 44 (**2018**) 568-572;
I. Jonane, A. Cintins, A. Kalinko, R. Chernikov, A. Kuzmin, **Probing the thermochromic phase transition in $CuMoO_4$ by EXAFS spectroscopy**, Phys. Status Solidi B 255 (**2018**) 1800074:1-5.

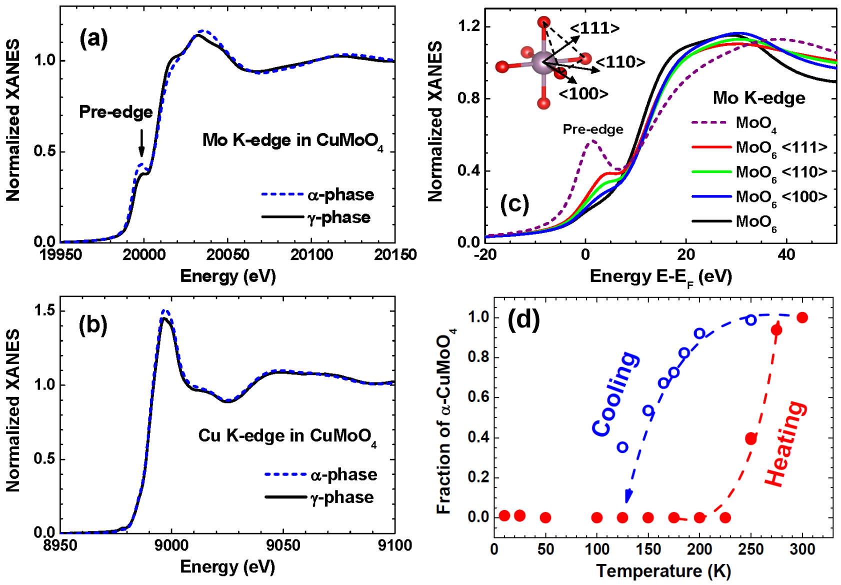

Figure 7.1.1: **The Mo and Cu K-edge XANES of α-$CuMoO_4$ and γ-$CuMoO_4$ phases**: Experimental Mo and Cu K-edge XANES of α-$CuMoO_4$ (at 300 K) and γ-$CuMoO_4$ (at 10 K) phases (a,b). Calculated Mo K-edge XANES for regular MoO_4 tetrahedron and distorted and regular MoO_6 octahedra. Numbers in brackets indicate the direction of molybdenum ion displacement from the center illustrated in the inset (c). Temperature dependence of the fraction of α-$CuMoO_4$ phase upon heating and cooling (d).

and 4d(Mo)/2p(O) orbital mixing. It is the largest for tetrahedral MoO_4 coordination. Therefore, it can be used to trace the α-to-γ phase transition in $CuMoO_4$.

The dependence of the Mo K-edge pre-peak amplitude on the local structure distortions are illustrated with theoretical FMS XANES calculations employing muffin-tin (10% overlap) self-consistent potential for five MoO_x clusters in Fig. 7.1.1(c). Calculations were performed for a regular MoO_4 tetrahedron ($R_{\text{Mo}-\text{O}}$=1.78 Å), a regular MoO_6 octahedron ($R_{\text{Mo}-\text{O}}$=1.98 Å) and distorted MoO_6 octahedra with molybdenum ion being displaced in the direction of octahedron apex ($\langle 100\rangle$) by 0.2 Å, to the octahedron edge ($\langle 110\rangle$) by 0.28 Å and to the octahedron face ($\langle 111\rangle$) by 0.35 Å.

Experimental Mo K-edge XANES spectra were treated with the linear combination analysis method described in Section 3.1.2. A fraction of α-$CuMoO_4$ phase was evaluated at each temperature during heating from 10 K to 300 K and cooling from 300 K down to 100 K using a linear combination of the lowest temperature (10 K) and highest temperature (300 K) Mo K-edge XANES spectra. A variation of the pre-edge shoulder was evaluated using Athena code [29] in the energy range from 19980 eV to

20010 eV. The estimated fraction of the α-phase in the total XANES at different temperatures is shown in Fig. 7.1.1(d).

The results show that the γ-to-α phase transition takes place in CuMoO$_4$ upon heating in the temperature range between $\sim$230 and 280 K, whereas the α-to-γ phase transition occurs at a lower temperature between $\sim$120 and 200 K. The hysteresis loop of the phase transition is well observed. Both phases are separated by a region where they coexist.

The two temperatures T$_{1/2H}$ and T$_{1/2C}$ corresponding to about 50% of the α and γ phases in the sample upon heating and cooling, respectively, are equal to T$_{1/2H} \approx$ 255 K and T$_{1/2C} \approx$ 143 K. The width of the hysteresis is defined as $\Delta T_{1/2} = T_{1/2H} - T_{1/2C} = 112$ K. Note that the $\Delta T_{1/2}$ values estimated from optical reflectivity ($\Delta T_{1/2} = 72$ K), differential scanning calorimetry ($\Delta T_{1/2} = 96$ K) and magnetic susceptibility ($\Delta T_{1/2} = 80$ K) measurements reported in [10] are slightly smaller.

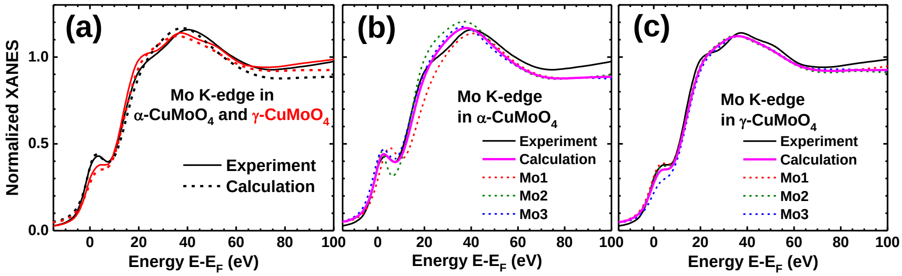

Figure 7.1.2: **FMS Mo K-edge XANES calculations for CuMoO$_4$:** Comparison of the experimental and calculated Mo K-edge XANES spectra of α-CuMoO$_4$ and γ-CuMoO$_4$ phases (a). Contributions from three non-equivalent molybdenum atoms (Mo1, Mo2, Mo3) to the Mo K-edge XANES for α-CuMoO$_4$ (b) and γ-CuMoO$_4$ (c).

FMS Mo K-edge XANES calculations were also performed for structural models corresponding to α- and γ-CuMoO$_4$ phases and constructed based on diffraction data from [1]. The total calculated Mo K-edge XANES spectra and individual contributions from non-equivalent molybdenum atoms (Mo1, Mo2 and Mo3) are compared with the experimental spectra in Fig. 7.1.2. The simulated XANES spectra are in a good agreement with experimental data. One can see that in the α-phase, the three non-equivalent Mo atoms, located in distorted tetrahedral local environment with the Mo–O distances ranged between 1.70 and 1.86 Å [1], give slightly different XANES spectra. In γ-phase, the three contributions to XANES from Mo atoms, located in a strongly distorted octahedral environment with the Mo–O bond lengths in the range from 1.68 and 2.49 Å [1], are close. However, some differences are evident in the pre-edge region, originated from the influence of more distant atoms located above 2.5 Å.

This study has shown that the XANES region is sensitive to changes in the molybdenum local environment. The amplitude of the pre-edge peak strongly correlates with the type and distortion of the molybdenum-oxygen coordination polyhedra. Thus, the variation in the pre-peak can be employed to trace the α-to-γ phase transition. However, more detailed analysis of the temperature dependence of the local environment in $CuMoO_4$, which is encoded in the EXAFS, is required to understand the relationship between the local structure and thermochromic properties of the material.

7.1.2 EXAFS experimental data

The Cu and Mo K-edge EXAFS spectra of $CuMoO_4$ were measured as a function of temperature upon heating from 10 to 300 K. Experimental EXAFS $\chi(k)k^2$ spectra were extracted following the conventional procedure [70] using Athena [29] package. The EXAFS spectra and their FTs calculated in the k-space range of 2.5-14.5 Å^{-1} at selected temperatures are shown in Fig. 7.1.3.

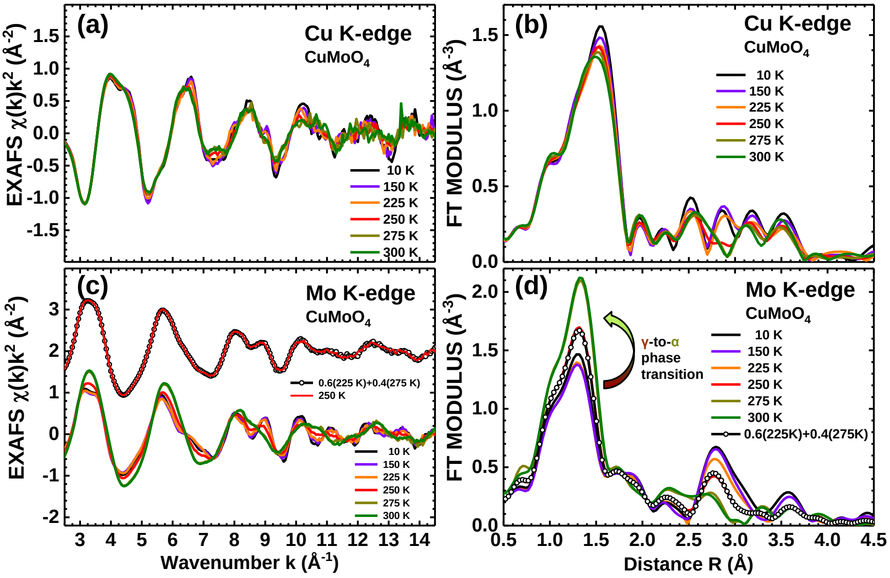

Figure 7.1.3: **Temperature-dependent experimental EXAFS data for crystalline $CuMoO_4$ at the Cu (a) and Mo (c) K-edge and their Fourier transforms (b,d)** (only modulus is shown). A weighted sum of the two Mo K-edge EXAFS spectra recorded at 225 and 275 K is shown by open circles and it is compared with the experimental EXAFS spectrum measured at 250 K in panels (c,d).

One can see that the Cu K-edge spectra are weakly affected during temperature increase, however, at 250 K some changes occur, that can be attributed to the transition from CuO_6 octahedra to CuO_5 square-pyramids.

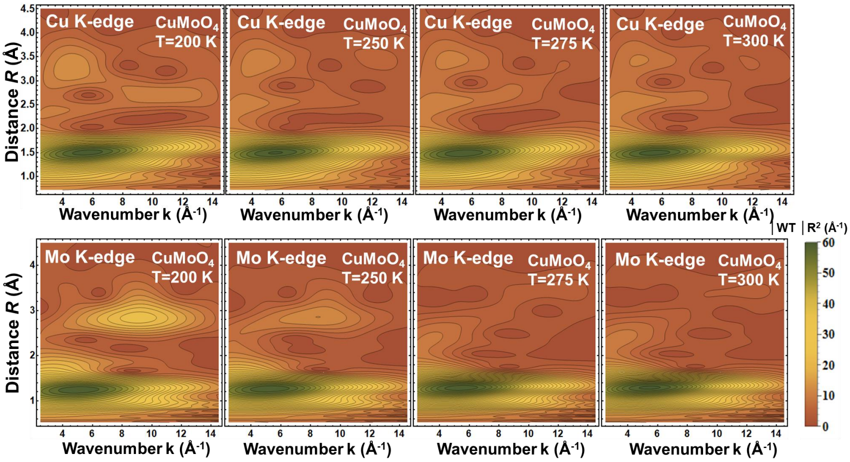

Figure 7.1.4: **Wavelet transforms of the Cu and Mo K-edges EXAFS at several temperatures for $CuMoO_4$.**

At the same time, the Mo K-edge is drastically affected during the phase transition because of the changes in molybdenum coordination from octahedral to tetrahedral. The changes in the atomic structure of the material occur in all coordination shells around Mo, leading to a variation of peaks in FTs. Also corresponding WTs shown in Fig. 7.1.4 qualitatively depict pronounced temperature-induced changes in the experimental data at the Mo K-edge. Metal-oxygen contributions dominate at small k-values, while heavy metal elements contribute at large k-values. Note that the analysis of distant coordination shells is a challenging task due to their substantial overlap and multiple-scattering contributions. Such research requires the use of advanced techniques as, for example, RMC simulations [17].

All experimental Mo K-edge EXAFS spectra can be classified into three series: (i) the spectra below 225 K correspond to pure γ-$CuMoO_4$ phase, (ii) the spectra above 275 K correspond to pure α-$CuMoO_4$ phase, and (iii) the spectrum at 250 K corresponds to the superposition of two coexisting phases. In particular, the EXAFS spectrum at 250 K can be reproduced by the weighted sum of two EXAFS spectra corresponding to γ-phase at 225 K and α-phase at 275 K with the weights of 60% and 40%, respectively (Fig. 7.1.3(c,d)). This result is in agreement with the linear combination analysis (LCA) of the Mo K-edge XANES spectra.

Recovery of structural information encoded in EXAFS data for such low-symmetry materials as $CuMoO_4$ is challenging. In the following sections we present two approaches to extract this information based on a regularization-like technique and the RMC/EA method.

7.1.3 EXAFS analysis using regularization-based technique

EXAFS spectra in the case of strongly distorted environment can be analysed using a regularization-like method, implemented in the EDARDF code [31]. This approach was employed to extract model-independent RDFs within the first coordination shell around molybdenum atoms in $CuMoO_4$, which can be further used to follow the thermochromic γ-to-α phase transition.

Here we limit our discussion to the first coordination shell of molybdenum atoms because their local atomic structure experiences the most considerable transformation upon thermochromic phase transition. The first coordination shell contribution into FTs in Fig. 7.1.3 corresponds to the first peak between $\sim$0.8 and $\sim$2.2 Å. The broad shape of the peak is due to the presence of three inequivalent Mo atoms and a distortion of the molybdenum-oxygen polyhedra. Due to the low symmetry of $CuMoO_4$, the coordination shells overlap strongly and, therefore, no unique peak assignment can be done in the FTs beyond the first shell.

The first coordination shell EXAFS signals were isolated from the high-frequency outer shell contributions in the total spectrum by the inverse FTs in the R-space range of 0.5-2.5 Å. The obtained Mo K-edge EXAFS spectra of the first coordination shell are shown in Fig. 7.1.5(a). EXAFS signals are damped due to static distortions and thermal disorder. Such contribution does not contain high-frequency signals, which originate in Fig. 7.1.3 from more distant coordination shells and MS effects. The same extended R-range was used at all temperatures to reliably include contributions of octahedral and tetrahedral environments of Mo atoms.

Theoretically, the EXAFS spectrum corresponding to the first coordination shell can be calculated by Eq. 2.23. In our case, the integration in Eq. 2.23 was performed over the range 0.8-2.8 Å. Theoretical backscattering amplitude and phase shift functions were calculated for γ-$CuMoO_4$ crystallographic structure [1] using the FEFF8.5L code [37]. The complex energy-dependent exchange-correlation Hedin-Lundqvist potential [159] was employed to account for inelastic effects. The obtained EXAFS fits for selected temperatures, and the corresponding RDFs $g_{Mo-O}(R)$ in the range from 1.55 Å to 2.6 Å are shown in Fig. 7.1.5(a,b).

According to the diffraction data [1], there are 12 different Mo–O bonds around three non-equivalent molybdenum atoms with tetrahedral coordination in α-$CuMoO_4$ as shown in Table 5.2.2. Thus, the mean distance to the nearest four oxygen atoms equals $\sim$1.77 Å with the standard deviation of 0.05 Å. At the same time, in γ-phase the coordination of molybdenum atoms is octahedral, and oxygen atoms are split into two groups of four nearest and two more distant atoms [1]. There are again three non-equivalent molybdenum atoms with the mean distance to the nearest four oxygen atoms $\sim$1.82 Å with the standard

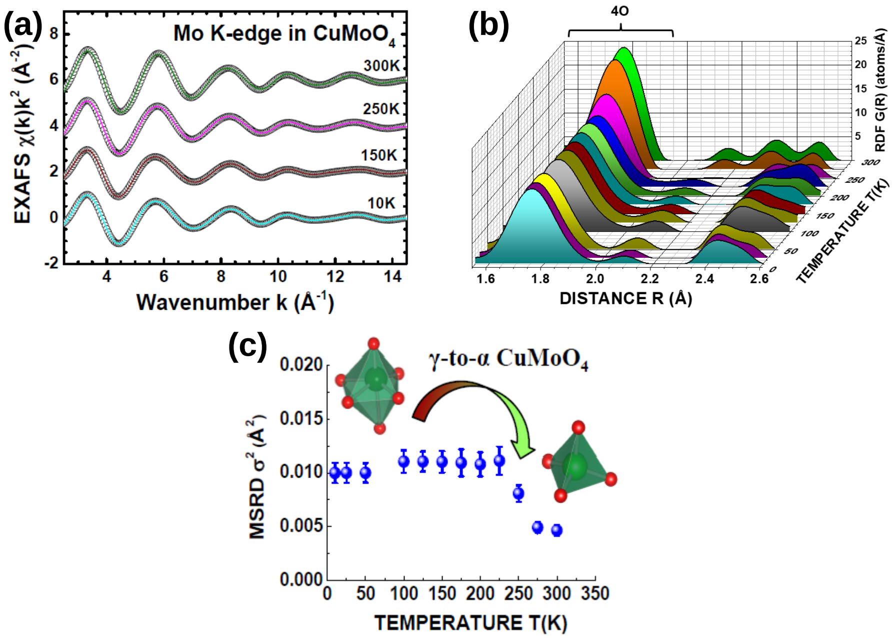

Figure 7.1.5: **Results of EXAFS data analysis with the regularization-like method:** Comparison of the experimental (open circles) and calculated by the regularization-like method [31] (solid lines) Mo K-edge EXAFS $\chi(k)k^2$ spectra for the first coordination shell of Mo atoms in CuMoO$_4$ at selected temperatures (a). Obtained temperature-dependent RDFs $g_{\mathrm{Mo-O}}(R)$ in CuMoO$_4$. The first peak due to the four nearest oxygen atoms is indicated (b). Temperature dependence of MSRD factor σ^2 for the four shortest Mo–O interatomic distances in CuMoO$_4$ (c).

deviation of 0.11 Å, being more than twice larger than that in the α-phase. Thus, the local environment of molybdenum atoms is more distorted in the γ-phase.

The first RDF peak (Fig. 7.1.5(b)) located in the range of 1.55–2.0 Å corresponds to the group of four nearest oxygen atoms. They are strongly bound to molybdenum atoms in both α- and γ-CuMoO$_4$ phases. The mean Mo–O distance estimated from the RDF maximum position is equal to 1.76±0.02 Å and remains the same in all temperature range in both phases. Note that the RDF determined by EXAFS includes both thermal and static disorder, and EXAFS is also more sensitive to shorter distances. As a result, there is some small difference in Mo–O distances for the nearest oxygen atoms observed by EXAFS and diffraction reported in [1].

The group of the nearest oxygen atoms is sensitive to structural distortions as reflected by the peak broadening. Therefore, the analysis of the first peak in RDFs $g(R)$ can be used to follow the phase transition continuously. This group of four oxygen atoms is also well separated from other contributions and can be analysed and discussed separately. The two distant oxygen atoms of $\mathrm{MoO_6}$ octahedra in γ-$\mathrm{CuMoO_4}$ (T<250 K) are also detectable in Fig. 7.1.5(b) at 2.0-2.6 Å. Note that the RDFs $g_{\mathrm{Mo-O}}(R)$ in α-$\mathrm{CuMoO_4}$ phase (T>250 K) contain several spurious peaks at distances R>2.1 Å, which come from some unfiltered MS contributions generated within $\mathrm{MoO_4}$ tetrahedra [160].

One can use an analytical model to parametrize the obtained RDFs and obtain a set of quantitative structural parameters (N, R, σ), which can be discussed more easily. When Gaussian model is applied, the amplitude of the RDF peak is given by $N/\sqrt{2\pi\sigma^2}$, where N is the coordination number, and σ^2 is the MSRD factor describing both static and thermal disorder. In our case, the RDF reported in Fig. 7.1.5(b) corresponds to the group of four nearest oxygen atoms, so that N=4 and R=1.76 Å for all temperatures. Therefore, the MSRD σ^2 can be extracted and used as the only free parameter. The variation of the obtained MSRD factor with temperature is shown in Fig. 7.1.5(c).

Note that the MSRD factor should increase upon heating due to larger amplitude of thermal vibrations. However, in our case, significant decrease in the MSRD factor values from $\sim$0.010 to $\sim$0.005 Å^2 is observed above $\sim$225 K, indicating on the phase transition and changes in the local environment of molybdenum atoms, i.e., transformation from strongly distorted octahedral environment in γ-$\mathrm{CuMoO_4}$ to less distorted tetrahedral in α-$\mathrm{CuMoO_4}$. Furthermore, the variation of the MSRD in the γ-phase below 225 K is negligible being within the error bars due to the dominant role of static distortions.

For comparison, calcium molybdate ($\mathrm{CaMoO_4}$) with the scheelite structure-type has molybdenum atoms with tetrahedral coordination and the average bond length ($R_{\mathrm{Mo-O}}$=1.775 Å [161]) close to that in α-$\mathrm{CuMoO_4}$. The MSRD values for this compound obtained from lattice dynamics calculations are $\sigma^2_{\mathrm{Mo-O}}$=0.00042 Å^2 and 0.00128 Å^2 at 10 K and 300 K, respectively [162]. Comparison of these small MSRD values with those reported in Fig. 7.1.5(c) for short Mo–O bonds support our conclusion on the dominant role of the static disorder in both $\mathrm{CuMoO_4}$ phases.

To sum up, the analysis of the Mo K-edge EXAFS spectra using the regularization-like method resulted in a good agreement with the experimental data and allowed us to obtain temperature-dependent RDFs $g_{\mathrm{Mo-O}}(R)$ of molybdenum atoms. Analysis of the first coordination shell was sufficient to follow the thermochromic phase transition since the change of the local coordination of molybdenum atoms is responsible for optical properties. The influence of temperature on the local environment around molybdenum atoms in both γ and α phases is rather weak, and the disorder is dominated by static distortions. The temperature dependence of the RDFs

$g_{\mathrm{Mo-O}}(R)$ and obtained MSRD factor $\sigma^2_{\mathrm{Mo-O}}$ values suggest that the γ-to-α phase transition occurs gradually within a temperature range of 225–275 K, in agreement with the results of previous studies [2, 10, 14] and linear combination analysis of the Mo K-edge XANES spectra reported above.

7.1.4 EXAFS analysis based on the RMC/EA approach

The analysis of the EXAFS spectra of CuMoO$_4$ can be performed using advanced reverse Monte Carlo (RMC) calculations based on the evolutionary algorithm (EA), as implemented in the EvAX code [17]. The strong advantage of this method is its ability to determine a single structural model by simultaneous analysis of more than one absorption edge, i.e. Cu and Mo in the case of CuMoO$_4$ within MS approach.

Calculation details

Initial structure models of CuMoO$_4$ corresponding to the α and γ phases were constructed based on the diffraction data reported in [1]. The RMC/EA calculations were performed for the Cu and Mo K-edges simultaneously using periodic boundary conditions for $4a_0\times4b_0\times4c_0$ (a_0, b_0 and c_0 are the lattice parameters) large supercell, containing 2304 atoms. At each RMC iteration, all atoms in the supercell were randomly displaced with the maximum allowed displacement of 0.4 Å. The RMC/EA calculations were performed for 32 atomic configurations simultaneously. The configuration-averaged EXAFS signals at the Cu and Mo K-edges were calculated using the *ab initio* self-consistent real space multiple-scattering FEFF8.5L code [25, 37]. MS contributions were accounted up to the 5^{th} order. The complex energy-dependent exchange-correlation Hedin-Lundqvist potential [159] was employed to account for inelastic effects. The amplitude scaling parameter S_0^2=1 was used in all simulations. The comparison between the experimental and calculated EXAFS spectra was performed using the Morlet WTs in the k-space range from 2.5 to 14.5 Å^{-1} for both edges and in the R-space range from 0.7 to 4.5 Å for the Cu K-edge and from 0.5 to 4.5 Å for the Mo K-edge. The fit was evaluated based on the difference between the WTs of experimental and simulated EXAFS spectra as $\xi = (\xi_{Cu} + \xi_{Mo})/2$. The convergence of RMC simulations was achieved after several thousands of iterations. Multiple calculations with different pseudo-random number sequences were performed.

Note that the RMC/EA method allows us to perform an accurate analysis of thermal disorder contribution but does not allow us to follow the variation of the unit cell upon a phase transition: the unit cell size and shape should be fixed in our realisation of the RMC. Most often it is set according to diffraction data. Thus, the RMC method is challenging when two different phases coexist.

In the case of CuMoO$_4$, the RMC/EA calculations of the experimental data close to the γ-to-α phase transition temperature were performed starting from the structure models for both phases. The final atomic configurations in RMC calculations were used to calculate the partial RDFs $g(R)$ for further analysis.

Results of RMC/EA calculations

The obtained RMC/EA fits for CuMoO$_4$ at selected temperatures are shown in Fig. 7.1.6. One can see that the experimental EXAFS spectra of CuMoO$_4$ at 200 K and 300 K are well described by the structure models of γ and α phases, respectively. At the same time, the structure models of both α and γ phases give reasonable agreement with the experimental data at T=250 K, indicating the coexistence of the two phases in close ratio. This conclusion agrees with the LCA results suggesting the presence of the 60% and 40% of γ- and α-CuMoO$_4$ phases, respectively [162]. However, γ-phase gives slightly smaller residual ξ.

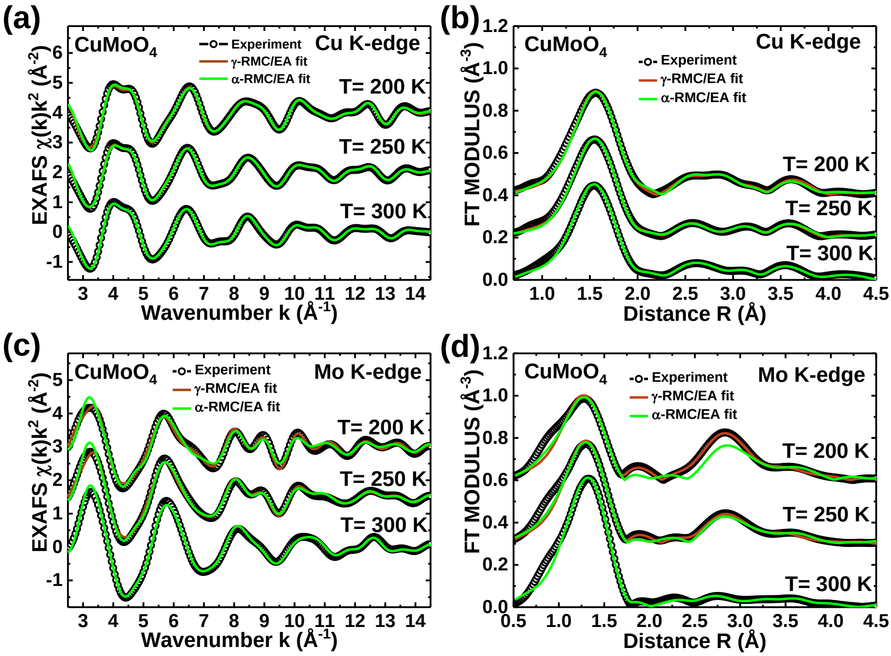

Figure 7.1.6: **Results of RMC/EA calculations for the Cu and Mo K-edges in CuMoO$_4$ at selected temperatures**: the experimental and calculated EXAFS spectra $\chi(k)k^2$ using α- and γ-CuMoO$_4$ initial structure models (a,c) and the corresponding Fourier transforms (only modulus is shown) (b,d).

Temperature-dependent partial RDFs $g(R)$ around copper and molybdenum atoms were calculated from the atom coordinates of the RMC/EA models. Distributions corresponding to the first coordination shell at 10 K and 300 K are compared in Fig. 7.1.7. Note that one can distinguish three non-equivalent crystallographic sites of Cu and Mo atoms with the different local environment. The MSRD values calculated by Eq. 3.16 for the first coordination shell around all metal atoms are shown in Figs. 7.1.8 and 7.1.9.

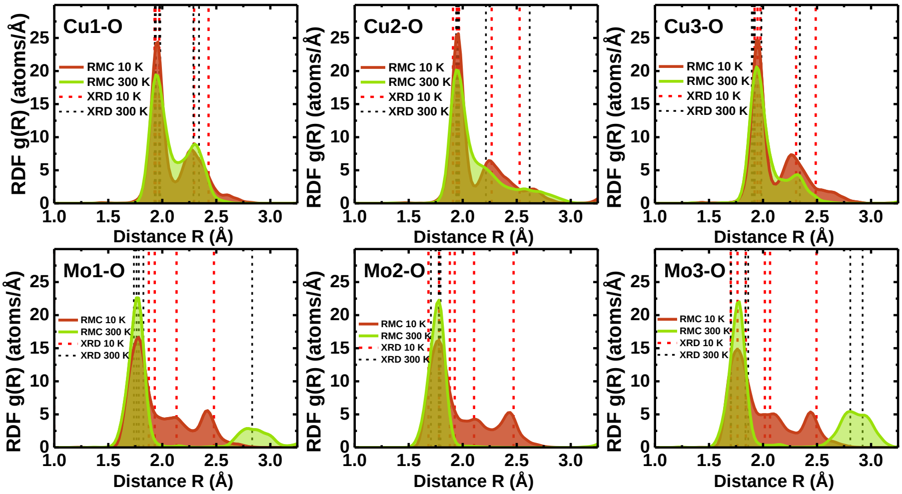

Figure 7.1.7: **Radial distribution functions for three non-equivalent Cu–O, Mo–O atom pairs in $CuMoO_4$ calculated from the atomic coordinates of the RMC/EA models.** Dashed vertical lines show interatomic distances according to diffraction data [1].

All non-equivalent Cu–O distributions are similar at the first RDF peak; however, differences appear for more distant atoms. The effect of temperature is evident as a change in peak widths and shape. The average MSRD factor for the closest four oxygen atoms at 300 K ($\sim$0.006 Å^2) is approximately twice larger than that at 10 K ($\sim$0.003 Å^2). The MSRD factors for longer Cu–O bonds, linking copper atoms with axially located oxygen atoms, are generally larger than those for the short Cu–O bonds. However, due to the limited sensitivity of EXAFS to distant oxygen atoms, whose contribution to the total EXAFS spectrum is weak, obtained MSRD factor values have big error bars and cannot be analysed in details.

The RDFs of Mo–O atom pairs at 10 and 300 K differ significantly already for the closest four oxygen atoms. The tetrahedral coordination in α-phase (300 K) is more ordered than the octahedral one in γ-phase (10 K). The MoO_6 octahedra are strongly distorted with a distribution of Mo–O distances from $\sim$1.5 Å to $\sim$2.8 Å. The four nearest oxygen atoms are responsible for a sharp peak in the RDFs at $\sim$1.8 Å. Corresponding averaged MSRD factor values $\sigma^2_{\mathrm{Mo-O}}$ are $\sim$0.010 Å^2 and $\sim$0.004 Å^2 at 10 and 300 K, respectively. As shown in Fig. 7.1.9, these results agree with those obtained by the regularization-like method reported before [163].

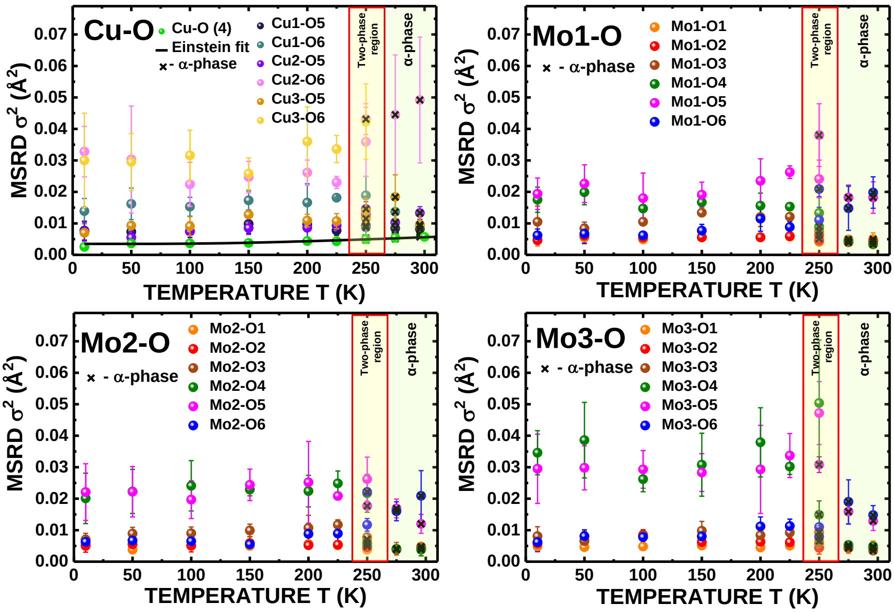

Figure 7.1.8: **MSRD factors as function of temperature for metal-oxygen atom pairs within the first coordination shell.** Average MSRD factors for atom pairs corresponding to copper and nearest four oxygen atoms together with MSRDs for non-equivalent copper and more distant oxygens (O5 and O6) are shown. MSRDs for non-equivalent molybdenum and nearest 6 oxygen atoms are plotted separately. Since at 250 K, γ and α phases coexist, both structure models were tested. Data points with cross correspond to results for α-phase structural model.

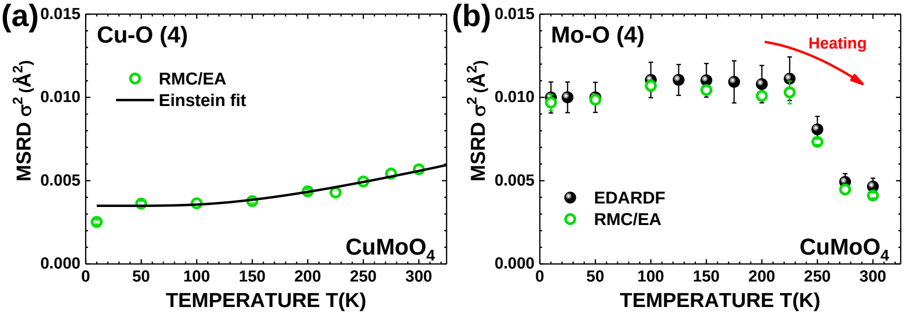

Figure 7.1.9: **Temperature-dependent average MSRD factors for four nearest Cu–O and Mo–O atom pairs**: results obtained by RMC/EA calculations together with correlated Einstein fit (a) and comparison between results obtained by the regularization-based method (EDARDF code [31]) and RMC/EA calculations (b).

The important advantage of RMC calculations is the possibility to analyse contributions to the experimental data beyond the first coordination shell. However, in the case of CuMoO$_4$ the separation of metal-metal contributions is very challenging due to six non-equivalent metal atoms present in the unit

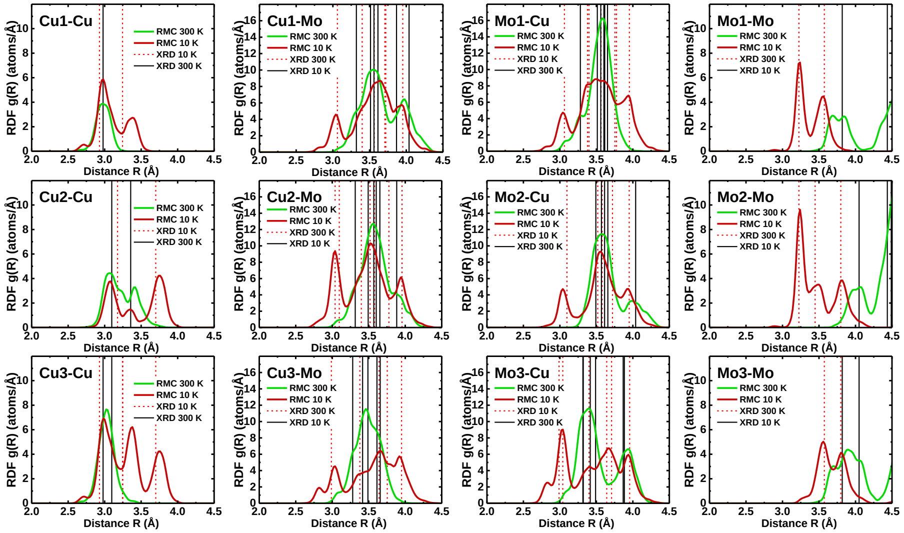

Figure 7.1.10: **Radial distribution functions for three non-equivalent metal-metal atom pairs in CuMoO$_4$ calculated from the atomic coordinates of the RMC/EA models.** Dashed vertical lines show interatomic distances according to the diffraction data [1].

cell. The RDFs shown in Fig. 7.1.10 contain complex and hardly comparable distribution functions. In γ-phase, the first metal-metal coordination shell is located at shorter distances than in α-phase. It is in agreement with the volume reduction predicted by XRD measurements [1]. Cu–Cu distributions at 10 K show a shift to larger distances in comparison with equilibrium positions known from XRD. The Mo–Mo RDFs at 300 K reveal peak splitting at distances between ~2.5-4.0 Å.

To sum up, RMC/EA method allowed us to reconstruct a temperature-dependent three-dimensional structure model of CuMoO$_4$ consistent with the experimental data at the Cu and Mo K-edges simultaneously. MSRD values for Mo–O atom pair obtained in RMC/EA calculations coincide with those obtained from the regularization method. Simulations of the EXAFS spectrum at 250 K were performed using both α and γ-phase initial structure models. γ structure gave slightly better agreement with the experimental EXAFS data.

7.1.5 Conclusions

Analysis of XAS data in the low-temperature range (10-300 K) provides valuable information on the evolution of the local structure around copper and molybdenum atoms in CuMoO$_4$ during the structural phase transition between α and γ phases.

The Mo K-edge XANES analysis, in particular, a variation in the pre-edge peak at $\sim$20 000 eV, allowed us to reconstruct the hysteresis of the α-to-γ phase transition in $CuMoO_4$. Based on these data, the change from γ-to-α phase occurs in the temperature range of 230-280 K upon heating, whereas the α-to-γ transition occurs between 120 and 200 K upon cooling. The transition occurs gradually with the temperature range where the two phases coexist. During heating, molybdenum coordination by oxygen atoms changes from strongly distorted octahedral to less distorted tetrahedral. At 250 K, the sample consisted of $\sim$60% γ-phase and $\sim$40% α-phase. The influence of thermal effects is weak.

The analysis of the Mo K-edge EXAFS spectra using the regularization-like method allowed us to obtain temperature-dependent RDFs $g_{\mathrm{Mo-O}}(R)$ and confirmed that the γ-to-α phase transition occurs gradually within a temperature range of 225–275 K. The influence of thermal effects on the local environment around molybdenum atoms in both γ and α phases is relatively weak, and the disorder is dominated by static distortions.

Further EXAFS data analysis by the RMC/EA method allowed us to reconstruct a three-dimensional structural model of $CuMoO_4$, consistent with the experimental data simultaneously at the Cu and Mo K-edges. MSRD values for the Mo–O atom pairs determined from RMC/EA calculations are very close to those obtained from the regularization method. At 250 K, γ-phase structure model gives slightly better agreement with the experimental EXAFS data supporting γ-phase predominance over α-phase.

7.2 $CuMoO_4$ at high temperatures[2]

In this section, the relationship between the structure and thermochromic properties of $CuMoO_4$ observed at high temperatures (the colour change from greenish to brownish as shown in Fig. 7.2.1) is discussed. Note that no structural phase transition occurs in $CuMoO_4$ at high temperatures (> 300 K), and it always remains in the α-phase.

XAS at the Cu and Mo K-edges was used to investigate the effect of heating on the local atomic structure and lattice dynamics in α-$CuMoO_4$ in the temperature range from 296 to 973 K. RMC/EA method was employed to get temperature-dependent 3D structural models of the material consistent with experimental EXAFS data. Obtained atomic coordinates were further used to follow the temperature-induced evolution of the local environment of Cu and Mo atoms. Moreover, the same models were able to interpret strong temperature-dependent variation of the Cu K-edge XANES spectra.

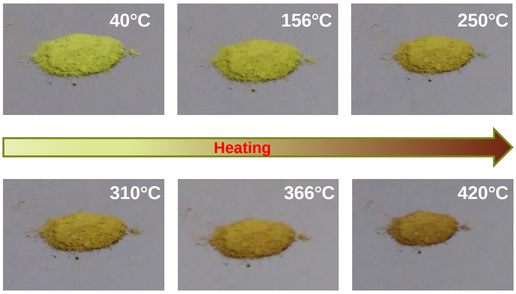

Figure 7.2.1: **Temperature-induced colour change of $CuMoO_4$ powder sample.**

7.2.1 XAS experimental data

Temperature-dependent normalized experimental XANES spectra at the Cu and Mo K-edges in α-$CuMoO_4$ are shown in Fig. 7.2.2. The most pronounced temperature effect can be seen for the Cu K-edge. As described in Section 3.6.8, most often XANES region is weakly affected by atomic thermal motion, however, in particular cases, XANES is sensitive to thermal disorder [94–98]. Theoretical XANES calculations were performed to interpret exceptional experimental data, and their results are discussed below.

The Cu and Mo K-edge EXAFS spectra, extracted following the conventional procedure [70] are shown in Fig. 7.2.3 together with their FTs

---

[2] The material, presented in this section, has been published as: I. Jonane, A. Anspoks, G. Aquilanti, A. Kuzmin, **High-temperature X-ray absorption spectroscopy study of thermochromic copper molybdate**, Acta Mater. 179 (**2019**) 26-35.

calculated for k-space range of 2.5-14.5 Å^{-1}. All spectra are dominated by the first coordination shell contributions. However, structural peaks up to ∼4 Å are well observed in FTs. Furthermore, clear effect of temperature induced disorder is visible in the experimental data and is more pronounced in the case of the Cu K-edge.

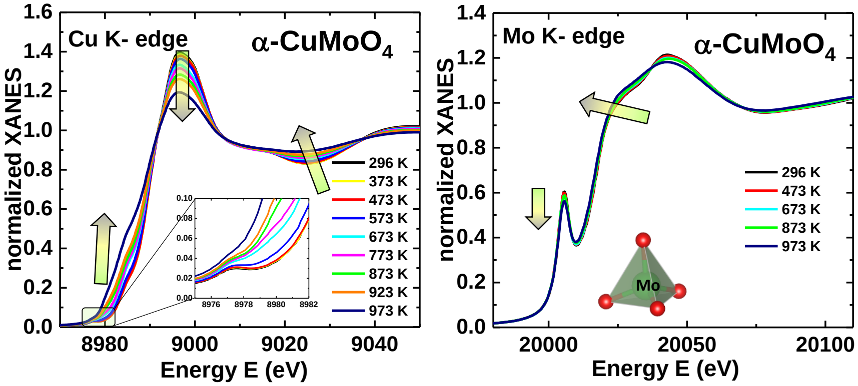

Figure 7.2.2: **Temperature-dependent experimental Cu and Mo K-edge XANES of α-$CuMoO_4$.**

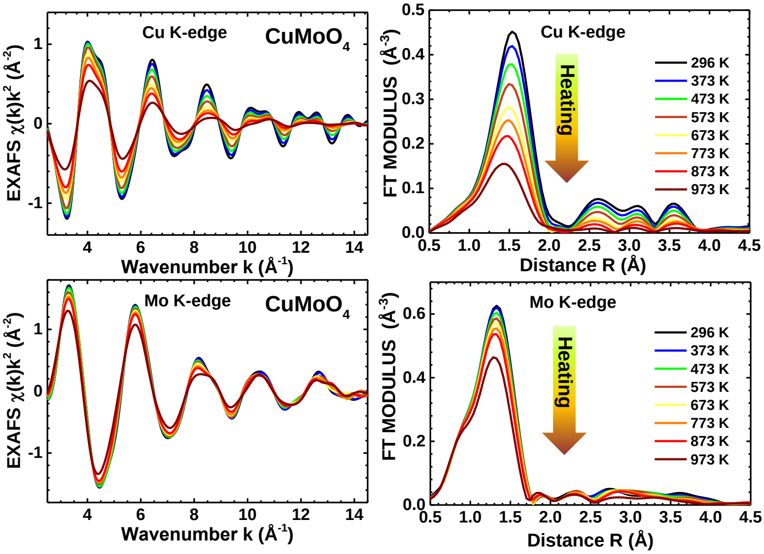

Figure 7.2.3: **The experimental Cu and Mo K-edge EXAFS $\chi(k)k^2$ spectra and their Fourier transforms for α-$CuMoO_4$ as a function of temperature.**

7.2.2 RMC/EA calculations

RMC/EA calculations were performed using the EvAX code [17] as described in Section 7.1.4. Initial structural models for the simulations were constructed based on the diffraction data for α-$CuMoO_4$ [1] taking into account temperature-induced lattice expansion. Random atomic displacements introduced during the RMC simulations allow one to mimic temperature induced distortions encoded in the XAS experiment.

Good agreement between experimental and calculated EXAFS data was obtained after several thousands of iterations, and the results are presented in Fig. 7.2.4 for selected temperatures. The RMC/EA calculations were repeated several times with different pseudo-random number sequences [17] to improve statistics and to estimate uncertainties of the results. The final structural models were used to determine the RDFs $g(R)$ for the first coordination shell of copper and molybdenum atoms, and to estimate MSRD factor values σ^2 for Cu–O and Mo–O atom pairs. Temperature dependences of the MSRDs were described by the correlated Einstein model (Eq. 3.5) [50].

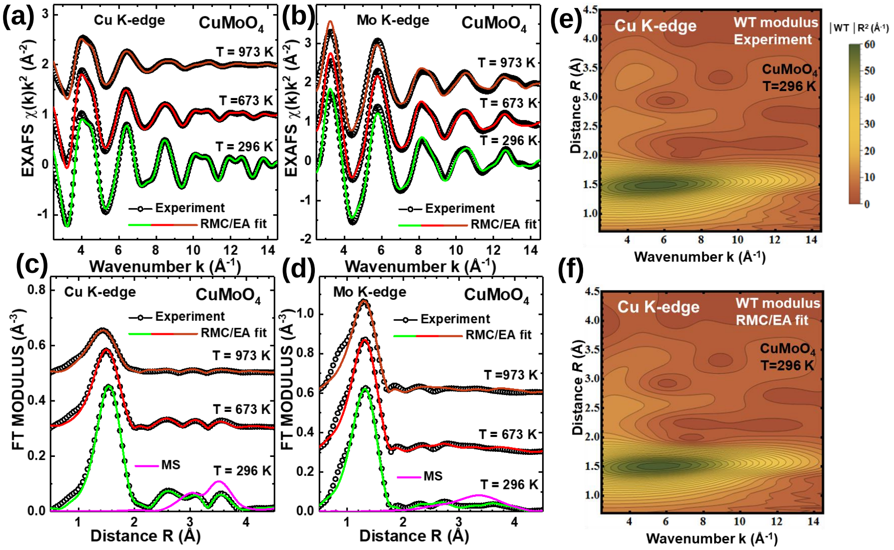

Figure 7.2.4: **The results of RMC/EA-EXAFS calculations for α-$CuMoO_4$ at selected temperatures**: The Cu and Mo K-edges EXAFS spectra $\chi(k)k^2$ (a,b) and their Fourier transforms (only modulus is shown) (c,d). The Morlet wavelet transforms (WTs) of the experimental and calculated EXAFS spectra at $T = 296$ K are also shown (e,f).

The 3D structural models obtained in RMC/EA calculations were validated against diffraction data. Namely, the coordinates of all atoms in the supercell were projected into a single unit cell, and the average position for each non-equivalent atom was calculated. Average positions of atoms correspond to their

Wyckoff positions in the unit cell, so that they can be used to calculate the diffraction pattern, which can be further compared with the experimental one. An example of such procedure is shown in Fig. 7.2.5 for α-CuMoO$_4$ at 973 K. As one can see, our RMC/EA calculations reproduce rather well the average positions of atoms and, thus, also the diffraction pattern.

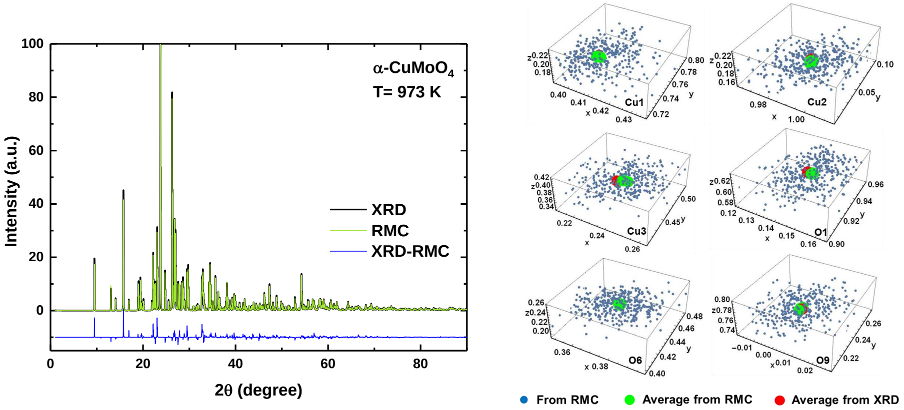

Figure 7.2.5: **Comparison of the structural model obtained in RMC/EA simulations with XRD data:** (a) Example of comparison of diffraction patterns for α-CuMoO$_4$ at 973 K: black curve – experimental data from [1], green curve – calculation from the average positions of the atoms in the unit cell obtained from the RMC/EA-EXAFS simulation, blue curve – the difference between two patterns. (b) An illustrative comparison of the atomic positions (small blue circles) of six non-equivalent atoms (Cu1, Cu2, Cu3, O1, O6 and O9) in the unit cell obtained in the RMC/EA-EXAFS simulations at 973 K with their Wyckoff positions (red circles) from the diffraction data [1] and evaluated from the RMC/EA simulations (green circles).

7.2.3 XANES calculations

XANES calculations were performed by the *ab initio* full-multiple-scattering FDMNES code [18, 19] employing muffin-tin self-consistent potential (10% overlap). The dipole and quadrupole allowed transitions were taken into account. Around each absorbing copper atom the cluster with the radius of 4.0 Å was constructed to account for all atoms producing significant contributions into the FTs in Fig. 7.2.3. Calculated XANES spectra were broadened by the Cu K-edge core level width $\Gamma_{core} = 1.55$ eV.

The theoretically calculated Cu K-edge XANES spectra for three non-equivalent copper atoms (Cu1, Cu2, Cu3) in the crystallographic structure known from diffraction [1] at 296 K, are shown in Fig. 7.2.7(a). XANES calculation for the Cu2 atom with removed two axial oxygen atoms (Cu2*), was also performed to test the influence of oxygen vacancies on the XANES spectrum shape.

Next, XANES calculations for the structural models obtained by the RMC/EA-EXAFS simulations, which include temperature-induced disorder effects, were performed. In this case, the Cu K-edge XANES spectra were calculated for 48 copper atoms located in the central $2a \times 2b \times 2c$ part of the supercell. Three or four independent RMC/EA simulations were performed for each temperature point. All calculated XANES spectra for selected temperatures are shown in Fig. 7.2.6. Corresponding averaged XANES spectra are plotted in Fig. 7.2.7(c). Note that some atomic configurations result in the XANES spectra deviating rather strongly from the average one; however, their percentage is small.

For comparison, the Cu K-edge XANES spectra were calculated for three selected temperatures using the experimental values of the temperature-dependent lattice parameters from the diffraction data [1]. They are shown in Fig. 7.2.7(d).

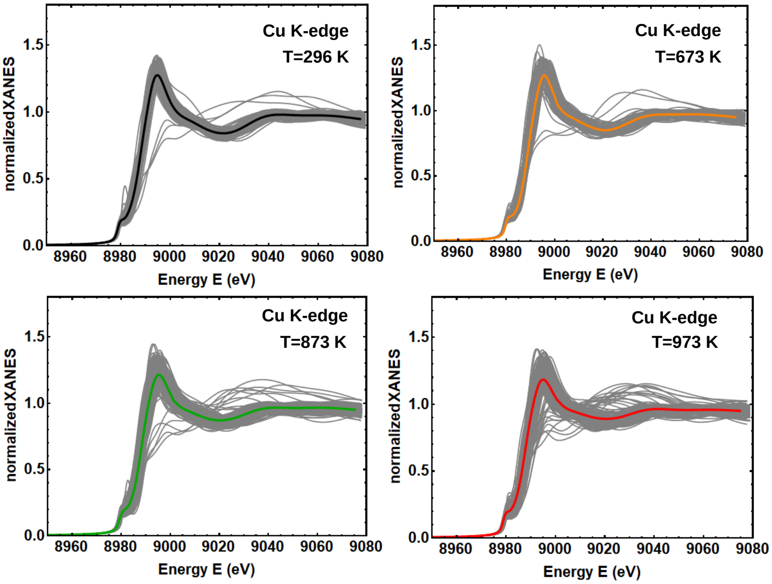

Figure 7.2.6: **The calculated Cu K-edge XANES spectra for structural models obtained in the RMC/EA-EXAFS simulations for selected temperatures:** Gray lines correspond to XANES spectra of individual copper atoms in the supercell, coloured lines show the configuration-averaged XANES spectra.

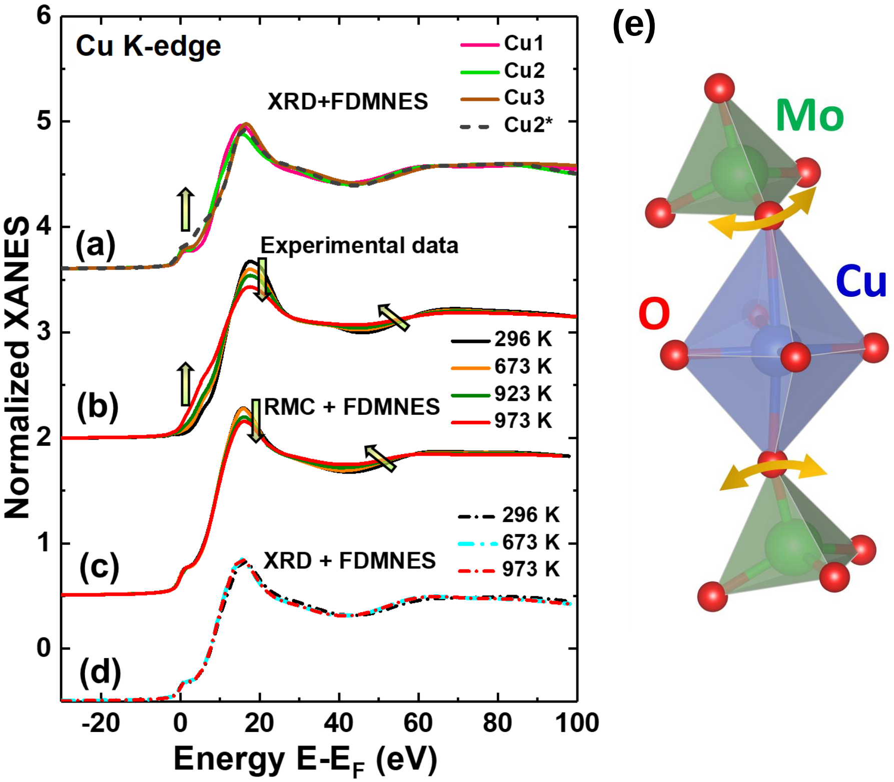

Figure 7.2.7: **The Cu K-edge XANES spectra of α-CuMoO$_4$:** The XANES spectra calculated for non-equivalent Cu1, Cu2 and Cu3 atoms in the average structure at 296 K known from diffraction measurements [1]. The XANES spectrum for Cu2* corresponds to the case of the Cu2 atom without two axial oxygen atoms (a). The experimental XANES at selected temperatures (b). The averaged XANES spectra calculated for the RMC/EA structure models at selected temperatures (c). The averaged XANES spectra calculated for the XRD structure models at selected temperatures taking into account lattice expansion [1] (d). Illustration of correlation reduction in atomic motion between copper and axial oxygen atoms (e).

7.2.4 Results and discussion

EXAFS analysis

The first peak in FT of the Cu K-edge EXAFS spectrum at ~1.5 Å and of the Mo K-edge EXAFS spectrum at ~1.3 Å corresponds to the single-scattering contribution from nearest oxygen atoms forming the first coordination shell around metal ions. Further peaks are due to contributions from more distant atoms and MS effects. The total MS signals were calculated at both edges at $T = 296$ K, and their FTs are shown in Fig. 7.2.4. One can see that MS contributions are important above ~2.2 Å and should be taken into account to reproduce the experimental signals accurately. Note also that the presence of

MS contributions add angular sensitivity into EXAFS and, thus, is important for 3D structure reconstruction in RMC/EA calculations.

The final atomic coordinates obtained in RMC/EA simulations were used to estimate partial RDFs $g_{\mathrm{Cu-O}}(R)$ and $g_{\mathrm{Mo-O}}(R)$ for all non-equivalent metal atoms (Fig. 7.2.8). The first peak in the Cu–O RDFs located at ~1.95 Å corresponds to the nearest 4 oxygen atoms. The second peak at ~2.3–2.7 Å is due to more distant axially placed oxygen atoms of the first coordination shell – two oxygen atoms in Cu1 and Cu2 octahedra or one oxygen in Cu3 square-pyramids (Table 5.2.2). The Cu2 atoms have the most distorted local environment because of the sixth weakly bound oxygen atom located at ~2.63 Å. Cu–O distributions become broader during heating due to an increase in the atomic vibrational amplitudes.

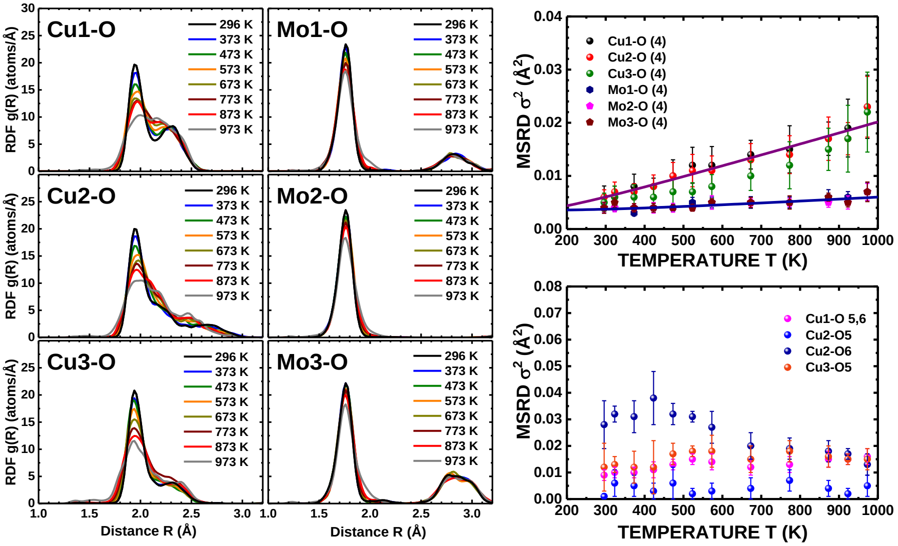

Figure 7.2.8: **Radial distribution functions and MSRD factors for the first coordination shell in α-$CuMoO_4$ reconstructed by the RMC/EA method:** Temperature-dependent RDFs $g(R)$ for three non-equivalent Cu–O and Mo–O atom pairs (left panels). Temperature dependence of the MSRD factors σ^2 for non-equivalent Cu–O and Mo–O atom pairs in α-$CuMoO_4$. Best fitted correlated Einstein models are shown by solid lines (right panels).

The local environment around Mo atoms is less affected by temperature due to relatively strong interatomic bonding within MoO_4 tetrahedra. All three non-equivalent molybdenum atoms have similar distributions of nearest 4 oxygen atoms with the average Mo–O distance ~ 1.78 Å (Fig. 7.2.8). However, some asymmetry of the Mo–O peak shape becomes visible above ~ 800 K due to anharmonic effects. Additionally, there are two groups of one and two oxygen atoms around Mo1 and Mo3 atoms, respectively, located at the distance ~ 2.8 Å. These atoms are not directly bound to the Mo atoms.

The MSRD factors σ^2 for the groups of the four shortest Cu–O and Mo–O bonds as a function of temperature are shown in Fig. 7.2.8. The MSRDs of the Cu–O atom pairs are rather close for all three non-equivalent copper atoms and are larger than those for stronger Mo–O bonds. The Cu–O MSRD factor for the four shortest Cu–O bonds increases from 0.006 ± 0.002 Å^2 to 0.022 ± 0.006 Å^2 when heated from 296 to 973 K. At the same time, the Mo–O MSRD factor increases from 0.004 ± 0.001 Å^2 to only 0.007 ± 0.002 Å^2. The small response to the temperature increase allows one to consider MoO_4 tetrahedra as rigid units. Temperature dependences of MSRD factors were fitted with the correlated Einstein models and obtained parameters (Einstein frequency (ω_E), Einstein temperature (Θ_E) and effective force constant (κ)) are summarized in Table 7.2.1. One can see that all Einstein model parameters for the Cu–O bonds are significantly smaller than those for the Mo–O bonds.

Temperature dependence of the MSRD factors for longer Cu–O bonds, linking copper atoms with axially located oxygen atoms, is also shown in Fig. 7.2.8. These MSRD values are generally larger than those for the short Cu–O bonds, especially at low temperatures. Larger error bars indicate on the limited sensitivity of EXAFS to more distant oxygen atoms, whose contribution to the total EXAFS spectrum is weak.

Table 7.2.1: **Average values of the Einstein frequency ω_E, the Einstein temperature Θ_E and the effective force constant κ calculated from the temperature dependences of the MSRD factors $\sigma^2(T)$ shown in Fig. 7.2.8 for the four nearest Cu–O and Mo–O atom pairs in α-$CuMoO_4$.**

Atom pair	Einstein frequency ω_E [THz]	Einstein temperature Θ_E [K]	Effective force constant κ [N/m]
Cu1–O	54 ± 5	411 ± 38	62 ± 12
Cu2–O	56 ± 6	428 ± 46	67 ± 14
Cu3–O	58 ± 6	447 ± 46	73 ± 15
Mo–O	122 ± 20	932 ± 153	341 ± 112

XANES analysis

The experimental Cu and Mo K-edge XANES spectra of α-$CuMoO_4$ are shown in Fig. 7.2.2. As it was demonstrated before, the pre-edge peak intensity at the Mo K-edge strongly correlates with molybdenum-oxygen coordination polyhedra type in $CuMoO_4$. Weak temperature dependence of the experimental Mo K-edge XANES indicates that molybdenum atoms remain in the tetrahedral coordination at all studied temperatures, in agreement with the diffraction data [1]. The decrease of the XANES oscillation frequency observable above the edge is related to the thermal expansion of the lattice.

The pre-edge peak at the Cu K-edge located at $\sim$ 8978 eV is very weak. Its origin is due to the 1s(Cu)$\rightarrow$3d(Cu)+2p(O) transition [164, 165], which is weaker in six-fold or five-fold coordination than in the tetrahedral one. Note that the small intensity of the pre-edge peak is mainly due to the limited number of unoccupied ($Cu^{2+}(3d^9)$) states. Note that the Cu K-edge pre-edge peak becomes even less pronounced at higher temperatures (see the inset in Fig. 7.2.2). Upon the temperature increase from 296 K to 973 K, the Cu K-edge XANES spectra show a rather strong response (Fig. 7.2.2). In particular, the shoulder appears at $\sim$ 8985 eV, the main peak at $\sim$ 8997 eV becomes smaller, and some increase of the absorption occurs at $\sim$ 9025 eV. Such strong changes in the Cu K-edge XANES cannot be related simply to the lattice expansion.

Theoretical XANES calculations performed for the equilibrium static structures at different temperatures [1] taking into account the thermal expansion of the lattice give close XANES spectra (Fig. 7.2.7(d)). The only difference is in the oscillation frequency above the absorption edge due to the expected increase of interatomic distances. Thus, equilibrium static structure models are not able to reproduce temperature induced variation in the XANES data observed in the experiment and thermal disorder should be explicitly included in the structural model.

Atoms in the structural models obtained from EXAFS spectra using the RMC/EA calculations are displaced from their equilibrium positions to reproduce thermal disorder and include correlation effects in atomic motion. Therefore, these atomic coordinates were used to interpret XANES temperature dependence.

The simulated Cu K-edge XANES spectra corresponding to RMC/EA structural models are shown in Fig. 7.2.6. One can see that some configurations produce quite different XANES spectra, but the configuration-averaged XANES are close to the experimental data (Fig. 7.2.7(b)). With these structure models it is possible to reproduce the experimentally observed temperature dependence, including the behaviour of the main peak at $\sim$ 8997 eV and the fine structure at $\sim$ 9025 eV. However, the origin of the shoulder increase at $\sim$ 8985 eV still remains puzzling.

Additional structural models with copper atoms in a square-like coordination were constructed imitating the loss of two axial oxygen (O5, O6) atoms. Theoretical calculations show that when the copper coordination changes from octahedral to square-like the intensity of the shoulder increases (see Cu2* spectrum in Fig. 7.2.7(a)) similar to the experimental data (Fig. 7.2.7(b)). Taking into account the fact, that these oxygen atoms (O5, O6) are always present in the structure, this effect should be of dynamic origin.

The two axial oxygen atoms have weak bonds with copper atoms. Simultaneously, they are strongly bound to molybdenum atoms forming rigid

MoO_4 tetrahedra (Fig. 7.2.7(e)). At high temperatures, the increase in the librational motion of MoO_4 tetrahedra might weaken the interaction between copper and axial oxygen atoms. As a result of uncorrelated relative vibrational motion the contribution from distant oxygens to the Cu K-edge XANES of $CuMoO_4$ reduces.

Since the contribution of axial oxygen atoms to the total Cu K-edge XAS spectra is weak, also our RMC/EA simulations are not able to provide a structural model that reproduces accurately the temperature dependence of the Cu K-edge shoulder at $\sim$ 8985 eV.

Thermochromic properties at high temperatures

As it is reported in the literature (see Section 5.1), the thermochromic behaviour of α-$CuMoO_4$ above room temperature is governed by an interplay between two optical absorption bands, located in the red and blue spectral ranges [13]. The change in colour from green to brown upon heating is caused by the red shift of the band gap, being responsible for the absorption in the blue spectral range. While the red band below $\sim$1.9 eV is related to the copper $3d^9 \rightarrow 4p$ or d-d transitions [10, 13, 120, 130]. The origin of the band gap ($\sim$2.5 eV) is still not fully understood and was attributed to $O^{2-} \rightarrow Mo^{6+}$ [10], $O^{2-} \rightarrow Cu^{2+}$ [120, 130] or $Cu^{2+} \rightarrow Mo^{6+}$ charge transfer processes [131].

For comparison, the optical bad gaps of other molybdates where molybdenum atoms are with tetrahedral coordination are equal to 4.3 eV for α-$ZnMoO_4$ [166], 5.1 eV for $CaMoO_4$ and 5.3 eV for $SrMoO_4$ [167]. They are related to the electronic transitions in MoO_4^{2-} groups from the top of the valence band (O 2p states) to the conduction band in which Mo 4d states dominate [168]. Note that the band gap of 3.17 eV was determined for β-$ZnMoO_4$ phase where molybdenum atoms are in octahedral coordination [169]. Thus, the blue band in α-$CuMoO_4$ located at even lower energy (about 2.5 eV) most probably is not related to $O^{2-} \rightarrow Mo^{6+}$ charge transfer transition.

Results of RMC/EA simulations (Fig. 7.2.8) show that MoO_4 tetrahedra in α-$CuMoO_4$ are present as rigid units with strong Mo–O bonds and weak temperature dependence. In contrast, there is a strong variation in RDFs around Cu atoms. Since axial oxygen atoms around Cu simultaneously belong to Mo, at high temperatures the librational movement of rigid MoO_4 tetrahedra weakens the interaction between copper and axial oxygen atoms, which results in an increase of the shoulder at $\sim$8985 eV at the Cu K-edge XANES (Fig. 7.2.2). Therefore, one can propose that this dynamic effect, complemented by the lattice expansion, is responsible for the blue band shift and the band gap narrowing of α-$CuMoO_4$ and as a result the colour change from green to brown upon temperature increase.

7.2.5 Conclusions

The local structure and dynamics were studied in thermochromic α-$CuMoO_4$ using XAS in the temperature range from 296 K to 973 K. It was found that the local environment of copper atoms is more affected during heating than that of molybdenum atoms. It was shown that thermal disorder affects strongly not only the Cu K-edge EXAFS, but also XANES region.

The RMC/EA simulations allowed us to perform accurate and simultaneous analysis of the Cu and Mo K-edge EXAFS spectra of polycrystalline α-$CuMoO_4$. The obtained 3D structure models include thermal disorder effect. At the same time, they are able to reproduce the Wyckoff positions of atoms in agreement with known diffraction data [1]. The partial RDFs $g_{\mathrm{Cu-O}}(R)$ and $g_{\mathrm{Mo-O}}(R)$ were obtained for all non-equivalent atoms in the unit cell and showed the temperature-dependent distortions of metal-oxygen coordination polyhedra.

The temperature dependences of the MSRD factors σ^2 for Cu–O and Mo–O atom pairs within the first coordination shell and calculated values of the Einstein frequency ω_E, the Einstein temperature Θ_E and the effective force constant κ support the rigidity of the MoO_4 tetrahedra.

The structural models obtained by RMC/EA simulations were used to calculate the configuration-averaged Cu K-edge XANES using the *ab initio* full-multiple-scattering theory. The calculated XANES spectra are in agreement with the experimental data and qualitatively reproduce the temperature-dependent behaviour. More detailed analysis allowed us also to interpret the variation in the Cu K-edge shoulder at $\sim$ 8985 eV which is related to the axial oxygen atoms. Namely, while the MoO_4 tetrahedra behave mostly as the rigid units, a reduction of correlation in atomic motion between copper and the axial oxygen atoms occurs upon temperature increase. This dynamic effect is the main cause for the temperature-induced changes in the $O^{2-} \rightarrow Cu^{2+}$ charge transfer processes and, thus, is the origin of the thermochromic properties of α-$CuMoO_4$ upon heating.

Chapter 8

XAS study of $\mathrm{CuMo}_{1-x}\mathrm{W}_x\mathrm{O}_4$

8.1 Introduction[1]

Several studies have revealed that the functional properties of CuMoO_4 are strongly affected by doping with tungsten ions when forming $\mathrm{CuMo}_{1-x}\mathrm{W}_x\mathrm{O}_4$ solid solutions [2, 3, 10, 11, 15]. It is believed that tungsten atoms substitute molybdenum; however, it is not known exactly how this affects the local structure of the material. The important question is whether tungsten creates its own local environment or it adapts to that of molybdenum atoms.

As it was shown in Chapter 6, all samples within $\mathrm{CuMo}_{1-x}\mathrm{W}_x\mathrm{O}_4$ series can be classified into two sets: greenish (0≤x≤0.15) and brownish (0.20≤x≤1.0) samples. At ambient conditions, $\mathrm{CuMo}_{1-x}\mathrm{W}_x\mathrm{O}_4$ solid solutions exist in one of the three crystal structures with triclinic $P\bar{1}$ symmetry, which is isostructural to the high-pressure phases of CuMoO_4 (α, γ, III) [1]. Samples with 0.075<x<0.1 can exist in both α and γ allotropic forms at room temperature [147]. The transition to the wolframite-type phase (CuMoO_4-III) occurs above x$\sim$0.15 together with a colour change from greenish to brownish.

This chapter discusses the effect of tungsten concentration on the structure and properties of $\mathrm{CuMo}_{1-x}\mathrm{W}_x\mathrm{O}_4$. Special attention is paid to the $\mathrm{CuMo}_{0.90}\mathrm{W}_{0.10}\mathrm{O}_4$ compound, since it seems to be the most attractive solid solution among the series for potential practical applications due to the γ-to-α phase transition in the temperature range between 0 and 100°C [4, 10]. The local structure relaxation in the wolframite-type phase of $\mathrm{CuMo}_{1-x}\mathrm{W}_x\mathrm{O}_4$ (x>0.15) with the octahedral coordination of metal ions is also discussed in details. Although this phase do not exhibit pronounced thermochromic behaviour, it has properties that are promising for possible use as photoanodes in water-splitting photoelectrochemical cells [1, 6, 8, 10].

The chromic properties of $\mathrm{CuMo}_{1-x}\mathrm{W}_x\mathrm{O}_4$ solid solutions are determined by the interband transitions due to the oxygen-to-metal charge transfer across the band gap and the intraband d-d transitions of Cu^{2+} ions [10, 11, 13, 120]. The intraband transitions contribute to the absorption in the red spectral range

---

[1] The results related to $\mathrm{CuMo}_{0.90}\mathrm{W}_{0.10}\mathrm{O}_4$, presented in this chapter, have been published as I. Jonane, A. Cintins, A. Kalinko, R. Chernikov, A. Kuzmin, **Low temperature X-ray absorption spectroscopy study of CuMoO_4 and $\mathrm{CuMo}_{0.90}\mathrm{W}_{0.10}\mathrm{O}_4$ using reverse Monte-Carlo method**, Rad. Phys. Chem. 175 (**2020**) 108411.

below 1.8 eV [10, 120, 130], whereas the interband one depends on the composition. The band gap is ~2.3 eV in pure $CuWO_4$ with distorted octahedral coordination of tungsten atoms [149, 150] but decreases to ~2.0 eV in $CuMo_{0.65}W_{0.35}O_4$ [6, 8]. The band gap reaches its minimum before the phase transition to the α-phase. When the transition occurs, the band gap starts to increase from ~2.2 eV in $CuMo_{0.88}W_{0.12}O_4$ [11] to above ~2.5 eV in α-$CuMoO_4$ with tetrahedral coordination of molybdenum atoms [10, 13, 120, 130]. Thus, the electronic structure and related properties of $CuMo_{1-x}W_xO_4$ solid solutions depend on the local environment of metal atoms, which can be successfully probed by XAS. However, the EXAFS data analysis is challenging due to a low symmetry of the compound structure and large number of scattering paths [23]. To address this issue, the RMC/EA method at several metal absorption edges simultaneously is employed to reconstruct a structure model consistent with the experimental data of a particular $CuMo_{1-x}W_xO_4$ solid solution and to evaluate the role of tungsten.

8.2 XAS experimental data

Multi-edge XAS experiments for $CuMo_{1-x}W_xO_4$ ($0 \leq x \leq 1.0$) samples were performed at room temperature at the XAFS bending-magnet beamline at the ELETTRA synchrotron as described in Section 6.4. The X-ray absorption spectra were collected at the Cu and Mo K-edges and W L_3-edge. Normalized XANES spectra together with the EXAFS and their FTs calculated in the k-space range of 2.5-14.5 Å^{-1} by employing Athena program [29] are shown in Fig. 8.2.1. First, compositional dependences of the experimental XANES and EXAFS spectra, as well as their FTs are described, while the structural changes obtained by the RMC/EA simulations will be discussed next.

All experimental EXAFS spectra can be classified into four series: (i) the spectra for x=0.04 and 0.06 are very close to pure α-$CuMoO_4$ phase, (ii) the samples with $0.10 \leq x \leq 0.15$ slightly differ from the first group suggesting the presence of an additional contribution from γ-$CuMoO_4$ phase [147], (iii) the brownish samples with $0.20 \leq x \leq 0.50$ show gradual change towards the spectra characteristic of the $CuWO_4$ phase, and (iv) the spectra for x=0.75 are very close to that of pure $CuWO_4$ phase.

The Cu K-edge XANES spectra of $CuMo_{1-x}W_xO_4$ solid solutions demonstrate relatively weak sensitivity to tungsten content (Fig. 8.2.1(a)). At the same time, the Cu K-edge EXAFS spectra (Fig. 8.2.1(d)) are more informative and reflect the gradual change in the copper local environment. In particular, there are pronounced changes in R-space above ~2 Å (Fig. 8.2.1(g)). The FT peak at ~2.6 Å for pure $CuMoO_4$ sample has larger amplitude with an increase in x and shifts to longer distances above x = 0.50.

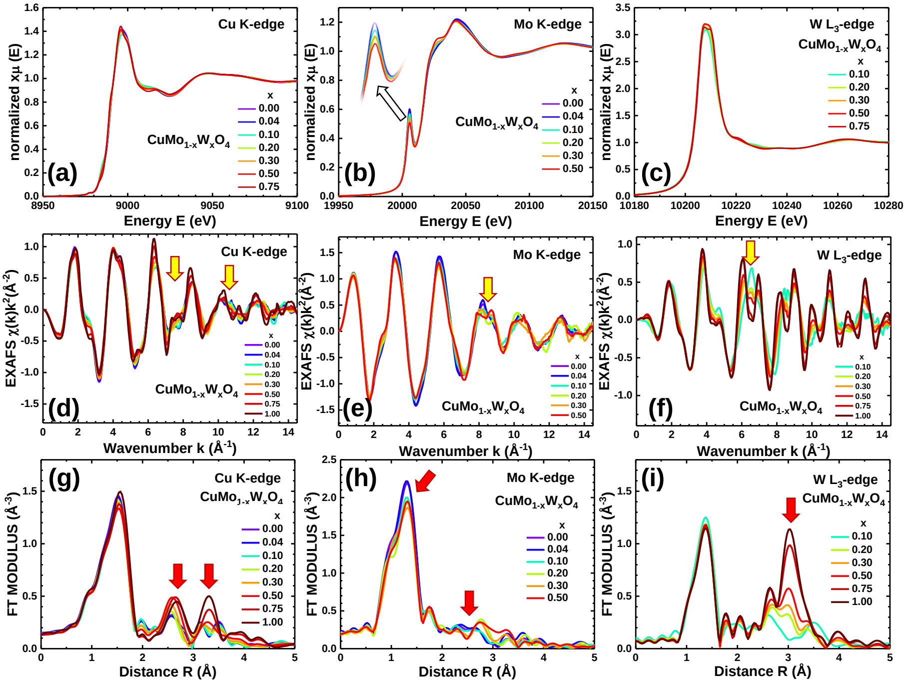

Figure 8.2.1: **The experimental Cu, Mo K-edge and W L_3-edge normalized XANES (a-c) and EXAFS $\chi(k)k^2$ (d-f) spectra and their Fourier transforms (g-i) for $CuMo_{1-x}W_xO_4$ solid solutions.** Arrows highlight the regions with the most pronounced changes in the spectra. FTs are calculated in the k-space range of 2.5-14.5 Å^{-1} with Athena program.

There is also a clear difference between the samples in FTs at ~3.3 Å: a single peak is observed for samples with x≥0.50, while a double peak is visible for the rest samples.

Molybdenum ions in α-$CuMoO_4$ have tetrahedral coordination [1] which is responsible for the high intensity of the pre-edge peak at the Mo K-edge originating from the 1s(Mo)→4d(Mo)+2p(O) transition (Fig. 8.2.1(b)) [163]. As it was demonstrated for temperature-dependent data of $CuMoO_4$, the Mo K-edge pre-peak amplitude changes depending on the local structure distortions. Upon increasing tungsten content in $CuMo_{1-x}W_xO_4$ solid solutions, the pre-peak amplitude decreases indicating a change of the local environment of molybdenum from tetrahedral to a more distorted one, which affects also the Mo K-edge EXAFS spectra as is highlighted by arrows in Fig. 8.2.1(e,h). The experimental Mo K-edge EXAFS spectra indicate a change to the octahedral environment above x=0.20. The sample with x=0.10 has a smaller amplitude of the main FT peak at ~1.3 Å compared to pure $CuMoO_4$ but close behaviour at larger R values. A deeper analysis of data for $CuMo_{0.90}W_{0.10}O_4$ solid solution will follow in the next section.

The W L_3-edge XANES spectra are dominated by a strong white line peak at 10207 eV due to the dipole allowed transition $2p_{3/2}(W)\rightarrow5d(W)+2p(O)$. The shape of the white line contains information on the crystal field splitting of the W 5d-states [170, 171], which is masked due to the large value of the natural broadening (~4.5 eV [172]) of the $2p_{3/2}(W)$ core level. As a result of limited resolution, the experimental XANES spectra do not show significant changes upon increase in tungsten content. However, one can overcome this problem by performing resonant X-ray emission spectroscopy (RXES) experiments and obtaining high-energy resolution fluorescence detected (HERFD) XANES as presented in Chapter 4.2.

The W L_3-edge EXAFS spectra were measured in transmission mode for samples with $x\geq0.10$ (sample with x=0.04 was also measured, however, the noise limited possibility to make further accurate analysis). The sample with x=0.10 differs significantly from other samples with x≥0.20 as is highlighted by the arrow in Fig. 8.2.1(f). The difference is well visible in k-space at ~6.5 Å^{-1} and in R-space at ~3 Å. Indeed, the continuous reduction of the amplitude of the FT peak at ~3 Å with an increase of the Mo-to-W ratio is remarkable. It is observed in k-space as visible damping of the EXAFS oscillations at higher k-values (Fig. 8.2.1(f)). The spectra of brownish samples with $0.20\leq x\leq0.50$ show gradual change towards the spectra characteristic of the $CuWO_4$ phase where tungsten ions are octahedrally coordinated. At even larger tungsten content x = 0.75, the W L_3-edge EXAFS spectrum becomes close to that of pure $CuWO_4$. The transition to $CuWO_4$ phase is accompanied by a significant increase of the second coordination shell peak at about 3 Å in the FT (Fig. 10.2.1(i)): its amplitude continuously increases with an exchange of Mo atoms with W ones.

Temperature-dependent measurements upon cooling and heating (10–300 K) were performed for $CuMo_{0.90}W_{0.10}O_4$ sample at the HASYLAB/DESY PETRA-III P65 undulator beamline. Normalized Cu and Mo K-edge XANES of $CuMo_{0.90}W_{0.10}O_4$ are compared with the spectra corresponding to pure $CuMoO_4$ in Fig. 8.2.2. For both samples, the response to temperature variation reflected as changes in XANES spectra is similar.

Experimental EXAFS spectra are shown in Fig. 8.2.3. The behaviour of the Cu K-edge EXAFS spectra is similar to that of pure $CuMoO_4$. The Mo K-edge shows clear structural changes during cooling, while during heating, the sample does not transform back to the α-phase with tetrahedral Mo environment in agreement with XANES data. The W L_3-edge XAS experiment was performed starting at 300 K, next cooling down to 10 K, following by heating up to 300 K, again cooling down to 50 K and finally heating back to 300 K (see the inset in Fig. 8.2.3(d)). While there are big changes at the Mo K-edge EXAFS spectra, only minor changes are observed in the W L_3-edge EXAFS in the sampled k-space range of 2.5–12.5 Å during the cooling-heating cycles.

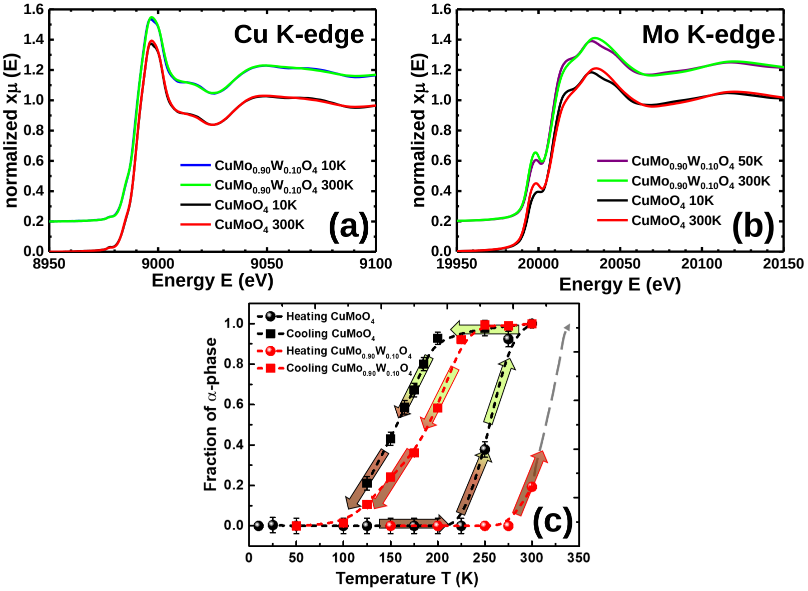

Figure 8.2.2: **The experimental Cu and Mo K-edge XANES of pure $CuMoO_4$ and $CuMo_{0.90}W_{0.10}O_4$ at 300 K (α-phase) and 10 K/50 K (γ-phase)** (a,b). Temperature dependence of the fraction of α-phase in $CuMoO_4$ and $CuMo_{0.90}W_{0.10}O_4$ samples upon heating and cooling obtained from the LCA of the Mo K-edge XANES spectra (c). The gray dashed arrow is an extrapolation above the room temperature for $CuMo_{0.90}W_{0.10}O_4$.

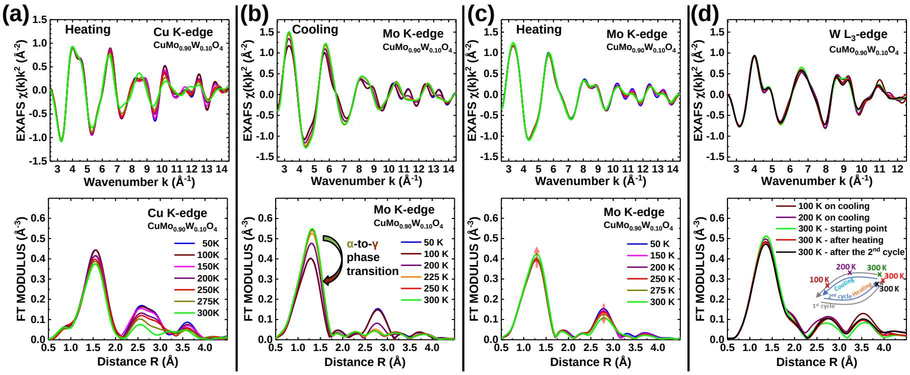

Figure 8.2.3: **Temperature-dependent Cu K-edge (a), Mo K-edge (b,c) and W L_3-edge (d) EXAFS spectra and their Fourier transforms for crystalline $CuMo_{0.90}W_{0.10}O_4$.** The inset in (d) illustrates the W L_3-edge data points selected for the plot from the cooling-heating cycles.

8.3 Temperature-dependent $CuMo_{0.90}W_{0.10}O_4$ study

8.3.1 XANES analysis

Temperature-dependent Mo K-edge XANES spectra for $CuMo_{0.90}W_{0.10}O_4$ sample were analysed similarly to that of pure $CuMoO_4$. The LCA of the Mo K-edge XANES in the temperature range from 10 K to 300 K indicates that the phase transition hysteresis in $CuMo_{0.90}W_{0.10}O_4$ is shifted to higher temperatures (Fig. 8.2.2) in agreement with the previous studies [2, 10, 15].

The transition from α to γ phase occurred between $\sim$250 and 100 K upon cooling. At the same time, the transition from γ to α phase started at $\sim$280 K upon heating and was still not finished at room temperature even after several hours. Thus, the addition of 10mol% of tungsten increases the phase transition temperature by $\sim$50–100 K. Note that optical, calorimetry and magnetic susceptibility measurements reported in [10] showed that the γ-to-α phase transition in $CuMo_{0.90}W_{0.10}O_4$ occurs during heating in the temperature range between 340 and 380 K.

8.3.2 EXAFS analysis

Temperature-dependent $CuMo_{0.90}W_{0.10}O_4$ EXAFS spectra were analysed based on RMC/EA calculations as described in Section 7.1.4. The initial structural model for $CuMo_{0.90}W_{0.10}O_4$ was created by randomly substituting Mo atoms by W atoms in $2a_0 \times 2b_0 \times 2c_0$ large supercells of α-$CuMoO_4$ and γ-$CuMoO_4$ structures, keeping the stoichiometric ratio of the elements. Each supercell was additionally enlarged $2 \times 2 \times 2$ times to get a final simulation box containing 2304 atoms. Several random substitutions were used.

The obtained RMC/EA fits for $CuMo_{0.90}W_{0.10}O_4$ at two selected temperatures (T=50 K and 300 K) are shown in Fig. 8.3.1. Since XAS spectra for $CuMo_{0.90}W_{0.10}O_4$ sample slightly deviate from pure $CuMoO_4$, both α- and γ-phase structure models were examined. Note that good agreement for all metal absorption edges is required for accurate reconstruction of crystal structure for multi-atom compounds [173].

One can see that at T=50 K, the EXAFS spectra at the Cu, Mo and W absorption edges are well reproduced using the γ-phase structure model. In the meantime, at T=300 K (before cooling), the α-phase structural model gives good agreement at the Cu and Mo K-edges, but slightly worse agreement at the W L_3-edge, indicating on some local environment relaxation around tungsten ions. It turns out that the W L_3-edge EXAFS can be slightly better described by the γ-phase structure (the residual ξ is smaller), which does not apply to the other two edges. This finding suggests that, despite the crystal lattice of $CuMo_{0.90}W_{0.10}O_4$ at T=300 K (before cooling) corresponds to the α-phase,

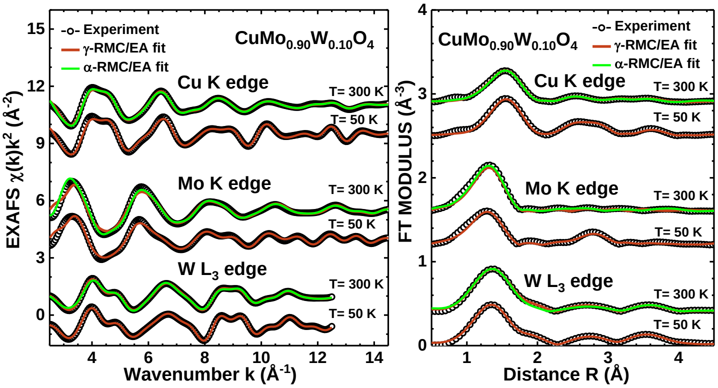

Figure 8.3.1: **Results of RMC/EA calculations for the Cu K-edge, Mo K-edge and W L_3-edge in $CuMo_{0.90}W_{0.10}O_4$ at T=50 K (γ-phase) and T=300 K (α-phase)**: The experimental and calculated EXAFS spectra $\chi(k)k^2$ and corresponding Fourier transforms.

the local structure around W atoms relaxes in an attempt to reconstruct distorted octahedral coordination which is characteristic of the γ-phase.

The partial RDFs for Cu–O, Mo–O and W–O atom pairs, calculated from the atom coordinates of the RMC/EA models of $CuMo_{0.90}W_{0.10}O_4$, are shown in Fig. 8.3.2. Note that the reported RDFs $g(R)$ are averaged over all non-equivalent atoms of the same type within the supercell.

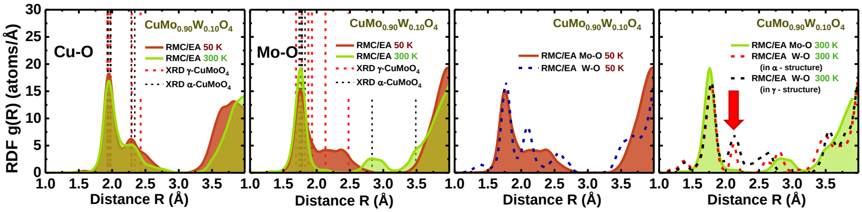

Figure 8.3.2: **Radial distribution functions for Cu–O, Mo–O, W–O atom pairs in $CuMo_{0.90}W_{0.10}O_4$**, calculated from the atom coordinates of the RMC models. Dashed vertical lines show interatomic distances according to diffraction data [1]. Vertical red arrow indicates a group of oxygen atoms which does not exist in the tetrahedral coordination.

The obtained RDFs $g(R)$ around Cu and Mo atoms are similar to that for pure $CuMoO_4$ (see Fig. 7.1.7). The Cu environment in the first coordination shell is quite close at low (50 K) and high (300 K) temperatures. Temperature induced changes in the Mo local environment are well absorbed already for the closest 4 oxygen atoms. Next, to evaluate how significant is the local structure relaxation around tungsten atoms, we compare the $g_{\mathrm{W-O}}(R)$ and $g_{\mathrm{Mo-O}}(R)$ distributions in $CuMo_{0.90}W_{0.10}O_4$ in Fig. 8.3.2.

At low temperature (50 K) in γ-phase, tungsten atoms have distorted octahedral coordination close to that of molybdenum. The distortion of WO_6

and MoO_6 octahedra originates from the second-order Jahn–Teller effect [174] caused by the charge transfer from oxygen atoms surrounding metal ion with the formal oxidation state 6+ (d^0 electronic configuration).

At 300 K (in α-phase), when the coordination of Mo atoms becomes tetrahedral, W atoms tend to have a more distorted environment. By comparing Mo–O and W–O RDFs $g(R)$ (Fig. 8.3.2), one can see that in the $g_{\mathrm{W-O}}(R)$ distribution, there is an additional group of oxygen atoms at about 2.1 Å, and the next group of oxygen atoms at 2.8 Å is slightly displaced and split. Furthermore, the RMC/EA calculations at the W L_3-edge for α-$CuMo_{0.90}W_{0.10}O_4$ using the structure model corresponding to γ-phase (tungsten in the distorted octahedral environment) give slightly better agreement with the experimental data, however, the shape of the $g_{W-O}(R)$ distribution is quite close to that in the α-phase.

These results confirm the tendency of tungsten atoms in $CuMo_{0.90}W_{0.10}O_4$ solid solutions to adapt more distorted environment that is closer to the octahedral than tetrahedral in α-phase, thus affecting the temperature/pressure of α-to-γ phase transition and helping to stabilize γ-phase at room temperature.

8.4 Composition-dependent $CuMo_{1-x}W_xO_4$ study

Composition-dependent $CuMo_{1-x}W_xO_4$ (x=0.20, 0.30, 0.50, 0.75) EXAFS spectra were analysed based on RMC/EA calculations as described in Section 7.1.4. The RMC/EA method provided an unique opportunity to simultaneously refine a structural model to a set of EXAFS spectra measured at three (for x = 0.20, 0.30, 0.50) or two (for x = 0.75) absorption edges. The structure of $CuMo_{0.25}W_{0.75}O_4$ was constructed based on XRD data reported in [1, 175]. For other solid solutions (x=0.20, 0.30, 0.50), the lattice parameters corresponding to the $CuMoO_4$-III phase [1] and Wyckoff positions of atoms taken from $CuWO_4$ structure [129] were combined to build an initial unit cell. Next, the unit cell was enlarged $3a\times3b\times3c$ times, and W atoms were randomly substituted with Mo atoms while maintaining the stoichiometric ratio of elements. The enlarged cell was additionally increased $2\times2\times2$ times. As a result, there were 2592 atoms in total in the RMC/EA simulation box. Such a large box was used to collect reasonable statistics for atoms that are the minority in the solid solution. Several RMC calculations with different random substitutions and pseudo-random number sequences were performed to obtain better statistics. Both SS and MS contributions were taken into account. MS contributions included scatterings up to the 5th order, as higher-order scatterings contribute at large distances outside of the analysis range. A large number of scattering paths was reduced by grouping similar ones and including into the analysis only important paths with the relative amplitude of corresponding partial contribution to the total EXAFS greater than 0.1-1% [17]. At each iteration of the RMC/EA simulation, all atoms in the supercell were randomly displaced with the maximum allowed displacement of 0.4 Å with the goal to minimize the difference between the Morlet WTs of the experimental and configuration-averaged EXAFS spectra [91].

Examples of the obtained RMC/EA fits for four solid solutions are shown in Fig. 8.4.1. As one can see, the calculated Cu and Mo K-edge and W L_3-edge EXAFS spectra, obtained from the multi-edge RMC/EA simulations, agree reasonably well with the corresponding experimental spectra. In all simulations, 6000 iterations were made to ensure the convergence of each calculation.

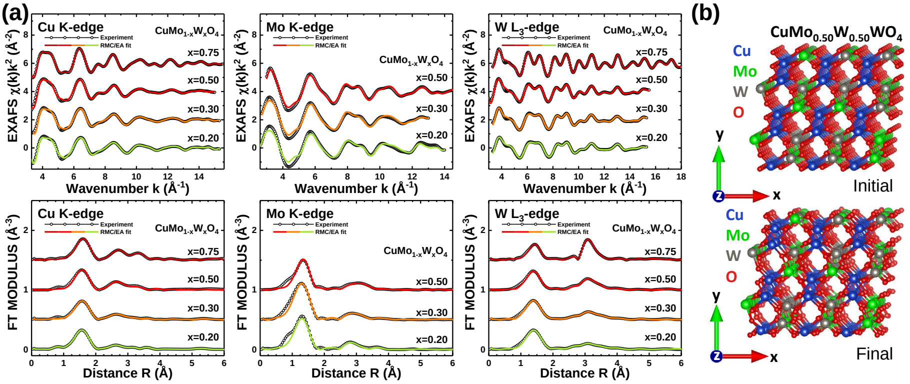

Figure 8.4.1: **Results of RMC/EA calculations for the Cu K-edge, Mo K-edge and W L_3-edge in $CuMo_{1-x}W_xO_4$ (x=0.20, 0.30, 0.50 and 0.75) at room temperature**: The experimental and calculated EXAFS spectra $\chi(k)k^2$ and corresponding Fourier transforms (only modulus is shown) (a). An initial and final structural models in RMC/EA calculation for $CuMo_{0.50}W_{0.50}O_4$ (only fragments are shown) (b).

An example of an initial and final structural models in RMC/EA calculation for $CuMo_{0.50}W_{0.50}O_4$ (only fragments) are illustrated in Fig. 8.4.1(b). An increase in the disorder after the RMC/EA simulation is well evident. The averaged partial RDFs $g(R)$ and BADFs $f(\varphi)$, calculated from the atomic coordinates of several RMC/EA models, are shown in Fig. 8.4.2. Data are compared with the results of RMC/EA calculations for pure $CuWO_4$ (the RMC/EA calculations for pure $CuWO_4$ were performed based on a structural model from [129] employing a 5×5×5 large supercell with 1500 atoms).

In the $CuMoO_4$-III phase, which was used as an initial model to simulate the structure of the solid solutions (x=0.20, 0.30, 0.50), all metal atoms are octahedrally coordinated by oxygen atoms. Due to the Jahn-Teller distortion,

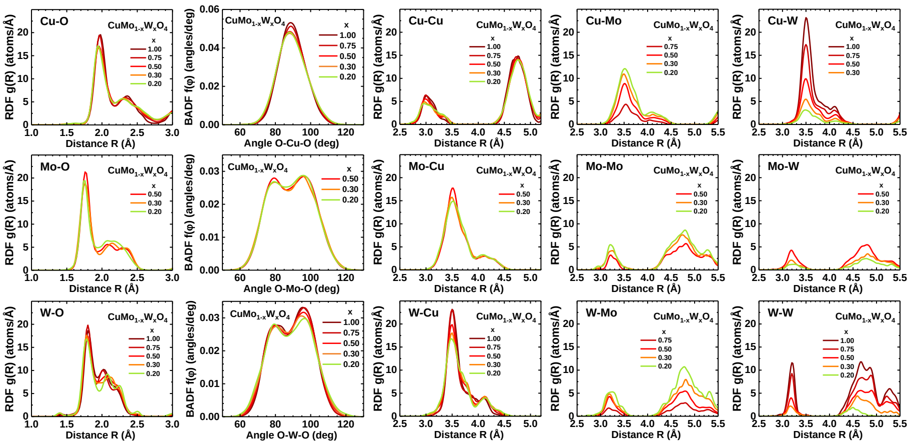

Figure 8.4.2: **Partial radial distribution functions (RDFs) and bond angle distribution functions (BADFs) in $CuMo_{1-x}W_xO_4$ (x=0.20, 0.30, 0.50, 0.75, 1.00) obtained from RMC/EA calculations.**

the CuO_6 octahedra are axially distorted with two groups of Cu–O bonds in an equilibrium structure: 4×1.97 Å, and 2×(2.38-2.42) Å [1, 129, 175]. Molybdenum and tungsten ions are present in the 6+ oxidation state, so that their coordination octahedra are subject to the second-order Jahn-Teller distortion with the off-center position of the metal ions [174].

It is visible (Fig. 8.4.2) that the MoO_6 octahedra are slightly stronger distorted than WO_6. For both Mo and W ions, two main groups of metal-oxygen distances can be distinguished in the RDFs $g_{\mathrm{Mo-O}}(R)$ and $g_{\mathrm{W-O}}(R)$. The nearest group of three oxygen atoms is responsible for the first sharp peak in the RDFs and is located at about 1.8 Å for both W and Mo. The second group of three oxygen atoms is quite broad and can be roughly divided into two subgroups with 2 and 1 oxygen atoms. In the case of W, two subgroups of oxygen atoms are located at distances of about 2.0-2.1 Å and 2.15-2.25 Å, while in the case of Mo, both distances are slightly longer and are about 2.05-2.15 Å and 2.20-2.40 Å.

Various types of distortions of metal-oxygen octahedra are well reflected by the BADFs $f(\varphi)$ (Fig. 8.4.2). Axial distortion of CuO_6 octahedra results in a monomodal BADF of ∠O–Cu–O with an average angle value of $\varphi \approx 88°$. At the same time, off-center displacement of Mo or W atoms from the center of the octahedra leads to bimodal BADFs of ∠O–Mo–O and ∠O–W–O with maxima at $\varphi \approx 80°$ and 96°, respectively.

Proper account for the MS and disorder effects in the calculated EXAFS spectra allows a reliable analysis of the contributions from the outer coordination shells. In Fig. 8.4.2, the partial RDFs $g(R)$ for metal–metal atom pairs are shown up to 5.0-5.5 Å. In the structure of $CuMo_{1-x}W_xO_4$

solid solutions with $x \geq 0.20$ (Fig. 8.4.1(b)), the metal–oxygen distorted octahedra of one type share edges and form zigzag chains along the c-axis [175]. The zigzag chains are arranged in alternating layers that are perpendicular to the a-axis direction [175].

The RDFs $g_{\mathrm{Cu-Cu}}(R)$ include contributions from two nearest copper atoms located within the same chain of CuO$_6$ octahedra (the peak at ~3.0 Å distance) and six more distant copper atoms (four in the neighbouring chains and two in the same chain), giving the origin of the peak at distance ~4.7 Å. Eight copper atoms located in the four neighbouring chains of CuO$_6$ octahedra contribute to the RDFs $g_{\mathrm{Mo/W-Cu}}(R)$. The change in the composition of solid solutions leads to some small modifications in the structure resulting in the broadening of the main peak at ~3.5 Å distance for low W content ($x \leq 0.50$).

The RDFs $g_{\mathrm{Cu/Mo/W-Mo/W}}(R)$ show a clear dependence on the number of Mo/W atoms varying with the composition. Upon increasing tungsten ratio, the amplitude of the peaks also increases in the RDFs $g_{\mathrm{Cu/Mo/W-W}}(R)$ but decreases in the RDFs $g_{\mathrm{Cu/Mo/W-Mo}}(R)$. The ability of Mo atoms to be in a locally distorted environment extends to the outer shells so that the RDFs $g_{\mathrm{Mo-Cu/Mo}}(R)$ are stronger broadened than the RDFs $g_{\mathrm{W-Cu/W}}(R)$. Thus, our results show that both Mo and W ions are octahedrally coordinated by oxygen ions in solid solutions with large W content ($x \gtrsim 0.20$). However, previous studies of CuMo$_{1-x}$W$_x$O$_4$ solid solutions revealed that at ambient conditions in samples with $x \leq 0.15$, tungsten ions co-exist in the octahedral and tetrahedral environment [111], while molybdenum ions have dominant tetrahedral coordination [10, 88, 147]. This allows one to conclude that tungsten atoms have a decisive influence on the structure of CuMo$_{1-x}$W$_x$O$_4$ solid solutions.

Finally, we would like to focus on the origin of large variations of some peaks in FTs, well observed in the range of 3-4 Å at the Cu K-edge and W L$_3$-edge in Fig. 8.4.3(a,b). Here the contributions of the SS and MS processes are compared for two samples – CuWO$_4$ and CuMo$_{0.50}$W$_{0.50}$O$_4$. Additionally, a set of the partial W L$_3$-edge EXAFS contributions for selected photoelectron scattering paths is presented for CuMo$_{0.50}$W$_{0.50}$O$_4$ in Fig. 8.4.3(c). Relatively small amplitude of the MS oscillations compared to the SS ones in k-space (Fig. 8.4.3(a,b)) looks deceiving because the SS signal coming from the first coordination shell dominates the total EXAFS spectrum. However, when compared in R-space, the MS contribution reaches from 20-30% (at the W L$_3$-edge) up to 50-60% (at the Cu K-edge) of the SS one in the range of 3-4 Å and even more at larger distances. Therefore, the MS contribution should not be ignored in the RMC/EA simulation to get a reliable structural model.

In CuMo$_{1-x}$W$_x$O$_4$ solid solutions having close crystallographic structures and, thus, close geometry of scattering paths, the changes in the

EXAFS spectra are caused by the different contributions of Mo and W atoms, due to the large difference in their atomic masses and electron configurations. Note that, the atomic mass of W (183.84 amu) is almost twice larger than that of Mo (95.95 amu) and should lead to the significant difference in the amplitude of their thermal vibrations and, thus, in the damping of EXAFS oscillations due to the difference in MSRD factors σ^2. Also, the molybdenum (Z=42) and tungsten (Z=74) atoms are well separated in the Periodic Table, so they will make different contributions to the EXAFS spectra due to the difference in their scattering amplitudes. Note that latter effect will influence only FTs but not RDFs. Both effects are responsible for a strong reduction of the peak at ~3.1-3.2 Å in the Cu K-edge and W L$_3$-edge FTs when a half of W atoms is substituted with Mo ones (Fig. 8.4.3(b)).

It is also interesting that the W L$_3$-edge EXAFS contributions from W–Mo and W–W scattering paths with distance $\sim$ 3.2 Å have nearly opposite phase (Fig. 10.3.2(c)) leading to destructive interference. Also, damping of the EXAFS oscillations is larger for W–Mo scattering path due to the $g_{\mathrm{W-Mo}}(R)$ distribution is broader (MSRD $\sigma^2_{\mathrm{W-Mo}} \approx$ 0.0163 Å^2) than that of $g_{\mathrm{W-W}}(R)$ (MSRD $\sigma^2_{\mathrm{W-W}} \approx$ 0.0049 Å^2), which is due to larger static distortions of the Mo environment (Fig. 8.4.2).

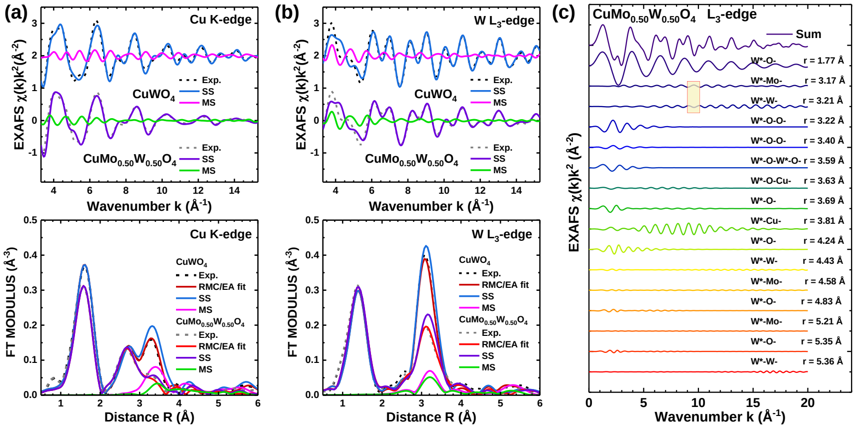

Figure 8.4.3: **Contributions of different scattering paths into the Cu K-edge and W L$_3$-edge EXAFS spectra of CuWO$_4$ and CuMo$_{0.50}$W$_{0.50}$O$_4$:** Cu K-edge (a) and W L$_3$-edge (b) EXAFS spectra and corresponding FTs calculated for the k-space range 3.3-15.3 Å^{-1} with the EvAX code. SS and MS contributions are calculated for a structure configuration obtained in RMC/EA simulation. Contributions of selected scattering paths are shown at the W L$_3$-edge for CuMo$_{0.50}$W$_{0.50}$O$_4$ structure (c). Mismatch of phases in W–Mo and W–W scattering paths is highlighted.

To sum up, the experimental EXAFS spectra show a clear composition dependence for CuMo$_{1-x}$W$_x$O$_4$ solid solutions. The structural models for solid solutions with x = 0.20, 0.30, 0.50, 0.75 were obtained from the simultaneous analysis of EXAFS spectra measured at several absorption edges by the RMC/EA method. It was shown that MS effects play an important role in the analysis of $CuMo_{1-x}W_xO_4$ solid solutions and should be taken into account to describe accurately the contributions from the outer coordination shells. A detailed analysis of the partial RDFs around absorbing metal atoms and BADFs gave information on the degree of distortion of the coordination shells and its dependence on the composition. Mo and W atoms are octahedrally coordinated by oxygen atoms in all studied solid solutions; however, MoO_6 octahedra are somewhat more distorted than WO_6. For both metals, the distorted octahedra consist of three short and three long metal–oxygen bonds, and the group of the nearest three oxygen atoms has narrow distribution. The ability of molybdenum atoms to adopt a locally distorted environment allows them to adjust to the solid solution structure determined by tungsten-related sublattice.

8.5 Conclusions

XAS was used to probe a variation of the local atomic structure in $CuMo_{1-x}W_xO_4$ ($0 \leq x \leq 1$) solid solutions at room temperature and in $CuMo_{0.90}W_{0.10}O_4$ in the temperature range of 10–300 K. Advanced data analysis of EXAFS spectra at several absorption edges simultaneously by the RMC/EA method allowed us to obtain 3D structural models of the solid solutions and analyse them in details.

$CuMo_{0.90}W_{0.10}O_4$ solid solution exhibits thermochromic properties similar to pure $CuMoO_4$. It was possible to monitor the α-to-γ thermochromic phase transition in $CuMo_{0.90}W_{0.10}O_4$. We observed that the addition of 10 mol% of tungsten to $CuMoO_4$ induces local distortions and stabilizes the γ-phase, leading to an increase of the phase transition temperature by $\sim$50–100 K.

Variation of the experimental EXAFS spectra at the metal absorption edges for $CuMo_{1-x}W_xO_4$ strongly correlates with Mo:W ratio. It was shown that multiple-scattering effects play an important role in the analysis of $CuMo_{1-x}W_xO_4$ solid solutions and should be taken into account to describe the contributions from the outer coordination shells accurately.

At room temperature, $CuMo_{1-x}W_xO_4$ solid solutions with tungsten content above $x \sim 0.15$ have the wolframite-type $CuMoO_4$-III phase isostructural to $CuWO_4$. The formation of solid solutions is accompanied by strong structural relaxations and both W and Mo atoms adopt to the octahedral environment. The ability of Mo atoms to adopt a locally distorted environment allows them to adjust to the solid solution structure determined by tungsten-related sublattice.

Chapter 9

RXES study at the W L_3-edge of $CuMo_{1-x}W_xO_4$

9.1 Introduction[1]

In the case of molybdates and tungstates, often composed from strongly distorted polyhedra, the extraction of structural information from XAS is not an easy task. The RMC/EA method presented in the previous chapters is advantageous in such cases, although it is computationally heavy and time-consuming approach [23, 78, 80, 81]. However, we have shown that a reliable structural analysis requires the knowledge of XAS spectra at least for all metal absorption edges [78, 88]. In the case of series of solid solutions, the low content of one of the components limits the quality of the experimental data, which also complicates the analysis. Furthermore, the close values of the metal–oxygen interatomic distances in the RDFs obtained using the RMC simulations make it sometimes difficult to unambiguously identify the atoms belonging to the first coordination shell of absorbing metal [88]. Thus, it is hard to distinguish different types of coordination polyhedrons.

In tungsten oxides and related materials, the tungsten 5d band is split due to the crystal field of ligands. This splitting can be experimentally probed by the W L_3-edge XAS [170, 171] and can be used to distinguish between different local symmetries of the tungsten coordination polyhedron. Tungsten 5d-band splits into 5d(t_{2g}) and 5d(e_g) sub-bands in octahedral and 5d(t_2) and 5d(e) sub-bands in tetrahedral coordination (Fig. 9.1.1). However, the small value of the crystal-field splitting Δ or 10Dq (several electron volts) and the large value of the natural width of the core level $2p_{3/2}$(W) ($\sim$4.5 eV [172]) often do not allow to discriminate the two coordinations of tungsten from the splitting of the L_3-edge white line [176–178]. Therefore, a more sophisticated experimental approach should be exploited to address this issue. Theoretically, by reducing the core-hole lifetime induced broadening, it is possible to resolve the splitting of 5d(W)-states (Fig. 9.1.2).

---

[1] The main results, presented in this chapter, have been published as I. Pudza, A. Kalinko, A. Cintins, A. Kuzmin, **Study of the thermochromic phase transition in $CuMo_{1-x}W_xO_4$ solid solutions at the W L_3-edge by resonant X-ray emission spectroscopy**, Acta Mater. 205 (**2021**) 116581.

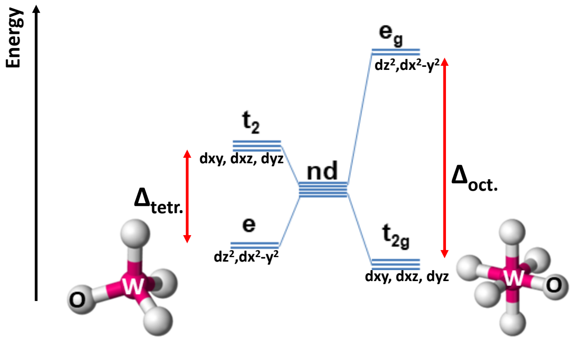

Figure 9.1.1: **A schematic representation of the 5d-band splitting into 5d(t_{2g}) and 5d(e_g) sub-bands in octahedral and 5d(t_2) and 5d(e) sub-bands in tetrahedral coordination of tungsten ions.** The crystal field splitting parameter Δ in the octahedral coordination is larger than that in the tetrahedral.

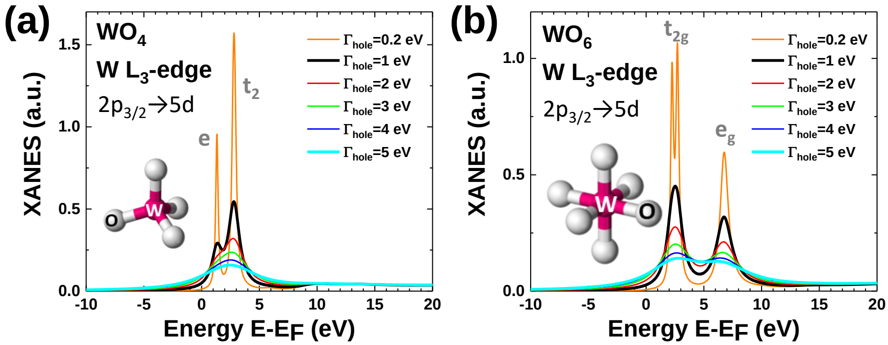

Figure 9.1.2: **Theoretically calculated W L_3-edge XANES spectra with different Lorentzian broadening:** for regular WO_6 octahedron (a) and regular WO_4 tetrahedron (b). By reducing the core-hole lifetime induced broadening Γ_{hole}, it is possible to resolve the splitting of 5d(W)-states into two sub-bands.

In this chapter, the resonant X-ray emission spectroscopy (RXES) study at the W L_3-edge of the previously described $CuMo_{1-x}W_xO_4$ solid solutions is presented. RXES was employed to follow a variation of the tungsten local atomic and electronic structure across observed thermochromic phase transition as a function of sample composition and temperature. The crystal field splitting parameter Δ for the 5d(W)-states was obtained from the RXES plane analysis and was used to evaluate the coordination of tungsten atoms. Temperature-dependent RXES measurements were successfully employed to determine the hysteretic behaviour of the structural phase transition between the α and γ phases in $CuMo_{1-x}W_xO_4$ solid solutions on cooling and heating even at low ($x < 0.10$) tungsten content. The experimental results were supplemented with *ab initio* calculations.

9.2 Theoretical XANES calculations

Theoretical calculations of the W L_3-edge XANES spectra were performed based on the finite difference method (FDM) by the *ab initio* real-space FDMNES code [18, 19], thus avoiding the muffin-tin potential approximation. The XANES spectra were calculated using real energy-dependent Hedin-Lundqvist exchange-correlation potential [159] taking into account spin-orbit interactions and the self-consistent cluster potential. Since the effect of the crystal field is originated from the interaction between tungsten and nearest oxygen atoms, the calculations were performed for 4.0 Å radius clusters constructed around the absorbing tungsten atom from the crystallographic structures of interest.

All calculated XANES spectra were convoluted with a Lorentzian broadening function with a FWHM (full-width at half-maximum) given by $\Gamma_{hole} = 1\ eV$ to mimic the broadening due to the core-hole lifetime and experimental resolution. The core-hole effect was also examined by performing calculations for the excited (with the core hole) and non-excited (without the core hole) absorbing tungsten atom.

As it was shown before, the structures of α-$CuMoO_4$ and γ-$CuMoO_4$ contain three non-equivalent sites for copper (Cu1, Cu2, Cu3) and molybdenum (Mo1, Mo2, Mo3) atoms (Table 5.2.2). All molybdenum atoms occupy either distorted tetrahedral (in α-$CuMoO_4$ phase) or distorted octahedral (in γ-$CuMoO_4$ phase) positions. For comparison, in copper tungstates ($CuWO_4$), there is only one tungsten position with disordered octahedral local environment [129].

The calculated W L_3-edge XANES spectra for $CuWO_4$ and tungsten atom substituting molybdenum atom at the Mo2 site in α-$CuMoO_4$ (distorted tetrahedral environment) and γ-$CuMoO_4$ (distorted octahedral environment) are shown in Fig. 9.2.1. The XANES spectra calculated for tungsten atoms placed at the Mo1 or Mo3 sites are close to that at the Mo2 site and are not shown. Note that all theoretical calculations were performed based on the crystallographic structures obtained from XRD data [1, 129] without any structure relaxation due to the substitution of atoms.

9.3 Results and discussion

The following subsections demonstrate that the RXES plane's analysis provides useful bulk sensitive information on the coordination of tungsten atoms and allows one to determine the crystal field splitting parameter Δ for the 5d(W)-states. This information is extracted from the RXES plane using two different approaches: by analysing the high-energy resolution

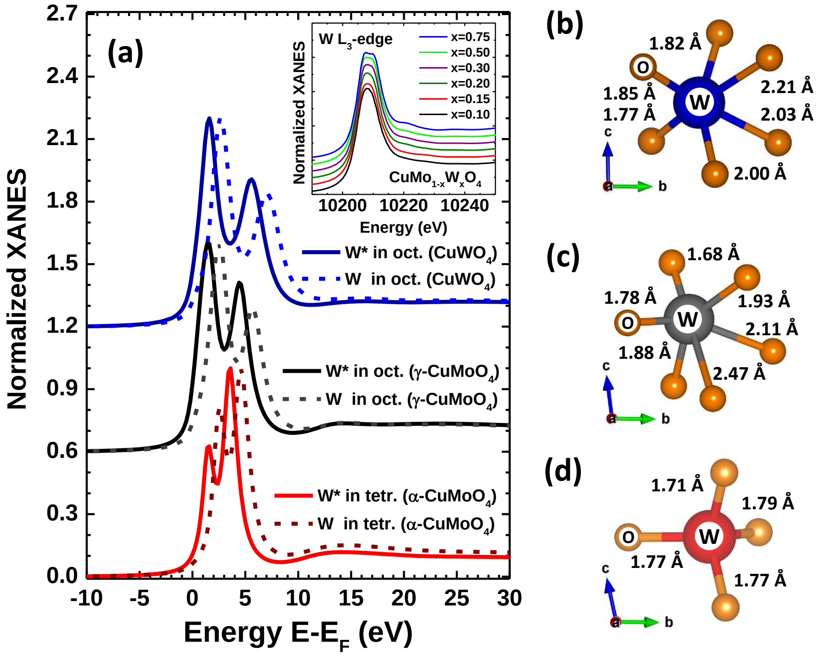

Figure 9.2.1: **Calculated W L$_3$-edge XANES spectra for a tungsten atom with different local environments:** Calculated W L$_3$-edge XANES for a tungsten atom in distorted octahedral (in the case of $CuWO_4$ and when W is substituting molybdenum atom at the Mo2 site in γ-$CuMoO_4$) and tetrahedral (when W is substituting molybdenum atom at the Mo2 site in α-$CuMoO_4$) environments. The results for the excited state with the core hole (W*, solid curves) and non-excited state without the core hole (W, dashed curves) are given (a). Tungsten–oxygen polyhedra with specified interatomic distances in $CuWO_4$ (b), W at the Mo2 site in γ-$CuMoO_4$ (c) and W at the Mo2 site in α-$CuMoO_4$ (d) are also shown. An inset shows the experimental W L$_3$-edge XANES spectra in $CuMo_{1-x}W_xO_4$ solid solutions measured in the transmission mode during the experiment described in Sec. 6.

fluorescence detected X-ray absorption near-edge structure (HERFD-XANES) and off-resonant X-ray emission spectra.

9.3.1 Crystal field splitting

According to the crystal field theory [179], the d-orbitals of the metal ion split in the octahedral field of oxygen ligands into triply degenerated t_{2g} orbitals and doubly degenerated e_g orbitals with the energy difference Δ_{oct}, where the t_{2g} orbitals have lower energy than the e_g ones (Fig. 9.1.1). In tetrahedral coordination, the splitting of the d orbitals occurs into two groups with the energy difference Δ_{tet} between the lower energy e orbitals and the higher energy t_2 orbitals. The splitting magnitude for regular tetrahedral and octahedral coordinations are related as $\Delta_{tet} = 4/9\Delta_{oct}$ for similar W–O distances [179]. For W with oxidation state 6+, all five d-orbitals are unoccupied; therefore, two electron transitions from $2p_{3/2}$ to split $5d$ states are possible and will have different X-ray absorption intensities. For tetrahedral WO$_4$ coordination, the intensity ratio will be e:t_2=2:3, whereas for octahedral WO$_6$ coordination, it will be t_{2g}:e_g=3:2. Thus, the knowledge of splitting magnitude and/or intensity ratio for the two transitions in CuMo$_{1-x}$W$_x$O$_4$ solid solutions allows one to determine the type of tungsten ion coordination.

Theoretical W L$_3$-edge XANES calculations using the FDMNES code [18, 19] were performed for three local geometries of tungsten ions similar to those in CuWO$_4$, α-CuMoO$_4$ and γ-CuMoO$_4$ (Fig. 9.2.1). The white line in the calculated XANES spectra is split by about 4.0 eV and 3.0 eV, respectively, in CuWO$_4$ and γ-CuMoO$_4$ phase (W substitutes Mo at the Mo2 site) due to the distorted octahedral crystal field. In contrast, a a smaller splitting of about 2.0 eV is characteristic of a tungsten ion in the tetrahedral local environment, as when it is located at the Mo2 site in α-CuMoO$_4$ phase.

The XANES spectra of CuMo$_{1-x}$W$_x$O$_4$ solid solutions at the W L$_3$-edge contain a strong resonance (see the inset in Fig. 9.2.1(a)), the so-called "white line" [180], located just below the continuum threshold and corresponding to the dipole-allowed electron transition from the 2p$_{3/2}$(W) level to a quasi-bound 5d(W)+2p(O) mixed-state in the presence of the core hole [176]. A very short natural lifetime of the excited state with the core hole at the 2p$_{3/2}$(W) level leads to significant natural broadening ($\sim$4.5 eV [172]) of the W L$_3$-edge absorption spectrum. Due to the limited resolution, the crystal field splitting of the 5d(W) states is smeared out and most often cannot be resolved in the conventional experiment in transmission mode. However, some evidence of splitting is nevertheless observed in the white line maximum of W L$_3$-edge XANES spectrum measured in the transmission mode for a high tungsten content ($x = 0.75$) (see the inset in Fig. 9.2.1(a)).

The splitting of the 5d(W) orbitals can be observed experimentally by detecting the RXES due to 3d$_{5/2}$(W)$\rightarrow$2p$_{3/2}$(W) electron transition (Fig. 9.3.1(c)), since the lifetime of the final state with a hole at the 3d$_{5/2}$(W) orbital (M$_5$-edge) is longer than that with a hole at the 2p$_{3/2}$(W) orbital (L$_3$-edge) [107]. Therefore, the lifetime broadening present in conventional XANES spectra is significantly reduced in the RXES experiment revealing additional features in the HERFD-XANES spectra.

In the RXES experiment, the intensities and energies of the incoming and emitted X-rays are monitored. The 2p3d RXES plane of W in CuMo$_{0.50}$W$_{0.50}$O$_4$ is shown in Fig. 9.3.1(a). Different plane cuts were made to obtain information on the structural and electronic properties of the material. The W L$_3$-edge HERFD-XANES spectra of CuMo$_{1-x}$W$_x$O$_4$ (0.04$\leq$x$\leq$1.00) solid solutions at 300 K were obtained from RXES planes

(Fig. 9.3.1(a)) by integrating the emission intensity in the narrow emission energy region of ±0.2 eV around 8398.5 eV and are shown in Fig. 9.3.1(d).

Besides the HERFD-XANES spectra, one can additionally obtain (Figs. 9.3.1(a,b)) high energy resolution off-resonant X-ray emission spectra by extracting them slightly below (bands B1 and B2 in Figs. 9.3.1(e,f)) and above (bands B3 and B4 in Figs. 9.3.1(g,h)) the W L_3 absorption edge, respectively. Both types of emission spectra (extracted slightly before and after the resonance) contain information on the crystal field splitting, while with a smaller signal-to-noise ratio compared to HERFD-XANES (Fig. 9.3.1(d)) due to weaker intensity. Furthermore, in the non-resonant case (Figs. 9.3.1(g,h)), the tails of the main X-ray emission line (W L_{α_1} in Fig. 9.3.1(b)) give some background under the B3 and B4 peaks, which also limits the accuracy of the analysis and should be removed in advance.

Further, the effect of concentration and temperature on the local structure of tungsten ions in $CuMo_{1-x}W_xO_4$ solid solutions observed in the RXES spectra is discussed.

9.3.2 Effect of composition

RXES spectra of $CuMo_{1-x}W_xO_4$ solid solutions with different concentrations ($0.04 \leq x \leq 1.00$) at 300 K are shown in Figs. 9.3.1(d-h). The observed bands are originated from the three different mechanisms, already discussed above (basically, they are three different RXES plane cuts).

The emission spectra for the incident X-ray energy E_i=10190 eV below the W L_3 absorption edge are shown in Figs. 9.3.1(e,f) and correspond to off-resonant conditions [110]. Two emission bands B1 at ~8312 eV and B2 at ~8376 eV can be observed in the spectra (Fig. 9.3.1(b)) and are related to the transitions from $3d_{3/2}$ and $3d_{5/2}$ levels, respectively (Figs. 9.3.1(c)). The intensity of the lower energy band B1 is smaller than that of the band B2, correlating with the intensity of the W $L\alpha_1$ and $L\alpha_2$ emission lines.

Crystal field of oxygen atoms split both (B1 and B2) bands to two peaks. The distance between these peaks and the ratio of their intensities (I_1/I_2) can be evaluated by fitting the spectra with two Lorentzian functions. These parameters can be used to estimate the symmetry of the crystal field. The difference between the position of the two fitted Lorentzian functions is related to the crystal field splitting parameter Δ (10Dq) used in the crystal field theory [179]. The changes in the spectral shape upon tungsten content increase (Figs. 9.3.1(e,f)) indicate that the local coordination of tungsten ions changes from tetrahedral (when $x = 0.04$) to octahedral (when $x > 0.15$).

The emission spectra recorded with the incident X-ray energy E_i=10242 eV well above the W L_3 absorption edge consist of four emission bands (W $L\alpha_2$, B3, W $L\alpha_1$ and B4) indicated in Fig. 9.3.1(b). The

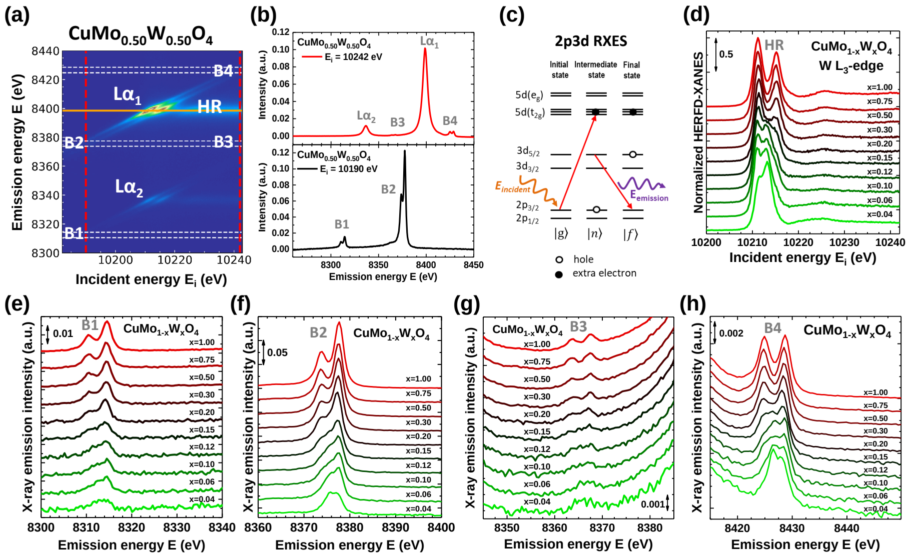

Figure 9.3.1: **Experimental data obtained from the composition-dependent RXES experiment of $CuMo_{1-x}W_xO_4$ solid solutions:** RXES intensity map as a function of incident and emitted energies for $CuMo_{0.50}W_{0.50}O_4$ solid solution measured at 300 K (a). Vertical cuts of the RXES plane at the incident energies E_i=10190 eV and 10242 eV, shown in (a) by vertical red dashed lines. Observed bands (Lα_1, α_2 and B1-B4) are labelled (b). A schematic diagram of 2p3d RXES process for an atom in octahedral coordination showing initial, intermediate and final states (c). The W L_3-edge HERFD-XANES spectra for different $CuMo_{1-x}W_xO_4$ solid solutions measured at the emission energy E_e=8398.5±0.2 eV, indicated by the horizontal orange line in (a) are shown in the panel (d). High energy resolution off-resonant X-ray spectra for different $CuMo_{1-x}W_xO_4$ solid solutions obtained with incident energy E_i=10190 eV – below the W L_3-edge (e,g). High energy resolution off-resonant X-ray emission spectra for different $CuMo_{1-x}W_xO_4$ solid solutions obtained at E_i=10242 eV – above the W L_3-edge (f,h).

composition-dependent B3 and B4 bands are reported in Figs. 9.3.1(g,h). The origin of these bands is similar to that of B1 and B2, i.e., is due to the transitions from $3d_{3/2}$ and $3d_{5/2}$ levels, respectively (Fig. 9.3.1(c)). Similarly, as before, the lower energy band (B3) has a much weaker intensity than that at the higher energy (B4), and the crystal field splits both bands to two peaks (Figs. 9.3.1(g,h)). Note that the B3 and B4 bands are located on top of the background originated from the W Lα_1 and partially W Lα_2 fluorescence, making it more difficult to determine the magnitude of the peaks splitting and the ratio of their intensities. Nevertheless, the obtained parameters agree with that obtained from the analysis of the bands B1 and B2 suggesting the octahedral coordination of tungsten ions for solid solutions with $x > 0.15$.

The composition-dependent HERFD-XANES spectra for the W L_3-edge are shown in Fig. 9.3.1(d). Pronounced splitting of the white line due to the

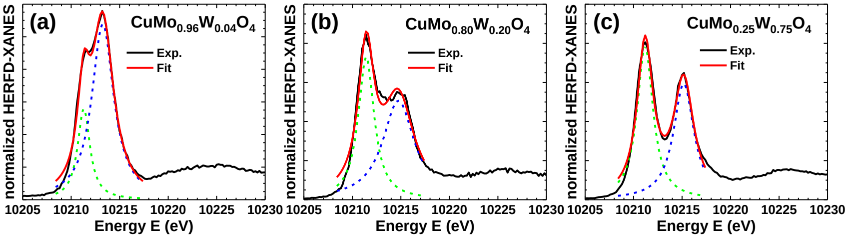

Figure 9.3.2: **Examples of HERFD-XANES spectra fitting with Lorentzian functions**: Black lines are experimental data; red lines are fitted curves. Contributions of two Lorentzian functions are additionally shown with blue and green dashed lines. The difference between the two fitted peak positions was used to estimate the crystal field splitting parameter Δ.

octahedral crystal field is visible for $CuMo_{1-x}W_xO_4$ samples with $x > 0.15$. It is in agreement with the results obtained from high energy resolution off-resonant X-ray emission spectra (Figs. 9.3.1(e-h)). The results for the crystal field splitting parameter Δ obtained from the fitting off-resonant XES (B2 band) and HERFD-XANES spectra of $CuMo_{1-x}W_xO_4$ solid solutions at 300 K and 90 K are combined in Fig. 9.3.3. Note that only the splitting of the white line (Figs. 9.3.2) is considered in Fig. 9.3.3 because it is weakly affected by the self-absorption effect, which can be neglected.

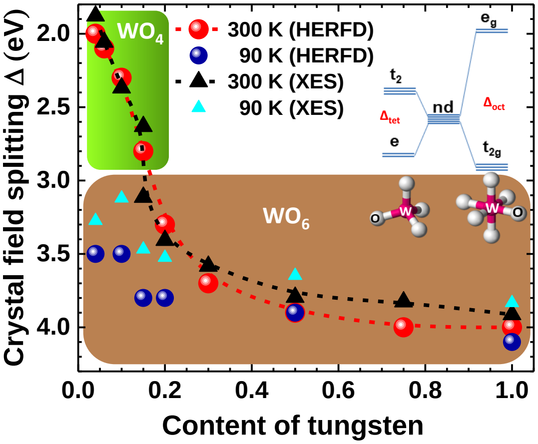

Figure 9.3.3: **Crystal field splitting parameter Δ as a function of tungsten content x in $CuMo_{1-x}W_xO_4$ solid solutions at 90 K and 300 K**: calculated from the off-resonant XES (Fig. 9.3.1(f)) and HERFD-XANES (Fig. 9.3.1(d)) spectra. A schematic energy level diagram showing crystal field splitting of tungsten 5d-states in the tetrahedral and octahedral environment is also shown. Note that Δ_{tet} is smaller than Δ_{oct}.

At 300 K, $CuWO_4$ and $CuMo_{0.96}W_{0.04}O_4$ have wolframite [129] and α-$CuMoO_4$ [1] phases, respectively, which correspond to the octahedral and tetrahedral coordination of tungsten ions. Upon cooling down to 90 K,

$CuWO_4$ remains in the same triclinic phase (space group $P\bar{1}$) [181], but $CuMo_{0.96}W_{0.04}O_4$ changes its phase from α to γ-$CuMoO_4$ phase [2, 10] with distorted octahedral coordination of Mo^{6+} and W^{6+} ions.

For intermediate compositions of $CuMo_{1-x}W_xO_4$ solid solutions, a mixture of α-$CuMoO_4$ and γ-$CuMoO_4$ phases co-exists with the relative amounts depending on the tungsten content and temperature [4, 10, 133]. In particular, when samples are cooled down from 300 K to 90 K, a transition from tetrahedral to octahedral tungsten coordination is observed for solid solutions with $x < 0.20$ but not for those with $x \geq 0.20$ (Fig. 9.3.3).

The theoretical XANES calculations for distorted WO_6 and WO_4 environments (Fig. 9.2.1) suggest a value of the crystal field splitting parameter $\Delta \sim 3 - 4$ eV for octahedral coordination and about 2 eV for tetrahedral one. By considering the experimentally observed α-to-γ phase transition and theoretical calculations, the crystal field splitting parameter Δ can be distributed into two ranges (see green and brown regions in Fig. 9.3.3). The tetrahedral coordination of W^{6+} ions is expected for $\Delta < 3$, whereas the octahedral coordination for $\Delta > 3$. This example shows that the simple analysis of the experimental off-resonant XES and HERFD-XANES spectra can provide useful information on the local coordination of tungsten ions.

Furthermore, the parameter Δ correlates well with optical properties of the $CuMo_{1-x}W_xO_4$ solid solutions (i.e. their colour). Namely, at 300 K, the samples with $x \leq 0.15$ have the crystal field splitting parameter $\Delta < 3$ eV and greenish colour, whereas the samples with $x \geq 0.20$ have $\Delta > 3$ eV and brown colour. Note, that upon cooling down to 90 K, the samples with $x \leq 0.15$ change their colour from greenish to brown, in agreement with previous studies [10], and the parameter Δ increases above 3 eV indicating the transition to the phase with the octahedral tungsten (and molybdenum) coordination.

In the next subsection, the sensitivity of the crystal field splitting parameter Δ to the temperature-induced phase transitions in $CuMo_{1-x}W_xO_4$ solid solutions with low tungsten rate is demonstrated.

9.3.3 Effect of temperature

It is known that the first-order structural phase transition between α and γ phases in $CuMo_{1-x}W_xO_4$ solid solutions (with low W concentration) has a pronounced hysteretic behaviour, which can be controlled by varying the tungsten content [4, 10]. In our previous studies of $CuMoO_4$ and $CuMo_{0.90}W_{0.10}O_4$ [88, 163], we have shown that the Mo K-edge XANES is sensitive to the α-to-γ phase transition due to the significant change in the coordination of molybdenum ions from tetrahedral to octahedral one. However, the sensitivity of the Mo K-edge XANES to the phase transition is based on a variation of the pre-edge peak amplitude which is affected by the natural broadening of the excited state (5.8 eV at the Mo K-edge [172]). Therefore, the high resolution off-resonant XES and HERFD-XANES spectra should be more favourable for tracking the α-to-γ phase transition.

The temperature-dependent W L_3-edge HERFD-XANES spectra of $CuMo_{0.96}W_{0.04}O_4$ sample are shown in Fig. 9.3.4. The spectral shape changes reflect the transition from tetrahedral (α-phase) to octahedral (γ-phase) tungsten coordination on cooling from 300 K to 120 K, whereas from octahedral to tetrahedral tungsten coordination on heating from 90 K up to 420 K. Note that the temperature effect is clearly observed in the corresponding RXES planes. The relative position of two bright spots is well resolved in the octahedral coordination. The two spots move closer and change their relative intensity in the case of tetrahedral coordination. A similar trend is observed for $CuMo_{0.90}W_{0.10}O_4$ experimental data, but the difference is not so pronounced since, at particular temperatures, W atoms coexist in both tetrahedral and octahedral environment (Fig. 9.3.5).

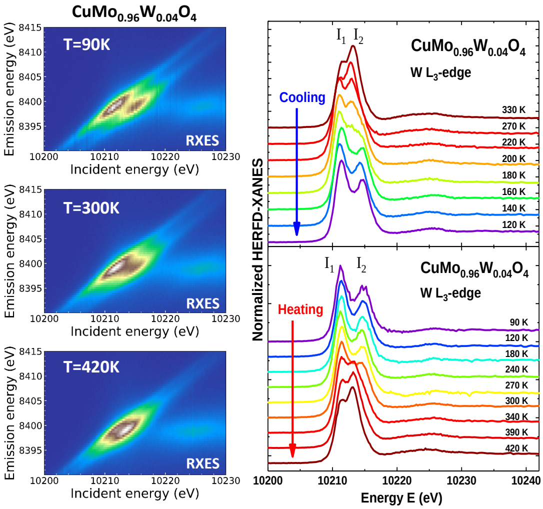

Figure 9.3.4: **Temperature-dependent RXES data for $CuMo_{0.96}W_{0.04}O_4$:** Parts of the RXES planes at 90 K, 300 K and 420 K on heating (left panels) and temperature dependent W L_3-edge HERFD-XANES spectra measured on cooling and heating (right panel).

The phase transition hysteresis loops for $CuMo_{0.96}W_{0.04}O_4$ and $CuMo_{0.90}W_{0.10}O_4$ solid solutions are shown in Fig. 9.3.6. They were determined from the temperature dependencies of the magnitude of the peak splitting (Δ) and the ratio of peak intensities (I_1/I_2) in the W L_3-edge HERFD-XANES and off-resonant XES spectra. The both parameters were normalized on a scale from 0 to 1 and averaged. Note that HERFD-XANES and off-resonant XES have slightly different sensitivity to the change of tungsten coordination leading to some scatter of the points. The results for

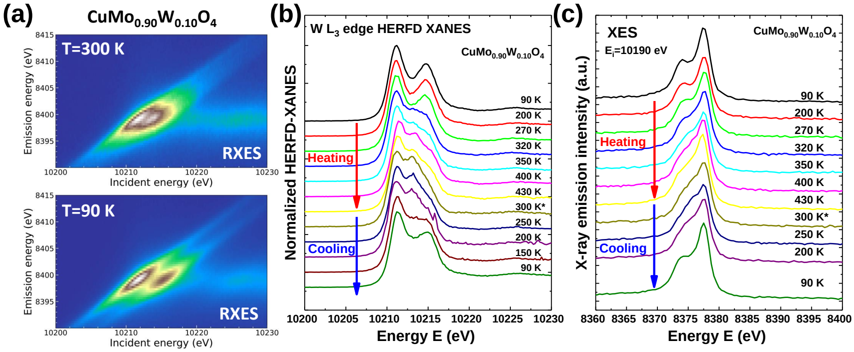

Figure 9.3.5: **Temperature-dependent RXES data for $CuMo_{0.90}W_{0.10}O_4$:** Parts of the RXES planes at 300 K (before cooling) and 90 K (a); temperature-dependent W L_3-edge HERFD-XANES spectra measured on heating and cooling and high energy resolution off-resonant X-ray emission spectra obtained with incident energy E_i=10190 eV (b,c).

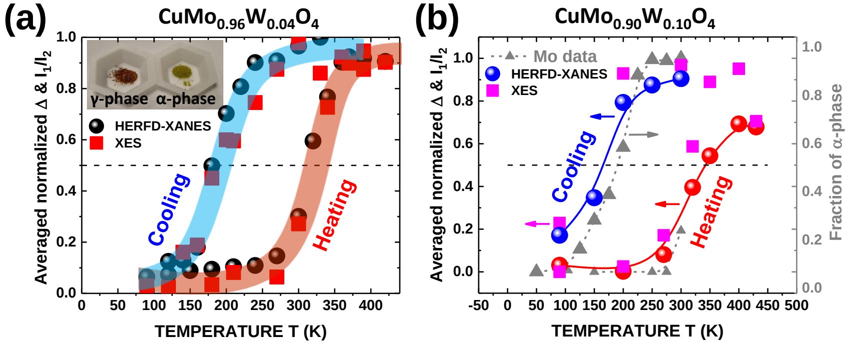

Figure 9.3.6: **Temperature dependencies of the normalized and averaged magnitude of the peak splitting (Δ) and the ratio of peak intensities (I_1/I_2):** for $CuMo_{0.96}W_{0.04}O_4$ (a) and $CuMo_{0.90}W_{0.10}O_4$ (b) samples. A fraction of the α-phase extracted from the linear combination analysis of the Mo K-edge XANES spectra of $CuMo_{0.90}W_{0.10}O_4$ [88] is also displayed for comparison (solid triangles). Inset shows a photo of two $CuMo_{0.96}W_{0.04}O_4$ samples at room temperature: the brown sample is in the γ-phase (after treatment at 77 K in liquid nitrogen), and the green sample is in the α-phase (at room temperature).

$CuMo_{0.90}W_{0.10}O_4$ (Fig. 9.3.5(b)) are also compared with a fraction of the α-phase extracted from the Mo K-edge XANES spectra analysis [88].

A small difference between the starting temperatures of the α-to-γ phase transition obtained from the W L_3 and Mo K-edges for $CuMo_{0.90}W_{0.10}O_4$ sample is observed. When probed at the Mo K-edge, the transition starts at slightly lower temperature than that measured at the W L_3-edge. This can be explained by the fact, that some part of the tungsten atoms is located in the octahedral environment already at 300 K, as was concluded from Fig. 9.3.3 and Fig. 9.3.5.

9.4 Conclusions

Resonant X-ray emission spectroscopy (RXES) at the W L_3-edge was used to study the changes in the local atomic structure of tungsten ions across the thermochromic phase transition in polycrystalline $CuMo_{1-x}W_xO_4$ solid solutions as a function of sample composition and temperature.

It was demonstrated that the analysis of the RXES plane provides valuable information on the coordination of tungsten atoms in the sample bulk and allows one to determine the crystal field splitting parameter Δ for the 5d(W)-states. Moreover, this information can be extracted from the analysis of RXES plane using two different perspectives: the high energy resolution fluorescence detected X-ray absorption near-edge structure (HERFD-XANES) and the high energy resolution off-resonant X-ray emission spectra excited below and above resonance conditions. The analysis of the experimentally obtained RXES planes shows a clear advantage over conventional XANES due to revealing spectral features with much higher resolution.

The RXES method is well suited for *in situ* measurements and was used here to track the hysteresis loop of the first-order structural phase transition between α and γ phases in $CuMo_{1-x}W_xO_4$ solid solutions on cooling and heating even at low ($x < 0.10$) tungsten content.

It was found that tungsten ions in $CuMo_{1-x}W_xO_4$ solid solutions have always octahedral coordination for samples with $x > 0.15$, whereas their coordination changes from tetrahedral to octahedral upon cooling for smaller tungsten content. Nevertheless, some amount of tungsten ions co-exists in the octahedral environment at 300 K for solid solutions with $x < 0.15$. The obtained results correlate well with the optical properties of these materials, namely, colour change from greenish to brown upon cooling or increasing tungsten concentration.

The electronic structure of $CuMo_{1-x}W_xO_4$ solid solutions governs their thermochromic properties, which are related to a variation of the transmission window in optical spectra [10,11]. A change in the tungsten local coordination from tetrahedral to octahedral affects the band gap, which is determined by the oxygen-to-metal charge transfer [10]. The band gap is smaller in the case of octahedral coordination of tungsten [11], i.e., at higher tungsten content or lower temperature.

Finally, this study demonstrates the possibilities of the RXES technique to probe the crystal field effect in functional materials with controllable properties on the example of thermochromic $CuMo_{1-x}W_xO_4$ solid solutions.

Chapter 10

XAS study of $Cu_{1-x}Zn_xMoO_4$

10.1 Introduction [1]

Copper and zinc molybdates form a complete solid solution series $Cu_{1-x}Zn_xMoO_4$ ($0 \leq x \leq 1$) [128, 135]. The substitution of copper by zinc produces a strong effect on the thermochromic properties of copper molybdate and changes its band gap from 2.78 eV in α-$CuMoO_4$ to 3.6 eV in α-$ZnMoO_4$ [138]. Recently it was found, that the substitution of Cu^{2+} ions with an ionic radii 0.73 Å by a few percent ($0 \leq x \leq 0.05$) of slightly larger Zn^{2+} ions (0.74 Å) reduces the phase transition temperature of $Cu_{1-x}Zn_xMo_{0.94}W_{0.06}O_4$ [134]. Magnetic susceptibility measurements of $Cu_{1-x}Zn_xMoO_4$ ($0 \leq x \leq 0.1$) reported in [137] indicate on the shift of $\alpha \leftrightarrow \gamma$ phase transition hysteresis to the lower temperatures by $\sim$75 K with increasing Zn^{2+} content. Diffraction data reported in [135] indicated that content of Zn atoms in $Cu_{1-x}Zn_xMoO_4$ solid solution higher than $\sim$17.5% leads to a phase similar to α-$ZnMoO_4$.

A deeper understanding of the relationship between crystal structure and thermochromic properties in $Cu_{1-x}Zn_xMoO_4$ requires detailed knowledge on the variation in the short-range order upon transition metal ion substitution and temperature change. In this chapter, we discuss the influence of zinc ions on the local structure and lattice dynamics of $Cu_{1-x}Zn_xMoO_4$ (x=0.10, 0.50, 0.90) solid solutions.

10.2 XAS experimental data

XAS experiments for $Cu_{1-x}Zn_xMoO_4$ ($0 \leq x \leq 1.0$) samples were conducted at HASYLAB PETRA III P65 undulator beamline [152] as a function of temperature as described in Section 6.4. The $Cu_{0.90}Zn_{0.10}MoO_4$ sample was measured on heating from 10 K to 300 K and on cooling from 300 K to 100 K. All other samples were measured only on heating from 10 K to 300 K.

---

[1] The main results, presented in this chapter, have been published as I. Pudza, A. Anspoks, A. Cintins, A. Kalinko, E. Welter, A. Kuzmin, **The influence of Zn^{2+} ions on the local structure and thermochromic properties of $Cu_{1-x}Zn_xMoO_4$ solid solutions**, Materials Today Communications 28 (**2021**) 102607.

Temperature dependence of the Mo K-edge XANES in $Cu_{0.90}Zn_{0.10}MoO_4$ was observed similar to pure $CuMoO_4$, indicating the change in molybdenum coordination. Its linear combination analysis (LCA) was performed using one of the low-temperature (50 K) and the highest temperature (300 K) XANES spectra as references. The analysis was done using the Athena package [29] in the energy range from 19985 eV to 20015 eV. The obtained temperature-dependent fraction of α-phase (300 K) in the sample is shown in Fig. 10.2.1, where the hysteresis loop is well observed.

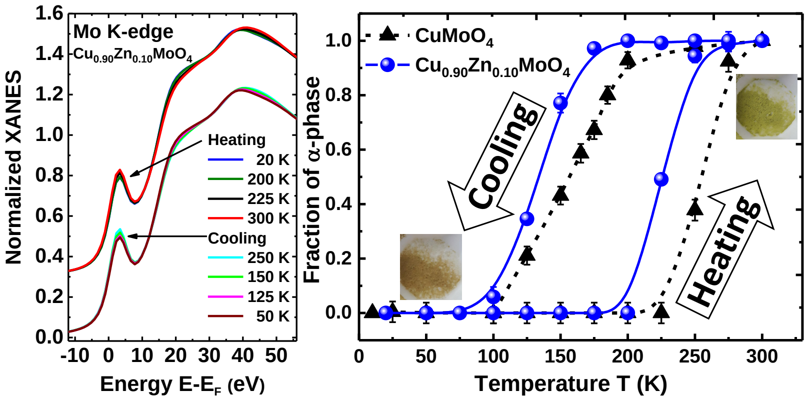

Figure 10.2.1: **Temperature dependence of $Cu_{0.90}Zn_{0.10}MoO_4$**: experimental Mo K-edge XANES as a function of temperature during the sample cooling and heating (left panel). Temperature dependence of the α-phase fraction in $CuMoO_4$ [88] and $Cu_{0.90}Zn_{0.10}MoO_4$ upon heating and cooling (right panel). Photographs of the $Cu_{0.90}Zn_{0.10}MoO_4$ sample at 77 K (brownish) and 300 K (green) are also shown for illustration.

Temperature-dependent experimental Cu, Zn and Mo K-edge EXAFS $\chi(k)k^2$ spectra of $Cu_{1-x}Zn_xMoO_4$ were extracted following the conventional procedure [70] using the Athena package [29]. The EXAFS spectra and their FTs at selected temperatures for several samples are shown in Fig. 10.2.2. The Zn K-edge EXAFS of $Cu_{0.90}Zn_{0.10}MoO_4$ was excluded from the analysis due it was corrupted by glitches. The FTs were calculated in the k-space range of 1.3–12.0 Å^{-1} (for Cu K-edge), 2.3–14.0 Å^{-1} (for Zn K-edge) and 2.4–15.0 Å^{-1} (for Mo K-edge).

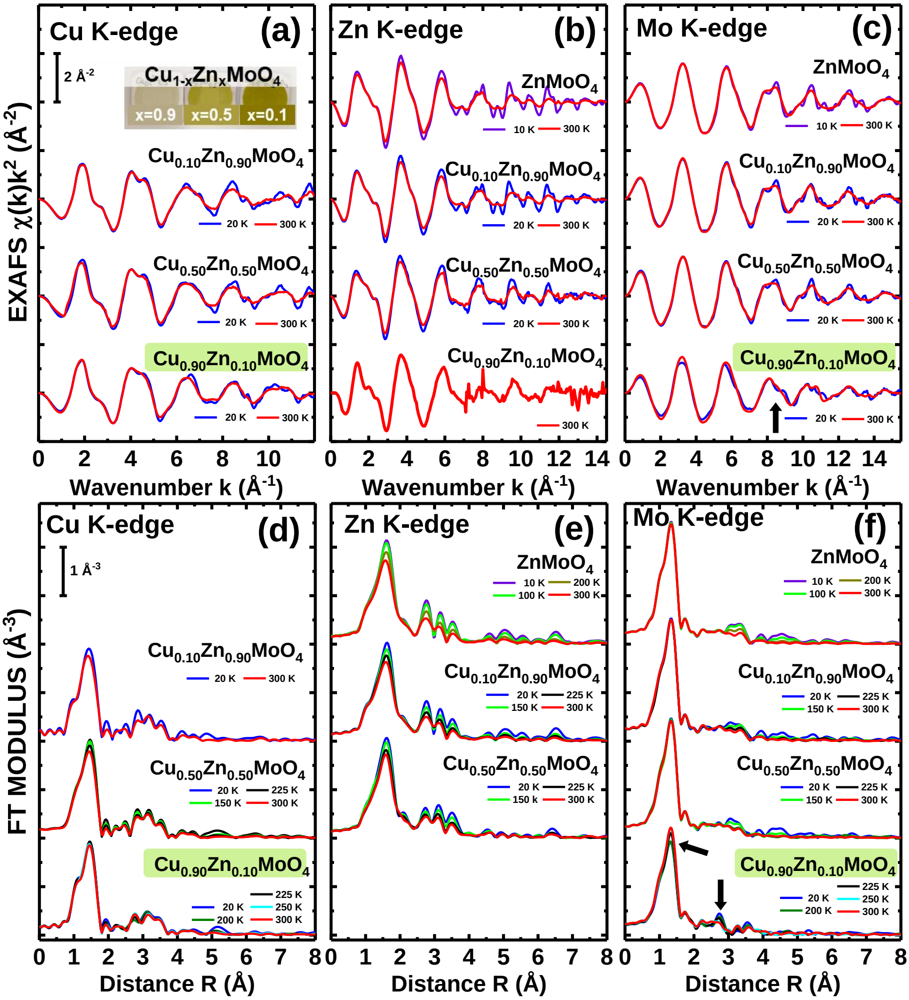

Figure 10.2.2: **Temperature-dependent experimental EXAFS data for $ZnMoO_4$ and $Cu_{1-x}Zn_xMoO_4$ (x=0.10, 0.50, 0.90)**: Cu, Zn and Mo K-edge EXAFS spectra $\chi(k)k^2$ at selected temperatures (a-c) and corresponding Fourier transforms (only modulus is shown) (d-f). The most pronounced changes in $Cu_{0.90}Zn_{0.10}MoO_4$ spectra are highlighted.

10.3 Results and discussion

10.3.1 XANES analysis

Temperature-dependent normalized Mo K-edge XANES spectra of $Cu_{0.90}Zn_{0.10}MoO_4$ are shown in Fig. 10.2.1. The LCA of the Mo K-edge XANES was performed in the temperature range from 20 to 300 K. In an analogy with pure $CuMoO_4$ [88, 163], we assume that $Cu_{0.90}Zn_{0.10}MoO_4$ exists in α-phase at 300 K, while in γ-phase at 20 K. As shown in Fig. 10.2.1, the sample colour changes from green to brownish after treatment with liquid nitrogen ($\sim$77 K) and returns to green at room temperature.

A fraction of the α-phase in $Cu_{0.90}Zn_{0.10}MoO_4$ at different temperatures (Fig. 10.2.1) demonstrates hysteresis behavior on cooling and heating similar to $CuMoO_4$. However, the phase transition hysteresis in $Cu_{0.90}Zn_{0.10}MoO_4$ is shifted to lower temperatures by about 25 K. At the same time, the variation of the pre-edge peak for $Cu_{0.90}Zn_{0.10}MoO_4$ is not as pronounced as for $CuMoO_4$ reported in [163] indicating on slightly different molybdenum local environment at low temperatures. Based on XANES data, the transition from α to γ phase occurs in $Cu_{0.90}Zn_{0.10}MoO_4$ between $\sim$175 K and $\sim$100 K upon cooling, whereas the transition from γ to α phase begins above $\sim$200 K and ends at $\sim$250 K.

10.3.2 EXAFS analysis

Experimental Cu, Zn and Mo K-edge EXAFS spectra $\chi(k)k^2$ of $Cu_{1-x}Zn_xMoO_4$ together with their FTs are compared in Fig. 10.2.2. The first FT peak located at about 1-2 Å is due to the contribution from the first coordination shell formed by oxygen atoms. More distant FT peaks originate from SS contributions of outer coordination shells and MS effects.

While the temperature dependence at the Mo K-edge (especially at low-k values) for samples with $x \geq 0.50$ is very weak, significant changes occur in the first coordination shell of molybdenum atoms in $Cu_{0.90}Zn_{0.10}MoO_4$ sample. Indeed, the amplitude of the FT peak at 1.3 Å slightly increases on heating, suggesting the less distorted local environment of molybdenum at 300 K (Fig. 10.2.2(f)). Such behaviour is similar to the Mo change from octahedral to tetrahedral coordination during the γ-to-α phase transition in pure $CuMoO_4$ [162].

Comparing EXAFS spectra at the Cu and Zn K-edges, one can see that the local environment of Zn atoms exhibits stronger temperature dependence than that of Cu atoms. The damping of the Zn K-edge EXAFS oscillations increases noticeably at high-k values with temperature increase due to enhanced thermal disorder.

EXAFS spectra $\chi(k)k^2$ were analysed based on RMC/EA calculations as described in Section 7.1.4. Initial structure models for the calculations were constructed based on diffraction data reported in [1, 127, 128] by randomly substituting Zn atoms with Cu and vice versa, keeping the stoichiometric ratio of the elements in the supercell ($4a \times 4b \times 4c$) containing 2304 atoms. Several random configurations were simulated. In the case of Cu$_{0.90}$Zn$_{0.10}$MoO$_4$, structure models based on both α-CuMoO$_4$ and γ-CuMoO$_4$ structures were tested, and the relaxed α-phase gave a slightly better fit (smaller residual ξ [17]) than the γ-phase for all examined temperatures (20-300 K).

RMC/EA calculations were performed simultaneously for two (in ZnMoO$_4$ and Cu$_{0.90}$Zn$_{0.10}$MoO$_4$) or three (in Cu$_{1-x}$Zn$_x$MoO$_4$ with x=0.50 and 0.90) metal absorption edges. An example of obtained EXAFS fits, along with corresponding Fourier and Wavelet transforms of the experimental and theoretically calculated EXAFS spectra, are shown in Fig. 10.3.1(a-c) for Cu$_{0.50}$Zn$_{0.50}$MoO$_4$ sample. Good agreement between experimental and simulated data was achieved at all three metal absorption edges at all temperatures. The convergence of each RMC simulation was achieved after several thousand iterations. At least three RMC/EA simulations with different sequences of pseudo-random numbers were performed for each experimental data set.

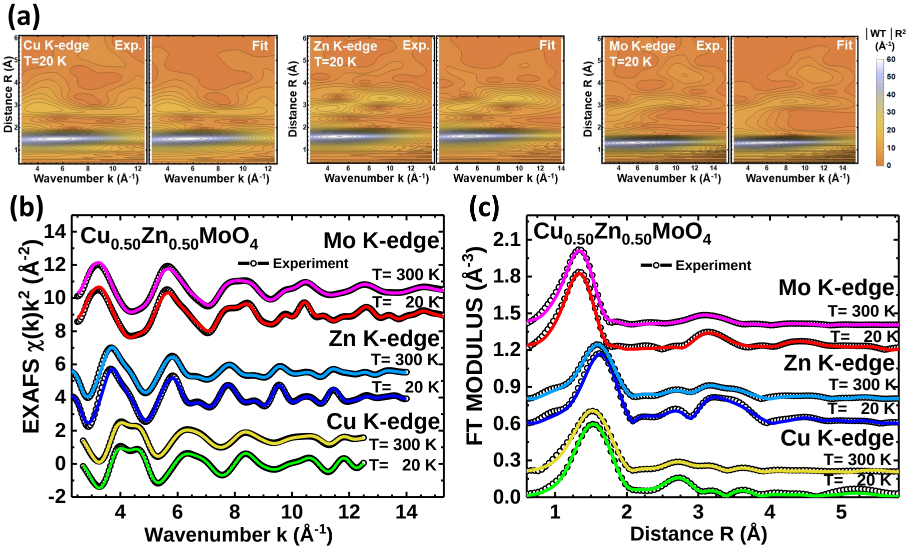

Figure 10.3.1: **Comparison of the experimental (T =20 K and 300 K) and calculated EXAFS data**: configuration-averaged Cu, Zn and Mo K-edge $\chi(k)k^2$ spectra of Cu$_{0.50}$Zn$_{0.50}$MoO$_4$ (b) and their Fourier (c) and Morlet wavelet transforms (T=20 K) (a).

The final atomic configurations were used to calculate the partial RDFs $g(R)$ for metal-oxygen and metal-metal atom pairs. Averaged distributions obtained from different pseudo-random number seeds are shown up to 6 Å for $ZnMoO_4$ at 10 K and 300 K in Fig. 10.3.2. As one can see, temperature induced peak broadening is well evident. Note that the first coordination shell is well separated, while outer shells overlap strongly. Further, we limit our discussion to the first coordination shell only. Temperature dependence of partial RDFs $g_{\mathrm{Zn-O}}(R)$, $g_{\mathrm{Cu-O}}(R)$, and $g_{\mathrm{Mo-O}}(R)$ for $ZnMoO_4$ and $Cu_{1-x}Zn_xMoO_4$ is shown in Fig. 10.3.3.

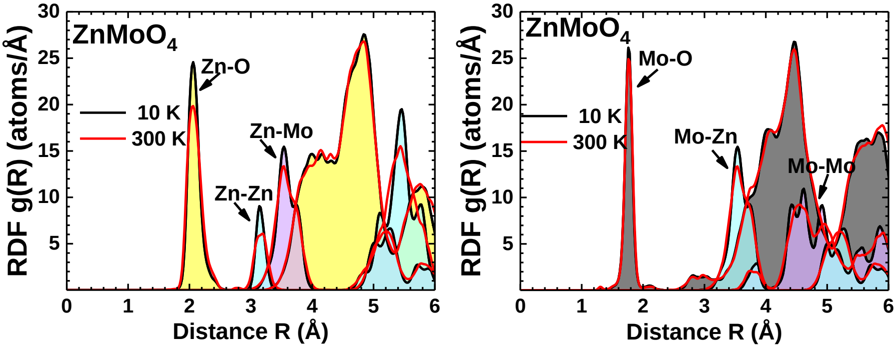

Figure 10.3.2: **Partial RDFs around zinc and molybdenum atoms in $ZnMoO_4$ at T=10 K and 300 K obtained in RMC/EA simulations.** Contributions from different atoms are indicated.

The RDFs $g_{\mathrm{Cu-O}}(R)$ for Cu–O atom pairs in $Cu_{1-x}Zn_xMoO_4$ have two maxima at ~1.9 Å and ~2.3 Å with a relative area of about 4:2. The first-order Jahn-Teller effect causes strong distortion of the first coordination shell of copper ions due to the Cu^{2+}[$3d^9$] electronic configuration. The RDFs of the nearest four oxygen atoms, located in the plane of the CuO_6 octahedron/CuO_5 square-pyramid, have a weak temperature dependence because of strong Cu–O bonds. The two more distant axial oxygen atoms contribute to the second broad peak of the RDF. Averaged interatomic distances for all six Cu–O sites within the first coordination shell calculated from atomic coordinates in the structural models are shown with vertical dashed lines in Fig. 10.3.3 for $Cu_{0.90}Zn_{0.10}MoO_4$. One can see that during heating, the longest Cu–O bond slightly lengthens.

Although α-$ZnMoO_4$ is isostructural to α-$CuMoO_4$, the local environment of zinc ions differs from that of copper. Zn^{2+} has an electronic configuration [Ar]$3d^{10}$ and, thus, the Jahn-Teller distortion is absent. The distribution $g_{\mathrm{Zn-O}}(R)$ can be characterised with one asymmetric peak with a maximum at about 2.05 Å because both ZnO_6 octahedron and ZnO_5 square-pyramid are slightly deformed.

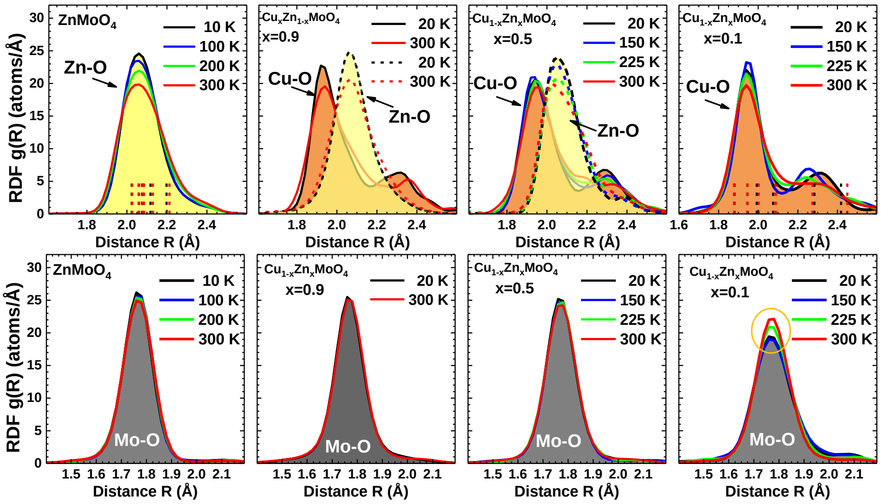

Figure 10.3.3: **Temperature-dependent partial RDFs $g_{\mathrm{Zn-O}}(R)$, $g_{\mathrm{Cu-O}}(R)$ and $g_{\mathrm{Mo-O}}(R)$ obtained in RMC/EA simulations.** Vertical dashed lines in $g_{\mathrm{Zn-O}}(R)$ plot for $ZnMoO_4$ and $g_{\mathrm{Cu-O}}(R)$ plot for $Cu_{0.90}Zn_{0.10}MoO_4$ indicate average Zn–O and Cu–O interatomic distances, respectively, at 10 K(20 K) and 300 K (black and red lines, respectively).

The distribution $g_{\mathrm{Mo-O}}(R)$ of the nearest four oxygen atoms, forming MoO_4 tetrahedron with $R_{\mathrm{Mo-O}}$ ≈1.77 Å, is rather narrow and has a weak dependence on temperature due to strong Mo–O bonds. The RDFs $g_{\mathrm{Mo-O}}(R)$ in pure α-$ZnMoO_4$ and $Cu_{1-x}Zn_xMoO_4$ solid solutions with x=0.50 and 0.90 remain nearly unchanged in the temperature range of 20-300 K. At the same time, some variation of the $g_{\mathrm{Mo-O}}(R)$ upon temperature increase is observed for $Cu_{0.90}Zn_{0.10}MoO_4$ sample and is related to structural changes.

The MSRD factor σ^2 values were evaluated directly from atomic coordinates by the MAD function [93]. Information on interatomic interactions was obtained by analysing the temperature dependencies of the MSRD factors σ^2, which are equal to a sum of thermal σ^2_{th} and static σ^2_{st} disorder. Due to the distorted environment of metal ions, only the groups of nearest oxygen atoms, which are responsible for the main peak in partial RDFs in Fig. 10.3.3, have been considered. The obtained MSRDs are plotted in Fig. 10.3.4 as a function of temperature and composition. The temperature dependencies of σ^2 were fitted with the correlated Einstein model [182], and the static disorder factors σ^2_{st} were estimated.

Similar to the result of the Mo K-edge XANES analysis (Fig. 10.2.1), the temperature dependence of the MSRD factors $\sigma^2_{\mathrm{Mo-O}}$ in $Cu_{0.90}Zn_{0.10}MoO_4$ exhibits hysteresis (Fig. 10.3.4(a)). Note that at temperatures below 250 K the MSRD values $\sigma^2_{\mathrm{Mo-O}}$ are much smaller than those for low-temperature γ-

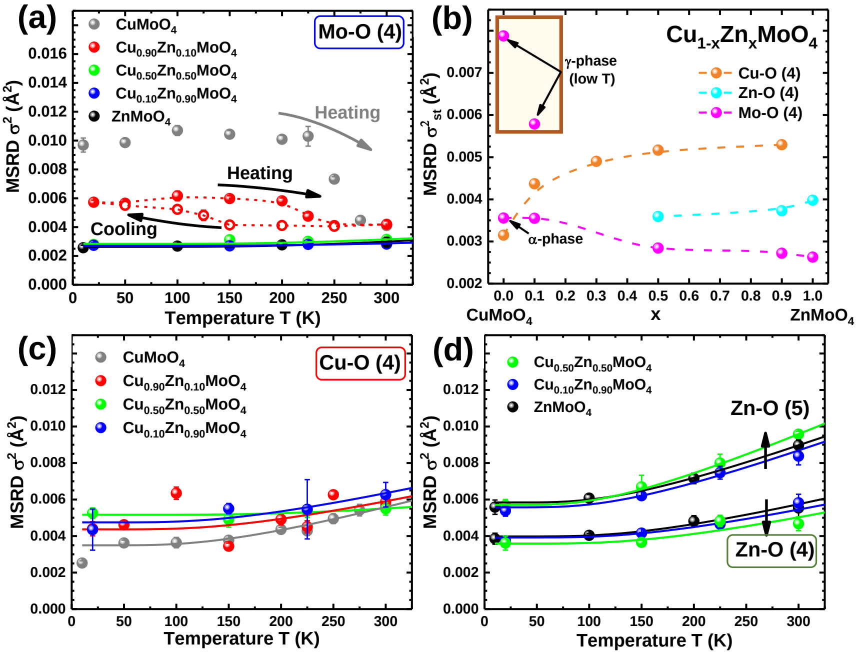

Figure 10.3.4: **MSRD factors σ^2, obtained in RMC/EA simulations**: temperature dependencies of σ^2 for metal (Mo, Cu, Zn) and surrounding four nearest oxygen atoms (a, c, d). Additionally σ^2 calculated for zinc and five nearest oxygens is plotted in panel (d) for comparison. Static disorder term σ^2_{st} as a function of zinc concentration x in $Cu_{1-x}Zn_xMoO_4$ is shown in panel (b). Solid lines are fits by the correlated Einstein model. Dashed lines are guide for eye.

$CuMoO_4$ phase. At the same time, at 300 K the value of the MSRD factor is close to that of α-$CuMoO_4$.

No hysteresis was found for pure $ZnMoO_4$ and $Cu_{1-x}Zn_xMoO_4$ solid solutions with x=0.50 and 0.90. In fact, small values of $\sigma^2_{\text{Mo-O}}$ and their weak temperature dependence indicate strong Mo–O bonding, which is characteristic of MoO_4 tetrahedral. The estimated Einstein frequency equals about ω_E=111±52 THz.

The MSRDs values $\sigma^2_{\text{Cu-O}}$ for the four shortest Cu–O bonds within error bars are close in all $Cu_{1-x}Zn_xMoO_4$ solid solutions and $CuMoO_4$ (Fig. 10.3.4(c)). Their Einstein frequencies are in the range of ω_E=78±39 THz.

The estimated $\sigma^2_{\text{Zn-O}}$ values for groups of the nearest four (Zn–O(4)) or five (Zn–O(5)) oxygen atoms show weak dependence on the composition (Fig. 10.3.4(d)) being close in α-$ZnMoO_4$ and $Cu_{1-x}Zn_xMoO_4$ samples with x=0.90 and 0.50. The calculated Einstein frequencies are equal to ω_E=68±10 THz when only four nearest oxygen atoms are considered and ω_E=52±4 THz when the fifth oxygen atom is included.

The composition dependence of the static disorder around metal ions in $\mathrm{Cu}_{1-x}\mathrm{Zn}_x\mathrm{MoO}_4$ solid solutions can be evaluated based on the values of σ^2_{st} for the nearest four Cu–O, Zn–O and Mo–O atom pairs (Fig. 10.3.4(b)). The extracted σ^2_{st} values for the Mo–O bonds reveal that the static distortions are much larger in the low-temperature γ-CuMoO_4 than in the low-temperature phase of $\mathrm{Cu}_{0.90}\mathrm{Zn}_{0.10}\mathrm{MoO}_4$, both having distorted octahedral coordination of Mo^{6+} ions.

Based on EXAFS data, 50% of α-$\mathrm{Cu}_{0.90}\mathrm{Zn}_{0.10}\mathrm{MoO}_4$ transforms to the low-temperature phase during cooling at $T_{1/2C}$ $\approx$125 K ($\approx$134 K from XANES (Fig. 10.2.1)) and returns to α-phase on heating at $T_{1/2H}$ $\approx$225 K (Fig. 10.3.4(a)). Both $T_{1/2C}$ and $T_{1/2H}$ values are shifted to lower temperatures in comparison to pure CuMoO_4, where $T_{1/2C}$ $\approx$143-155 K and $T_{1/2H}$ $\approx$255 K (Figs. 10.2.1 and 7.1.1). Thus, the substitution of Cu^{2+} by Zn^{2+} ions stabilizes the α-phase, which is natural for α-ZnMoO_4.

The tetrahedral coordination of Mo^{6+} ions in α-CuMoO_4, α-ZnMoO_4 and α-$\mathrm{Cu}_{1-x}\mathrm{Zn}_x\mathrm{MoO}_4$ solid solutions is responsible for small values of σ^2_{st} for Mo–O bonds in Fig. 10.3.4(b). The distorted octahedral environment of Zn^{2+} ions results in larger σ^2_{st} values for the Zn–O bonds and is almost constant for samples with $x \geq 0.5$. An increase of σ^2_{st} for the Cu–O bonds can be related to the role played by Cu^{2+} ions upon increasing x (content of Zn^{2+} ions) in $\mathrm{Cu}_{1-x}\mathrm{Zn}_x\mathrm{MoO}_4$ solid solutions. Namely, static distortions are the smallest in pure α-CuMoO_4; they increase upon a formation of $\mathrm{Cu}_{1-x}\mathrm{Zn}_x\mathrm{MoO}_4$ solid solutions with a maximum at x=0.50 and remain constant for a smaller amount of copper ($x>0.50$) when the zinc sublattice determines the structure.

So, the local environment of molybdenum ions in $\mathrm{Cu}_{1-x}\mathrm{Zn}_x\mathrm{MoO}_4$ solid solutions is significantly influenced by the substitution of copper by zinc, since the electronic configurations of the two 3d-ions differ significantly. Namely, the Zn^{2+} ion 3d subshell is filled, while the $3\mathrm{d}^9$ electronic configuration of Cu^{2+} results in the first-order Jahn-Teller distortion. Thus, CuO_6 octahedra have tetragonal deformation. The substitution modifies the electronic structure of the molybdate by increasing its band gap [138] and leads to a disappearance of thermochromic properties, which are closely related to the local structure of molybdenum ions.

The coordination of molybdenum ions in γ-$\mathrm{Cu}_{0.90}\mathrm{Zn}_{0.10}\mathrm{MoO}_4$ solid solutions changes from distorted octahedral at low-temperature to tetrahedral in α-$\mathrm{Cu}_{0.90}\mathrm{Zn}_{0.10}\mathrm{MoO}_4$ above 250 K, similar to the temperature or pressure-induced γ-to-α phase transitions in CuMoO_4 [1]. At the same time, molybdenum ions have always tetrahedral coordination in α-$\mathrm{Cu}_{1-x}\mathrm{Zn}_x\mathrm{MoO}_4$ with $x>0.10$ and α-ZnMoO_4.

10.4 Conclusions

The XAS was used to study the influence of Zn^{2+} ions on the thermochromic properties of polycrystalline $Cu_{1-x}Zn_xMoO_4$ (x=0.10, 0.50, 0.90) solid solutions. The RMC/EA simulations allowed us to perform simultaneous analysis of the EXAFS spectra at three metal absorption edges and to reconstruct temperature and composition dependence of partial RDFs $g_{\text{Cu}-\text{O}}(R)$, $g_{\text{Zn}-\text{O}}(R)$ and $g_{\text{Mo}-\text{O}}(R)$.

The XANES and EXAFS spectra analysis revealed that the substitution of Cu^{2+} by Zn^{2+} ions stabilizes the α-phase, which is natural for α-$ZnMoO_4$, and significantly affects the thermochromic phase transition temperature in the materials. The substitution modifies the electronic structure of the solid solutions due to the presence of the Jahn-Teller effect for Cu^{2+} ions with $3d^9$ electronic configuration and absence of it for Zn^{2+} ions with filled 3d subshell.

Among sampled solid solutions, only $Cu_{0.90}Zn_{0.10}MoO_4$ exhibited thermochromic phase transition between α and γ phases which can be described with a hysteresis. This result is in agreement with the previous work [137].

From the Mo K-edge XANES analysis, about 50% of the α-$Cu_{0.90}Zn_{0.10}MoO_4$ transforms to the low-temperature γ-phase at $T_{1/2C}$≈125–134 K during cooling, whereas 50% of the γ-$Cu_{0.90}Zn_{0.10}MoO_4$ transforms back to the α-phase at $T_{1/2H}$≈226 K upon heating. These temperatures are smaller than those for pure $CuMoO_4$, where $T_{1/2C}$≈143-155 K and $T_{1/2H}$≈255 K [88, 163]. Note that only α-$Cu_{0.90}Zn_{0.10}MoO_4$ phase exists at room temperature.

To understand the structural origin of the thermochromic phase transition in $Cu_{0.90}Zn_{0.10}MoO_4$, a detailed analysis of the MSRD factors for metal-oxygen bonds within the first coordination shell was performed. We found that the substitution of copper by zinc affects the local environment of Mo^{6+} ions strongly. This result can be explained by the instability of molybdenum coordination, which is tetrahedral in α-$Cu_{0.90}Zn_{0.10}MoO_4$ solid solution but changes to distorted octahedral under lattice contraction at low temperatures in γ-$Cu_{0.90}Zn_{0.10}MoO_4$. This effect is similar to the temperature or pressure-induced α-to-γ phase transitions in $CuMoO_4$ [1].

Thus, tuning the thermochromic properties of $CuMoO_4$ by doping with zinc may find applications for monitoring storage conditions of temperature-sensitive products in the low-temperature range.

Chapter 11

Summary and conclusions

In this thesis, the results of temperature and composition-dependent X-ray absorption and resonant X-ray emission spectroscopy (XAS and RXES) studies of copper molybdate ($CuMoO_4$) and its solid solutions with tungsten ($CuMo_{1-x}W_xO_4$) and zinc ($Cu_{1-x}Zn_xMoO_4$) are presented. High quality XAS and RXES experimental data were obtained during four experiments conducted at synchrotron radiation facilities.

The interpretation of EXAFS and XANES spectra is not straightforward and often requires advanced simulation tools, especially for such low symmetry materials as $CuMoO_4$ and related solid solutions. It was shown that while treatment of thermal fluctuations and static disorder in XAS is a complex task, it can be successfully addressed by the reverse Monte Carlo method with evolutionary algorithm approach (RMC/EA) simulations coupled with *ab initio* mutiple-scattering calculations. However, simple linear combination analysis of XANES data and the regularization-based method for EXAFS data analysis can also give valuable information on the local structure in the material.

Local structure probes allowed us to investigate the relationship between structural and thermochromic properties of $CuMoO_4$ in the temperature range between 10 and 973 K. The influence of composition on thermochromic properties of the solid solutions was also discussed. EXAFS spectra analysis at several absorption edges simultaneously by the RMC/EA method allowed us to obtain three-dimensional structure models of $CuMoO_4$ and its solid solutions and to analyse them in details.

Atomic coordinates obtained from RMC/EA simulations were used to reconstruct radial distribution functions (RDFs), bond angle distribution functions (BADFs) and extract structural parameters (interatomic distances, means-square relative displacements (MSRDs)) as a function of temperature. The first coordination shell of metal ions was the most sensitive to structural changes. Temperature dependences allowed us to evaluate the Einstein frequencies and effective force constants. Besides, we were able to extract the Wyckoff positions of atoms in the unit cell from the results of RMC/EA fits: they are in good agreement with the known experimental diffraction data. The sensitivity of RXES was further used to study the local structure in $CuMo_{1-x}W_xO_4$ from a tungsten perspective. The RXES method is well suited for *in situ* measurements and was used here to track the structural phase transitions in $\mathrm{CuMo}_{1-x}\mathrm{W}_x\mathrm{O}_4$ solid solutions even at low ($x < 0.10$) tungsten content.

The analysis of XAS data in the low-temperature range (10–300 K) gave valuable information on the evolution of the local structure around copper and molybdenum atoms in CuMoO_4 during the structural phase transition between α and γ phases. The Mo K-edge XANES analysis allowed us to reconstruct the hysteresis of α-to-γ phase transition in CuMoO_4. Based on these data, the γ-to-α phase transition occurs in the temperature range of 230–280 K upon heating, whereas the α-to-γ transition occurs between 120 and 200 K upon cooling. During heating, molybdenum coordination by oxygen atoms gradually changes from strongly distorted octahedral to less distorted tetrahedral. At 250 K, the sample consisted of $\sim$60% γ-phase and $\sim$40% α-phase.

The analysis of the temperature-dependent Mo K-edge EXAFS spectra using the regularization-like method and RMC/EA simulations (simultaneously at the Mo and Cu K-edges) allowed us to obtain a temperature dependence of RDFs $g_{\mathrm{Mo-O}}(R)$ and confirmed that the γ-to-α phase transition occurs gradually within a temperature range of 225–275 K. The influence of thermal effects on the local environment around molybdenum atoms in both γ and α phases is relatively weak, and the disorder is dominated by static distortions.

Further, the XAS was used to study the influence of W^{6+} and Zn^{2+} ions on the thermochromic properties of polycrystalline $\mathrm{CuMo}_{1-x}\mathrm{W}_x\mathrm{O}_4$ and $\mathrm{Cu}_{1-x}\mathrm{Zn}_x\mathrm{MoO}_4$ solid solutions.

$\mathrm{CuMo}_{0.90}\mathrm{W}_{0.10}\mathrm{O}_4$ solid solution exhibits thermochromic properties similar to pure CuMoO_4. We observed that the addition of 10 mol% of tungsten to CuMoO_4 induces local distortions and stabilizes the γ-phase, leading to an increase of the phase transition temperatures by $\sim$50–100 K.

XANES and EXAFS spectra revealed that the substitution of Cu^{2+} ions by Zn^{2+} stabilizes α-phase, which is natural for α-ZnMoO_4. The substitution modifies the electronic structure of the solid solutions due to the presence of the Jahn-Teller effect for Cu^{2+} ions with $3\mathrm{d}^9$ electronic configuration and absence of it for Zn^{2+} ions with filled 3d subshell. In $\mathrm{Cu}_{0.90}\mathrm{Zn}_{0.10}\mathrm{MoO}_4$, the phase transition hysteresis shifts to lower temperatures, while larger Zn^{2+} concentration stabilizes α-phase in all low-temperature range. The substitution of copper by zinc affects the local environment of Mo^{6+} ions strongly. This result can be explained by the instability of molybdenum coordination, which is tetrahedral in α-phase but changes to distorted octahedral under lattice contraction at low temperatures in γ-phase.

The phase transition temperatures corresponding to about 50% of the α and γ phases in the sample upon heating ($T_{1/2H}$) and cooling ($T_{1/2C}$)

obtained from XANES analysis for the solid solutions with W and Zn where $x = 0.10$ are compared to pure $CuMoO_4$ in Table 11.0.1. Tuning the thermochromic properties of $CuMoO_4$ to more desired temperature range by doping with tungsten or zinc may be the key for the material to find applications as an indicator for monitoring storage/processing conditions of temperature-sensitive products.

Table 11.0.1: The α-to-γ and γ-to-α phase transition temperatures during cooling ($T_{1/2C}$) and heating ($T_{1/2H}$) obtained from the Mo K-edge XANES analysis for $Cu_{0.90}Zn_{0.10}MoO_4$, $CuMoO_4$ and $CuMo_{0.90}W_{0.10}O_4$. The difference between the two temperatures ΔT also is shown.

	$Cu_{0.90}Zn_{0.10}MoO_4$ [89]	$CuMoO_4$ [163]	$CuMo_{0.90}W_{0.10}MoO_4$ [84]
$T_{1/2C}$	~134 K	~ 143 K	~ 190 K
$T_{1/2H}$	~226 K	~ 255 K	~ 340 K
ΔT	~ 92 K	~ 112 K	~ 150 K

The thermochromic properties of $CuMoO_4$ in the high-temperature range (300-973 K) are not related to any phase transition. It was found that the local environment of copper atoms is more affected during heating than that of molybdenum atoms. It was shown that the thermal disorder affects strongly not only the Cu K-edge EXAFS but also XANES region.

The RMC/EA simulations allowed us to obtain 3D structure models taking into account the thermal disorder effect. At the same time, they are able to reproduce the average (Wyckoff) positions of atoms inside the unit cell in agreement with known diffraction data. The structural models obtained by the RMC/EA simulations were used to calculate the configuration-averaged Cu K-edge XANES using *ab initio* full-multiple-scattering theory. The calculated XANES spectra agree with the experimental data and qualitatively reproduce the main temperature-dependent XANES features. While the MoO_4 tetrahedra behave mostly as the rigid units, a reduction of the correlation in atomic motion between copper and axial oxygen atoms occurs upon temperature increase. This dynamic effect is the main cause of the temperature-induced changes in the $O^{2-} \rightarrow Cu^{2+}$ charge transfer processes and, thus, affects the thermochromic properties of α-$CuMoO_4$ upon heating above room temperature.

A variation of the experimental EXAFS spectra at the metal absorption edges in $CuMo_{1-x}W_xO_4$ strongly correlates with Mo:W ratio. It was shown that multiple-scattering effects play an important role in the analysis of $CuMo_{1-x}W_xO_4$ solid solutions and should be taken into account to describe the contributions from the outer coordination shells accurately.

At room temperature, $CuMo_{1-x}W_xO_4$ solid solutions with tungsten content above x~0.15 have the wolframite-type $CuMoO_4$-III phase isostructural to $CuWO_4$. Strong structural relaxations accompany the formation of solid solutions. The ability of molybdenum atoms to adopt a locally distorted environment allows them to adjust to the solid solution structure determined by tungsten-related sublattice.

The role of tungsten ions was studied in more detail using RXES at the W L_3-edge (2p3d RXES), which allowed us to trace the crystal field induced splitting of the 5d states of tungsten. Moreover, this information was extracted from the analysis of RXES plane using two different approaches: the high-energy resolution fluorescence detected X-ray absorption near-edge structure (HERFD-XANES) and the high energy resolution off-resonant X-ray emission spectra excited below and above the resonance conditions. The analysis of the experimentally obtained RXES planes shows a clear advantage over conventional XANES due to revealing spectral features with much higher resolution.

It was found that tungsten ions in $CuMo_{1-x}W_xO_4$ solid solutions always have octahedral coordination for samples with $x > 0.15$, whereas their coordination changes from tetrahedral to octahedral upon cooling for smaller tungsten content. Nevertheless, some amount of tungsten ions co-exists in the octahedral environment at 300 K for solid solutions with $x < 0.15$. The obtained results correlate well with the thermochromic properties of these materials, namely, colour change from greenish to brown upon cooling or increasing tungsten concentration.

The electronic structure of $CuMo_{1-x}W_xO_4$ solid solutions governs their thermochromic properties, which are related to the variation of the transmission window in optical spectra [10,11]. A change in the tungsten local coordination from tetrahedral to octahedral affects the band gap, which is determined by the oxygen-to-metal charge transfer [10]. The band gap is smaller in the case of octahedral coordination of tungsten [11], i.e., at higher tungsten content or lower temperature.

Main conclusions:

- XAS and RXES techniques are well suited for local structure studies in low-symmetry materials such as $CuMoO_4$ and its solid solutions.
- Thermal disorder in $CuMoO_4$ at high temperatures affects stronger the local environment of copper atoms than that of molybdenum.
- The thermochromic phase transition of $CuMoO_4$ at low temperatures is related to the change of molybdenum coordination between distorted octahedral and tetrahedral.
- An addition of tungsten and zinc ions to $CuMoO_4$ modifies its thermochromic properties.

Chapter 12

Main theses

1. The hysteresis of the thermochromic phase transition between α and γ phases in $CuMoO_4$, occurring in the temperature range of 120–280 K and related to the gradual transformation of strongly distorted octahedral molybdenum coordination by oxygen atoms to less distorted tetrahedral, can be successfully probed by X-ray absorption spectroscopy at the Mo K-edge.
   *(Published in **[A6, A7]**.)*
2. In pure $CuMoO_4$ at temperatures above 300 K, the local environment of Cu atoms is more affected by the thermal disorder than that of Mo atoms. While the MoO_4 tetrahedra behave mostly as rigid units, a reduction of the correlation in atomic motion between copper and axial oxygen atoms occurs upon heating. This dynamic effect is the main cause of the temperature-induced changes in the $O^{2-}\rightarrow Cu^{2+}$ charge transfer processes and, thus, is the origin of the thermochromic properties of α-$CuMoO_4$.
   *(Published in **[A5]**.)*
3. *In situ* high energy resolution fluorescence detected X-ray absorption near-edge structure (HERFD-XANES) and the high energy resolution off-resonant X-ray emission spectra excited below and above resonance conditions at the W L_3-edge allow one to obtain the crystal field splitting parameter for the 5d(W)-states and, thus, to follow the coordination of tungsten atoms in $CuMo_{1-x}W_xO_4$ solid solutions.
   *(Published in **[A2]**.)*
4. In $CuMo_{1-x}W_xO_4$ ($x \leq 0.10$) solid solutions, the addition of W^{6+} ions induces local structural distortions and stabilizes γ-phase that leads to a shift of the phase transition hysteresis to higher temperatures. The addition of Zn^{2+} ions, in turn, stabilizes α-phase and shifts the phase transition hysteresis of $Cu_{1-x}Zn_xMoO_4$ ($x \leq 0.10$) to lower temperatures. Both W^{6+} and Zn^{2+} ion additions thus modify the thermochromic behaviour of the material.
   *(Published in **[A1, A3]**.)*

Author's publication list

Publications directly related to the dissertation:

A1. **I. Pudza**, A. Anspoks, A. Cintins, A. Kalinko, E. Welter, A. Kuzmin, The influence of Zn^{2+} ions on the local structure and thermochromic properties of $Cu_{1-x}Zn_xMoO_4$ solid solutions, *Materials Today Communications* 28 (**2021**) 102607, DOI:10.1016/j.mtcomm.2021.102607.

A2. **I. Pudza**, A. Kalinko, A. Cintins, A. Kuzmin, Study of the thermochromic phase transition in $CuMo_{1-x}W_xO_4$ solid solutions at the W L_3-edge by resonant X-ray emission spectroscopy, *Acta Mater.* 205 (**2021**) 116581, DOI: 10.1016/j.actamat.2020.116581.

A3. **I. Jonane**, A. Cintins, A. Kalinko, R. Chernikov, A. Kuzmin, Low temperature X-ray absorption spectroscopy study of $CuMoO_4$ and $CuMo_{0.90}W_{0.10}O_4$ using reverse Monte-Carlo method, *Rad. Phys. Chem.* 175 (**2020**) 108112, DOI: 10.1016/j.radphyschem.2019.108411.

A4. A. Kuzmin, J. Timoshenko, A. Kalinko, **I. Jonane**, A. Anspoks, Treatment of disorder effects in X-ray absorption spectra beyond the conventional approach, *Rad. Phys. Chem.* 175 (**2020**) 108072, DOI: 10.1016/j.radphyschem.2018.12.032.

A5. **I. Jonane**, A. Anspoks, G. Aquilanti, A. Kuzmin, High-temperature X-ray absorption spectroscopy study of thermochromic copper molybdate, *Acta Mater.* 179 (**2019**) 26-35, DOI: 10.1016/j.actamat.2019.06.034.

A6. **I. Jonane**, A. Cintins, A. Kalinko, R. Chernikov, A. Kuzmin, Probing the thermochromic phase transition in $CuMoO_4$ by EXAFS spectroscopy, *Phys. Status Solidi B* 255 (**2018**) 1800074:1-5, DOI: 10.1002/pssb.201800074.

A7. **I. Jonane**, A. Cintins, A. Kalinko, R. Chernikov, A. Kuzmin, X-ray absorption near edge spectroscopy of thermochromic phase transition in $CuMoO_4$, *Low Temp. Phys.* 44 (**2018**) 568-572, DOI: 10.1063/1.5034155.

A8. **I. Jonane**, A. Kuzmin, and A. Anspoks, Advanced approach to the local structure reconstruction and theory validation on the example of the W L_3-edge extended X-ray absorption fine structure of tungsten, *Modelling Simul. Mater. Sci. Eng.* 26 (**2018**) 025004, DOI: 10.1088/1361-651X/aa9bab.

Publications indirectly related to the dissertation:

B1. D. Bocharov, A. Chesnokov, G. Chikvaidze, J. Gabrusenoks, R. Ignatans, R. Kalendarev, M. Krack, K. Kundzins, A. Kuzmin, N. Mironova-Ulmane, **I. Pudza**, L. Puust, I. Sildos, E. Vasil'chenko, M. Zubkins, J. Purans, A comprehensive study of structure and properties of nanocrystalline zinc peroxide, *J. Phys. Chem. Solids* 160 (**2022**) 110318, DOI: 10.1016/j.jpcs.2021.110318.

B2. D. Bocharov, **I. Pudza**, K. Klementiev, M. Krack, A. Kuzmin, Study of high-temperature behaviour of ZnO by ab initio molecular dynamics simulations and X-ray absorption spectroscopy, *Materials* 14 (**2021**) 5206. DOI: 10.3390/ma14185206.

B3. J. Purans, A. P. Menushenkov, S. P. Besedin, A. A. Ivanov, V. S. Minkov, **I. Pudza**, A. Kuzmin, K. V. Klementiev, S. Pascarelli, O. Mathon, A. D. Rosa, T. Irifune, M. I. Eremets, Local electronic structure rearrangements and strong anharmonicity in YH_3 under pressures up to 180 GPa, *Nat. Commun.* 12 (**2021**) 1765, DOI: 10.1038/s41467-021-21991-x.

B4. F. C. Correia, J. M. Ribeiro, A. Kuzmin, **I. Pudza**, A. Kalinko, E. Welter, A. Mendes, J. Rodrigues, N. Ben Sedrine, T. Monteiro, M. R. Correia, C. J. Tavares, The role of Ga and Bi doping on the local structure of transparent zinc oxide thin films, *J. Alloys Compd.* 870 (**2021**) 159489, DOI:10.1016/j.jallcom.2021.159489.

B5. B. Polyakov, E. Butanovs, A. Ogurcovs, S. Vlassov, M. Zubkins, **I. Jonane**, A. Cintins, A. Kalinko, A. Kuzmin, J. Purans, Understanding the conversion process of magnetron-deposited thin films of amorphous ReO_x to crystalline ReO_3 upon thermal annealing, *Cryst. Growth Des.* 20 (**2020**) 6147-6156, DOI:10.1021/acs.cgd.0c00848.

B6. J.M. Ribeiro, F.C. Correia, A. Kuzmin, **I. Jonane**, M. Kong, A.R. Goni, J.S. Reparaz, A. Kalinko, E. Welter, C.J. Tavares, Influence of Nb-doping on the local structure and thermoelectric properties of transparent TiO_2:Nb thin films, *J. Alloys Compd.* 838 (**2020**) 155561, DOI:10.1016/j.jallcom.2020.155561.

B7. L. Nataf, F. Baudelet, A. Polian, **I. Jonane**, A. Anspoks, A. Kuzmin, T. Irifune, Recent progress in high-pressure X-ray absorption spectroscopy studies at the ODE beamline, *High Pressure Res.* 40 (**2020**) 82-87, DOI: 10.1080/08957959.2019.1700979.

B8. T. Schenk, A. Anspoks, **I. Jonane**, R. Ignatans, B.S. Johnson, J.L. Jones, M. Tallarida, C. Marini, L. Simonelli, P. Hönicke, C. Richter, T. Mikolajick, U. Schroeder, Local structural investigation of hafnia-zirconia polymorphs in powders and thin films by X-ray absorption spectroscopy, *Acta Mater.* 180 (**2019**) 158-169, DOI:10.1016/j.actamat.2019.09.003.

B9. **I. Jonane**, A. Anspoks, L. Nataf, F. Baudelet, T. Irifune, A. Kuzmin, Pressure-induced structural changes in α-MoO_3 probed by X-ray absorption spectroscopy, *IOP Conf. Ser.: Mater. Sci. Eng.* 503 (**2019**) 012018, DOI: 10.1088/1757-899X/503/1/012018.

B10. **I. Jonane**, J.Timoshenko, and A. Kuzmin, Atomistic simulations of the Fe K-edge EXAFS in FeF_3 using molecular dynamics and reverse Monte Carlo methods, *Phys. Scr.* 91 (**2016**) 104001, DOI: 10.1088/0031-8949/91/10/104001.

B11. **I. Jonane**, K. Lazdins, J. Timoshenko, A. Kuzmin, J. Purans, P. Vladimirov, T. Gräning, J. Hoffmann, Temperature-dependent EXAFS study of the local structure and lattice dynamics in cubic Y_2O_3, *J. Synchrotron Rad.* (**2016**) 510-518, DOI: 10.1107/S1600577516001181.

B12. **I. Jonane**, J. Timoshenko, A. Kuzmin, EXAFS study of the local structure of crystalline and nanocrystalline Y_2O_3 using evolutionary algorithm method, *IOP Conf. Ser.: Mater. Sci. Eng.* 77 (**2015**) 012030:1-5, DOI: 10.1088/1757-899X/77/1/012030.

B13. J. Timoshenko, A. Anspoks, A. Kalinko, **I. Jonane**, A. Kuzmin, Local structure of multiferroic $MnWO_4$ and $Mn_{0.7}Co_{0.3}WO_4$ revealed by the evolutionary algorithm, *Ferroelectrics* 483 (**2015**) 68-74, DOI: 0.1080/00150193.2015.1058687.

Participation in conferences

International conferences and workshops

1. 14.08.-22.08.2021. – 25th Congress of International Union of Crystallography IUCr25 (online)
   oral presentation "*Treatment of disorder effects in X-ray absorption spectra by reverse Monte Carlo simulations: $CuMoO_4$ case*" (I. Pudza, A. Kuzmin).
2. 12.07.-13.07.2021. – International Conference on X-Ray Absorption Fine Structure - XAFS 2021 Virtual (online),
   oral presentation "*XAS and RXES studies of phase transitions in $CuMo_{1-x}W_xO_4$ solid solutions*" (I. Pudza, A. Kalinko, A. Cintins, A. Kuzmin).
3. 05.07.-07.07.2021. – YOUNG MULTIS - Multiscale Phenomena in Condensed Matter Online conference for young researchers (online),
   oral presentation "*Local structure studies of multifunctional $CuMoO_4$ and $CuWO_4$ solid solutions*" (I. Pudza, A. Kalinko, A. Cintins, A. Kuzmin).
4. 28.04.2021. – Bilateral workshop of Taiwan and the Baltic States Research Center on Physics (online),
   oral presentation "*Resonant X-ray emission spectroscopy to reveal coordination of W ions in $CuMo_{1-x}W_xO_4$ thermochromic materials*" (I. Pudza).
5. 25.01.-29.01.2021. – DESY Photon Science Users' Meeting 2021 (online),
   poster presentation "*Resonant X-ray emission spectroscopy of the thermochromic phase transition in $CuMo_{1-x}W_xO_4$ solid solutions*" (I. Pudza, A. Kalinko, A. Cintins, A. Kuzmin).
6. 22.01.2021. – DESY Photon Science Users' Meeting 2021 - Satellite meeting "X-Ray Absorption Spectroscopy at P64/65" (online),
   oral presentation "*Thermochromic phase transition in $CuMo_{1-x}W_xO_4$ solid solutions probed by Resonant X-ray emission spectroscopy at the W L_3-edge*" (I. Pudza, A. Kalinko, A. Cintins, A. Kuzmin).
7. 16.09.-20.09.2019. – EMRS Fall Meeting 2019 (Warsaw, Poland),
   poster presentation "*Temperature and doping induced evolution of the local structure of thermochromic copper molybdate*" (I. Jonane, A. Anspoks, A. Cintins, G. Aquilanti, A. Kalinko, R. Chernikov, A. Kuzmin).
8. 11.04.-12.04.2019. – 15th International Young Scientist conference "Developments in Optics and Communications 2018" (Riga, Latvia),
   poster presentation "*Structural investigations of $CuMo_{1-x}W_xO_4$ solid solution*" (I. Jonane, A. Cintins, A. Anspoks, G. Aquilanti, A. Kalinko, G. Aquilanti, A. Kuzmin).
9. 02.11.-05.11.2018. – 12th International Scientific Conference "Functional Materials and NanoTechnology" (Riga, Latvia),
   oral presentation "*Functional and structural properties of copper molybdate*" (I. Jonane, A. Anspoks, A. Cintins, G. Aquilanti, A. Kalinko, G. Aquilanti, R. Chernikov, A. Kuzmin) and
   poster presentation "*Pressure-induced structural changes in α-MoO_3 probed by X-ray*

absorption spectroscopy" (I. Jonane, A. Anspoks, L. Nataf, F. Baudelet, T. Irifune, A. Kuzmin) - achieved poster prize.

10. 20.09.-22.09.2018. – conference "The First 30 Years of Reverse Monte Carlo Modelling" (Budapest, Hungary),
oral presentation "*Treatment of disorder in XANES by RMC simulations*" (I. Jonane, A. Kuzmin).
11. 22.07.-27.07.2018. – 17th International Conference on X-Ray Absorption Fine Structure (Krakow, Poland),
oral presentation "*Low temperature X-ray absorption spectroscopy study of* $CuMoO_4$ *and* $CuMo_{0.90}W_{0.10}O_4$ *using reverse Monte-Carlo method*" (I. Jonane, A. Cintins, A. Kalinko, R. Chernikov, A. Kuzmin).
12. 05.04.-06.04.2018. – 14th International Young Scientist conference "Developments in Optics and Communications 2018" (Riga, Latvia),
oral presentation "*Structural investigations of thermochromic phase transition in copper molybdate*" (I. Jonane, A. Cintins, A. Kalinko, R. Chernikov, A. Kuzmin).
13. 12.03.-14.03.2018. – COST TO-BE (Towards oxide-based electronics (MP1308)) Spring Meeting (Sant Feliu de Guixols, Spain),
poster presentation "*X-ray absorption spectroscopy for structural analysis of* $CuMoO_4$" (I. Jonane, A. Cintins, A. Anspoks, A. Kuzmin).
14. 11.09.-13.09.2017. – COST TO-BE (Towards oxide-based electronics (MP1308)) Fall Meeting (Riga, Latvia),
poster presentation "*Temperature-dependent X-ray absorption spectroscopy study of* $CuMoO_4$" (I. Jonane, A. Kuzmin, A. Anspoks) - achieved poster prize.
15. 16.05.-19.05.2017. – 16. International conference of Plasma-Facing Materials and Components for Fusion Applications (Düsseldorf, Germany),
poster presentation "*X-ray absorption spectroscopy study of yttria nanoparticles using simulation-based methods*" (I. Jonane, A. Kuzmin, A. Anspoks, A. Cintins, V.E. Serga, J. Purans) and
poster presentation "*Advanced approach to the local structure reconstruction and theory validation on example of the W* L_3*-edge EXAFS of tungsten*" (I. Jonane, A. Kuzmin, A. Anspoks).
16. 24.04.-27.04.2017. – 11th International Scientific Conference "Functional Materials and NanoTechnology" (Tartu, Estonia),
poster presentation "*Temperature-dependent EXAFS study of the local structure of copper molybdate using reverse Monte-Carlo method*" (I. Jonane, A. Kuzmin, A. Anspoks).
17. 06.04.-07.04.2017. – 13th International Young Scientist conference "Developments in Optics and Communications 2017" (Riga, Latvia),
oral presentation "*Relationship between local structure and optical properties of copper molybdate*" (I. Jonane, A. Anspoks, A. Kuzmin).
18. 10.06.-12.06.2015. – EURONANOFORUM 2015 (Riga, Latvia),
poster presentation "*Static disorder in nanocrystalline yttria probed by X-ray absorption spectroscopy*" (I. Jonane, J. Timoshenko, A. Kuzmin).
19. 08.04.-10.04.2015. – 11th International Young Scientist conference "Developments in Optics and Communications 2015" (Riga, Latvia),
oral presentation "*Temperature dependence of the local structure of* Y_2O_3 *from EXAFS analysis using evolutionary algorithm method*" (I. Jonane, J. Timoshenko, A. Kuzmin)
20. 29.09.-01.10.2014. – 9th International Scientific Conference "Functional Materials and

NanoTechnology" (Riga, Latvia),
poster presentation "*EXAFS study of the local structure of crystalline and nanocrystalline* Y_2O_3 *using evolutionary algorithm method*" (I. Jonane, J. Timoshenko, A. Kuzmin).

Local conferences

1. 23.02.-25.02.2021. – 37. annual ISSP UL scientific conference (online),
oral presentation "*Resonant X-ray emission spectroscopy of* $CuMo_{1-x}W_xO_4$ *solid solutions*" (I. Pudza, A. Kalinko, A. Cintins, A. Kuzmin).
2. 13.08.2020. – The 78th conference of the University of Latvia (Riga),
oral presentation "*Correlation between the local structure and functional properties of molybdates*" (I. Pudza, A. Cintins, A. Anspoks, A. Kalinko, A. Kuzmin).
3. 11.02.-13.02.2020. – 36. annual ISSP UL scientific conference (Riga),
oral presentation "*The influence of zinc ions on the structure and thermochromic properties of* $Cu_{1-x}Zn_xMoO_4$ *solid solutions*" (I. Jonane, A. Cintins, A. Anspoks, A. Kalinko, A. Kuzmin).
4. 29.03.2019. – The 77th conference of the University of Latvia (Riga),
oral presentation "*Structural studies of functional materials using synchrotron radiation*" (I. Jonane, A. Cintins, A. Anspoks, A. Kalinko, R. Chernikov, G. Aquilant, L. Nataf, F. Baudelet, T. Irifune, A. Kuzmin).
5. 20.02.-22.02.2019. – 35. annual ISSP UL scientific conference (Riga),
oral presentation "*Resonant X-ray emission spectroscopy study of tungstates*" (I. Jonane, A. Kalinko, A. Kuzmin).
6. 06.04.2018. – The 76th conference of the University of Latvia (Riga),
oral presentation "*Investigation of the local structure and functional properties of copper molybdate*" (I. Jonane, A. Kuzmin).
7. 20.02.-22.02.2018. – 34. annual ISSP UL scientific conference (Riga),
oral presentation "*Study of the local structure and thermochromic properties in* $CuMoO_4$ *and* $CuMo_{1-x}W_xO_4$ *using X-ray absorption spectroscopy*" (I. Jonane, A. Cintins, A. Anspoks, A. Kuzmin).
8. 22.02.-24.02.2017. – 33. annual ISSP UL scientific conference (Riga),
oral presentation "*Study of nanocrystalline compounds using reverse Monte-Carlo method*" (I. Jonane, A. Kuzmin).
9. 17.02.–19.02.2016. – 32. annual ISSP UL scientific conference (Riga),
oral presentation "*Temperature dependence of the local structure of scandium fluoride*" (I. Jonane, J. Timoshenko, A. Kuzmin, D. Bocharov, M. Krack).
10. 24.02. – 26.02.2015. – 31. annual ISSP UL scientific conference (Riga),
oral presentation "*Modeling and analysis of* FeF_3 *structure using evolutionary algorithm*" (I. Jonane, J. Timoshenko).
11. 11.04.2014. 54th international scientific conference of University of Daugavpils (Daugavpils),
oral presentation "*Analysis of the local structure of solid materials using EXAFS spectroscopy*" (I. Jonane, J. Timoshenko).
12. 19.02. – 21.02.2014. – 30. annual ISSP UL scientific conference (Riga),
poster presentation "*Analysis of* Y_2O_3 *structure using EXAFS-RMC method*" (I. Jonane, J. Timoshenko).

Participation in international schools

1. 13.09.-17.09.2021. – 1st on-line School on Synchrotron Radiation "Gilberto Vlaic": Fundamentals, Methods and Application (online).
2. 05.11.-09.11.2019. – BESSY II visit within CALIPSOplus Twinning Programme - visit of HE-SGM beamline dedicated to NEXAFS/XPS spectroscopy experiments (Berlin, Germany).
3. 16.06.-21.06.2019. – ESRF synchrotron school "High-pressure techniques at the ESRF-EBS" (Grenoble, France), poster presentation "*High pressure effect on the local structure of* α*-*MoO_3 *and* α*-*H_xMoO_3".
4. 30.03.-05.04.2019. – MATRAC 2 School "Application of Neutrons and Synchrotron Radiation in Materials Science with special focus on Fundamental Aspects of Materials" (Munich, Germany), poster presentation "*Pressure-dependent X-ray absorption spectroscopy study of* α*-*MoO_3 *and* α*-*H_xMoO_3".
5. 15.03.-17.03.2018. – MP1308 COST TO-BE Action School "Technologies for oxide electronics" (Sant Feliu de Guixols, Spain).
6. 19.08.-26.08.2017. – RACIRI summer school "Grand Challenges and Opportunities with the Best X-ray and Neutron Sources" (Ronneby, Sweden), poster presentation "*Advanced analysis of X-ray absorption spectra: the case of tungsten*".
7. 01.03.-03.03.2017. – DESY research course "Nanoscience at Modern X-ray Sources" (Hamburg, Germany), poster presentation "*X-ray absorption spectroscopy study of nanocrystalline yttria*" - achieved poster prize.
8. 18.07.-22.07.2016. – 1st NFFA Europe Summer School "Nanoscience Foundries and Fine Analysis" (Barcelona, Spain), poster presentation "*RMC analysis of the Y K-edge EXAFS spectra in micro- and nano-crystalline* Y_2O_3".
9. 27.06.-06.07.2014. – Summer school at Merseburg Technical University "Basic Experiments in Sensor Technology and Laser Physics" (Merseburg, Germany).

Participation in synchrotron experiments [1]

1. 02.12.-06.12.2021. – XAS measurements within project "*X-ray absorption spectroscopy of medium-entropy alloys*" at PETRA III.
2. 26.11.-01.12.2021. – XAS measurements within project "*The colouration of tungstates by proton intercalation: the effect on the local structure*" at PETRA III.
3. 01.10.-04.10.2021. – XAS measurements within project "*Local structure instabilities and lattice dynamics in 2D layered materials upon charge-density-wave transitions*" at PETRA III.
4. 04.05.-10.05.2021. & 27.09-29.09.2021. – RXES measurements within project "*Temperature-dependent HERFD-XANES spectroscopy study of thermochromic effects in* $CuMo_{1-x}W_xO_4$ *at the Mo K-edge*" at PETRA III (remotely & on-site).
5. 29.10.-02.11.2020. – XAS measurements within project "*Local structure and disorder in thermoelectric ZnO:Sb thin films*" at PETRA III.
6. 29.09.-05.10.2020. – RXES measurements within project "*Resonant X-ray emission spectroscopy of polaronic effects in nanocrystalline tungstates*" at PETRA III.
7. 10.09.-14.09.2020. – XAS measurements within project "*Unravelling the structure of rhenium oxide thin films*" at PETRA III.
8. 25.11.-29.11.2019. – XAS measurements within project "***The influence of zinc ions on the thermochromic properties of*** $Cu_{1-x}Zn_xMoO_4$ ***solid solutions***" at PETRA III.
9. 25.06.-01.07.2019. – XAS measurements within project "*Impact of pressure on the atomic structure and lattice dynamics in* ReS_2 *and* $ReSe_2$" at SOLEIL.
10. 23.05.-28.05.2019. – RXES measurements within project "***Resonant X-ray emission spectroscopy of mixed*** $CuMo_{1-x}W_xO_4$ ***thermochromic materials***" at PETRA III.
11. 13.12.-17.12.2018. – XAS measurements within project "*X-ray absorption spectroscopy of oxide thermoelectric materials*" at PETRA III.
12. 13.05.-18.06.2018. – XAS measurements within project "*X-ray absorption spectroscopy of lattice dynamics in 2D layered materials*" at PETRA III.
13. 24.01.-29.01.2018. – XAS measurements within project "*Impact of pressure and electron doping on the lattice distortion in* α-MoO_3" at SOLEIL.
14. 22.06.-27.06.2017. – XAS measurements within project "*XAS Local Atomic Structure Studies of Ferroelectric* HfO_2" at PETRA III.
15. 03.11.-08.11.2016. – XAS measurements within project "***Low temperature thermochromic phase transition in*** $CuMo_{1-x}W_xO_4$ ***solid solutions***" at PETRA III.
16. 26.05.-30.05.2016. – XAS measurements within project "*EXAFS study of negative thermal expansion in nanocrystalline CuO*" at PETRA III.
17. 07.12.-13.12.2015. – XAS measurements within project "***Study of the thermochromic phase transition in*** $CuMoO_4$ ***and mixed*** $CuMo_{1-x}W_xO_4$" at ELETTRA.

---

[1] PETRA III synchrotron is located in Hamburg, Germany, SOLEIL synchrotron – in Paris, France, ELETTRA synchrotron – in Trieste, Italy.

References

[1] M. Wiesmann, H. Ehrenberg, G. Miehe, T. Peun, H. Weitzel, H. Fuess, $p-T$ phase diagram of $CuMoO_4$, J. Solid State Chem. 132 (1997) 88–97. `doi:10.1006/jssc.1997.7413`.

[2] M. Gaudon, P. Deniard, A. Demourgues, A. E. Thiry, C. Carbonera, A. Le Nestour, A. Largeteau, J. F. Létard, S. Jobic, Unprecedented "one-finger-push"-induced phase transition with a drastic color change in an inorganic material, Adv. Mater. 19 (2007) 3517–3519. `doi:10.1002/adma.200700905`.

[3] M. Gaudon, C. Riml, A. Turpain, C. Labrugere, M. H. Delville, Investigation of the chromic phase transition of $CuMo_{0.9}W_{0.1}O_4$ induced by surface protonation, Chem. Mater. 22 (2010) 5905–5911. `doi:10.1021/cm101824d`.

[4] L. Robertson, N. Penin, V. Blanco-Gutierrez, D. Sheptyakov, A. Demourgues, M. Gaudon, $CuMo_{0.9}W_{0.1}O_4$ phase transition with thermochromic, piezochromic, and thermosalient effects, Journal of Materials Chemistry C 3 (2015) 2918–2924. `doi:10.1039/C4TC02463J`.

[5] N. Joseph, J. Varghese, M. Teirikangas, H. Jantunen, A temperature-responsive copper molybdate polymorph mixture near to water boiling point by a simple cryogenic quenching route, ACS Appl. Mater. Interfaces 12 (2020) 1046–1053. `doi:10.1021/acsami.9b17300`.

[6] J. C. Hill, Y. Ping, G. A. Galli, K.-S. Choi, Synthesis, photoelectrochemical properties, and first principles study of n-type $CuW_{1-x}Mo_xO_4$ electrodes showing enhanced visible light absorption, Energy Environ. Sci. 6 (2013) 2440–2446. `doi:10.1039/C3EE40827B`.

[7] D. Tanasic, A. Rathner, J. P. Kollender, P. Rathner, N. Müller, K. C. Zelenka, A. W. Hassel, C. C. Mardare, Silver-, calcium-, and copper molybdate compounds: Preparation, antibacterial activity, and mechanisms, Biointerphases 12 (2017) 05G607. `doi:10.1116/1.4996434`.

[8] Q. Liang, Y. Guo, N. Zhang, Q. Qian, Y. Hu, J. Hu, Z. Li, Z. Zou, Improved water-splitting performances of $CuW_{1-x}Mo_xO_4$ photoanodes synthesized by spray pyrolysis, Science China Materials 61 (2018) 1297–1304. `doi:10.1007/s40843-018-9287-5`.

[9] W. Tan, J. Luan, Investigation into the synthesis conditions of $CuMoO_4$ by an in situ method and its photocatalytic properties under visible light irradiation, RSC Advances 10 (2020) 9745–9759. `doi:10.1039/D0RA00496K`.

[10] M. Gaudon, C. Carbonera, A. E. Thiry, A. Demourgues, P. Deniard, C. Payen, J. F. Létard, S. Jobic, Adaptable thermochromism in the $CuMo_{1-x}W_xO_4$ series ($0 \leq x < 0.1$): A behavior related to a first-order phase transition with a transition temperature depending on x, Inorg. Chem. 46 (2007) 10200–10207. `doi:10.1021/ic701263c`.

[11] X. Wu, C. Fu, J. Cao, C. Gu, W. Liu, Effect of W doping on phase transition behavior and dielectric relaxation of $CuMoO_4$ obtained by a modified sol-gel method, Mater. Res. Express 7 (2020) 016309. `doi:10.1088/2053-1591/ab6546`.

[12] A. Seeboth, D. Lötzsch, Thermochromic and thermotropic materials, CRC Press, 2013.

[13] G. Steiner, R. Salzer, W. Reichelt, Temperature dependence of the optical properties of $CuMoO_4$, Fresenius J. Anal. Chem. 370 (2001) 731–734. `doi:10.1007/s002160000630`.

[14] A.-E. Thiry, M. Gaudon, C. Payen, N. Daro, J.-F. Létard, S. Gorsse, P. Deniard, X. Rocquefelte, A. Demourgues, M.-H. Whangbo, S. Jobic, On the cyclability of the

thermochromism in $CuMoO_4$ and its tungsten derivatives $CuMo_{1-x}W_xO_4$ (x <0.12), Chem. Mater. 20 (2008) 2075. `doi:10.1021/cm703600g`.

[15] I. Yanase, T. Mizuno, H. Kobayashi, Structural phase transition and thermochromic behavior of synthesized W-substituted $CuMoO_4$, Ceramics International 39 (2013) 2059–2064. `doi:10.1016/j.ceramint.2012.08.059`.

[16] H. Fricke, The K-characteristic absorption frequencies for the chemical elements magnesium to chromium, Physical Review 16 (1920) 202. `doi:0.1103/PhysRev.16.202`.

[17] J. Timoshenko, A. Kuzmin, J. Purans, EXAFS study of hydrogen intercalation into ReO_3 using the evolutionary algorithm, Journal of Physics: Condensed Matter 26 (2014) 055401. `doi:10.1088/0953-8984/26/5/055401`.

[18] Y. Joly, X-ray absorption near-edge structure calculations beyond the muffin-tin approximation, Physical Review B 63 (2001) 125120. `doi:10.1103/PhysRevB.63.125120`.

[19] O. Bunău, Y. Joly, Self-consistent aspects of x-ray absorption calculations, Journal of Physics: Condensed Matter 21 (2009) 345501. `doi:10.1088/0953-8984/21/34/345501`.

[20] A. Kuzmin, Application of cluster computing in materials science, Latvian Journal of Physics and Technical Sciences (2006) 7–14.

[21] M. Newville, Fundamentals of XAFS, Reviews in Mineralogy and Geochemistry 78 (2014) 33–74.

[22] A. C. Thompson, D. Vaughan, et al., X-ray data booklet, Vol. 8, Lawrence Berkeley National Laboratory, University of California Berkeley, CA, 2001.

[23] A. Kuzmin, J. Timoshenko, A. Kalinko, I. Jonane, A. Anspoks, Treatment of disorder effects in X-ray absorption spectra beyond the conventional approach, Radiation Physics and Chemistry`doi:10.1016/j.radphyschem.2018.12.032`.

[24] F. De Groot, A. Kotani, Core level spectroscopy of solids, CRC press, 2008.

[25] J. J. Rehr, R. C. Albers, Theoretical approaches to x-ray absorption fine structure, Reviews of modern physics 72 (2000) 621. `doi:10.1103/RevModPhys.72.621`.

[26] E. P. Jahrman, W. M. Holden, A. S. Ditter, D. R. Mortensen, G. T. Seidler, T. T. Fister, S. A. Kozimor, L. F. Piper, J. Rana, N. C. Hyatt, et al., An improved laboratory-based x-ray absorption fine structure and x-ray emission spectrometer for analytical applications in materials chemistry research, Review of Scientific Instruments 90 (2019) 024106. `doi:10.1063/1.5049383`.

[27] D. Mills, J. Helliwell, Å. Kvick, T. Ohta, I. Robinson, A. Authier, Report of the Working Group on Synchrotron Radiation Nomenclature–brightness, spectral brightness or brilliance?, Journal of synchrotron radiation 12 (2005) 385–385. `doi:10.1107/S090904950500796X`.

[28] P. Pfalzer, J.-P. Urbach, M. Klemm, S. Horn, M. L. denBoer, A. I. Frenkel, J. Kirkland, Elimination of self-absorption in fluorescence hard-x-ray absorption spectra, Physical Review B 60 (1999) 9335. `doi:10.1103/PhysRevB.60.9335`.

[29] B. Ravel, M. Newville, ATHENA, ARTEMIS, HEPHAESTUS: data analysis for X-ray absorption spectroscopy using IFEFFIT, J. Synchrotron Radiat. 12 (2005) 537–541. `doi:10.1107/S0909049505012719`.

[30] G. Bunker, Introduction to XAFS: a practical guide to X-ray absorption fine structure spectroscopy, Cambridge University Press, 2010.

[31] A. Kuzmin, EDA: EXAFS data analysis software package, Physica B: Condensed Matter 208 (1995) 175–176. `doi:10.1016/0921-4526(94)00663-G`.

[32] A. Kalinko, XAESA (2020).
URL `https://github.com/aklnk/xaesa`

[33] M. Newville, Larch: an analysis package for XAFS and related spectroscopies, in: J Phys Conf Ser, Vol. 430, 2013, p. 012007. `doi:10.1088/1742-6596/430/1/012007`.

[34] S. Calvin, XAFS for Everyone, CRC press, 2013.

[35] S. Zabinsky, J. Rehr, A. Ankudinov, R. Albers, M. Eller, Multiple-scattering calculations of X-ray-absorption spectra, Physical Review B 52 (1995) 2995. `doi:10.1103/PhysRevB.52.2995`.

[36] J. J. Rehr, J. J. Kas, M. P. Prange, A. P. Sorini, Y. Takimoto, F. Vila, Ab initio theory and calculations of X-ray spectra, Comptes Rendus Physique 10 (2009) 548–559. `doi:10.1016/j.crhy.2008.08.004`.

[37] A. Ankudinov, B. Ravel, J. Rehr, S. Conradson, Real-space multiple-scattering calculation and interpretation of x-ray-absorption near-edge structure, Physical Review B 58 (1998) 7565. `doi:10.1103/PhysRevB.58.7565`.

[38] I. Jonane, A. Anspoks, A. Kuzmin, Advanced approach to the local structure reconstruction and theory validation on the example of the W L_3-edge extended x-ray absorption fine structure of tungsten, Modelling and Simulation in Materials Science and Engineering 26 (2018) 025004. `doi:10.1088/1361-651X/aa9bab`.

[39] A. Filipponi, A. Di Cicco, C. R. Natoli, X-ray-absorption spectroscopy and n-body distribution functions in condensed matter. I. Theory, Physical Review B 52 (1995) 15122. `doi:10.1103/PhysRevB.52.15122`.

[40] O. Keski-Rahkonen, M. O. Krause, Total and partial atomic-level widths, At. Data Nucl. Data Tables 14 (1974) 139–146. `doi:10.1016/S0092-640X(74)80020-3`.

[41] J. Timoshenko, B. Roldan Cuenya, In Situ/Operando Electrocatalyst Characterization by X-ray Absorption Spectroscopy, Chemical Reviews 121 (2020) 882–961. `doi:10.1021/acs.chemrev.0c00396`.

[42] J. Evans, M. Tromp, X-ray Absorption Spectroscopy for the Chemical and Materials Sciences, Wiley Online Library, 2018.

[43] M. Benfatto, C. Meneghini, A close look into the low energy region of the XAS spectra: the XANES region, in: Synchrotron Radiation, Springer, 2015, pp. 213–240.

[44] J. J. Rehr, J. J. Kas, F. D. Vila, M. P. Prange, K. Jorissen, Parameter-free calculations of X-ray spectra with FEFF9, Physical Chemistry Chemical Physics 12 (2010) 5503–5513. `doi:10.1039/B926434E`.

[45] M. Benfatto, A. Congiu-Castellano, A. Daniele, S. Della Longa, MXAN: a new software procedure to perform geometrical fitting of experimental XANES spectra, Journal of Synchrotron Radiation 8 (2001) 267–269. `doi:10.1107/S0909049500015338`.

[46] G. Smolentsev, A. Soldatov, M. Feiters, Three-dimensional local structure refinement using a full-potential XANES analysis, Physical Review B 75 (2007) 144106. `doi:10.1103/PhysRevB.75.144106`.

[47] J. Timoshenko, A. I. Frenkel, “Inverting” X-ray absorption spectra of catalysts by machine learning in search for activity descriptors, ACS Catalysis 9 (2019) 10192–10211. `doi:10.1021/acscatal.9b03599`.

[48] M. Newville, EXAFS analysis using FEFF and FEFFIT, Journal of synchrotron radiation 8 (2001) 96–100. `doi:10.1107/S0909049500016290`.

[49] A. Kuzmin, J. Purans, Dehydration of the molybdenum trioxide hydrates $MoO_3 \cdot nH_2O$: in situ x-ray absorption spectroscopy study at the Mo K edge, Journal of Physics: Condensed Matter 12 (2000) 1959. `doi:10.1088/0953-8984/12/9/301`.

[50] P. Fornasini, R. Grisenti, On EXAFS Debye-Waller factor and recent advances, Journal of synchrotron radiation 22 (2015) 1242–1257. `doi:10.1107/S1600577515010759`.

[51] M. Vaccari, P. Fornasini, Einstein and Debye models for EXAFS parallel and perpendicular mean-square relative displacements, Journal of synchrotron radiation 13 (2006) 321–325.

[52] J. D. Gale, A. L. Rohl, The general utility lattice program (GULP), Mol. Simul. 29 (2003) 291. `doi:10.1080/0892702031000104887`.

[53] S. Plimpton, Fast parallel algorithms for short-range molecular dynamics, Journal of computational physics 117 (1995) 1–19. `doi:10.1006/jcph.1995.1039`.

[54] N. Metropolis, A. W. Rosenbluth, M. N. Rosenbluth, A. H. Teller, E. Teller, Equation of state calculations by fast computing machines, Journal of Chemical Physics 21 (1953) 1087–1092. `doi:10.1063/1.1699114`.

[55] R. McGreevy, L. Pusztai, Reverse Monte Carlo simulation: a new technique for the determination of disordered structures, Molecular simulation 1 (1988) 359–367. `doi:10.1080/08927028808080958`.

[56] J. Timoshenko, A. Anspoks, A. Cintins, A. Kuzmin, J. Purans, A. I. Frenkel, Neural network approach for characterizing structural transformations by X-ray absorption fine structure spectroscopy, Physical review letters 120 (2018) 225502. `doi:10.1103/PhysRevLett.120.225502`.

[57] F. F. Abraham, Computational statistical mechanics methodology, applications and supercomputing, Advances in Physics 35 (1986) 1–111. `doi:10.1080/00018738600101851`.

[58] W. F. Van Gunsteren, H. J. Berendsen, Computer simulation of molecular dynamics: methodology, applications, and perspectives in chemistry, Angewandte Chemie International Edition in English 29 (1990) 992–1023. `doi:10.1002/anie.199009921`.

[59] A. Kuzmin, R. Evarestov, Quantum mechanics–molecular dynamics approach to the interpretation of X-ray absorption spectra, Journal of Physics: Condensed Matter 21 (2009) 055401. `doi:10.1088/0953-8984/21/5/055401`.

[60] A. Kuzmin, A. Anspoks, A. Kalinko, J. Timoshenko, The use of X-ray absorption spectra for validation of classical force-field models, Zeitschrift für Physikalische Chemie 230 (2016) 537–549. `doi:10.1515/zpch-2015-0664`.

[61] M. W. Finnis, J. E. Sinclair, A simple empirical N-body potential for transition metals, Phil. Mag. A 50 (1984) 45–55. `doi:10.1080/01418618408244210`.

[62] B.-J. Lee, M. Baskes, H. Kim, Y. Koo Cho, Second nearest-neighbor modified embedded atom method potentials for bcc transition metals, Phys. Rev. B 64 (2001) 184102. `doi:10.1103/PhysRevB.64.184102`.

[63] A. Kuno, M. Matsuo, Nondestructive speciation of solid mixtures by multivariate calibration of X-ray absorption near-edge structure using artificial neural networks and partial least-squares, Analytical sciences 16 (2000) 597–602. `doi:10.2116/analsci.16.597`.

[64] J. Timoshenko, D. Lu, Y. Lin, A. I. Frenkel, Supervised machine-learning-based determination of three-dimensional structure of metallic nanoparticles, The journal of physical chemistry letters 8 (2017) 5091–5098. `doi:10.1021/acs.jpclett.7b02364`.

[65] Y. LeCun, Y. Bengio, G. Hinton, Deep learning, nature 521 (2015) 436–444. `doi:10.1038/nature14539`.

[66] M. G. Tucker, M. T. Dove, D. A. Keen, Application of the reverse Monte Carlo method to crystalline materials, Journal of applied crystallography 34 (2001) 630–638. `doi:10.1107/S002188980100930X`.

[67] D. Keen, M. Tucker, M. Dove, Reverse Monte Carlo modelling of crystalline disorder, Journal of Physics: Condensed Matter 17 (2005) S15. `doi:10.1088/0953-8984/17/5/002`.

[68] M. G. Tucker, D. A. Keen, M. T. Dove, A. L. Goodwin, Q. Hui, RMCProfile: reverse Monte Carlo for polycrystalline materials, Journal of Physics: Condensed Matter 19 (2007) 335218. `doi:10.1088/0953-8984/19/33/335218`.

[69] V. Petkov, N. Bedford, M. R. Knecht, M. G. Weir, R. M. Crooks, W. Tang, G. Henkelman, A. Frenkel, Periodicity and atomic ordering in nanosized particles of crystals, The Journal of Physical Chemistry C 112 (2008) 8907–8911. `doi:10.1021/jp801195c`.

[70] A. Kuzmin, J. Chaboy, EXAFS and XANES analysis of oxides at the nanoscale, IUCrJ 1 (2014) 571–589. `doi:10.1107/S2052252514021101`.

[71] M. Leetmaa, K. T. Wikfeldt, L. G. Pettersson, SpecSwap-RMC: a novel reverse Monte Carlo approach using a discrete set of local configurations and pre-computed properties, Journal of Physics: Condensed Matter 22 (2010) 135001. `doi:10.1088/0953-8984/22/13/135001`.

[72] O. Gereben, L. Pusztai, RMC_POT: a computer code for Reverse Monte Carlo modeling the structure of disordered systems containing molecules of arbitrary complexity, Journal of computational chemistry 33 (2012) 2285–2291. `doi:10.1002/jcc.23058`.

[73] S. Gurman, R. McGreevy, Reverse Monte Carlo simulation for the analysis of EXAFS data, Journal of Physics: Condensed Matter 2 (1990) 9463. `doi:10.1088/0953-8984/2/48/001`.

[74] J. Timoshenko, A. Kuzmin, J. Purans, Reverse Monte Carlo modeling of thermal disorder in crystalline materials from EXAFS spectra, Computer Physics Communications 183 (2012) 1237–1245. `doi:10.1016/j.cpc.2012.02.002`.

[75] J. Timoshenko, Reverse Monte Carlo modelling of structural and thermal disorder in crystalline materials, Ph.D. thesis, University of Latvia (2015).

[76] I. Jonane, J. Timoshenko, A. Kuzmin, EXAFS study of the local structure of crystalline and nanocrystalline Y_2O_3 using evolutionary algorithm method, in: IOP Conference Series: Materials Science and Engineering, Vol. 77, IOP Publishing, 2015, p. 012030. `doi:10.1088/1757-899X/77/1/012030`.

[77] I. Jonane, K. Lazdins, J. Timoshenko, A. Kuzmin, J. Purans, P. Vladimirov, T. Gräning, J. Hoffmann, Temperature-dependent EXAFS study of the local structure and lattice dynamics in cubic Y_2O_3, Journal of synchrotron radiation 23 (2016) 510–518. `doi:10.1107/S1600577516001181`.

[78] J. Timoshenko, A. Anspoks, A. Kalinko, I. Jonane, A. Kuzmin, Local structure of multiferroic $MnWO_4$ and $Mn_{0.7}Co_{0.3}WO_4$ revealed by the evolutionary algorithm, Ferroelectrics 483 (2015) 68–74. `doi:10.1080/00150193.2015.1058687`.

[79] J. Timoshenko, A. Anspoks, A. Kalinko, A. Kuzmin, Local structure of nanosized tungstates revealed by evolutionary algorithm, physica status solidi (a) 212 (2015) 265–273. `doi:10.1002/pssa.201431561`.

[80] A. Kalinko, M. Bauer, J. Timoshenko, A. Kuzmin, Molecular dynamics and reverse Monte Carlo modeling of scheelite-type AWO_4 ($A = $ Ca, Sr, Ba) W L_3-edge EXAFS spectra, Phys. Scr. 91 (2016) 114001. `doi:10.1088/0031-8949/91/11/114001`.

[81] J. Timoshenko, A. Anspoks, A. Kalinko, A. Kuzmin, Local structure of cobalt tungstate revealed by EXAFS spectroscopy and reverse Monte Carlo/evolutionary algorithm simulations, Zeitschrift für Physikalische Chemie 230 (2016) 551–568. `doi:10.1515/zpch-2015-0646`.

[82] I. Jonane, J. Timoshenko, A. Kuzmin, Atomistic simulations of the Fe K-edge EXAFS in FeF_3 using molecular dynamics and reverse Monte Carlo methods, Physica Scripta 91 (2016) 104001. `doi:10.1088/0031-8949/91/10/104001`.

[83] J. Timoshenko, A. Anspoks, A. Kalinko, A. Kuzmin, Thermal disorder and correlation effects in anti-perovskite-type copper nitride, Acta Materialia 129 (2017) 61–71. `doi:10.1016/j.actamat.2017.02.074`.

[84] I. Jonane, A. Anspoks, L. Nataf, F. Baudelet, T. Irifune, A. Kuzmin, Pressure-induced structural changes in α-MoO_3 probed by X-ray absorption spectroscopy, in: IOP Conference Series: Materials Science and Engineering, Vol. 503, IOP Publishing, 2019, p. 012018. `doi:10.1088/1757-899X/503/1/012018`.

[85] L. Nataf, F. Baudelet, A. Polian, I. Jonane, A. Anspoks, A. Kuzmin, T. Irifune, Recent progress in high pressure X-ray absorption spectroscopy studies at the ODE beamline, High Pressure Research (2020) 1–6`doi:10.1080/08957959.2019.1700979`.

[86] J. Purans, A. Menushenkov, S. Besedin, A. Ivanov, V. Minkov, I. Pudza, A. Kuzmin, K. Klementiev, S. Pascarelli, O. Mathon, et al., Local electronic structure rearrangements and strong anharmonicity in YH_3 under pressures up to 180 GPa, Nature Communications 12 (2021) 1–10. `doi:10.1038/s41467-021-21991-x`.

[87] I. Jonane, A. Anspoks, G. Aquilanti, A. Kuzmin, High-temperature X-ray absorption spectroscopy study of thermochromic copper molybdate, Acta Materialia 179 (2019) 26–35. `doi:10.1016/j.actamat.2019.06.034`.

[88] I. Jonane, A. Cintins, A. Kalinko, R. Chernikov, A. Kuzmin, Low temperature X-ray absorption spectroscopy study of $CuMoO_4$ and $CuMo_{0.90}W_{0.10}O_4$ using reverse Monte-Carlo method, Radiation Physics and Chemistry 175 (2020) 108411. `doi:0.1016/j.radphyschem.2019.108411`.

[89] I. Pudza, A. Anspoks, A. Cintins, A. Kalinko, E. Welter, A. Kuzmin, The influence of Zn^{2+} ions on the local structure and thermochromic properties of $Cu_{1-x}Zn_xMoO_4$ solid solutions, Materials Today Communications (2021) 102607`doi:10.1016/j.mtcomm.2021.102607`.

[90] M. Matsumoto, T. Nishimura, Mersenne twister: a 623-dimensionally equidistributed uniform pseudo-random number generator, ACM Transactions on Modeling and Computer Simulation (TOMACS) 8 (1998) 3–30. `doi:10.1145/272991.272995`.

[91] J. Timoshenko, A. Kuzmin, Wavelet data analysis of EXAFS spectra, Computer Physics Communications 180 (2009) 920–925. `doi:10.1016/j.cpc.2008.12.020`.

[92] S. Kirkpatrick, C. D. Gelatt, M. P. Vecchi, Optimization by simulated annealing, science 220 (1983) 671–680. `doi:10.1126/science.220.4598.671`.

[93] M. Daszykowski, K. Kaczmarek, Y. Vander Heyden, B. Walczak, Robust statistics in data analysis—A review: Basic concepts, Chemometrics and intelligent laboratory systems 85 (2007) 203–219. `doi:10.1016/j.chemolab.2006.06.016`.

[94] O. Durmeyer, J. Kappler, E. Beaurepaire, J. Heintz, M. Drillon, Ti K XANES in superconducting $LiTi_2O_4$ and related compounds, Journal of Physics: Condensed Matter 2 (1990) 6127. `doi:10.1088/0953-8984/2/28/004`.

[95] S. Nozawa, T. Iwazumi, H. Osawa, Direct observation of the quantum fluctuation controlled by ultraviolet irradiation in $SrTiO_3$, Physical Review B 72 (2005) 121101. `doi:10.1103/PhysRevB.72.121101`.

[96] D. Manuel, D. Cabaret, C. Brouder, P. Sainctavit, A. Bordage, N. Trcera, Experimental evidence of thermal fluctuations on the X-ray absorption near-edge structure at the aluminum K edge, Physical Review B 85 (2012) 224108. `doi:10.1103/PhysRevB.85.224108`.

[97] R. Nemausat, D. Cabaret, C. Gervais, C. Brouder, N. Trcera, A. Bordage, I. Errea, F. Mauri, Phonon effects on x-ray absorption and nuclear magnetic resonance spectroscopies, Physical Review B 92 (2015) 144310. `doi:10.1103/PhysRevB.92.144310`.

[98] R. Nemausat, C. Gervais, C. Brouder, N. Trcera, A. Bordage, C. Coelho-Diogo, P. Florian, A. Rakhmatullin, I. Errea, L. Paulatto, et al., Temperature dependence of X-ray absorption and nuclear magnetic resonance spectra: probing quantum vibrations of light elements in oxides, Physical Chemistry Chemical Physics 19 (2017) 6246–6256. `doi:10.1039/C6CP08393E`.

[99] H. A. Kramers, W. Heisenberg, Über die Streuung von Strahlung durch Atome, Z. Physik 31 (1925) 681–708. `doi:10.1007/BF02980624`.

[100] J.-P. Rueff, A. Shukla, Inelastic x-ray scattering by electronic excitations under high pressure, Rev. Mod. Phys. 82 (2010) 847–896. `doi:10.1103/RevModPhys.82.847`.

[101] P. Glatzel, M. Sikora, G. Smolentsev, M. Fernández-García, Hard X-ray photon-in photon-out spectroscopy, Catalysis Today 145 (2009) 294–299. `doi:10.1016/j.cattod.2008.10.049`.

[102] J.-P. Rueff, A. Shukla, A RIXS cookbook: Five recipes for successful RIXS applications, J. Electron Spectrosc. Relat. Phenom. 188 (2013) 10–16. `doi:10.1016/j.elspec.2013.04.014`.

[103] M. Rovezzi, P. Glatzel, Hard x-ray emission spectroscopy: a powerful tool for the characterization of magnetic semiconductors, Semicond. Sci. Technol. 29 (2014) 023002. `doi:10.1088/0268-1242/29/2/023002`.

[104] P. Glatzel, U. Bergmann, High resolution 1s core hole X-ray spectroscopy in 3d transition metal complexes—electronic and structural information, Coordination chemistry reviews 249 (2005) 65–95. `doi:10.1016/j.ccr.2004.04.011`.

[105] O. Lundquist, Über die$K\beta$-Linien in den Röntgenemissionsspektra der Elemente Phosphor und Kalium, Zeitschrift für Physik 33 (1925) 901–915. `doi:10.1007/BF01328379`.

[106] D. Coster, M. Druyvesteyn, Über die Satelliten der Röntgendiagrammlinien, Zeitschrift für Physik 40 (1927) 765–774. `doi:10.1007/BF01400235`.

[107] A. Wach, J. Sá, J. Szlachetko, Comparative study of the around-Fermi electronic structure of $5d$ metals and metal-oxides by means of high-resolution X-ray emission and absorption spectroscopies, J. Synchrotron Rad. 27 (2020) 689–694. `doi:10.1107/S1600577520003690`.

[108] v. Hámos, L, Röntgenspektroskopie und Abbildung mittels gekrümmter Kristallreflektoren, Naturwissenschaften 20 (1932) 705–706.

[109] H. H. Johann, Die erzeugung lichtstarker röntgenspektren mit hilfe von konkavkristallen, Zeitschrift für Physik 69 (1931) 185–206. `doi:10.1007/BF01798121`.

[110] W. Błachucki, J. Hoszowska, J.-C. Dousse, Y. Kayser, R. Stachura, K. Tyrała, K. Wojtaszek, J. Sá, J. Szlachetko, High energy resolution off-resonant spectroscopy: A review, Spectrochimica Acta B 136 (2017) 23–33. `doi:10.1016/j.sab.2017.08.002`.

[111] I. Pudza, A. Kalinko, A. Cintins, A. Kuzmin, Study of the thermochromic phase transition in $\mathrm{CuMo_{1-x}W_xO_4}$ solid solutions at the W L_3-edge by resonant X-ray emission spectroscopy, Acta Materialia 205 (2021) 116581. `doi:10.1016/j.actamat.2020.116581`.

[112] L. Zhang, S. Zheng, L. Wang, H. Tang, H. Xue, G. Wang, H. Pang, Fabrication of metal molybdate micro/nanomaterials for electrochemical energy storage, Small 13 (2017) 1700917. `doi:10.1002/smll.201700917`.

[113] V. Blanco-Gutierrez, L. Cornu, A. Demourgues, M. Gaudon, $\mathrm{CoMoO_4/CuMo_{0.9}W_{0.1}O_4}$ mixture as an efficient piezochromic sensor to detect temperature/pressure shock parameters, ACS applied materials & interfaces 7 (2015) 7112–7117. `doi:10.1021/am508652h`.

[114] Q. Morelle, S. Senani, L. Nicole, M. Gaudon, L. Rozes, E. Le Bourhis, Hybrid piezochromic coatings for impact detection on composite substrates for aeronautic, Materials Letters 253 (2019) 140–143. `doi:10.1016/j.matlet.2019.06.045`.

[115] W. Zhang, J. Yin, F. Min, L. Jia, D. Zhang, Q. Zhang, J. Xie, Preparation and photoluminescence properties of $\mathrm{MMoO_4}$ (M= Cu, Ni, Zn) nano-particles synthesized via electrolysis, J. Mol. Struct. 1127 (2017) 777–783. `doi:10.1016/j.molstruc.2016.08.020`.

[116] K. S. Makarevich, N. V. Lebukhova, P. G. Chigrin, N. F. Karpovich, Catalytic Properties of $\mathrm{CuMoO_4}$ Doped with Co, Ni, and Ag, Inorg. Mater. 46 (2010) 1359–1364. `doi:10.1134/S0020168510120162`.

[117] P. Chigrin, N. Lebukhova, A. Y. Ustinov, Structural transformations of $CuMoO_4$ in the catalytic oxidation of carbon, Kinetics and Catalysis 54 (2013) 76–80. `doi:10.1134/S0023158413010035`.

[118] J. Baek, A. S. Sefat, D. Mandrus, P. S. Halasyamani, A new magnetically ordered polymorph of $CuMoO_4$: synthesis and characterization of ε-$CuMoO_4$, Chemistry of Materials 20 (2008) 3785–3787. `doi:10.1021/cm801162j`.

[119] S. Hara, H. Sato, Structure and magnetism of novel copper molybdenum oxides η-$CuMoO_4$ and β-$Cu_3Mo_2O_9$, J. Phys. Soc. Japan 82 (2013) 054802. `doi:10.7566/JPSJ.82.054802`.

[120] F. Rodríguez, D. Hernández, J. Garcia-Jaca, H. Ehrenberg, H. Weitzel, Optical study of the piezochromic transition in $CuMoO_4$ by pressure spectroscopy, Phys. Rev. B 61 (2000) 16497–16501. `doi:10.1103/PhysRevB.61.16497`.

[121] H. Ehrenberg, H. Weitzel, H. Paulus, M. Wiesmann, G. Wltschek, M. Geselle, H. Fuess, Crystal structure and magnetic properties of $CuMoO_4$ at low temperature (γ-phase), J. Phys. Chem. Solids 58 (1997) 153–160. `doi:10.1016/S0022-3697(96)00108-4`.

[122] T. Ito, H. Takagi, T. Asano, Drastic and sharp change in color, shape, and magnetism in transition of $CuMoO_4$ single crystals, Chem. Mater. 21 (2009) 3376–3379. `doi:10.1021/cm901029v`.

[123] C. Fu, X. Wu, J. Cao, C. Gu, W. Liu, Oxygen-vacancy and charge hopping related dielectric relaxation of $CuMoO_4$ ceramic, Physica B: Condensed Matter 573 (2019) 62–66. `doi:10.1016/j.physb.2019.08.029`.

[124] R. Kohlmuller, J.-P. Faurie, MoO_3-CuO system, C. R. Acad. Sci., Ser. C 264 (1967) 1751–1752.

[125] I. E. Sajó, L. P. Bakos, I. M. Szilágyi, G. Lendvay, J. Magyari, M. Mohai, Á. Szegedi, A. Farkas, A. Jánosity, S. Klébert, et al., Unexpected sequential NH_3/H_2O solid/gas phase ligand exchange and quasi-intramolecular self-protonation yield $[NH_4Cu(OH)MoO_4]$, a photocatalyst misidentified before as $(NH_4)_2Cu(MoO_4)_2$, Inorganic chemistry 57 (2018) 13679–13692. `doi:10.1021/acs.inorgchem.8b02261`.

[126] S. C. Abrahams, J. L. Bernstein, P. B. Jamieson, Crystal structure of the transition-metal molybdates and tungstates. IV. Paramagnetic $CuMoO_4$, J. Chem. Phys. 48 (1968) 2619–2629. `doi:10.1063/1.1669492`.

[127] S. Abrahams, Crystal structure of the transition-metal molybdates and tungstates. III. Diamagnetic α-$ZnMoO_4$, The Journal of Chemical Physics 46 (1967) 2052–2063. `doi:10.1063/1.1841001`.

[128] W. Reichelt, T. Weber, T. Söhnel, S. Däbritz, Mischkristallbildung im System $CuMoO_4/ZnMoO_4$, Zeitschrift für anorganische und allgemeine Chemie 626 (2000) 2020–2027. `doi:10.1002/1521-3749(200009)626:9<2020::AID-ZAAC2020>3.0.CO;2-K`.

[129] J. Forsyth, C. Wilkinson, A. Zvyagin, The antiferromagnetic structure of copper tungstate, $CuWO_4$, J. Phys.: Condens. Matter 3 (1991) 8433. `doi:10.1088/0953-8984/3/43/010`.

[130] D. Hernández, F. Rodrıguez, J. Garcia-Jaca, H. Ehrenberg, H. Weitzel, Pressure-dependence on the absorption spectrum of $CuMoO_4$: study of the green→ brownish-red piezochromic phase transition at 2.5 kbar, Physica B: Condensed Matter 265 (1999) 181–185. `doi:10.1016/S0921-4526(98)01366-0`.

[131] S. Dey, R. A. Ricciardo, H. L. Cuthbert, P. M. Woodward, Metal-to-metal charge transfer in AWO_4 (A = Mg, Mn, Co, Ni, Cu, or Zn) compounds with the wolframite structure, Inorg. Chem. 53 (2014) 4394. `doi:10.1021/ic4031798`.

[132] M. Benchikhi, R. El Ouatib, S. Guillemet-Fritsch, L. Er-Rakho, B. Durand, Characterization and photoluminescence properties of ultrafine copper molybdate (α-$CuMoO_4$) powders prepared via a combustion-like process, International Journal

of Minerals, Metallurgy, and Materials 23 (2016) 1340–1345. `doi:10.1007/s12613-016-1356-3`.

[133] M. Benchikhi, R. El Ouatib, S. Guillemet-Fritsch, L. Er-Rakho, B. Durand, Investigation of structural transition in molybdates $CuMo_{1-x}W_xO_4$ prepared by polymeric precursor method, Processing and Application of Ceramics 11 (2017) 21–26. `doi:10.2298/PAC1701021B`.

[134] I. Yanase, R. Koda, R. Kondo, R. Taiji, Improvement of thermochromic property at low temperatures of $CuMo_{0.94}W_{0.06}O_4$ by Zn substitution, Journal of Thermal Analysis and Calorimetry (2019) 1–12`doi:10.1007/s10973-019-09025-7`.

[135] U. Steiner, W. Reichelt, S. Däbritz, Chemischer Transport von Mischkristallen im System $CuMoO_4$/$ZnMoO_4$, Zeitschrift für anorganische und allgemeine Chemie 629 (2003) 116–122. `doi:10.1002/zaac.200390002`.

[136] A. Sleight, B. Chamberland, Transition metal molybdates of the type $AMoO_4$, Inorganic Chemistry 7 (1968) 1672–1675. `doi:10.1021/ic50066a050`.

[137] T. Asano, T. Nishimura, S. Ichimura, Y. Inagaki, T. Kawae, T. Fukui, Y. Narumi, K. Kindo, T. Ito, S. Haravifard, et al., Magnetic ordering and tunable structural phase transition in the chromic compound $CuMoO_4$, Journal of the Physical Society of Japan 80 (2011) 093708. `doi:10.1143/JPSJ.80.093708`.

[138] S. K. Tiwari, A. Singh, P. Yadav, B. K. Sonu, R. Verma, S. Rout, E. Sinha, Structural and dielectric properties of Cu-doped α-$ZnMoO_4$ ceramic system for enhanced green light emission and potential microwave applications, Journal of Materials Science: Materials in Electronics (2020) 1–9`doi:10.1007/s10854-020-04225-6`.

[139] L. Cornu, V. Jubera, A. Demourgues, G. Salek, M. Gaudon, Luminescence properties and pigment properties of A-doped (Zn, Mg) MoO_4 triclinic oxides (with A= Co, Ni, Cu or Mn), Ceramics International 43 (2017) 13377–13387. `doi:10.1016/j.ceramint.2017.07.040`.

[140] L.-Y. Zhou, J.-S. Wei, F.-Z. Gong, J.-L. Huang, L.-H. Yi, A potential red phosphor $ZnMoO_4$:Eu^{3+} for light-emitting diode application, Journal of Solid State Chemistry 181 (2008) 1337–1341. `doi:10.1016/j.jssc.2008.03.005`.

[141] X. Ju, X. Li, W. Li, W. Yang, C. Tao, Luminescence properties of $ZnMoO_4$:Tb^{3+} green phosphor prepared via co-precipitation, Materials Letters 65 (2011) 2642–2644. `doi:10.1016/j.matlet.2011.05.105`.

[142] A. E. S. Raj, C. Mallika, K. Swaminathan, O. Sreedharan, K. Nagaraja, Zinc (II) oxide-zinc (II) molybdate composite humidity sensor, Sensors and Actuators B: Chemical 81 (2002) 229–236. `doi:0.1016/S0925-4005(01)00957-1`.

[143] V. Mikhailik, H. Kraus, D. Wahl, H. Ehrenberg, M. Mykhaylyk, Optical and luminescence studies of $ZnMoO_4$ using vacuum ultraviolet synchrotron radiation, Nuclear Instruments and Methods in Physics Research Section A: Accelerators, Spectrometers, Detectors and Associated Equipment 562 (2006) 513–516. `doi:10.1016/j.nima.2006.03.005`.

[144] D. Spassky, A. Vasil'Ev, I. Kamenskikh, V. Kolobanov, V. Mikhailin, A. Savon, L. Ivleva, I. Voronina, L. Berezovskaya, Luminescence investigation of zinc molybdate single crystals, physica status solidi (a) 206 (2009) 1579–1583. `doi:10.1002/pssa.200824311`.

[145] N. Leyzerovich, K. Bramnik, T. Buhrmester, H. Ehrenberg, H. Fuess, Electrochemical intercalation of lithium in ternary metal molybdates $MMoO_4$ (M: Cu, Zn, Ni and Fe), Journal of power sources 127 (2004) 76–84. `doi:10.1016/j.jpowsour.2003.09.010`.

[146] B. Del Amo, R. Romagnoli, V. Vetere, Performance of zinc molybdenum phosphate in anticorrosive paints by accelerated and electrochemical tests, Journal of applied electrochemistry 29 (1999) 1401–1407. `doi:10.1023/A:1003887614368`.

[147] M. Gaudon, A.-E. Thiry, A. Largeteau, P. Deniard, S. Jobic, J. Majimel, A. Demourgues, Characterization of the Piezochromic Behavior of Some Members of the $CuMo_{1-x}W_xO_4$ Series, Inorganic chemistry 47 (2008) 2404–2410. `doi:10.1021/ic702282t`.

[148] A. Kuzmin, R. Kalendarev, A. Kursitis, J. Purans, Confocal spectromicroscopy of amorphous and nanocrystalline tungsten oxide films, J. Non-Cryst. Solids 353 (2007) 1840–1843.

[149] J. Ruiz-Fuertes, D. Errandonea, R. Lacomba-Perales, A. Segura, J. González, F. Rodríguez, F. J. Manjón, S. Ray, P. Rodríguez-Hernández, A. Muñoz, Z. Zhu, C. Y. Tu, High-pressure structural phase transitions in $CuWO_4$, Phys. Rev. B 81 (2010) 224115. `doi:10.1103/PhysRevB.81.224115`.

[150] A. Kuzmin, A. Kalinko, R. Evarestov, Ab initio LCAO study of the atomic, electronic and magnetic structures and the lattice dynamics of triclinic $CuWO_4$, Acta Mater. 61 (2013) 371–378. `doi:10.1016/j.actamat.2012.10.002`.

[151] N. Joseph, J. Varghese, T. Siponkoski, M. Teirikangas, M. T. Sebastian, H. Jantunen, Glass-free $CuMoO_4$ ceramic with excellent dielectric and thermal properties for ultralow temperature cofired ceramic applications, ACS Sustain. Chem. Eng. 4 (2016) 5632–5639. `doi:10.1021/acssuschemeng.6b01537`.

[152] E. Welter, R. Chernikov, M. Herrmann, R. Nemausat, A beamline for bulk sample x-ray absorption spectroscopy at the high brilliance storage ring PETRA III, in: AIP Conference Proceedings, Vol. 2054, AIP Publishing LLC, 2019, p. 040002. `doi:10.1063/1.5084603`.

[153] A. Di Cicco, G. Aquilanti, M. Minicucci, E. Principi, N. Novello, A. Cognigni, L. Olivi, Novel XAFS capabilities at ELETTRA synchrotron light source, in: J. Phys.: Conf. Ser., Vol. 190, 2009, p. 012043. `doi:10.1088/1742-6596/190/1/012043`.

[154] W. A. Caliebe, V. Murzin, A. Kalinko, M. Görlitz, High-flux XAFS-beamline P64 at PETRA III, AIP Conf. Proc. 2054 (2019) 060031. `doi:10.1063/1.5084662`.

[155] A. Kalinko, W. A. Caliebe, R. Schoch, M. Bauer, A von Hamos-type hard X-ray spectrometer at the PETRA III beamline P64, J. Synchrotron Rad. 27 (2020) 31–36. `doi:10.1107/S1600577519013638`.

[156] A. Kuzmin, J. Purans, X-ray absorption spectroscopy study of the local environment around tungsten and molybdenum ions in tungsten-phosphate and molybdenum-phosphate glasses, Proc.SPIE 2968 (1997) 180. `doi:10.1117/12.266831`.

[157] A. Kuzmin, J. Purans, P. Parent, H. Dexpert, Low and high-temperature in situ X-ray absorption study of the local order in orthorhombic α-MoO_3 upon hydrogen reduction, Le Journal de Physique IV 7 (1997) C2–891. `doi:10.1051/jp4:1997267`.

[158] F. Rocca, A. Kuzmin, P. Mustarelli, C. Tomasi, A. Magistris, XANES and EXAFS at Mo K-edge in $(AgI)_{1-x}(Ag_2MoO_4)_x$ glasses and crystals, Solid State Ionics 121 (1999) 189–192. `doi:10.1016/S0167-2738(98)00546-3`.

[159] L. Hedin, B. I. Lundqvist, Explicit local exchange-correlation potentials, J. Phys. C: Solid State Phys. 4 (1971) 2064–2083. `doi:10.1088/0022-3719/4/14/022`.

[160] A. Kuzmin, R. Grisenti, Evaluation of multiple-scattering contribution in extended X-ray absorption fine structure for MO_4 and MO_6 clusters, Phil. Mag. B 70 (1994) 1161. `doi:10.1080/01418639408240281`.

[161] A. Senyshyn, H. Kraus, V. B. Mikhailik, L. Vasylechko, M. Knapp, Thermal properties of $CaMoO_4$: Lattice dynamics and synchrotron powder diffraction studies, Phys. Rev. B 73 (2006) 014104. `doi:10.1103/PhysRevB.73.014104`.

[162] I. Jonane, A. Cintins, A. Kalinko, R. Chernikov, A. Kuzmin, Probing the thermochromic phase transition in $CuMoO_4$ by EXAFS spectroscopy, Physica Status Solidi (B) 255 (2018) 1800074. `doi:10.1002/pssb.201800074`.

[163] I. Jonane, A. Cintins, A. Kalinko, R. Chernikov, A. Kuzmin, X-ray absorption near edge spectroscopy of thermochromic phase transition in $CuMoO_4$, Low Temperature Physics 44 (2018) 434–437. `doi:10.1063/1.5034155`.

[164] K.-i. Shimizu, H. Maeshima, H. Yoshida, A. Satsuma, T. Hattori, Ligand field effect on the chemical shift in XANES spectra of Cu(II) compounds, Phys. Chem. Chem. Phys. 3 (2001) 862–866. `doi:10.1039/B007276L`.

[165] A. Kuzmin, A. Anspoks, A. Kalinko, A. Rumjancevs, J. Timoshenko, L. Nataf, F. Baudelet, T. Irifune, Effect of pressure and temperature on the local structure and lattice dynamics of copper(II) oxide, Phys. Procedia 85 (2016) 27–35. `doi:10.1016/j.phpro.2016.11.077`.

[166] D. A. Spassky, A. N. Vasil'ev, I. A. Kamenskikh, V. V. Mikhailin, A. E. Savon, Y. A. Hizhnyi, S. G. Nedilko, P. A. Lykov, Electronic structure and luminescence mechanisms in $ZnMoO_4$ crystals, J. Phys.: Condens. Matter 23 (2011) 365501. `doi:10.1088/0953-8984/23/36/365501`.

[167] D. Spassky, S. Ivanov, I. Kitaeva, V. Kolobanov, V. Mikhailin, L. Ivleva, I. Voronina, Optical and luminescent properties of a series of molybdate single crystals of scheelite crystal structure, Phys. Status Solidi C 2 (2005) 65–68. `doi:10.1002/pssc.200460112`.

[168] Y. Zhang, N. A. W. Holzwarth, R. T. Williams, Electronic band structures of the scheelite materials $CaMoO_4$, $CaWO_4$, $PbMoO_4$, and $PbWO_4$, Phys. Rev. B 57 (1998) 12738–12750. `doi:10.1103/PhysRevB.57.12738`.

[169] L. Cavalcante, E. Moraes, M. Almeida, C. Dalmaschio, N. Batista, J. Varela, E. Longo, M. S. Li, J. Andres, A. Beltran, A combined theoretical and experimental study of electronic structure and optical properties of β-$ZnMoO_4$ microcrystals, Polyhedron 54 (2013) 13–25. `doi:10.1016/j.poly.2013.02.006`.

[170] S. Yamazoe, Y. Hitomi, T. Shishido, T. Tanaka, XAFS study of tungsten L_1- and L_3-edges: structural analysis of WO_3 species loaded on TiO_2 as a catalyst for photo-oxidation of NH_3, J. Phys. Chem. C 112 (2008) 6869–6879. `doi:10.1021/jp711250f`.

[171] U. Jayarathne, P. Chandrasekaran, A. F. Greene, J. T. Mague, S. DeBeer, K. M. Lancaster, S. Sproules, J. P. Donahue, X-ray absorption spectroscopy systematics at the tungsten L-edge, Inorg. Chem. 53 (2014) 8230–8241. `doi:10.1021/ic500256a`.

[172] O. Keski-Rahkonen, M. O. Krause, Total and partial atomic-level widths, At. Data Nucl. Data Tables 14 (1974) 139–146. `doi:10.1016/S0092-640X(74)80020-3`.

[173] J. Timoshenko, A. Anspoks, A. Kalinko, A. Kuzmin, Analysis of extended x-ray absorption fine structure data from copper tungstate by the reverse Monte Carlo method, Physica Scripta 89 (2014) 044006. `doi:10.1088/0031-8949/89/04/044006`.

[174] M. Kunz, I. D. Brown, Out-of-center distortions around octahedrally coordinated d^0 transition metals, Journal of Solid State Chemistry 115 (1995) 395–406. `doi:10.1006/jssc.1995.1150`.

[175] B. C. Schwarz, H. Ehrenberg, H. Weitzel, H. Fuess, Investigation on the Influence of Particular Structure Parameters on the Anisotropic Spin-Exchange Interactions in the Distorted Wolframite-Type Oxides $CuMo_xW_{1-x}O_4$, Inorganic chemistry 46 (2007) 378–380. `doi:10.1021/ic061944d`.

[176] A. Balerna, E. Bernieri, E. Burattini, A. Kuzmin, A. Lusis, J. Purans, P. Cikmach, XANES studies of MeO_{3-x} (Me = W, Re, Ir) crystalline and amorphous oxides, Nucl. Instrum. Methods Phys. Res. A 308 (1991) 240–242. `doi:10.1016/0168-9002(91)90637-6`.

[177] A. Kuzmin, J. Purans, X-ray absorption spectroscopy study of the local environment around tungsten and molybdenum ions in tungsten-phosphate and molybdenum-phosphate glasses, Proc. SPIE 2968 (1997) 180–185. `doi:10.1117/12.266831`.

[178] P. Charton, L. Gengembre, P. Armand, TeO_2–WO_3 glasses: infrared, XPS and XANES structural characterizations, J. Solid State Chem. 168 (2002) 175–183. `doi:10.1006/jssc.2002.9707`.

[179] I. B. Bersuker, Electronic Structure and Properties of Transition Metal Compounds: Introduction to the Theory, 2nd Edition, John Wiley & Sons, Hoboken, New Jersey, 2010. `doi:10.1002/9780470573051`.

[180] M. Brown, R. E. Peierls, E. A. Stern, White lines in x-ray absorption, Phys. Rev. B 15 (1977) 738–744. `doi:10.1103/PhysRevB.15.738`.

[181] von Hans Weitzel, Magnetische struktur von $CoWO_4$, $NiWO_4$ und $CuWO_4$, Solid State Commun. 8 (1970) 2071–2072. `doi:10.1016/0038-1098(70)90221-8`.

[182] E. Sevillano, H. Meuth, J. Rehr, Extended x-ray absorption fine structure Debye-Waller factors. I. Monatomic crystals, Phys. Rev. B 20 (1979) 4908. `doi:10.1103/PhysRevB.20.4908`.

Acknowledgements

I want to express sincere gratitude to my supervisor Dr. phys. Alexei Kuzmin who helped, motivated and guided me during the whole period of my PhD studies. His immense knowledge, plentiful experience and continuous support have encouraged me in all the time of my research and daily life. I am genuinely grateful for the possibility to work under his leadership.

I would also like to express my special thanks to Dr. phys. Janis Timoshenko, who supported and inspired me during my first steps in science when I started work at the Institute during my Bachelor studies.

I would like to acknowledge my colleagues from the EXAFS spectroscopy laboratory - M.Sc. Arturs Cintins, Dr. phys. Andris Anspoks, Dr. rer. nat. Georgijs Bakradze - for the great working atmosphere they created in our laboratory and at synchrotron beamlines, conferences and schools all around Europe. A separate acknowledgement is expressed to Dr. phys. Aleksandr Kalinko for invaluable help and care during the experiments at PETRA III synchrotron.

And, of course, many thanks to my family for the patience and support throughout my studies. Special thanks to my husband Kaspars, mum Lolita and sister Laura. Thanks also to Ilze Oshina – my soulmate during the whole studies at the university.

I would like to thank the Institute of Solid State Physics for being a nice place where to work and develop my career. Additionally, I would like to acknowledge Scientific Research Projects for Students and Young Researchers No. SJZ/2017/5, No. SJZ/2018/1 and No. SJZ/2019/1 realized at the Institute of Solid State Physics, University of Latvia. Institute of Solid State Physics, University of Latvia as the Center of Excellence has received funding from the European Union's Horizon 2020 Framework Programme H2020-WIDESPREAD-01-2016-2017-TeamingPhase2 under grant agreement No. 739508, project CAMART2.

I also want to thank the Faculty of Physics, Mathematics and Optometry of the University of Latvia for the support during studies and research.

This research was financially supported by philanthropist MikroTik and administrated by the University of Latvia Foundation. This support was precious during my PhD studies.

Finally, I am deeply honoured for the prestigious prize in the year 2021 from the L'ORÉAL Baltic "For Women In Science" Program with the support of the Latvian National Commission for UNESCO and the Latvian Academy of Sciences.

LATVIJAS UNIVERSITĀTES
CIETVIELU FIZIKAS INSTITŪTS
INSTITUTE OF SOLID STATE PHYSICS
UNIVERSITY OF LATVIA

MikroTik

UNIVERSITY OF LATVIA
FOUNDATION

For Women
in Science
UNESCO
FONDATION
L'ORÉAL